US Department of Transportation Federal Highway Administration
Research, Development, and Technology Turner-Fairbank Highway
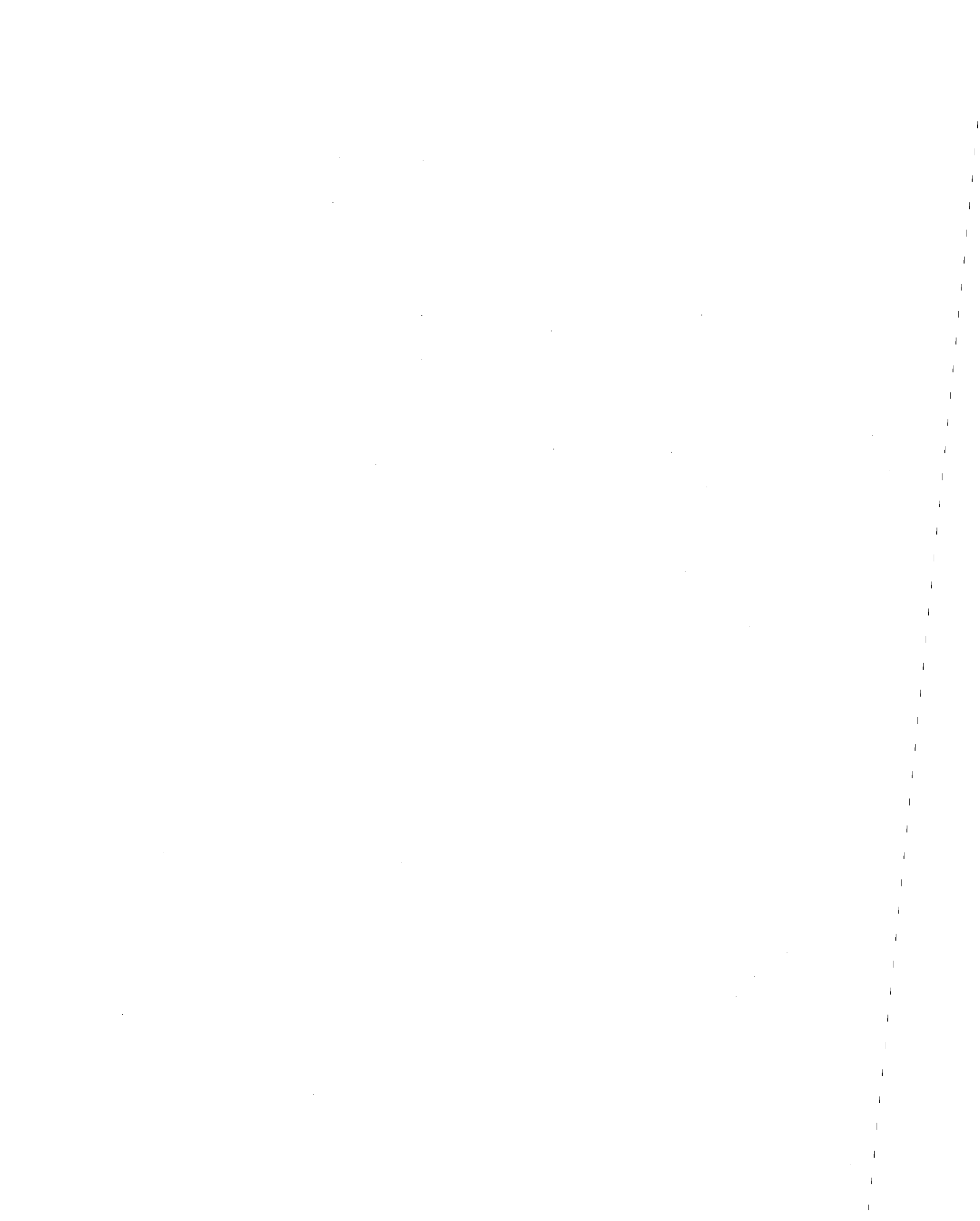Research Center 6300 Georgetown Pike McLean, VA 22101-2296

A Predictive Approach for Long-Term Performance of Recycled
Materials Using Accelerated Aging, Volume 2: Appendices

FHWA-RD-01-023

June 2001

FOREWORD

There is increasing interest in the use of recycled materials in the highway environment on the part of States, municipalities, the private sector and the public. As stewards of the Nation's highways, FHWA desires to maintain a quality infrastructure and good roads. Use of recycled materials must promote this concept. Substitution of alternative materials must provide the same economic, engineering, and environmental benefits as traditional materials.

Using recycled materials in a proposed highway application frequently requires assessment of both the physical and environmental performance; however, future behavior is often difficult to predict and long-term results of actual field installations are often unavailable. The objective of this research was to investigate an approach to predicting long-term physical and environmental performance of candidate recycled materials in typical highway applications using accelerated aging. The project was geared specifically towards the use of recycled materials in Portland cement concrete, but similar approaches may be possible for other materials.

The accelerated aging methodology investigated in this project allows the researcher or materials engineer to explore the phenomenon of aging, the complex interactions between physical and environmental performance that occur during aging, and the potential compatibility of candidate recycled materials in a portland cement concrete matrix under controlled conditions. Such aging methods could eventually become standard practices for predicting future behavior.

T. Paul Teng, P.E.
Director, Office of Infrastructure
Research and Development

NOTICE

This document is disseminated under the sponsorship of the Department of Transportation in the interest of information exchange. The United States Government assumes no liability for its contents or use thereof. This report does not constitute a standard, specification, or regulation.

The United States Government does not endorse products or manufacturers. Trade and manufacturers' names appear in this report only because they are considered essential to the object of this document.

1. Report No. FHWA-RD-01-023	2. Government Accession No.	3. Recipient's Catalog No.

4. Title and Subtitle A Predictive Approach for Long-Term Performance of Recycled Materials Using Accelerated Aging Volume 2: Appendices		5. Report Date June 2001
		6. Performing Organization Code 480017
7. Author(s) T.T Eighmy, R.A. Cook, A. Coviello, J.C.M. Spear, K.C. Hover, et. al.		8. Performing Organization Report No.
9. Performing Organization Name and Address University of New Hampshire Recycled Materials Resource Center 120 Nesmith Hall Durham, NH 03824		10. Work Unit No. (TRAIS)
		11. Contract or Grant No. DTFH61-97-X-00021
12. Sponsoring Agency Name and Address Federal Highway Administration Office of Infrastructure R&D 6300 Georgetown Pike McLean, VA 22101		13. Type of Report and Period Covered Final Report Sept. 1997 - Jan. 2001
		14. Sponsoring Agency Code

15. Supplementary Notes
Agreement Officer's Technical Representative (AOTR): Marcia Simon (HRDI-12)

16. Abstract
Use of recycled materials in a proposed highway application frequently requires the assessment of physical and environmental performance. Future behavior is often difficult to predict. As an alternative to field demonstrations, there is a need to develop strategies to predict long-term physical and environmental performance. Accelerated aging is one means of exploring the long-term physical and environmental performance of recycled materials in a highway.

Coal fly ash (CFA) use in portland cement concrete (PCC) was selected as a model system to develop an accelerated aging approach. Three types of accelerated aging were chosen for this project: Arrhenius aging (AA), cyclic loading (CL), and freeze-thaw exposure (FT). This approach, incorporated in an experimental design, allowed a systematic exploration of the separate effects and combined interactions of both developmental and degradative accelerated aging variables. A slab from U.S. Route 20 in northwest Iowa was used as a both the basis for the concrete mixes and as a field verification site.

The aging protocol impacted both physical and chemical properties of the prism monoliths. Generally speaking, the main effects were more important than the interactive effects, which was unexpected. It took about 9 months of elapsed time to age specimens to an equivalent age of up to 4 years. The equivalent ages matched well with the time frame seen in the field in Iowa for the onset of early distress and also matched well the chronological age of the field pavement. AA significantly reduced the compressive strength of the concrete, possibly indicating the onset of a deleterious reaction in the mix. CL affected the microcracking in the concrete. All aging variables affected the fine pore structure of the concrete. CL affected the Ca diffusional leaching from the monoliths. Logically, there appears to be a linkage between strength loss, microcracking, and leaching behavior of a major matrix constituent in the concrete (notably Ca). Most response variables from the aged laboratory prisms and the field samples were similar, suggesting that the method did a reasonable job of producing a laboratory pavement of similar age and distress to the field pavement. Certain field aging phenomena (microcracking from unknown sources, road salting, and carbonation) could not be recreated in the laboratory specimens.

17. Key Words recycled materials, accelerated aging, Arrhenius aging, cyclical loading, freeze-thaw distress, coal fly ash, portland cement concrete, physical properties, leaching, geochemical modeling	18. Distribution Statement No restrictions. This document is available to the public through the National Technical Information Service, Springfield, Virginia, 22161

19. Security Classif. (of this report) Unclassified	20. Security Classif. (of this page) Unclassified	21. No. of Pages 223	22. Price

Form DOT F 1700.7 (8-72) Reproduction of completed page authorized

This form was electronically produced by Elite Federal Forms, Inc.

SI* (MODERN METRIC) CONVERSION FACTORS

APPROXIMATE CONVERSIONS TO SI UNITS

Symbol	When You Know	Multiply By	To Find	Symbol
LENGTH				
in	inches	25.4	millimeters	mm
ft	feet	0.305	meters	m
yd	yards	0.914	meters	m
mi	miles	1.61	kilometers	km
AREA				
in²	square inches	645.2	square millimeters	mm²
ft²	square feet	0.093	square meters	m²
yd²	square yards	0.836	square meters	m²
ac	acres	0.405	hectares	ha
mi²	square miles	2.59	square kilometers	km²
VOLUME				
fl oz	fluid ounces	29.57	milliliters	mL
gal	gallons	3.785	liters	L
ft³	cubic feet	0.028	cubic meters	m³
yd³	cubic yards	0.765	cubic meters	m³

NOTE: Volumes greater than 1000 l shall be shown in m³.

Symbol	When You Know	Multiply By	To Find	Symbol
MASS				
oz	ounces	28.35	grams	g
lb	pounds	0.454	kilograms	kg
T	short tons (2000 lb)	0.907	megagrams (or "metric ton")	Mg (or "t")
TEMPERATURE (exact)				
°F	Fahrenheit temperature	5(F-32)/9 or (F-32)/1.8	Celcius temperature	°C
ILLUMINATION				
fc	foot-candles	10.76	lux	lx
fl	foot-Lamberts	3.426	candela/m²	cd/m²
FORCE and PRESSURE or STRESS				
lbf	poundforce	4.45	newtons	N
lbf/in²	poundforce per square inch	6.89	kilopascals	kPa

APPROXIMATE CONVERSIONS FROM SI UNITS

Symbol	When You Know	Multiply By	To Find	Symbol
LENGTH				
mm	millimeters	0.039	inches	in
m	meters	3.28	feet	ft
m	meters	1.09	yards	yd
km	kilometers	0.621	miles	mi
AREA				
mm²	square millimeters	0.0016	square inches	in²
m²	square meters	10.764	square feet	ft²
m²	square meters	1.195	square yards	yd²
ha	hectares	2.47	acres	ac
km²	square kilometers	0.386	square miles	mi²
VOLUME				
mL	milliliters	0.034	fluid ounces	fl oz
L	liters	0.264	gallons	gal
m³	cubic meters	35.71	cubic feet	ft³
m³	cubic meters	1.307	cubic yards	yd³
MASS				
g	grams	0.035	ounces	oz
kg	kilograms	2.202	pounds	lb
Mg (or "t")	megagrams (or "metric ton")	1.103	short tons (2000 lb)	T
TEMPERATURE (exact)				
°C	Celcius temperature	1.8C + 32	Fahrenheit temperature	°F
ILLUMINATION				
lx	lux	0.0929	foot-candles	fc
cd/m²	candela/m²	0.2919	foot-Lamberts	fl
FORCE and PRESSURE or STRESS				
N	newtons	0.225	poundforce	lbf
kPa	kilopascals	0.145	poundforce per square inch	lbf/in²

(Revised September 1993)

* SI is the symbol for the International System of Units. Appropriate rounding should be made to comply with Section 4 of ASTM E380.

TABLE OF CONTENTS

LIST OF TABLES

LIST OF FIGURES

APPENDIX A. MIP THEORY

Washburn (1921) first proposed the idea of forcing mercury into capillary pores. He developed the relationship between the diameter of a cylindrical pore, d, filled by a liquid with a surface tension, γ, and a contact angle, θ, for a given pressure, p (equation 1). This equation, known as the *Washburn Equation*, is expressed as:

$$d = \frac{-4\gamma \cos \theta}{p}.$$

(1)

The surface tension is the intermolecular force at the surface of a liquid. As pores get smaller more pressure is necessary to succeed in forcing mercury to intrude a sample. For example, to decrease from pores of 4.6 nm in size to pores of 2.3 nm, the pressures would have to be increased from roughly 200 MPa to 400 MPa.

Mercury's surface tension has been calculated to be 0.473 to 0.485 N/m by numerous researchers (Worthington, 1885; Kemball, 1946; and Nicholas et al., 1961). A value of 0.480 N/m was used in this work. Use of other values in the given range would have resulted in differences in pore size of less than 3 percent.

The contact angle is the angle at which the meniscus of a liquid interacts with a surface as measured through the liquid. The angle is different for different combinations of liquids and surfaces. Liquids are said to be *wetting* or *non-wetting* with respect to surfaces. A wetting liquid has a contact angle less than 90 degrees (see figure A-1). Water is an example of a liquid that is wetting to most surfaces. Mercury tends to be non-wetting to most surfaces having an angle greater than 90 degrees. This "beading-up" behavior corresponds to mercury's large surface tension and its strong affinity for itself.

The contact angle for mercury on cementitious materials has also been studied extensively (Winslow and Diamond, 1970; Good and Koo, 1979; and Cook and Hover, 1993). Reported values range from 117° to 141°. Differences have been attributed to mercury purity, water/cement ratio, drying technique, age of the sample, samples containing fly ash, and pore size under investigation (Palmer and Rowe, 1975; Winslow and Diamond, 1970; Kloubek, 1981a; and Shi and Winslow, 1985). However, research by Cook and Hover (1991) has shown that some of these parameters do not have a significant effect on the contact angle. The research discussed herein made no attempt to resolve this issue. Instead, a commonly accepted value of 130° was chosen (Cook and Hover, 1991) and used throughout.

Washburn acknowledged the importance of accounting for compression of materials and the expansion of the pressure vessel under high pressures (Washburn, 1921). In addition to these, corrections also have to be made to allow for pores of varying shapes and for changes in surface tension as pore diameters decrease.
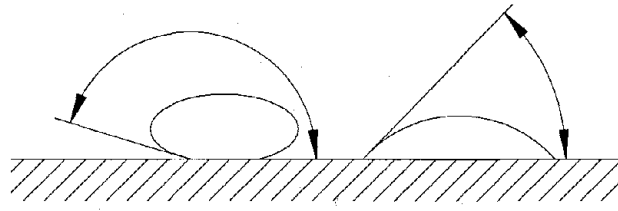
Figure A-1: The contact angle for non-wetting and wetting liquids.

The Washburn equation was derived with the assumption that pores are cylindrical in shape. The value of 4 in the numerator of equation 1 can be thought of as a shape factor, φ, for a pore of circular cross-section. Thus, a more general form of equation 1 is

$$d = \frac{-\varphi\gamma\cos\theta}{p} \tag{2}$$

Concrete can have pores of many cross-sectional shapes, including circular, flat slits, and star-like patterns formed between packed spheres (see figure A-2) as described by Frevel and Kressley, 1963; Lee and Maskell, 1974; and Young, 1974. Many shape factors have been used to account for this (Rootare and Nyce, 1971; Wardlaw and McKellar, 1981.) Their values can range from the maximum shape factor of 4, for a circle, to 2 for the openings formed between two parallel surfaces (see figure a-2 and Cook and Hover, 1993.) Considering that mercury will pass through voids of many shapes, an intermediate shape factor of 3 was applied here. In recognition of the fact that pores are not just to be considered circular, "pore width" will be used in replacement of "pore diameter" when describing pore size, d.

The surface tension of mercury has typically been, and in some cases is still, considered a constant in MIP (Micromeritics, 1998). Kloubek (1981a) put forth the opinion that the surface tension of mercury is influenced by the radius of curvature of the meniscus. Applying the formula for the surface tension of a curved surface results in:

$$\gamma = \frac{\gamma_\infty}{1 + \frac{2d'}{R}}, \tag{3}$$

where:

γ_∞ is the surface tension of a plane liquid surface (0.480 N/m),
d' is the effective diameter of a mercury atom (267 picometers), and
R is the radius of curvature of the liquid surface (Ahn et al., 1972).

Substituting equation 3 into the Washburn equation yields,

$$Pd = \frac{-\varphi\gamma_\infty \cos\theta}{p} + 4d'\cos\theta \quad \text{(Cook 1991)}. \tag{4}$$

Equation 4 was used to determine pore widths in this work. The effects of such changes are greater than 5 percent at pressures of 69 MPa or pore widths of 13 nm and can be as much as 16 percent at 207 MPa.

Measurement of pore widths requires accurate readings for the pressure as well as volume of intrusion, V_{int}. The pressure is related to the pore size while increments of the volume of intrusion correspond to the volume of pores that are intruded through a particular width.[1]

---

1 Note some of this volume increment may correspond to a volume of larger pores that have small openings or necks. These types of voids are called *ink-bottle* pores.
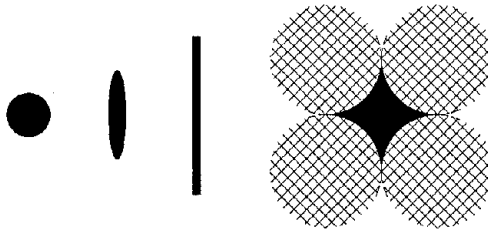
Figure A-2: Different pore shapes in concrete (Cook, 1991).

Small differences, due to compression or expansion of materials can skew the results. If an empty sample tube, called a penetrometer, is placed in an experimental run, machine expansion, penetrometer compression, and mercury compression indicate a certain amount of intrusion took place. (This type of run is called a *blank run* and the volume intruded at any given pressure during the blank run is designated as V_{blank}.) By subtracting blank run volumes from sample run volumes, a first order correction for the expansion of the machine, V_{em}, the compression of the penetrometer can be obtained:

$$V_{int} \approx V_o - V_{blank} \tag{5}$$

However, corrections still need to be made for the difference in the compression of mercury between the sample and blank runs, V_{cHg}, and the compression of the sample, V_{cs} The volume of mercury present in the blank run is larger than the volume of mercury present during the sample run because the sample volume itself takes up space in the sample chamber during the sample run (figure A-3). Thus, the difference in mercury compression between the blank run and the sample run is that the blank run includes the compression of too much mercury. As the extra volume of mercury is known (it is the bulk sample volume) this discrepancy can be corrected by adding back the compression of this extra mercury.[2]

$$V_{int} \approx V_o - V_{blank} + V_{cHg} \tag{6}$$

where:

V_{cHg} is the extra compression which in turn can be estimated by the Tait equation (Smithwick, 1982):

$$V''_{cHg} = 0.175(BV_{sample})\log_{10}\left(1 + \frac{p}{1820\,\text{MPa}}\right) \tag{7}$$

The only remaining correction is for the compression of the unintruded portion of the sample itself which masquerades as additional intrusion and porosity, V_{cs}. This is a complicated correction to make given that the unintruded amount of concrete being compressed is decreasing as intrusion proceeds. Cook and Hover (1993) used an equation for the change in volume of a solid to solve for compressibility of the sample,

$$V_{cs} = p(\iota_{sample})(UV_{sample}) \tag{8}$$

Thus, the final correction equation is rewritten as:

$$V_{int} = V_o - V_{blank} + V_{cHg} - V_{cs} \text{ (Cook 1991).} \tag{9}$$

The configuration of the porosimeter used in this work was such that no correction to the pressure data was needed for additional pressure produced by a mercury head. There also exists

---

2   The average of three blank runs was used in this correction.

V$_{cHg}$ -Volume of
Hg surrounding a
sample

V"$_{cHg}$ -Volume of
Hg filling bulk
volume of concrete
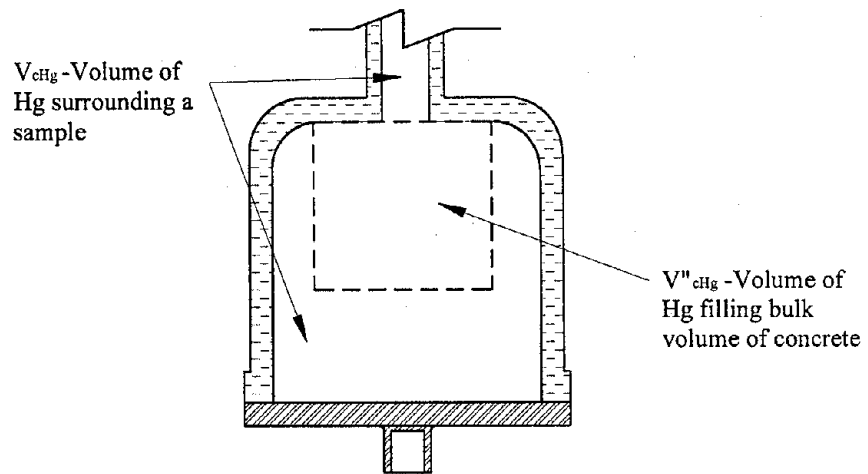
Figure A-3: Mercury filling the concrete bulk volume during a blank run.

a possibility for heat to be generated during the pressurization and thus, expansion of the materials. The porosimeter runs performed in this project were configured to rest between pressure increases/decreases until equilibrium was reached, thus minimizing potential temperature effects. The delay between measurements was set at a minimum of 60 s.

As the mercury present at transfer matches that present at the filling pressure, the blank volume of the sample taken, BV_{sample}, can be calculated as:

$$BV_{sample} = V_{pen} - \frac{W_{after} - W_{before}}{\gamma_{Hg}} , \qquad (10)$$

where:

V_{pen} is the volume of an empty penetrometer,
W_{after} is the weight of the penetrometer assembly after a low-pressure run,
W_{before} is the weight of the penetrometer assembly before mercury is intruded in a low-pressure run, and
γ_{Hg} is the density of mercury (13.5364 g/cm^3).

During the high pressure phase, the pressure was brought to the last pressure of the low-pressure analysis (138.5 kPa) and raised in set logarithmic increments to 207 MPa and then back down to 0.345 MPa before finishing (see table A-1). A 90 s minimum equilibrium time was used for each step in the high-pressure run. It is important to note that the actual pressure data do not match exactly with the goal pressures listed in table A-1 due to a specified tolerance for pressure equilibrium of ± 0.1 percent of the goal pressures.

A plot of the pairs of corrected pressure and volume readings, for an individual run, yields a cumulative intrusion graph (see figure A-4). Volume of intrusion is placed on the y-axis and pressure on a logarithmically scaled x-axis.

The depressurization (extrusion) portion of the graph does not follow the intrusion curve, resulting in what is known as a hysteresis effect. There are many opinions as to the reasons why this occurs (ink-bottle pores, contact angle changing from advancing to receding, etc. (Drake and Ritter, 1945; and Kloubek, 1981)). It was not necessary to examine the extrusion data for the work presented here.

The coefficient of compressibility can change the shape of the MIP intrusion graph near the highest pressures (greater than 20000 kPa) as shown in figure A-5. Cook (1991) proposed that, with the proper coefficient of compressibility, the initial part of the extrusion curve should be flat due to the contact angle changing from an advancing to a receding angle. The coefficient of compressibility for each sample was determined by this method.

Table A-1: Goal pressures used in MIP (kPa).

Point	Pressure	Point	Pressure	Point	Pressure
1	13.79	35	9535	68	20677
2	16.69	36	11556	69	18188
3	20.3	37	14003	70	16003
4	24.5	38	16975	71	14086
5	29.8	39	20574	72	12390
6	36.1	40	24938	73	10901
7	43.7	41	30227	74	9591
8	53.0	42	36639	75	8439
9	64.3	43	44409	76	7426
10	77.8	44	53827	77	6536
11	94.4	45	65238	78	5750
12	114.4	46	79076	79	5061
13*	138.6	47	95837	80	4454
14	168.2	48	116170	81	3916
15	203	49	140798	82	3447
16	247	50	170652	83	3034
17	299	51	206843	84	2668
18	363	52	160145	85	2344
19	439	53	140915	86	2062
20	533	54	123988	87	1813
21	645	55	109103	88	1600
22	783	56	95996	89	1407
23	949	57	84461	90	1239
24	1149	58	74325	91	1090
25	1393	59	65397	92	959
26	1689	60	57544	93	844
27	2048	61	50635	94	743
28	2482	62	44554	95	654
29	3006	63	39204	96	575
30	3647	64	34494	97	506
31	4420	65	30351	98	445
32	5357	66	26710	99	392
33	6488	67	23497	100	345
34	7867				

*This point marked the end of the low-pressure analysis and the beginning of the high-pressure run.
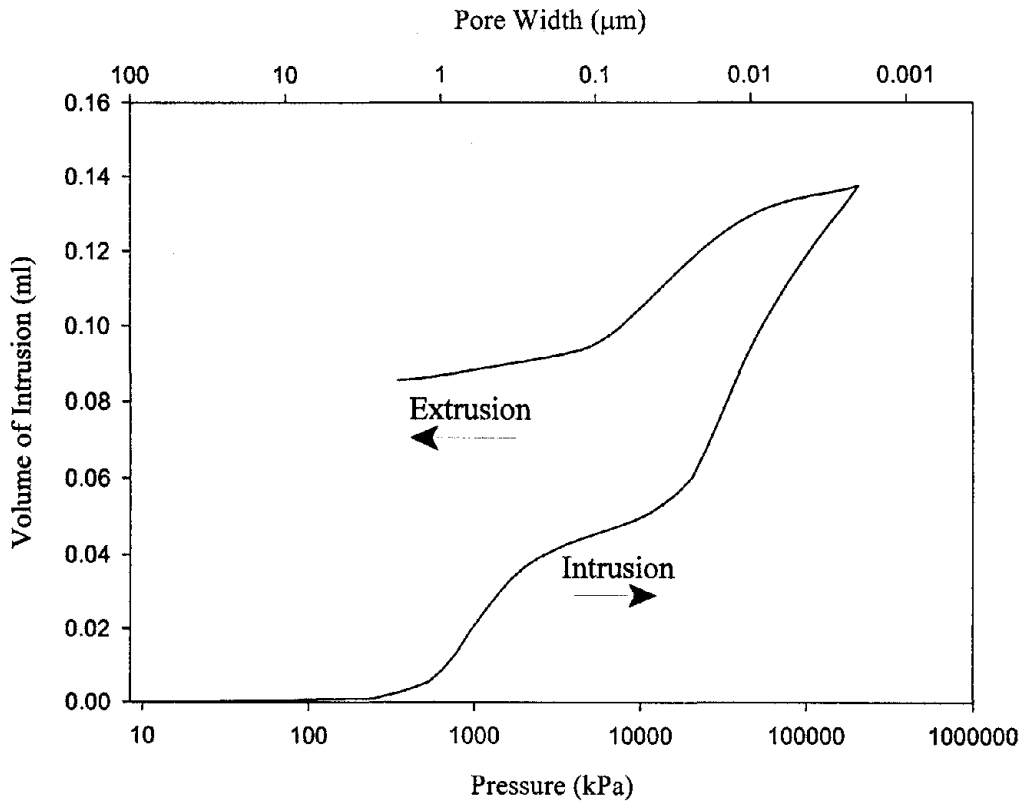
Figure A-4: Typical volume of intrusion vs. log of pressure graph.
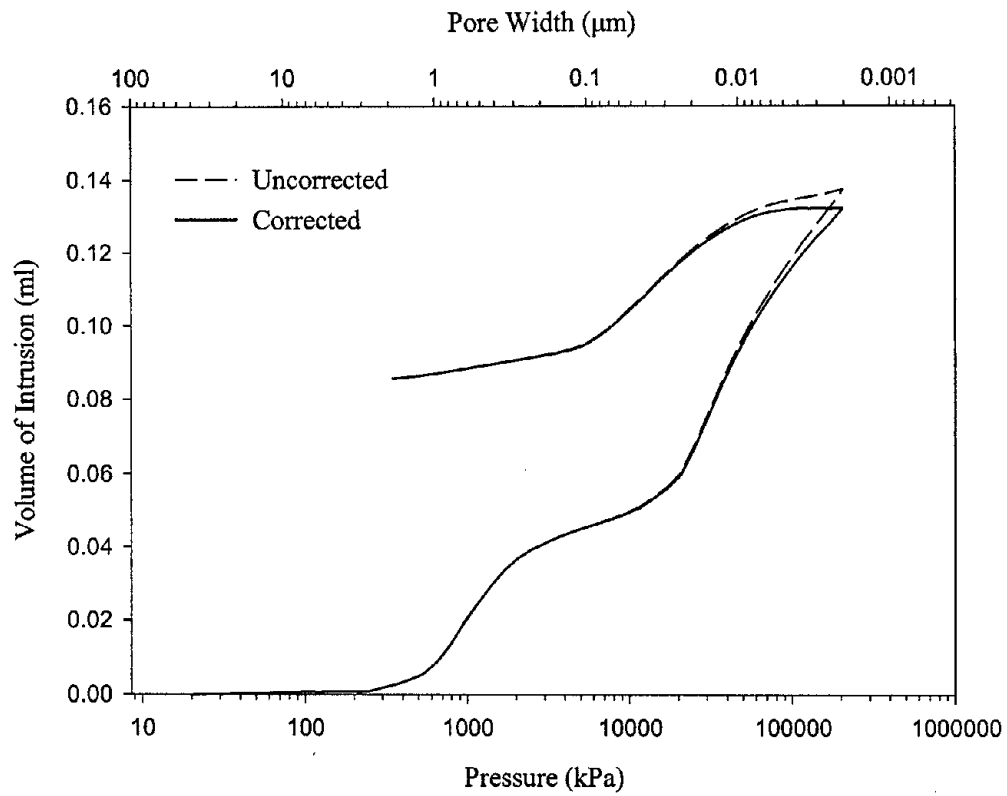
Figure A-5: Coefficient of compressibility is determined by
the slope of the extrusion line.

Cumulative intrusion graphs can be difficult to use for comparing concrete samples. Reasons for this are:

1.   Samples of varying volumes will have different volumes of intrusion.

2.   The pressure data vary slightly from one another, making interpretation between points necessary.

3.   The relative differences in pore size volumes are not easily discernible using the graph shown above.

To correct the first problem, the porosity, is plotted on the y-axis to normalize the sample sizes, where

$$Porosity = \frac{V_{int}}{BV_{sample}} \times 100\% \,.$$ (11)

The second problem can be resolved by finding intrusion volumes corresponding to a set of goal pressures through linear interpolation or extrapolation.

The third problem can be addressed by recognizing that the slope of the volume/pore width curve at a specific pore width indicates the amount of intrusion that occurred through pores of that width. Steeper sections indicate pores filling, while flat sections indicate a lack of intrusion through pores at those sizes. By plotting the logarithmic slope along the y-axis, an average differential pore size distribution can be generated (see figure A-6). The slope is, m_i, where

$$m_i = \frac{\Delta r}{\Delta \log(d)} = \left[\frac{Porosity_{i+1} - Porosity_i}{\log d_{i+1} - \log d_i} \right],$$ (12)

and the width, $\overline{d_i}$, is the logarithmic average of the two widths used to calculate the ith slope (Cook 1991).

$$\overline{d_i} = 10^{\left[\frac{\log(d_i) + \log(d_{i+1})}{2} \right]}$$ (13)
$$= \sqrt{(d_{i+1})(d_i)}$$

This equation is multiplied by –1 to account for the pore widths decreasing with increasing pressure. (Figure A-6) has been rotated about the y-axis so that pore widths increase from left to right.) The y-axis can also be considered as an *incremental pore volume* for each width. The area under the graph is equal to the porosity of the test sample.
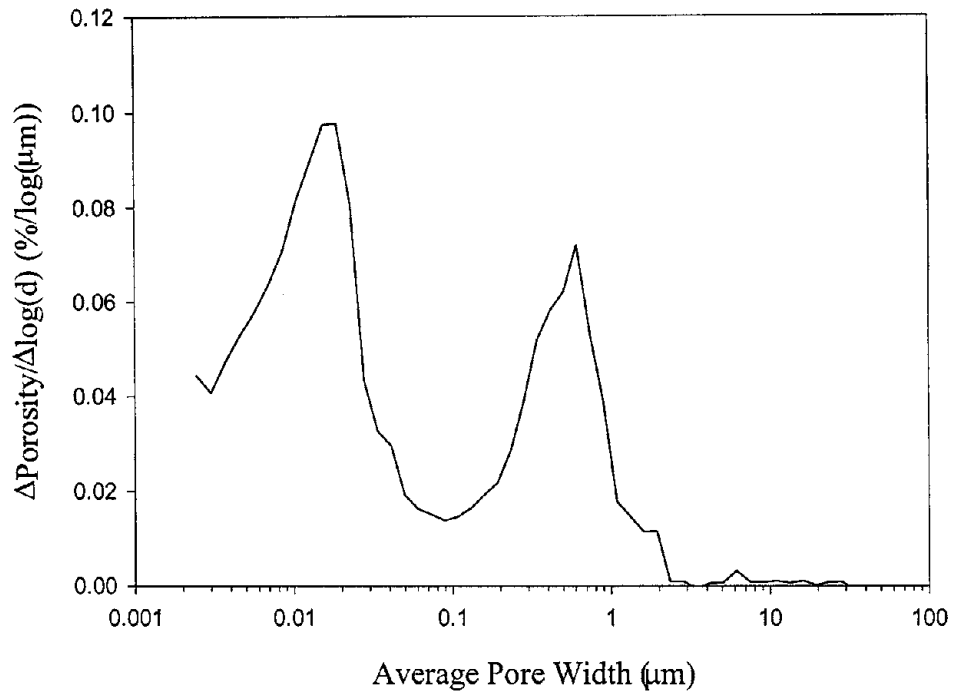
Figure A-6: Typical average differential pore size distribution
vs. pore width plot.

Given that the sample sizes are smaller than the largest pieces of aggregate and that the percentage of mortar and coarse aggregate in each sample is unknown, the porosity of a particular sample is not necessarily a good estimate of the overall porosity in the concrete. Mortars typically range from 10 to 20 percent porosity (Cook, 1991; Delagrave et al., 1998; and Willis et al., 1998) and the limestone coarse aggregate used in this work had values of 2 to 4 percent. Testing larger samples would be ideal but this is not possible given the current technology and apparatuses available. Instead, the results of the three samples tested from each specimen can be summed to create a larger virtual sample. This is done by adding the corrected volumes of intrusion values for the three samples and dividing this value by the sum of their bulk volumes:

$$\frac{V_{int_{A_i}} + V_{int_{B_i}} + V_{int_{C_i}}}{BV_{sample_A} + BV_{sample_B} + BV_{sample_C}} \times 100 = Porosity_{wgt_i} \; (\%) \tag{14}$$

The result is a weighted porosity, $Porosity_{wgt_i}$, which is then used in equation 12. This weighted averaging of samples reduces aberrations caused by any one particular sample (see figure A-7). Though this results in an improvement, the volume of three samples may still not be large enough to provide a consistent estimate of total porosities. For this reason, the focus of the analysis will be on those pore widths through which most intrusion occurred (the widths corresponding to the peaks of the ΔPorosity/Δlog(d) graphs).

The pore size distribution plots for concrete samples tested in this project typically have a bimodal shape as shown in figure A-7. The peaks are referred to numerically in the order at which they are intruded: the first peak is that of the, right (low pressure); the second peak is that of the left (high pressure). The apexes of these two peaks correspond to *threshold pore widths*. A threshold pore width is the width at which mercury gains access into the interior of the sample. Two peaks may indicate that initially one connective mercury network was formed followed by one that penetrated into a network of smaller connected pores (Willis et al., 1998 and figure A-8). Sharp, distinct, apexes correspond to well-defined threshold pore widths. Flat peaks occur when there are poorly defined threshold pore widths.

Difficulties can arise when trying to define the threshold pore widths to use in a statistical analysis. Researchers typically choose the width corresponding to the maximum incremental increase in porosity as the threshold width (Winslow and Diamond, 1970; Dullien, 1981, and Moukwa and Aïtcin, 1988). Use of this value ignores the fact that peaks may have been poorly defined. It also gives the same weighting to small, insignificant peaks of intrusion as to large significant peaks. Figure A-9 is a depiction of two fictitious intrusion runs where these problems can be explained in further detail. The pore size distributions in figure A-9 have been greatly simplified for clarification purposes. Visually, the two graphs are roughly similar with respect to the first peak (corresponding to the larger pores) and different with respect to the second. Traditional procedures used in MIP data reduction indicate the opposite. Sample Y's threshold pore width for the first peak is roughly 4 μm. Sample X's is 0.4 μm due to the small rise at the left end. The second peaks, while appearing different in shape, have the same threshold pore width (0.02 μm). Thus, traditional descriptions can be misleading and it would appear that the current definition of threshold pore width must be modified to measure these differences.
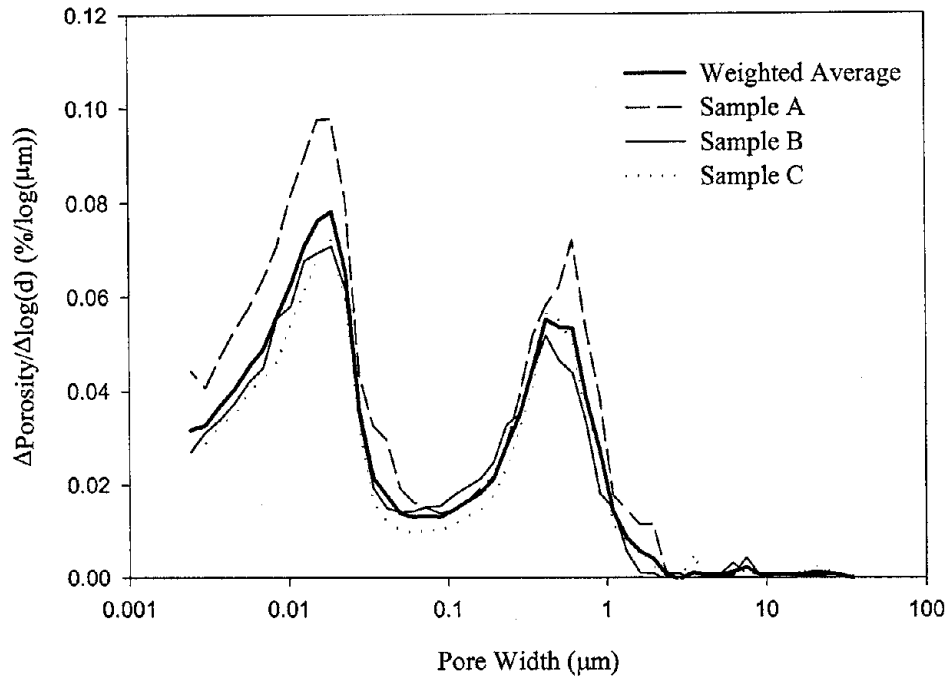
Figure A-7: Weighted averaging of the three sample points.

| (a) | (b) |
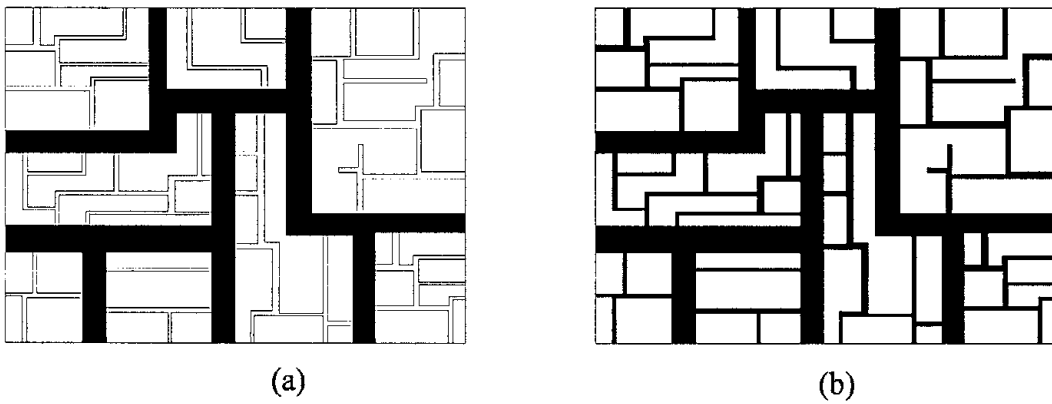
Figure A-8: Mercury forming the first (a) and second
(b) connective networks during intrusion.
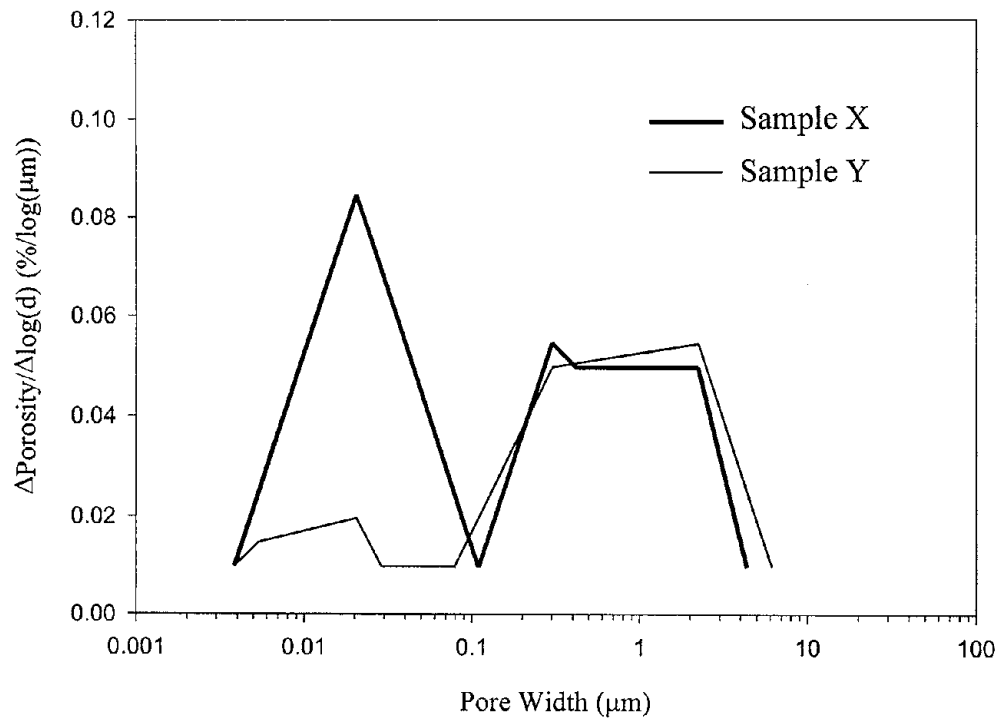
Figure A-9: Simplified representation of two pore-size distributions.

Two parameters were developed to define the location and shape of the peaks. The first defines a new threshold pore width, called the *weighted average threshold pore width*, d_{wgt}. It is calculated by grouping the nine highest incremental pore volumes for a given peak and their respective pore widths. Each pore width is multiplied by its incremental pore volume, V_P, summed, and then divided by sum of all nine incremental pore volumes (equation 15).

$$d_{wgt} = \frac{d_1 V_{P1} + d_2 V_{P2} + \cdots + d_9 V_{P9}}{\sum\limits_{i=1}^{9} V_{Pi}} \qquad (15)$$

The second parameter is a peak shape uniformity indicator. This value will find differences between flat and sharply defined peaks. The uniformity indicator, U_i, is calculated as the inverse of the standard deviation in the widths of the nine highest incremental porosities used in equation 15. Larger values indicate steep shapes associated with well-defined threshold pore widths. Smaller values indicate a flattened peak, corresponding to poorly defined threshold widths.

Each peak's weighted average threshold pore width and uniformity indicator were compared with one another in the ANOVA tables. The differences between the first and second peak, though not quantified, are discussed where significant changes were observed.

Samples of coarse aggregate were analyzed using MIP. Samples were of the same sizes used for regular concrete samples. Results of these tests are shown in figure A-10. From these graphs it is evident that the amount of intrusion into the aggregates is negligible compared with the amount generated with concrete samples containing portland cement paste.

Results for fine aggregate samples have not been presented here because of instrument difficulties from an overwhelming percentage of voids occurring between sand particles and not inside the individual sand particles.
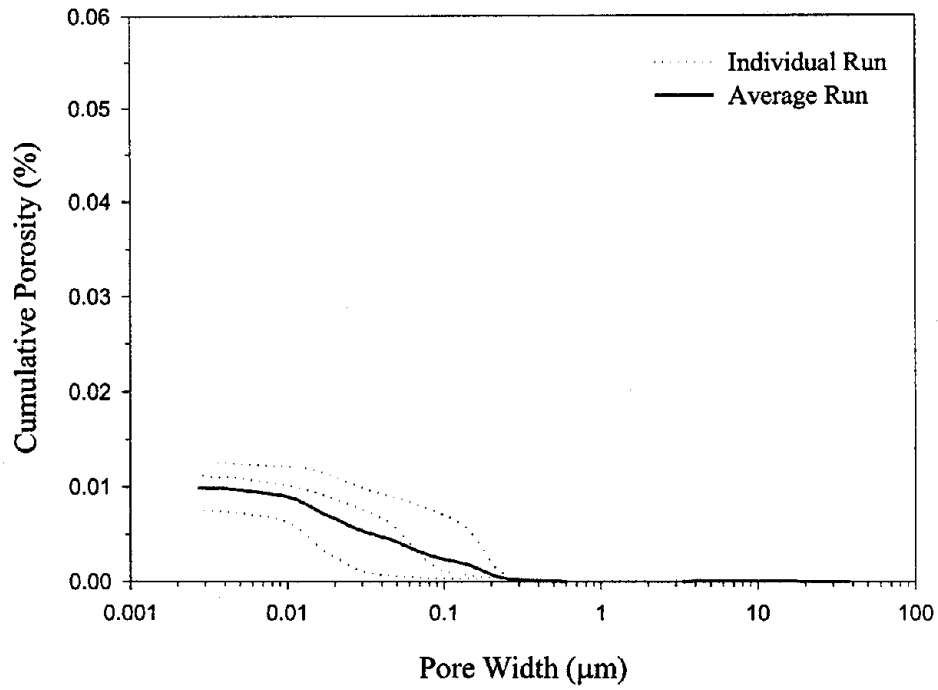
(a)
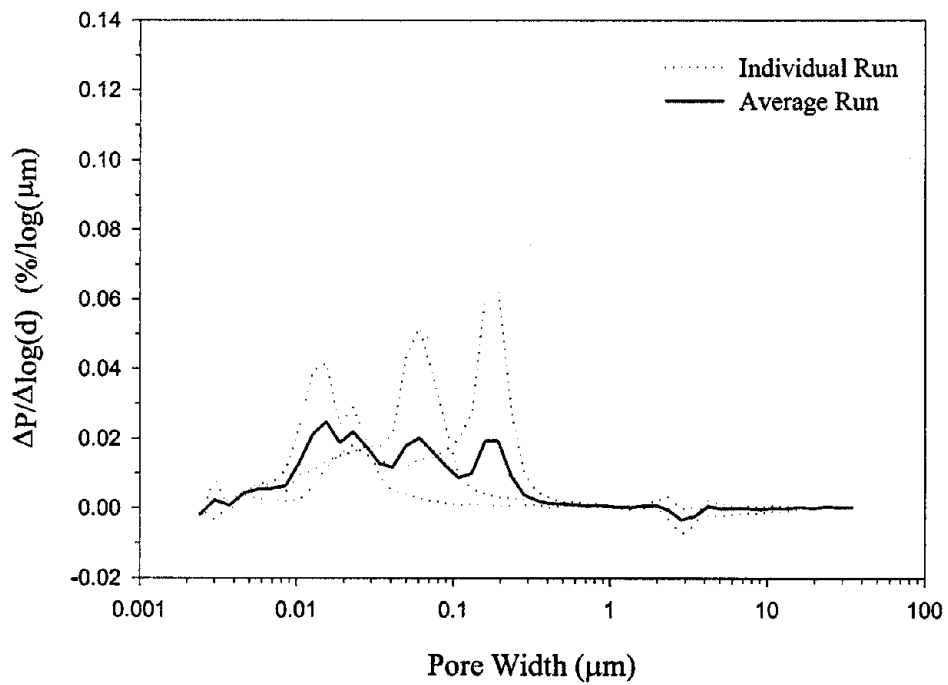
(b)

Figure A-10: MIP results for coarse aggregate: (a) cumulative porosity
vs. pore width; (b) average differential pore size distribution vs. pore width.

APPENDIX B. BET ADSORPTION THEORY

Adsorption is an exothermic (heat releasing) process where molecules attach themselves to the surface of a material. (Adsorption is different from absorption, where molecules are taken up and made a part of another material.) Adsorption occurs when atoms or ions at the surface of a material are reactive due to unfilled valence requirements and gas molecules are attracted to these sites. Materials typically have impurities filling some of these active sites; however, there are methods to free the solids of these impurities for more accurate measurements (Ma et al., 1995 and Hill et al., 1997).

Langmuir's work on the improvement of military gas masks led to his theory of adsorption (Langmuir, 1918). Langmuir's theory says that gas molecules will form a molecular monolayer when adsorbed onto a solid surface. The collision of gas molecules with a surface is an inelastic one. The molecules stay on the material for a short time before returning to the gas phase. This constant interchange of gas molecules attaching (condensing) and detaching (vaporizing) from a solid is sorption. Under constant temperature and increasing pressure, the rate of condensation will exceed the rate of evaporation, eventually forming a single layer of molecules (adsorption). The volume of that monolayer, V_m, is related to the volume of gas adsorbed, V_a, at a particular pressure, P, by

$$V_a = \frac{V_m bP}{1 + bP} \tag{16}$$

where b is an empirical constant. Equation 16 is normally represented in its linear form,

$$\frac{P}{V_a} = \frac{1}{V_m b} + \frac{P}{V_m} \tag{17}$$

Plots of P/V_a vs. P will form a straight line, from which V_m and b are evaluated from the slope and y-intercept. With the volume of the monolayer, the surface area of the sample (1 gram of it), s_m, is calculated by

$$S_m = \frac{V_m \sigma N_A}{mV_g} , \tag{18}$$

where:

σ is the cross-sectional area of the adsorbed gas molecule (16.2×10^{-20} m^2 for nitrogen),
N_A is Avogadro's constant,
m is the mass of the solid, and
V_g is the molar volume of the gas (22,414 cm^3 for nitrogen).

When nitrogen is the adsorbed gas (called the adsorptive prior to adsorption and adsorbate afterwards), equation 18 can be simplified to

$$S_m (m^2/g) = \frac{4.35 V_m (cm^3 \text{ @ STP})}{m(g)} \ . \tag{19}$$

Brunauer, Emmett, and Teller (1938) improved upon the Langmuir theory by introducing the idea that multiple molecular layers form on the surface of the adsorbent (solid). BET theory assumes that the forces responsible for the adsorption are also responsible for the binding energy of subsequent layers. It is assumed that no layer begins to form before the previous layer of molecules is complete.[3]

Figure B-1 represents the results from an example adsorption experiment, where volume of adsorption data is taken for the full range of partial pressures (P/P_o). The gas adsorptive and sample are brought to low temperatures during analysis. The adsorptive would be in the liquid phase under normal atmospheric pressure and these low temperatures. Section 1 of the graph is where molecules have just begun adsorbing onto the surface, but areas of the surface remain empty. Section 2 is the area used by BET analysis. This is the range of partial pressures where the surface has been completely covered by nitrogen molecules and additional layers have begun to form. The experiment can, and usually does, stop here. However, if the experiment continued it would experience a rapid rate of adsorption due to the partial pressures reaching the state where all the gas begins changing into the liquid phase, referred to as *bulk condensation*.

Investigations into the rate of condensation of the gas molecules in the multiple molecular layers and the rate of evaporation from those layers led BET to the expression,

$$V_a = \frac{V_m C P}{(P_o - P)\left[1 + (C-1)\dfrac{P}{P_o} \right]} \ , \tag{20}$$

where C is a constant and P_o is the saturation pressure of the gas. The constant C is related to the difference in energy involved in adsorption of the first layer and liquefaction of the adsorptive. Its exact value is determined empirically. Equation 21 can also be expressed in the linear form,

$$\frac{P}{V_a(P_o - P)} = \frac{1}{V_m C} + \frac{C-1}{V_m C}\left(\frac{P}{P_o} \right) \ . \tag{21}$$

The plot of $P/[V_a(P_o-P)]$ vs. P/P_o yields a straight line is the second section with a y-intercept of $1/V_m C$ and a slope of $(C-1)/V_m C$ (see figure B-2). The values of V_m and C are obtained from a regression analysis of this line. V_m can then be used in equation 21 to estimate a sample's surface area.

---

3 Webb and Orr (1997) point out that BET theory can be criticized for the assumption that all locations along a surface will have the same energies and that it does not account for decreasing adsorption forces as the layers increase in distance from the surface. However, they also mention that these criticisms are typically overlooked due to its large usage and foundation for other advanced theories.
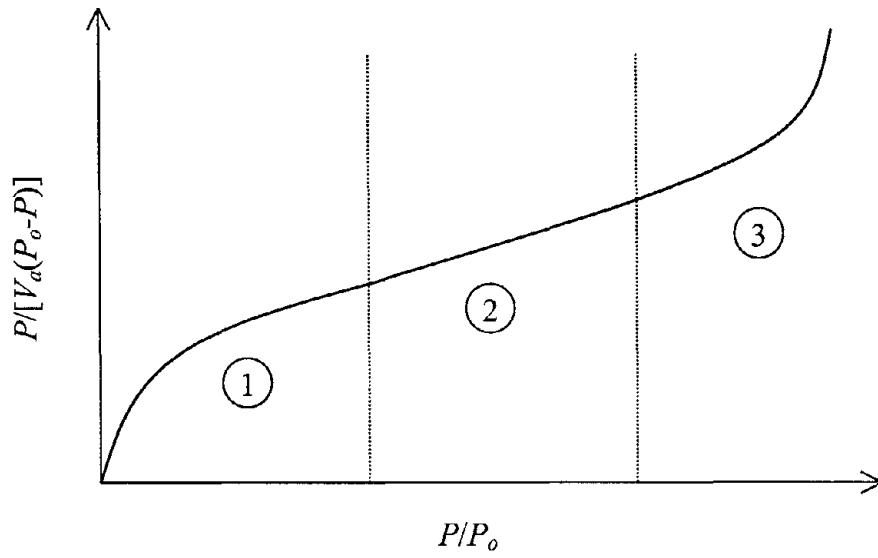
Figure B-1: Theoretical adsorption isotherm.
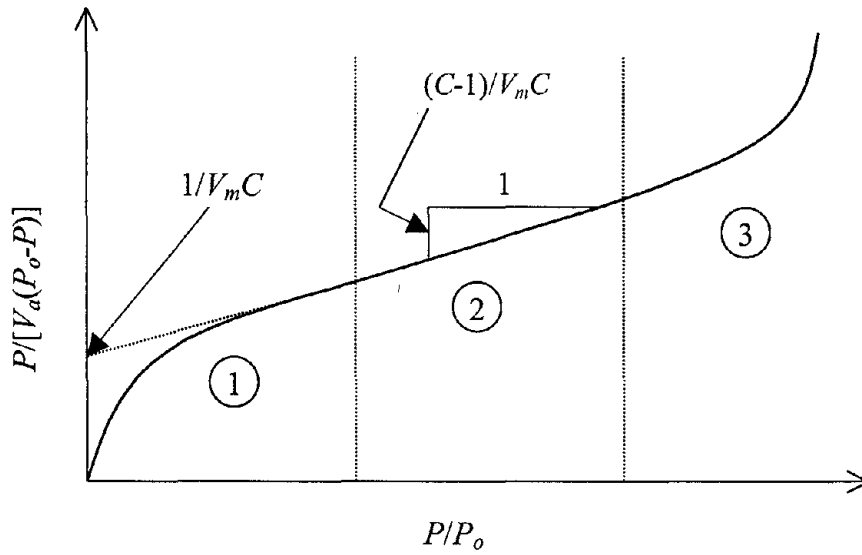
Figure B-2: Slope and intercept of adsorption isotherm.

APPENDIX C. ANOVA DEFINITIONS AND USE IN FACTORIAL EXPERIMENTS

Definitions that may be useful in any statistical discussion for this project follow:

ANOVA – analysis of variance.

Curvature – assesses the linearity between the low (-) and high (+) levels of a treatment factor or interaction based on the response at the median (0) level. A low curvature value indicates a linear response over the range of treatment levels.

Experimental variable – an independent variable, a treatment that a sample undergoes at one of several levels. In this project there were three experimental variables: AA, CL, and FT.

Effect – the difference between the mean response at the high (+) level of a factor or interaction and the mean response at the low (-) level of the same factor or interaction.

Factor - an experimental variable.

Full factorial design –every level of a treatment is tested over every level of one or more other treatments.

Interaction – the combined effect of two or more factors.

Pure error – the variance of replicate samples.

Response variable – a dependent variable, something that is measured or analyzed in order to assess change due to an applied treatment. For this research, some examples are porosity, mineral phase content, and observed diffusion coefficient (D_{obs}).

A common ANOVA table (based on an Excel macro) was developed for use with the different response variables. Whenever possible, this table was used for all ANOVA calculations for the $2^3 + 3$ design. Alternative ANOVA tables were developed for specific situations when data sets, for one reason or another, did not conform to the experimental design.

An ANOVA table allows the variation in the data to be broken down into different components and it looks for the source of the data variation. The basic components of variation are total variability, within treatment or error variability, and between treatment or factor variability (Guadard and Schoof, 1995). If the factor variability is large compared with the error variability, then this suggests that the factor levels have a measurable effect on the response. Conversely, if the error variability is large compared with the factor variability, then this suggests that any difference due to the factor levels is overshadowed by the response differences of replicate treatments.

The first step to creating the ANOVA table is to create a table of factorial effect coefficients. This is done by identifying the different treatment schemes the samples have

undergone using the (-,0,+) designations for the treatment factors, listing all possible factor interactions, and multiplying the -, 0, and + signs as in normal arithmetic. Data values for samples subjected to a specific combination of treatment factor levels can now also be associated with the interactions of those factors.

The next step is to develop the ANOVA table itself (see table C-1). The equations that are part of that table relate to the -, 0, and + values in table C-2. The ANOVA table used to examine the $2^3 + 3$ experimental design is shown in table C-3. The letters in the shaded area correspond to the equations and definitions that follow.

Effect:

$$E = \frac{\sum (+)}{n} - \frac{\sum (-)}{n} \tag{22}$$

where:

n is defined as the number of observations at the high (+) level of treatment .

Sums of Squares for a factor or interaction:

$$SS_{\text{factor or interaction}} = \frac{C^2}{N} \tag{23}$$

where:

N is the total number of observations, and
where C is the contrast.

$$C = \sum (+) - \sum (-) \tag{24}$$

C is defined:
Total Sums of Squares:

$$SST = \sum (\text{observation}^2) - \frac{T^2}{N} \tag{25}$$

where:

T is the sum of all observations.

Degrees of Freedom of a factor:

$$df_{\text{factor}} = (x-1) \tag{26}$$

where:
x is the number of levels in factor x.

Table C-1: Key to project and statistical designations.

Statistical designation	Project designation	Level of AA	Level of CL	Level of FT
(-,-,+)	(NNH)	none	none	high
(0,0,0)	(LLL)	low	low	low
(+,-,+)	(HNH)	high	none	high

Table C-2: Factorial coefficients.

Row	Factors			Interactions			
	AA	CL	FT	AAxCL	AAxFT	CLxFT	AAxCLxFT
1	-	-	-	+	+	+	-
2	-	-	+	+	-	-	+
3	-	+	-	-	+	-	+
4	-	+	+	-	-	+	-
5	+	-	-	-	-	+	+
6	+	-	+	-	+	-	-
7	+	+	-	+	-	-	-
8	+	+	+	+	+	+	+
9	0	0	0	0	0	0	0
10	0	0	0	0	0	0	0
11	0	0	0	0	0	0	0

Table C-3: ANOVA equations table.

Row	Source	Effect	SS	df	MS	Computed F value
1	AA	a	b	d	k	p
2	CL	a	b	d	k	p
3	FT	a	b	d	k	p
4	AAxCL	a	b	e	k	p
5	AAxFT	a	b	e	k	p
6	CLxFT	a	b	e	k	p
7	AAxCLxFT	a	b	f	k	p
8	Curvature		n	j	o	q
9	Pure Error		m	h	1	
10	Total		c	g		

Degrees of Freedom of a 2-way interaction:

$$dt_{2\text{-way interaction}} = (x-1)*(y-1) \tag{27}$$

where:

x is the number of levels in factor x, and
y is the number of levels in factor y.

Degrees of Freedom of a 3-way interaction:

$$dt_{3\text{-way interaction}} = (x-1)*(y-1)*(z-1) \tag{28}$$

where:

x is the number of levels in factor x,
y is the number of levels in factor y, and
z is the number of levels in factor z.

Degrees of Freedom total:

$$df_{total} = N - 1 \tag{29}$$

where:

N is the total number of observations; corner and center points

Degrees of Freedom of pure error:

$$df_{pure\ error} = n_c - 1 \tag{30}$$

where:

n_c is the number of observations at the center point.

Degrees of Freedom of curvature:

$$df_{curvature} = 1 \tag{31}$$

Mean Square of a factor or interaction:

$$MS_{factor\ or\ interaction} = \frac{SS_{factor\ or\ interaction}}{df_{factor\ or\ interaction}} \tag{32}$$

24

Mean Square pure error:

$$MS_{pure\ error} = s^2 \qquad (33)$$

where s² is the sample variance at the center point of the experimental design and defined by:

$$s^s = \left(\frac{1}{n_c - 1}\right) * \sum \left[\left(y_{c_i} - y_{c_{average}}\right)^2\right] \qquad (34)$$

where:

> n_c is the number of observations at the center point,
> y_{ci} is an observation at the center point, and
> $y_{c\ average}$ is the average of the observations at the center point.

Sums of Squares pure error:

$$SS_{pure\ error} = MS_{pure\ error} - df_{pure\ error} \qquad (35)$$

Sums of Squares curvature:

$$SS_{curvature} = \frac{(y_{f_{average}} - y_{c_{average}})^2}{\left[\left(\frac{1}{n_f}\right) + \left(\frac{1}{n_c}\right)\right]} \qquad (36)$$

where:

> $y_{f\ average}$ is the average of the observations at all the corner points,
> $y_{c\ average}$ is the average of the observations at the center point,
> n_f is the number of total number of observations at all the corner points, and
> n_c is the number of total observations at the center point.

Mean Square of curvature:

$$MS_{curvature} = \frac{SS_{curvature}}{df_{curvature}} \qquad (37)$$

Computed F value of a factor or interaction:

$$F_{factor\ or\ interaction} = \frac{MS_{factor\ or\ interaction}}{MS_{pure\ error}} \qquad (38)$$

Computer F value of curvature:

$$F_{curvature} = \frac{MS_{curvature}}{MS_{pure\ error}} \qquad (39)$$

25

It should be emphasized that for this project the computed F values are based on the mean square of the pure error, the variance of the replicate center point samples. Typically the computed F values for factors and interactions would be based on the mean square of the total error. Total error in this case is the sum of the pure error and the curvature. For some response variables the curvature contribution to the total error dominates the pure error, resulting in small, statistically insignificant computed F values. Since the purpose of the mean square error is to account for natural variability between replicate samples, it was determined that using the pure error rather than the total error for computing F values, an accepted practice, would better represent variation between samples resulting from differences in treatment levels.

The computed F values should be compared to tabular F values to determine if the variation between the high (+) and low (-) levels of a factor or interaction is statistically significant at a chosen confidence interval.

APPENDIX D. ANOVA AND TUKEY-KRAMER MULTIPLE COMPARISONS

It was necessary to compare results from different tests between the CFA-C, CFA-F, and PCC prisms. Each group is called a mix treatment, and the number of mix treatments, k, is 3 in this case. Each group's mean was calculated. The three means are considered as a new set of data points and that set's variance is estimated. This would be considered a second estimate of the true (population) variance, σ^2, if the three treatments were not different. The first estimate of σ^2 comes from the pooled variance, s_R^2. A significant difference between the first estimate of σ^2 and the second would imply that a difference exists between the three treatments.

The between-treatment sum of squares, S_T, where

$$S_T = \sum_{t=1}^{k} n_t (\overline{x}_t - \overline{x})^2 , \tag{41}$$

is needed to calculate the between treatment variance. The value n_t is a weighting factor. It is the number of samples in a given treatment and allows larger sample sets to have more weight in the S_T calculation than smaller sample sets.

The between-treatment variance, s_T^2, is calculated as

$$s_T^2 = \frac{\sum_{t=1}^{k} n_t (\overline{x}_t - \overline{x})^2}{k - 1} = \frac{S_T}{K - 1} . \tag{42}$$

This is sometimes called the between-treatment mean square. This is the value that is compared to s_R^2. The s_T^2 is divided by s_R^2 to get what is known as the F-statistic.

$$F = \frac{s_T^2}{s_R^2} \tag{43}$$

An F-value of 1 or less indicates that there is no difference between treatments as individual groups give a similar estimate of σ^2 as does the combined data. An F-value greater than 1 indicates different treatments produced an effect on the samples.

A check is performed on the analysis by ignoring the separation of treatments. The overall sum of squares, S_D, can be calculated as

$$S_D = \sum_{t-1}^{k} \sum_{i=1}^{n_t} (x_{ti} - \overline{x})^2 . \tag{44}$$

This provides the total sum of squares about the total average.

A unique characteristic of the ANOVA is that:

$$S_D = S_T + S_R \text{ and} \qquad (45)$$

$$v_D = v_T + v_R . \qquad (46)$$

The results of an ANOVA analysis are presented herein per the format of table D-1. When the F-Statistic is greater than the tabular F-values, the ANOVA indicates a true difference in the variances. Thus, it indicates a significant effect.

An ANOVA determines only if the means are different. If they are found to be significantly different, the treatments were then compared on pair-by-pair bases (i.e. CFA-C vs. PCC, CFA-C vs. CFA-F, and CFA-F vs. PCC).

A technique developed by Tukey (1949), now referred to as the Tukey-Kramer comparison of means test, is used to compare the difference between sample population means by an associated confidence interval. The confidence interval,

$$(\bar{x}_i - \bar{x}_j) \pm \frac{q_{k,v'} \frac{\alpha}{2}}{\sqrt{2}} s \sqrt{\frac{1}{n_i} + \frac{1}{n_j}} , \qquad (47)$$

is applied to all pairs of treatments, i and j, within, k total treatments, and v degrees of freedom. The appropriate statistic, q, is acquired from a table of Studentized t-distribution values for confidence intervals, 1-α, equal to 95 percent and 99 percent (Larsen, 1986). The value,

$$\frac{q_{k,v'} \frac{\alpha}{2}}{\sqrt{2}} s \sqrt{\frac{1}{n_i} + \frac{1}{n_j}} , \qquad (48)$$

termed the Tukey range, is compared to the differences $(\bar{x}_i - \bar{x}_j)$. A table similar to table D-2 is used for all analyses of pairs (TV = Tukey range at a 95 percent confidence interval). If the value of any pair's difference falls outside the Tukey range then the pair is said to be significantly different at that appropriate confidence interval.

28

Table D-1: Analysis of variance table.

Source of variation	Sum of squares	Degrees of freedom	Mean square	F-statistic	Tabular F-values	
					99%	95%
Between treatments	S_T	v_T	s_T^2	s_T^2/s_R^2	F_{99}	F_{95}
Within treatments (error)	S_R	v_R	s_R^2			
Total	S_D	v_D				

Table D-2: Tukey's paired comparison table.

Treatment	t_i	t_j	t_l
Average	$\overline{x}_i$	$\overline{x}_j$	$\overline{x}_i$
Differences	TV	$(\overline{x}_i - \overline{x}_j)$	$(\overline{x}_i - \overline{x}_l)$
	$(\overline{x}_l - \overline{x}_i)$	TV	$(\overline{x}_j - \overline{x}_l)$
	$(\overline{x}_l - \overline{x}_i)$	$(\overline{x}_l - \overline{x}_j)$	TV

APPENDIX E. PRISM AND CYLINDER MINI-STUDY

Prism Casting

This is described in section 4.2.6 of volume 1.

Cylinder Casting

Cylinders were cast individually in standard 100- by 200- mm plastic molds. Fresh concrete was consolidated in three lifts with a 10-mm stainless steel rod. Surface finishes were prepared with hand trowels. The tops of the molds were sealed with plastic sheeting secured by rubber bands. Cylinders were cured with the same procedures described in section 3.5.4.

Uniaxial Compressive Strength Testing

Four cylinders of the CFA-C were subject to AA at none, low, and high treatment levels. In addition, four cylinders from CFA-F and PCC mixes were subjected to AA at the low level. Three cylinders from each group were tested for compressive strength per ASTM C 39. Three prismatic samples from the CFA-C mix that had undergone no, low, and high AA as well as the three from the CFA-F and PCC mixes were also tested for compressive strength.

For testing, two steel end caps were machined to the specifications shown in figure E-1. Neoprene pads with the dimensions of 85- by 85- by 12-mm were inserted inside each cap. A cap was placed on the top and bottom of the test sample such that the neoprene pads faced the concrete sample. The end caps and sample were placed between a spherically seated bearing block on the bottom of the testing machine and the machine's platen on the top (see figure E-2). A loading rate as prescribed in ASTM C 39 was applied to obtain the compressive strengths. Results from the compressive strength tests performed on the cylinders and prisms are presented in table E-1.

Similarities Between Cylinders and Prisms

The compressive strength for each of the treatment schemes was calculated by averaging the three individual test values. From this, it was determined that a prismatic sample's compressive strength was 85 ± 11 percent (at a 95 percent confidence interval) of its cylindrical equivalent. This number appeared to decrease with higher values of equivalent aging. However, due to a lack of test samples this could not be confirmed.
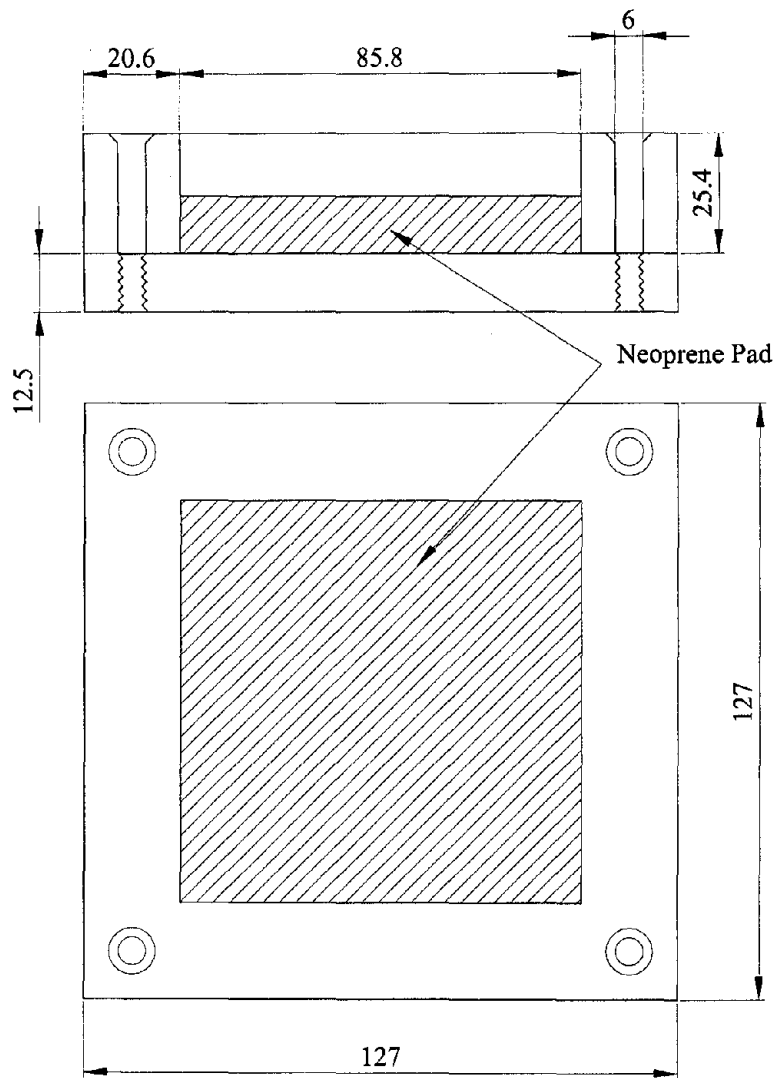
Figure E-1: Steel end cap design for compressive strength
testing and cyclic loading of prisms (dimensions are in mm).

Load Cell

Top Platen

Prismatic Sample

Spherical Seat

Actuator
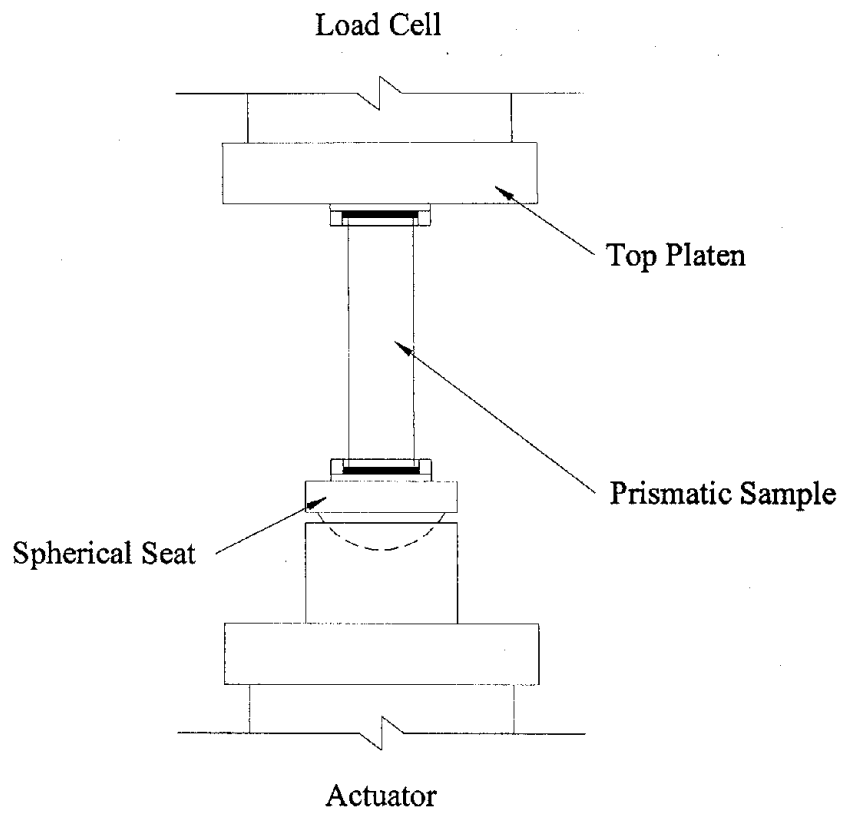
Figure E-2: Testing configuration for compressive testing
of prisms and cyclic loading.

Table E-1: Compressive strengths of cylinders and prisms.

Cylinder	Compressive strength kPa		Prism
C(NTX)01-C	57.0	*	C(NTX)01
C(NTX)02-C	57.3	53.8	C(NTX)02
C(NTX)03-C	61.0	53.9	C(NTX)03
C(LTX)01-C	43.8	39.3	C(LTX)01
C(LTX)02-C	46.3	41.5	C(LTX)02
C(LTX)03-C	48.0	41.3	C(LTX)03
C(HTX)01-C	42.9	33.0	C(HTX)01
C(HTX)02-C	42.7	38.2	C(HTX)02
C(HTX)03-C	45.3	34.9	C(HTX)03
F(LTX)01-C	42.7	35.0	F(LTX)01
F(LTX)02-C	43.1	36.1	F(LTX)02
F(LTX)03-C	43.8	37.8	F(LTX)04
P(LTX)01-C	46.0	38.5	P(LTX)01
P(LTX)02-C	45.2	34.9	P(LTX)02
P(LTX)05-C	44.4	36.3	P(LTX)04

* Value was lost during data reduction (dimensions in mm)

APPENDIX F. AGING CALIBRATION EXPERIMENTS

Overview

A comprehensive experiment was performed to calibrate the extent of the AA process on the temperature-aged specimens. The temperature dependence of the chemical reactions in each of the three mixtures (PCC, CFA-C, and CFA-F) was assessed following the procedure in ASTM C 1074, "Standard Practice for Estimating Concrete Strength by the Maturity Method." According to this procedure, the apparent activation energy, E_a, of cement hydration is estimated from the development of compressive strength in at least three isothermal curing conditions.

In actuality, the ASTM C 1074 method calculates an index of the temperature dependence of the development of compressive strength with time. Since the levels of compressive strength acquired are an indication of the extent of cement hydration, this calculated index is often referred to as the "apparent activation energy" of cement hydration, even though this method does not assess the extent of cement hydration directly. Nevertheless, the ASTM C 1074 method used to calculate E_a is largely recognized as reasonable approximation, mostly because it is often applied to estimate compressive strength at early ages.

In this project, however, the main focus was to accelerate the aging process of concrete in order to predict long-term environmental performance based on the following parameters: monolith integrity, environmental characterization, and product leaching. Therefore, assessing temperature-aging effects based on an index from only compressive strength development (ASTM C 1074) may not be appropriate, since this single mechanical property is not indicative of all material parameters of interest. To further investigate this issue, apparent activation energy (E_a) was also estimated in this project based on the development of both non-evaporable water content and ultrasonic pulse velocity. Non-evaporable water content gives an indication of the extent of cement hydration, whereas ultrasonic pulse velocity is related to the modulus of elasticity and stiffness of the mixtures. This three-fold approach (compressive strength, non-evaporable water content, and ultrasonic pulse velocity) likely gave a better estimation of AA effects on the aforementioned parameters of interest. For each mix, the calculated activation energies from the three different concrete properties were used to compute "equivalent ages" of the control, 100-day, and 200-day prisms and cylinders.

Mortar mixtures reproducing the mortar fraction of the concrete mixtures from this project were prepared. ASTM Type I cement, the same CFA-C and CFA-F, and an ASTM C 33 concrete sand graded to match the same gradation as that in the aging prisms were used. The materials were mixed in a 0.1 m^3 drum mixer in the laboratory. Four batches were prepared for each mixture to be used in one of the four curing temperatures (10, 25, 45, and 60°C). For each batch, many 5- by 5- by 5-cm cubes and four 2.5- by 2.5- by 25-cm beams were cast in metal molds according to ASTM C 109. The casting process for a set of cubes is illustrated in figure F-1. After casting, the cubes and beams were wrapped in plastic bags (see figure F-2) and transferred to a temperature controlled environment until they were strong enough to be demolded. At this point, they were removed from their molds, measured, labeled, and placed in a water curing environment at the designated temperature (see figure F-3).

Figure F-1: Cube casting.

Figure F-2: Wrapped samples.

Figure F-3: Sample curing.

Over time, the compressive strength (f_c), ultrasonic pulse velocity (P-wave speed), and non-evaporable water content per unit mass of ignited cement (w_n/c) were assessed for all 12 batches (3 mixtures, 4 temperatures). Initial measurements were made after the specimens were demolded (a time which varied with each mix and curing temperature), and subsequent data were taken at times twice that of the previous measurement, until at least eight data points had been taken for each batch. Additionally, at early ages extra samples were tested between these times.

Compressive Strength

For each data point, the maximum compressive load for each of three mortar cubes was measured (see figure F-4) following ASTM C 109. If the result for any one cube differed more than about 15 percent from the average of compressive loads, a fourth cube was assessed as well. The compressive strength of each of the cubes was then calculated from its maximum compressive load and measured cross-sectional area, and the results from all three (or four) cubes were averaged (neglecting outliers beyond a 25 percent threshold of the mean) to yield the compressive strength for the given data point.

Non-Evaporable Water Content

The non-evaporable water content per unit mass of ignited cement was determined following a loss-on-ignition procedure. Samples for non-evaporable water content measurements were taken from the same cubes tested for compressive strength. After the maximum compressive load was achieved, each cube was further crushed to about half of its original height. Some of the semi-crushed material was then collected to fill three-fourths of a 15-mL crucible (see figure F-5). This sample was then manually ground with a mortar and pestle, placed in a clean container, and covered with methanol to halt the hydration process.

The final ground sample and methanol mixture was flushed in a vacuum apparatus to remove some of the material's surface water. The flushed sample was transferred to two clean, pre-weighed crucibles and heated in an oven for at least 12 hours at 105°C. After the oven stage, the crucibles were weighed and then heated in a furnace for 3 hours at 1050°C. (Since the furnace required 2 hours to reach this set point, the crucibles were actually left in the furnace for 5 hours during heating, and then 1 additional hour once the furnace had been turned off and was cooling.) The crucibles were weighed again following the furnace stage. The amount of non-evaporable water per unit mass of ignited cement was calculated based on the mass difference of the material before and after ignition, corrected for the loss on ignition of the component materials, according to the following equation (Byfors, 1980):

$$\frac{w_n}{c} = \frac{(1+g)\ (m_{105} - m_{1050}) -\ x\ g\ m_{105} -\ y\ m_{105}}{(1+g)\ m_{1050} -\ (1-x)\ g\ m_{105}} \tag{49}$$

where:
w_n/c is the mass of non-evaporable water content per ignited mass of cement,

37
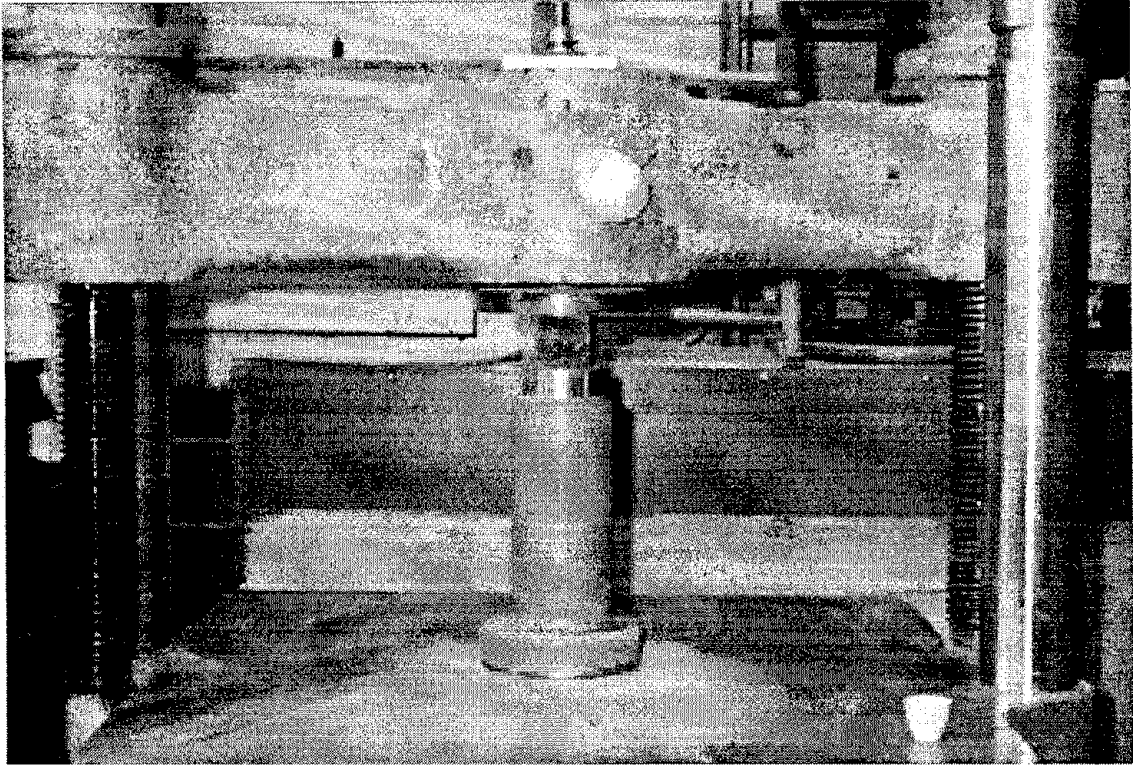
Figure F-4: Compressive strength testing.

Figure F-5: Non-evaporable water content testing.

m_{105} is the mass of the sample after the oven drying,
m_{1050} is the mass of the sample after the furnace ignition,
x is the loss on ignition of the fine aggregate,
y is the loss on ignition of the cement, and
g is the original dry fine aggregate-cement ratio.

The w_n term in the equation above represents the total non-evaporable water in the hydrated products, which in this case are from cement hydration only.

For mixtures with fly ash, a different equation assuming fly ash in the calculation of w_n (still with respect to unit mass of ignited cement) was used as follows:

$$\frac{w_n}{c} = \frac{(1+g+h)\ (m_{105}-m_{1050})\ -\ (gx+hz)\ m_{105}\ -\ y\ m_{105}}{(1+g+h)\ m_{1050}\ -\ [g(1-x)+h(1-z)]\ m_{105}} \tag{50}$$

where:

z is the loss on ignition of the fly ash, and
h is the original dry fly ash-cement ratio.

The w_n term in the equation above still represents the total non-evaporable water in the hydrated products, which in this case are not only from cement hydration but also from the fly ash pozzolanic reaction and the fly ash hydration. The observed losses on ignition for the component materials were 1.5 percent for cement, 8.9 percent for fine aggregate, 0.7 percent for the CFA-C, and 0.9 percent for the CFA-F.

The variability of the non-evaporable water content procedure was evaluated before its use, specifically with respect to sample location in the cube, crushed sample size, and operator crushing performance. Based on this evaluation, a standardized procedure was developed and utilized throughout the experiment. Although the inherent variability in the w_n/c procedure far exceeds that of the f_c and P-wave speed tests, it was minimized through the use of the standardized procedure.

Degree of hydration can be estimated most simply from the non-evaporable water content of cement pastes and mortars in which cement is the only hydrating material, and thus the only component which binds water. The conversion of w_n to DoH is based on the non-evaporable water content for the specific cement at full hydration, according to the following equation (Powers and Brownyard, 1948):

$$\alpha = \frac{w_n/c}{K} \tag{51}$$

where:

a is the degree of cement hydration, and

w_n/c is the of non-evaporable water content per ignited mass of cement.

The value of K varies depending on the age of the specimen, the type of cement, and the w/c (Copeland et al., 1960). A typical value of K is 0.25 (Byfors, 1980; Lea, 1971).

The estimation of degree of hydration becomes much more complicated, however, in mixtures with additional cementitious materials since the non-evaporable water is no longer a result of only cement hydration. In CFA-F mixtures, the hydration process encompasses both cement hydration and pozzolanic reactions. In CFA-C mixtures, however, bound water results from not only the aforementioned cement hydration and pozzolanic reactions, but also direct hydration of the ash itself, since CFA-C commonly has high percentages of CaO .

Before bound water measurements can be converted to degree of hydration for any of these mixtures, the locations and relative proportions of the bound water must be known. If, for example in the CFA-F mixtures, the pozzolanic reaction does not bind any additional water beyond that already bound in the cement hydrates, then all bound water would still be indicative of the original cement hydration. If, on the other hand, the pozzolanic reaction does bind additional water from the system, then a calculation based on equation 51 would tend to overestimate the degree of cement hydration. In CFA-C mixtures, equation 51 overestimates the extent of cement hydration since it does not differentiate between the non-evaporable water content resulting from cement hydration or fly ash hydration.

As such, the determination of degree of hydration in mixtures with fly ash should be based on modified versions of equation 51, which accounts for the effect of the pozzolanic reactions, supplementary hydration, and possible interactions with the bound water. The process of modifying equation 51, however, cannot be accurately completed based on the knowledge currently available, but will require further study.

Ultrasonic Pulse Velocity

Measurements of ultrasonic pulse velocity were performed on the mortar beams rather than on the cubes, since the high aspect ratio of the long, thin beams is more appropriate for wave propagation tests. For each data point (at the same time as the compressive strength and w_n/c tests), the pulse travel time was evaluated following ASTM C 597, as seen in figure F-6. Upon completion of each reading, the beams were returned to their curing environment until the next measurement time. The P-wave speed was then calculated from the pulse travel time and the measured beam length.

Aging Calibration Results

The results for compressive strength, non-evaporable water content, and ultrasonic pulse velocity for all 12 batches are presented in tables F-1 through F-3.

Table F-1: Calibration experiments results for PCC mixture.

PCC Age (days)	10°C fc (MPa)	10°C wn/c (g/g-ic)	10°C p-wave (m/s)	25°C fc (MPa)	25°C wn/c (g/g-ic)	25°C p-wave (m/s)	45°C fc (MPa)	45°C wn/c (g/g-ic)	45°C p-wave (m/s)	60°C fc (MPa)	60°C wn/c (g/g-ic)	60°C p-wave (m/s)
3 hr	-	-	-	-	-	-	-	-	-	3.0	0.023	1383
4 hr	-	-	-	-	-	-	2.4	0.031	2739	-	-	-
4.5 hr	-	-	-	-	-	-	-	-	-	13.6	0.083	3096
6 hr	-	-	-	-	-	-	11.1	0.079	3200	18.2	0.091	3385
9 hr	-	-	-	4.7	0.058	2801	16.7	0.118	3472	22.5	0.114	3536
12 hr	-	-	-	-	-	-	-	-	-	26.7	0.120	3639
13 hr	-	-	-	7.6	0.083	3166	23.2	0.106	3676	-	-	-
16 hr	-	-	-	-	-	-	-	-	-	26.2	0.135	3738
18 hr	-	-	-	13.6	0.099	3477	25.7	0.129	3718	-	-	-
1	9.5	0.082	3196	19.1	0.103	3659	28.2	0.142	3806	27.2	0.138	3799
1.5	22.0	0.106	3467	22.9	0.136	3799	27.7	0.152	3851	-	-	-
2	23.8	0.136	3563	-	-	-	-	-	-	30.2	0.156	3892
3	25.7	0.140	3665	31.2	0.157	3940	35.4	0.153	3963	-	-	-
4	29.1	0.140	3730	35.4	0.170	4011	-	-	-	34.6	0.154	3956
6	-	-	-	42.5	0.184	4108	36.3	0.175	4005	-	-	-
8	32.5	0.159	3865	42.9	0.190	4158	-	-	-	37.0	0.165	4018
11	-	-	-	-	-	-	41.8	0.164	4080	-	-	-
13	-	-	-	-	-	-	-	-	-	-	-	-
16	39.4	0.189	4056	-	-	-	-	-	-	-	-	-
24	-	-	-	-	-	-	-	-	-	-	-	-
33	45.4	0.210	4114	-	-	-	-	-	-	-	-	-
49	-	-	-	-	-	-	-	-	-	44.7	0.198	4067
57	-	-	-	-	-	-	46.6	0.191	4138	-	-	-
65	51.6	0.208	4235	-	-	-	-	-	-	-	-	-
87	-	-	-	-	-	-	-	-	-	-	-	-
127	59.7	0.225	4296	56.0	0.220	4303	-	-	-	-	-	-

Curing temperatures

Table F-2: Calibration experiments results for CFA-C mixture.

CFA-C												
	Curing temperatures											
	10°C			25°C			45°C			60°C		
Age (days)	f_c (MPa)	w_n/c (g/g-ic)	p-wave (m/s)	f_c (MPa)	w_n/c (g/g-ic)	p-wave (m/s)	f_c (MPa)	w_n/c (g/g-ic)	p-wave (m/s)	f_c (MPa)	w_n/c (g/g-ic)	p-wave (m/s)
3 hr	-	-	-	-	-	-	-	-	-	2.5	0.035	1443
4.5 hr	-	-	-	-	-	-	2.3	0.025	1623	10.2	0.057	2997
6 hr	-	-	-	2.0	0.059	1986	8.5	0.049	2786	14.8	0.088	3218
9 hr	-	-	-	5.2	0.069	2590	15.4	0.076	3385	17.1	0.097	3381
12 hr	-	-	-	10.1	0.079	3079	-	-	-	19.1	0.133	3495
13 hr	-	-	-	-	-	-	20.4	0.118	3547	-	-	-
16 hr	6.8	0.088	2600	14.2	0.086	3383	-	-	-	23.4	0.151	3742
17 hr	-	-	-	-	-	-	-	-	-	-	-	-
18 hr	-	-	-	-	-	-	21.9	0.129	3635	25.5	0.153	3625
1	11.2	0.107	3030	19.0	0.128	3579	26.2	0.134	3758	-	-	-
1.5	17.2	0.123	3461	23.7	0.146	3711	25.7	0.167	3887	-	-	-
2	22.2	0.121	3585	26.4	0.173	3783	-	-	-	30.0	0.176	3776
3	25.8	0.120	3661	-	-	-	31.8	0.159	3892	-	-	-
4	-	-	-	32.2	0.189	3912	-	-	-	32.9	0.195	3898
6	-	-	-	-	-	-	34.5	0.187	3999	-	-	-
7	33.3	0.186	3924	-	-	-	-	-	-	-	-	-
8	-	-	-	35.3	0.223	3963	38.5	0.196	4164	36.2	0.196	3907
13	-	-	-	-	-	-	-	-	-	-	-	-
14	40.1	0.195	4005	41.4	0.251	4064	-	-	-	-	-	-
16	-	-	-	-	-	-	-	-	-	-	-	-
24	41.0	0.215	4096	-	-	-	43.3	0.214	4142	-	-	-
36	-	-	-	-	-	-	-	-	-	42.7	0.202	3954
37	-	-	-	-	-	-	-	-	-	-	-	-
58	46.3	0.269	4259	-	-	-	-	-	-	-	-	-
63	-	-	-	54.2	0.265	4307	-	-	-	-	-	-
99	51.8	0.266	4265	-	-	-	-	-	-	-	-	-

Table F-3: Calibration experiments results for CFA-C mixture.

CFA-F	Curing temperatures											
	10°C			25°C			45°C			60°C		
Age (days)	f_c (MPa)	w_n/c (g/g-ic)	p-wave (m/s)	f_c (MPa)	w_n/c (g/g-ic)	p-wave (m/s)	f_c (MPa)	w_n/c (g/g-ic)	p-wave (m/s)	f_c (MPa)	w_n/c (g/g-ic)	p-wave (m/s)
2 hr	-	-	-	-	-	-	-	-	-	2.4	0.018	1852
4 hr	-	-	-	-	-	-	1.2	0.024	1458	-	-	2961
4.5 hr	-	-	-	-	-	-	-	-	-	9.6	0.050	3214
6 hr	-	-	-	2.5	0.057	2000	7.2	0.072	2803	12.8	0.082	3408
9 hr	-	-	-	4.8	0.077	2514	14.0	0.080	3300	17.4	0.129	3546
12 hr	-	-	-	-	-	-	-	-	-	19.5	0.121	-
13 hr	-	-	-	9.3	0.095	2912	19.3	0.088	3511	-	-	-
16 hr	-	-	-	-	-	-	-	-	-	22.4	0.126	3571
18 hr	9.1	0.093	3016	13.3	0.098	3256	22.1	0.122	3617	-	-	-
1	11.7	0.106	3172	17.8	0.110	3480	26.4	0.122	3707	25.0	0.152	3654
1.5	17.0	0.098	3494	21.0	0.123	3661	28.3	0.141	3795	-	-	-
2	21.9	0.114	3585	23.7	0.154	3761	-	-	-	31.7	0.186	3817
3	25.1	0.131	3681	-	-	-	33.1	0.147	3795	-	-	-
4	-	-	-	32.1	0.173	3887	-	-	-	34.7	0.178	3856
7	31.4	0.136	3922	-	-	-	39.3	0.163	3960	-	-	-
8	-	-	-	37.7	0.191	4008	-	-	-	36.6	0.179	4044
11	-	-	-	-	-	-	44.8	0.173	4119	-	-	-
14	36.2	0.178	4034	-	-	-	-	-	-	-	-	-
16	-	-	-	38.8	0.204	4068	-	-	-	-	-	-
24	42.3	0.183	4072	-	-	-	-	-	-	-	-	-
29	-	-	-	-	-	-	-	-	-	29.0	0.177	4215
49	49.8	0.229	4228	-	-	-	-	-	-	-	-	-
51	-	-	-	-	-	-	52.5	0.172	4250	-	-	-
70	-	-	-	56.8	0.246	4270	-	-	-	-	-	-
98	54.7	0.226	4511	-	-	-	-	-	-	-	-	-

Figure F-6: Ultrasonic pulse velocity.

development of non-evaporable water content and ultrasonic pulse velocity, respectively, versus time for each of the three mixtures at all four temperatures.

Aging Calibration Analysis

AA Fundamentals

The purpose of the aging calibration tests was to estimate the apparent activation energy, and thus the temperature sensitivity of the cement hydration for each mixture (PCC, CFA-C, CFA-F). Since the mixture compositions and components of the aging calibration mortar samples corresponded to the mortar fraction of the concrete prisms and cylinders aged in the curing tanks, the E_a estimated can be used for the concrete mixtures, as per ASTM C 1074.

The basis for accelerating aging is that cement hydration is a chemical reaction, which follows the Arrhenius equation shown:

$$k_t = Ae^{-\frac{E_a}{R}\frac{1}{T}} \tag{52}$$

or,

$$\ln(k_t) = \ln(A) - \frac{E_a}{R}\frac{1}{T} \tag{53}$$

where:

k_t is the rate constant of a chemical reaction,
A is the constant,
E_a is the apparent activation energy (J/mol),
R is the universal gas constant (8.314 J/mol-K), and
T is the absolute temperature.

Equation 53 indicates that when the natural logarithm of the rate constant is plotted with the inverse of the absolute temperature, a linear plot (called an Arrhenius plot) is obtained in which the apparent activation energy is the slope divided by the universal gas constant.

The rate constant is obtained by specific functions (k_t dependent) that model the property of interest with time in isothermal conditions. Two functions were investigated; a linear-hyperbolic function and a parabolic-hyperbolic function. Thus, by obtaining k_t at various isothermal conditions, E_a can be estimated from the Arrhenius plot (Laidler, 1987; Ladd and Lee, 1986).

Once E_a has been estimated, it can be used to determine the equivalent age of the specimen at a reference temperature (20 °C) according to the Freiesleben-Hansen and Pedersen (FHP) maturity equation (Freiesleben-Hansen and Pedersen, 1977):

46

$$t_e = \sum_0^t \exp\left[-\frac{E_a}{R}\left(\frac{1}{T} - \frac{1}{T_r}\right)\right]\Delta t$$

(54)

where:

t_e is the equivalent age at a reference temperature T_r,

T_r is the absolute reference temperature (293 °K),

T is the absolute concrete temperature during interval Δt(K).

Δt is the time interval.

This equivalent age indicates the equivalent curing time at 20 °C necessary to achieve the same level of development achieved in the actual curing temperatures. For example, a concrete mixture cured at 45 °C for 100 days might have the same level of development as the same mixture cured at 20 °C for 300 days. In this case, the equivalent age of the 45 °C cured mixture at 100 days would be 300 days at 20 °C.

Linear-Hyperbolic Model

In the ASTM C 1074 procedure to obtain E_a, mortar specimens are cured in isothermal conditions, and the specific linear-hyperbolic function (k_t dependent), as shown in equation 55, is assumed to describe mortar compressive strength over time.

$$S = S_\infty \frac{k_t(t_e - t_o)}{1 + k_t(t_e - t_o)}$$

(55)

where:

S is the compressive strength at equivalent age t_e,

S_∞ is the compressive strength at infinite equivalent age, or limiting strength,

t_o is the equivalent age when compressive strength development is assumed to begin.

For a particular mortar mixture, the parameters , k_t, and t_o are estimated for each isothermal curing temperature and the corresponding Arrhenius plot is drawn, to yield E_a.

The data from the aging calibration tests were analyzed using the ASTM C 1074 compressive strength-based procedure. In addition, a similar, parallel procedure was applied to ultrasonic pulse velocity and non-evaporable water content developments over time. For these cases, equation 56 (similar to equation 55) was assumed to describe the development of the property of interest over time.

$$P = P_\infty \frac{k_t(t_e - t_{op})}{1 + k_t(t_e - t_{op})}$$

(56)

where:

47

P is the property at equivalent age t_e,

P_∞ is the property at infinite equivalent age, or limiting strength, and

t_{op} is the equivalent age when the development of the property is assumed to begin.

For each mixture (PCC, CFA-C, and CFA-F), the estimated values of S and k_t from equation 56, based on the compressive strength, ultrasonic pulse velocity and non-evaporable water content results presented in tables F-1 through F-3, are shown in tables F-4 through F-6.

Equivalent ages for each testing time at all curing temperatures were calculated with the values of E_a from table F-7, using equation 54. The development of the relative property of interest (P/P_∞) with actual times and equivalent ages for all mixtures were examined graphically. The best-fit linear hyperbolic curves, according to equation 56, were also examined.

Table F-8 shows the values of the statistical parameters (dof-adjusted-R^2 and fit-standard-error) obtained from each best-fit curve that was graphically examined The dof-adjusted-R^2 is the coefficient of determination adjusted for the degree of freedom while the fit-standard-error is the actual least squares error of the fit. The closer the value of dof-adjusted-R^2 is to 1, and the closer the value of the fit-standard error is to zero, the better the fit.

The calculated apparent activation energies, presented in table F-7, were used to estimate the equivalent ages of the temperature aged concrete cylinders and prisms, according to their curing temperature. It was assumed that the specimens were all cured at 25 °C for the first 28 days, before having arrived at Cornell. After this 28-day initial curing period, the specimens with no thermal aging remained in a curing tank of 30°C for the next 200 days. The specimens with low thermal aging stayed in the 60°C curing tank for 100 days and then were transferred to the 30°C curing tank for the next 100 days. The specimens with high thermal aging stayed in the 60°C tank for 200 days. The equivalent ages at the final 228 days (initial 28 plus 200 days at Cornell) for each level of thermal aging for each mixture by the three properties studied (f_c p-wave, and w_n/c) are presented in table F-9.

The means of the equivalent ages in table F-9 were calculated according to ASTM C 1074 using the activation energies listed in table F-7. This procedure makes no allowance for variability. The variability in table F-9 reflects one standard deviation in the calculation of E_a.

Parabolic-Hyperbolic Model

A parabolic-hyperbolic function, of the following form, is used to describe the development of f_c, p-wave, and w_n/c over time:

$$P = P_\infty \frac{\sqrt{k_t(t_e - t_{op})}}{1 + \sqrt{k_t(t_e - t_{op})}}$$

$$(57)$$

48

Table F-4: Estimated values of S_∞ and k_t - linear-hyperbolic model.

Temperature	Mixture					
	PCC		CFA-C		CFA-F	
(C)	S_∞ (MPa)	k_t	S_∞ (MPa)	k_t	S_∞ (MPa)	k_t
10	60.2	0.0095	51.0	0.0161	59.2	0.0109
25	58.1	0.0217	50.5	0.0303	56.5	0.0236
45	45.0	0.0973	42.7	0.0790	52.1	0.0540
60	43.1	0.1611	41.1	0.1068	38.9	0.0930

Table F-5: Estimated values of p-wave$_\infty$ and k_t - linear-hyperbolic model.

Temperature	Mixture					
	PCC		CFA-C		CFA-F	
(C) p-wave	p-wave$_\infty$ (m/s)	k_tp-wave	p-wave$_\infty$ (m/s)	k_tp-wave	p-wave$_\infty$ (m/s)	k_t
10	4299	0.046	4320	0.0520	4132	0.1050
25	4279	0.2291	4228	0.2053	4224	0.1955
45	4127	0.4529	4193	0.3632	4217	0.3041
60	4065	0.7452	3966	0.6827	4163	0.3749

Table F-6: Estimated values of $(w_n/c)\infty$ and k_t - linear-hyperbolic model.

Temperature	Mixture					
	PCC		CFA-C		CFA-F	
(C) (w_n/c)	∞	$k_t(w_n/c)$	∞	$k_t(w_n/c)$	∞	k_t
10	0.227	0.0101	0.289	0.0085	0.240	0.0066
25	0.214	0.0375	0.275	0.0318	0.236	0.0329
45	0.179	0.1565	0.218	0.0908	0.173	0.1216
60	0.167	0.2793	0.224	0.1633	0.185	0.1886

Table F-7: Calculated values of E_a (kJ/mol) - linear-hyperbolic model.

Mixture	Based on f_c	Based on p-wave	Based on w_n/c
PCC	47.6	42.7	54.1
CFA-C	30.7	38.2	45.8
CFA-F	34.5	20.3	54.2

Table F-8: Statistical parameters of the best-fit- linear hyperbolic curves.

Mixture	Property					
	f_c		w_n/c		p-wave	
	dof-R^2	F-S-E	dof-R^2	F-S-E	dof-R^2	F-S-E
PCC	0.917	0.077	0.901	0.076	0.757	0.060
CFA-C	0.923	0.080	0.889	0.086	0.923	0.043
CFA-F	0.952	0.062	0.921	0.071	0.863	0.053

Table F-9: Equivalent ages (in years) at 20°C after the end of thermal aging treatment - linear-hyperbolic model.

Thermal Aging	Equivalent Age		
	by f_c	by p-wave	by w_n/c
	PCC		
none	1.2	1.1 ± 0.1	1.3
low	3.5 ± 0.6	2.8 ± 0.8	4.6 ± 1.0
high	5.9 ± 1.2	4.6 ± 1.5	8.0 ± 2.0
	CFA-C		
none	0.9	1.0	1.1
low	1.8 ± 0.2	2.4 ± 0.5	3.2 ± 0.6
high	2.6 ± 0.4	3.7 ± 1.0	5.4 ± 1.2
	CFA-F		
none	1.0	0.8	1.3 ± 0.1
low	2.0 ± 0.1	1.2 ± 0.1	4.6 ± 1.3
high	3.1 ± 0.2	1.6 ± 0.2	8.0 ± 3.6

where:

> P is the property at equivalent age t_e,
> P_∞ is the property at infinite equivalent age, or limiting strength, and
> t_{op} is the equivalent age when the development of the property is assumed to begin.

For each mixture (PCC, CFA-C, and CFA-F), the estimated values of S_∞ and k_t from equation 57, based on the compressive strength, ultrasonic pulse velocity, and non-evaporable water content results are shown in tables F-10 through F-12.

The Arrhenius plots generated by these values of k_t for each mixture were examined graphically The calculated E_a for each mixture by each property development are listed in table F-13.

After obtaining equivalent ages at each testing time according to the same procedure used to analyze the data when using the linear-hyperbolic model, the development of the P/P_∞ (for f_c, p-wave, and w_n/c) with actual times and equivalent ages were graphed. The statistical parameters of the best-fit parabolic hyperbolic curves are shown in table F-14.

The equivalent ages of the temperature aged concrete cylinders and prisms were then calculated and are presented in table F-15.

Table F-10: Estimated values of S^∞ and k_t - parabolic-hyperbolic model.

Temperature	Mixture					
	PCC		CFA-C		CFA-F	
(C) S^∞	S^∞ (MPa)	$k_t S$	S^∞ (MPa)	$k_t S$	S^∞ (MPa)	k_t
10	70.1	0.0056	65.4	0.0071	71.0	0.0043
25	68.3	0.0083	65.8	0.0111	69.3	0.0060
45	51.6	0.0562	52.1	0.0436	63.4	0.0192
60	45.8	0.1280	47.8	0.0480	48.7	0.0456

Table F-11: Estimated values of p-wave$_\infty$ and k_t - parabolic-hyperbolic model.

Temperature	Mixture					
	PCC		CFA-C		CFA-F	
(C) p-wave	∞ (m/s)	k_t p-wave	∞ (m/s)	k_t p-wave	∞ (m/s)	k_t
10	4390	0.3686	4370	0.5146	4396	0.4235
25	4329	1.5606	4348	0.8625	4339	0.7482
45	4178	4.8602	4283	2.1566	4335	1.9351
60	4140	5.4553	4046	4.0811	4214	2.9042

Table F-12: Estimated values of (w_n/c) ∞ and k_t - parabolic-hyperbolic model.

Temperature	Mixture					
	PCC		CFA-C		CFA-F	
(C) (w_n/c)	∞	$k_t(w_n/c)$	∞	$k_t(w_n/c)$	∞	k_t
10	0.246	0.0282	0.338	0.0069	0.306	0.0045
25	0.238	0.0444	0.331	0.0188	0.283	0.0223
45	0.195	0.2668	0.242	0.0667	0.195	0.1392
60	0.185	0.4100	0.260	0.1025	0.197	0.4065

Table F-13: Calculated values of E_a (kJ/mol) -
parabolic-hyperbolic model.

Mixture	Based on f_c	Based on p-wave	Based on w_n/c
PCC	54.0	43.9	47.1
CFA-C	33.1	32.9	43.4
CFA-F	39.1	32.0	59.6

Table F-14: Statistical parameters of the best-fit parabolic
hyperbolic curves.

Mixture	Property					
	f_c		w_n/c		p-wave	
	dof-R^2	F-S-E	dof-R^2	F-S-E	dof-R^2	F-S-E
PCC	0.954	0.051	0.965	0.044	0.977	0.035
CFA-C	0.929	0.059	0.927	0.061	0.900	0.074
CFA-F	0.967	0.022	0.949	0.035	0.955	0.029

Table F-15: Equivalent ages (in years) at 20°C after the end of
thermal aging treatment - parabolic-hyperbolic model.

Thermal Aging	Equivalent age		
	by f_c	by p-wave	by w_n/c
PCC			
none	1.2 ± 0.2	1.1 ± 0.1	1.1 ± 0.2
low	4.6 ± 1.9	3.0 ± 1.5	3.4 ± 1.3
high	8.0 ± 3.6	4.9 ± 2.9	5.7 ± 2.5
CFA-C			
none	1.0	1.0	1.1 ± 0.1
low	1.9 ± 0.6	1.9 ± 0.2	2.9 ± 0.6
high	2.9 ± 1.1	2.9 ± 0.3	4.8 ± 1.1
CFA-F			
none	1.0	0.9	1.6 ± 0.1
low	2.5 ± 0.6	1.8 ± 0.2	10.9 ± 2.0
high	3.9 ± 1.1	2.8 ± 0.3	20.1 ± 3.9

APPENDIX G. PRELIMINARY EVALUATIONS OF FREEZE-THAW DATA AND CYCLE SELECTION FOR THE EXPERIMENTAL DESIGN

Of the 365 prisms shipped to CRREL, 63 received 60 cycles of freezing and thawing, while 139 prisms received 30 cycles. The remaining prisms received no treatment at CRREL. Tables G-1 through G-4 show the final relative dynamic modulus of elasticity (RDM) of each prism in this study. Figure G-1 shows a typical series of freeze-thaw cycles. Figure G-2 shows change in RDM as a function of cycles for three prisms.

Table G-1 shows the RDM of the concrete prisms made with CFA-C after 60 cycles of freezing and thawing. Sixteen received no AA or CL (NNH), 16 received only high CL (NHH), 16 received only high AA (HNH), and 15 received high levels of both AA and CL (HHH) prior to being freeze-thaw cycled the high number of times. Table G-2 shows the results of concrete prisms made with CFA-C but exposed to only 30 cycles (L) of freezing and thawing. All of the prisms in this table were previously exposed to low levels of both AA and CL (LLL). The prisms in tables G-3 and G-4 were similarly exposed to low levels of both AA and CL, but they were made with CFA-F and with or just PCC, respectively.

A brief look at the data in tables G-1 through G-4 shows that there is broad range of damage caused by the FT. One would expect that, all else being equal, 60 FT cycles would cause more change in RDM than would 30 cycles. However, the prisms in table G-1 were clearly less affected by 60 cycles of FT than were some of the other prisms exposed to just 30 cycles. Figure G-3 illustrates this point by plotting the average of each RDM column in tables G-1 through G-4.

Of the prisms exposed to 60 cycles of FT, those that had received no AA or CL (NNH) prior to coming to CRREL were among the prisms the least affected by FT. They had an average RDM of nearly 90 percent. This came as no surprise as untreated prisms would be expected to contain the least amount of internal microcracks, which generally, by their amount, reduce durability. However, it was surprising to see that the prisms that received CL (NHH) appeared to be equally unaffected by FT. Their average RDM was slightly above 90 percent. Either the stressing regime was not severe enough to introduce a sufficient amount of cracks into the prisms or autogenous healing occurred. The prisms that received just AA (HNH) prior to being shipped to CRREL were somewhat affected by FT. They averaged about 78 percent RDM. This suggests that AA adversely affects durability. The prisms subjected to both AA and CL (HHH) prior to coming to CRREL faired the worst in this grouping as expected. Their average RDM was about 63 percent.

The rest of the prisms were pretreated to low levels of both AA and CL and to the low level of FT (LLL). For these prisms, the ones made with CFA-C and CFA-F performed about equally. Their RDMs centered on 60 percent. The PCC prisms had a collective RDM of less than 50 percent. In fact, table G-4 contained by far the highest number of prisms with RDMs below 40 percent. It is clear for this grouping that CFA appears to improve the durability of concrete. But it is not clear why the prisms in table G-1 performed better than those in tables G-2 or G-3.

Though air contents varied amongst the prisms, there was no strong correlation between RDM, the number of FT cycles, and air content.

Table G-1: Results of CFA-C prisms subjected
to 60 cycles of FT.

NNH[*]	RDM[**]	NHH	RDM	HNH	RDM	HHH	RDM
C(NNH)01	89.9	C(NHH)01	89.63	C(HNH)01	89.55	C(HHH)01	73.02
C(NNH)02	91.11	C(NHH)02	87.97	C(HNH)02	66.94	C(HHH)02	75.11
C(NNH)03	90.42	C(NHH)03	91.17	C(HNH)03	81	C(HHH)03	64.73
C(NNH)04	90.38	C(NHH)04	89.9	C(HNH)04	74.7	C(HHH)04	75.13
C(NNH)05	89.09	C(NHH)05	91.05	C(HNH)05	76.19	C(HHH)05	69.15
C(NNH)06	91.11	C(NHH)06	90.9	C(HNH)06	86.22	C(HHH)06	66.94
C(NNH)07	87.77	C(NHH)07	93.06	C(HNH)07	67.56	C(HHH)07	N/A
C(NNH)08	89.98	C(NHH)08	92.53	C(HNH)08	85.98	C(HHH)08	58.28
C(NNH)09	92.46	C(NHH)09	89.55	C(HNH)09	68.34	C(HHH)09	59.51
C(NNH)10	87.77	C(NHH)10	87.77	C(HNH)10	83.48	C(HHH)10	64.11
C(NNH)11	91.11	C(NHH)11	90.58	C(HNH)11	81.97	C(HHH)11	35.99
C(NNH)12	90.1	C(NHH)12	89.98	C(HNH)12	78.45	C(HHH)12	71.19
C(NNH)13	89.09	C(NHH)13	88.93	C(HNH)13	77.46	C(HHH)13	54.87
C(NNH)14	86.46	C(NHH)14	86.22	C(HNH)14	82.87	C(HHH)14	74.27
C(NNH)15	86.02	C(NHH)15	91.38	C(HNH)15	76.19	C(HHH)15	43.6
C(NNH)16	90.03	C(NHH)16	91.61	C(HNH)16	78.08	C(HHH)16	61.12

[*] The three letter sequence signifies whether the beams have been exposed to AA, CL or FT and the level of exposure. For example, "N" is no exposure and "H" is high level exposure.

[**] Relative dynamic modulus of elasticity.

Table G-2: Results of CFA-C prisms subjected to 30 cycles of FT.

LLL*	RDM**	LLL	RDM	LLL	RDM
C(LLL)01	55.83	C(LLL)17	52.51	C(LLL)33	69.57
C(LLL)02	61.52	C(LLL)18	58.78	C(LLL)34	48.45
C(LLL)03	61.15	C(LLL)19	44.14	C(LLL)35	42.36
C(LLL)04	36.94	C(LLL)20	70.23	C(LLL)36	77.15
C(LLL)05	67.29	C(LLL)21	N/A	C(LLL)37	72.10
C(LLL)06	69.04	C(LLL)22	60.37	C(LLL)38	51.86
C(LLL)07	59.54	C(LLL)23	54.91	C(LLL)39	60.37
C(LLL)08	54.53	C(LLL)24	65.80	C(LLL)40	76.64
C(LLL)09	67.56	C(LLL)25	52.43	C(LLL)41	75.19
C(LLL)10	N/A	C(LLL)26	50.36	C(LLL)42	30.56
C(LLL)11	52.61	C(LLL)27	51.97	C(LLL)43	53.02
C(LLL)12	61.00	C(LLL)28	70.36	C(LLL)44	76.88
C(LLL)13	67.41	C(LLL)29	67.68	C(LLL)45	64.73
C(LLL)14	N/A	C(LLL)30	56.94	C(LLL)46	53.42
C(LLL)15	63.88	C(LLL)31	51.60	C(LLL)47	50.59
C(LLL)16	51.11	C(LLL)32	77.12	C(LLL)48	74.23

* The three letter sequence signifies whether the beams have been exposed to AA, CL or FT and the level of exposure. For example, "L" is low exposure.

** Relative dynamic modulus of elasticity.

Table G-3: Results of CFA-F prisms subjected to 30 cycles of FT.

LLL*	RDM**	LLL	RDM	LLL	RDM
F(LLL)01	52.73	F(LLL)17	79.44	F(LLL)33	60.86
F(LLL)02	74.79	F(LLL)18	49.36	F(LLL)34	69.62
F(LLL)03	60.75	F(LLL)19	72.1	F(LLL)35	73.47
F(LLL)04	67.41	F(LLL)20	63.88	F(LLL)36	60.41
F(LLL)05	67.98	F(LLL)21	71.69	F(LLL)37	77.11
F(LLL)06	36.35	F(LLL)22	69.83	F(LLL)38	71.91
F(LLL)07	64.7	F(LLL)23	69.77	F(LLL)39	61.07
F(LLL)08	64.35	F(LLL)24	58.34	F(LLL)40	65.47
F(LLL)09	68.4	F(LLL)25	71.69	F(LLL)41	72.24
F(LLL)10	39.71	F(LLL)26	42.52	F(LLL)42	75.86
F(LLL)11	72.29	F(LLL)27	72.83	F(LLL)43	76.64
F(LLL)12	66.72	F(LLL)28	53.08	F(LLL)44	67.82
F(LLL)13	53.63	F(LLL)29	66.8	F(LLL)45	75.45
F(LLL)14	22.11	F(LLL)30	43.15	F(LLL)46	79.37
F(LLL)15	N/A	F(LLL)31	69.86	F(LLL)47	64.5
F(LLL)16	78.45	F(LLL)32	38.72	F(LLL)48	71.05

* The three letter sequence signifies whether the beams have been exposed to AA, CL or FT and the level of exposure. For example, "L" is low exposure.

** Relative dynamic modulus of elasticity.

Table G-4: Results of PCC prisms subjected to 30 cycles of FT.

LLL*	RDM**	LLL	RDM	LLL	RDM
P(LLL)01	59.37	P(LLL)17	35.45	P(LLL)33	57.94
P(LLL)02	30.96	P(LLL)18	59.1	P(LLL)34	35.74
P(LLL)03	40.09	P(LLL)19	N/A	P(LLL)35	48.64
P(LLL)04	38.56	P(LLL)20	47.76	P(LLL)36	47.25
P(LLL)05	38.23	P(LLL)21	35.81	P(LLL)37	72.28
P(LLL)06	34.82	P(LLL)22	61.62	P(LLL)38	40.76
P(LLL)07	60.71	P(LLL)23	18.4	P(LLL)39	64.02
P(LLL)08	38.81	P(LLL)24	66.86	P(LLL)40	29.49
P(LLL)09	55.54	P(LLL)25	39.06	P(LLL)41	67.54
P(LLL)10	60.27	P(LLL)26	47.99	P(LLL)42	62.14
P(LLL)11	71.31	P(LLL)27	38.67	P(LLL)43	66
P(LLL)12	62.69	P(LLL)28	63.27	P(LLL)44	46.71
P(LLL)13	63.15	P(LLL)29	31.71	P(LLL)45	67.25
P(LLL)14	34.89	P(LLL)30	36.18	P(LLL)46	41.38
P(LLL)15	59.37	P(LLL)31	31.08	P(LLL)47	63.15
P(LLL)16	42.78	P(LLL)32	71.6	P(LLL)48	47.6

* The three letter sequence signifies whether the beams have been exposed to AA, CL or FT and the level of exposure. For example, "L" is low exposure.
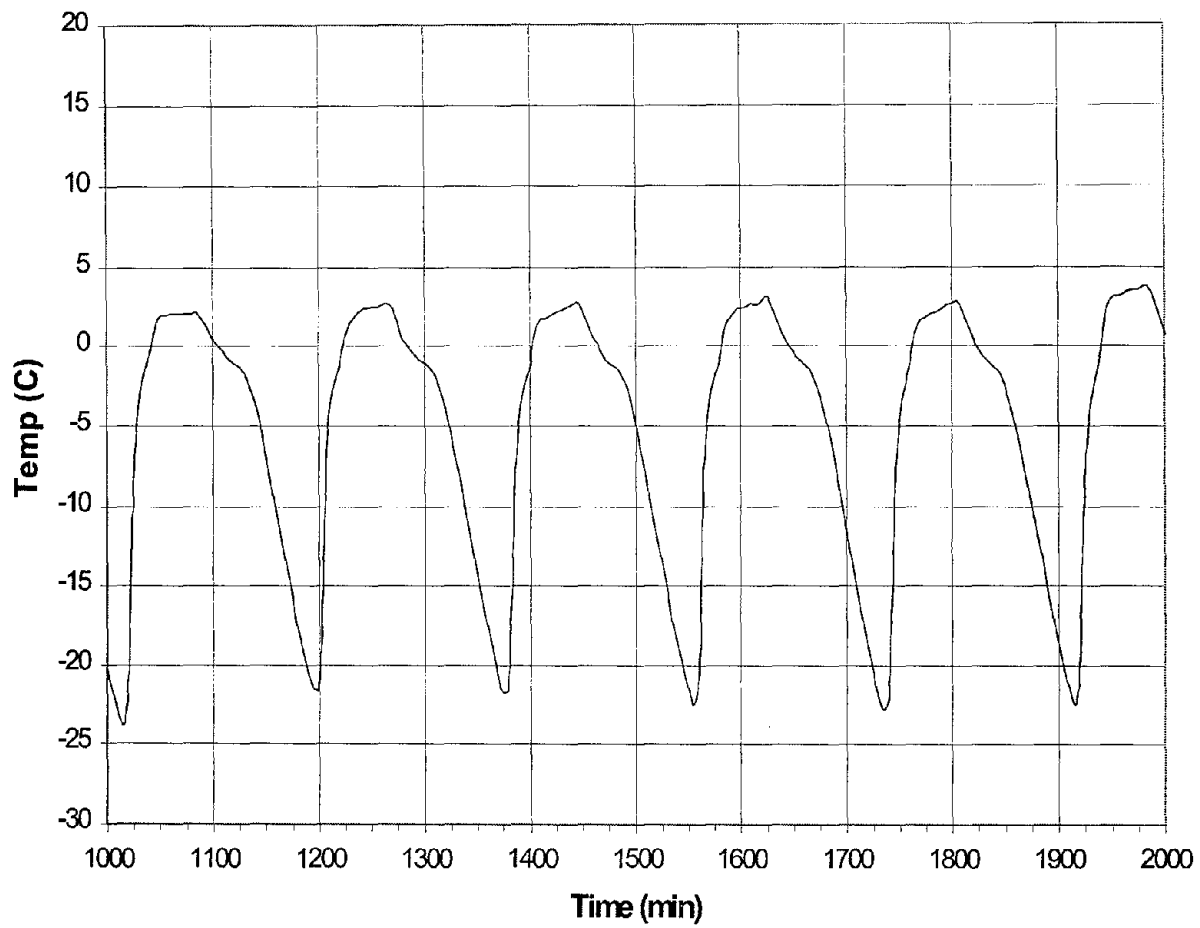
** Relative dynamic modulus of elasticity.

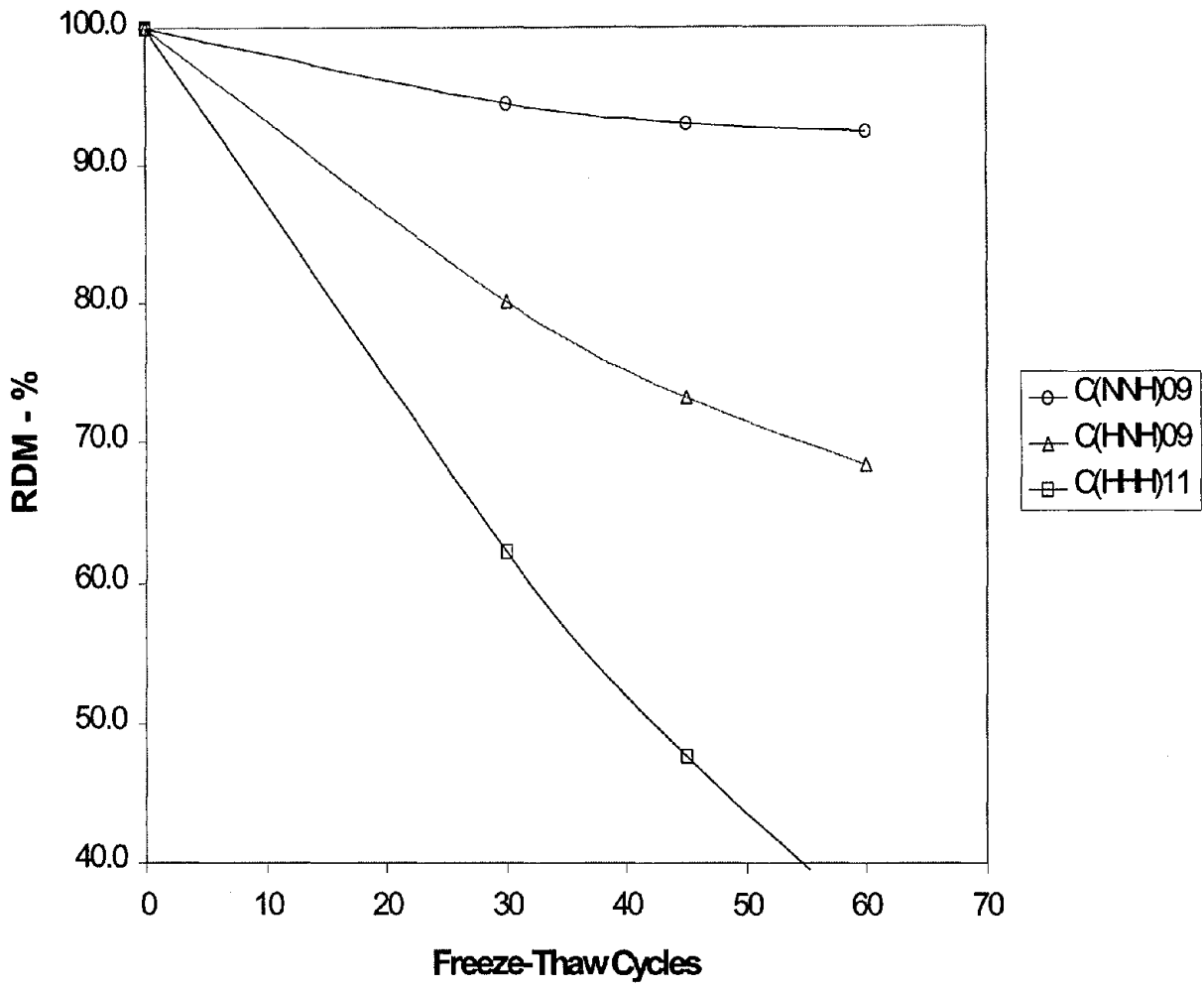Figure G-1: Typical freezing and thawing cycles.

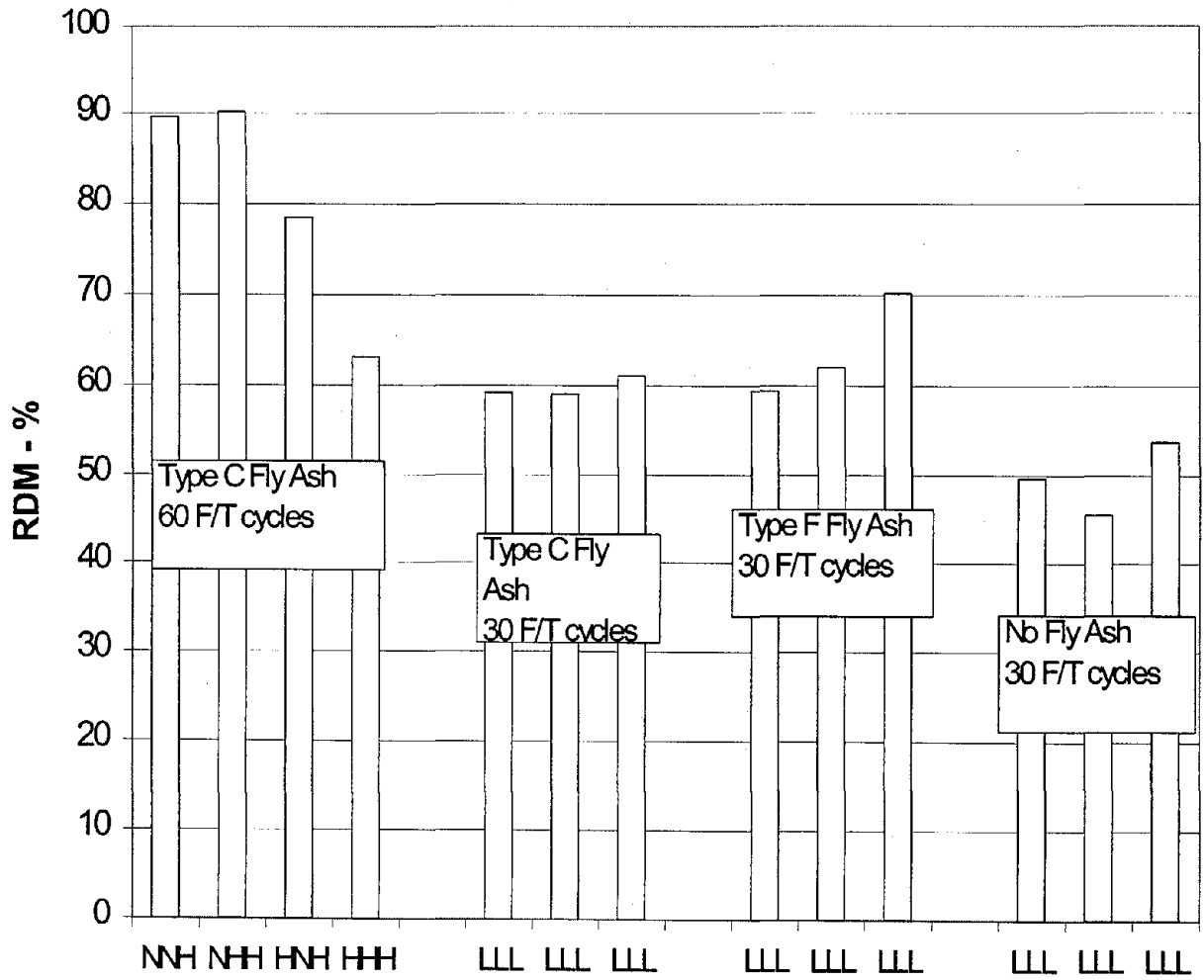Figure G-2: Results from three beams exposed to 60 freeze-thaw cycles.

Figure G-3: The average of each RDM column in tables G-1 through G-4.

APPENDIX H. ASSESSMENT OF LEACHING FROM HETEROGENEOUS MONOLITHS

Introduction

The release to the environment is of concern in relation to the use of alternative materials as cement replacement or sand replacement, or use of artificial aggregates. Since release to the environment is controlled by transport through the water phase, leaching tests are the most appropriate means of assessing environmental impact from cement-based products. Extrapolation of short-term laboratory testing results to long-term field conditions is reliant on using mathematical models that accurately represent the system under consideration. Most current models for extrapolation assume that the constituents of interest are uniformly distributed within the concrete matrix. However, this is often not the case. Different concrete components (e.g., cement, fine aggregate, coarse aggregate) may have different total contents and mass transfer rates for constituents of concern. Thus, it may be necessary to consider the long-term release behavior in the context of a heterogeneous matrix.

In this study, as part of the larger program on the use of alternative materials in paving applications, a selection of relevant tests have been carried out on concrete cubes prepared by replacing different components by Pb and Zn containing materials to examine the impacts of matrix heterogeneity on leaching behavior. The emphasis of the study is to identify the differences in release characteristics when Pb and Zn are introduced as sand replacement, as aggregate, and as Pb or ZnO addition to the cement paste. However, if materials prove to perform well during service life, that is no guarantee that the use of these additives or replacements are justified, as the long-term problems may arise in the recycling stage or in "end of life" conditions (use as soil like material or disposal). A key question is how to evaluate long-term behavior during the service life of intact cement-based products, in the recycling stage of construction debris, and their ultimate "end of life" (disposal). Recently, this issue has been addressed (van der Sloot, 2000). Besides the commonly used tank leach test (NEN 7345, 1994), additional tests are needed, such as the pH dependence leaching test (CEN TC 292, 2000), which covers pH conditions resulting from carbonation of size-reduced and largely carbonated construction debris. Test methods also can be integrated to provide a more comprehensive evaluation, while minimizing the number of extractions required (Kosson and van der Sloot, 1997; van der Sloot, et al., 1994).

Experimental Procedures

Experimental Design and Test Material Preparation

Examination of results from leaching tests on the field slab and laboratory aged materials indicated that the heterogeneous nature of the matrices (cement mortar and aggregates) results in the need for different assessment than typically used for homogeneous materials. Relative release rates from each primary matrix component should be considered. The impact of matrix heterogeneity on constituent leaching was examined using model matrices and mathematical modeling of limit cases.

63

Experimental studies to examine the impact of matrix heterogeneity on constituent leaching were carried out by employing tank leaching studies using the following cases for comparison:

1. Portland cement with lead/zinc (Pb/Zn) slag formed into cubes (1.0- by 1.0- by 1.0-cm) used as aggregate.

2. Portland cement with gravel used as aggregate (reference case).

3. Portland cement with Pb/Zn slag size reduced to (a) < 0.125 mm and (b) < 2mm as a partial sand replacement.

4. Portland cement with lead oxide and zinc oxide powder.

Each case was designed to have approximately the same amount of lead and zinc oxide present (except the reference case), but for the lead and zinc oxides to be present in different physical forms (e.g., dispersed as cubes, sand-sized particles, or fine powder). Thus, case 1 explores the effect when the contaminant source is present as a coarse aggregate bound together by a cement mortar. Case 2 provides an experimental control where an aggregate without contaminant source is used with the same cement mortar as in case 1. Case 3 examines when the slag is finely ground and dispersed as a fine aggregate within the mortar or used as a true sand replacement. Testing for leaching is carried out on the fine ground material to see if the slag in fine ground state has an effect on release. The material with the < 2-mm fraction is checked with SEM and Hg porosimetry. Case 4 examines the case when the same contaminants (lead and zinc as oxides) are dispersed in the matrix but not incorporated in a slag. Results are to be compared with case 3. Previously obtained data on the leaching of the Pb/Zn slag alone (Mandin et al. 1997; van der Sloot et al., 1997) are also presented along with results from this study to provide additional comparison.

Appropriate amounts of cement, aggregate, Pb/Zn slag (or oxides), and water were mixed to form each test case (table H-1). Conditions and mixing ratios were chosen in accordance with EN-196 (CEN TC 51, 1996). After mixing of the components, test samples were molded into 10- by 10- by 10-cm cubes. The cubes were wet cured in plastic bags. After 28 days, the mortars were subjected to testing. For some of the leaching tests the cement cubes were crushed in a jaw crusher to a size 95 percent < 4 mm. For the total composition and for the availability test the material was further size reduced to 95 percent < 125 μm.

Total Elemental Composition

The total composition of the mortars was determined in the solution resulting from dissolution of the < 125 μm size reduced material in a mixture of HF, $HClO_4$, and HNO_3. Eluates obtained from the tests are filtered through 0.45-μm membrane filters and acidified to pH 2 prior to analysis. Induction coupled plasma emission spectrometry (ICP) was used to provide quantification of a wide range of elements resulting from the mortar dissolution.

Table H-1. Amounts of each component mixed to form each test case.

	Cement [g]	Water [g]	Aggregates [g]		Total [g]
Case 1 - Pb/Zn Slag as aggregate	1400	400		1400	3200
Case 2 - Gravel cement (reference)	1400	400		1400	3200
Case 3 - Ground Pb/Zn slag as partial sand replacement	1400	400	Slag Sand	700 700	3200
Case 4 - Pb/Zn Oxide in cement	1400	450		1535*	3385

*1400g of agg + 135g of oxide (100g of ZnO + 35 g of Pb_3O_4; this is 80.3g of Zn and 31.7g of Pb)

	Cement [%]	Water [%]	Aggregates [%]		Total [%]
Case 1- Pb/Zn Slag as aggregate	43.75	12.5		43.75	100
Case 2 - Gravel cement (reference)	43.75	12.5		43.75	100
Case 3 - Ground Pb/Zn slag as partial sand replacement	43.75	12.5	Slag Sand	21.9 21.9	100
Case 4 - Pb/Zn Oxide in cement	41.4	13.3		45.3*	100

* 41.4% of agg + 4% of oxide (3% of ZnO + 1% of Pb_3O_4; this is 2.4% of Zn and 0.9% of Pb)

Leaching Tests

Three independent leaching tests were used to determine constituent availability (NEN 7341, 1994), equilibrium solubility and release as a function of pH (CEN TC 292, 2000), and release rate (NEN 7345, 1994). Each test is summarized below. Aqueous extracts from the leaching tests were analyzed by ICP for elemental concentrations.

NEN 7341 Availability Test (NEN 7341, 1994): Dutch standard extraction test for assessment of maximum potential leachability. The construction material is ground to < 125 μm and extracted in two steps of L/S = 50 l/kg each with demineralized water at pH = 7 (the first extraction) and pH = 4 (the second extraction), respectively. pH is kept constant by feed-back control and addition of HNO_3 or NaOH. The contact time in each extraction is 3 hours. The two extracts are combined prior to analysis.

pH static leach test ("pH stat"; CEN TC 292, 2000): This test provides information on the pH sensitivity of leaching behavior of the material. The test consists of a number of parallel extractions of a material at an L/S 10 during 24 hours at a series of pre-set pH values. Since pH is one of the main leaching controlling parameters, the information can be used to evaluate the repeatability in testing (resulting from measurement at steep concentration - pH slopes) and to provide information on the sensitivity to pH in specific field scenarios. The acid neutralization capacity (ANC) derived from the test is a useful property in this respect. For material characterization this has proved to be a very useful method (van der Sloot et al., 1997). The method is being standardized in two experimental modes by CEN TC 292 Working Group 6 (CEN TC 292, 2000).

NEN 7345 Tank leach test (NEN 7345, 1994): In this test the specimen is subjected to leaching in a closed tank. The leachant is renewed after 8 hours, 1, 2.25, 4, 9, 16, 36, 64 days at a leachant to specimen volume ratio (L/V) of approximately 5. The results are expressed in mg/m^2. This test is a procedure to evaluate the release rate from monolithic material by predominantly diffusion control (e.g., exposure of structures to external influences). The distinction is necessary, as the transport limitations set by a solid form result in a significantly lower environmental impact than derived from crushed material. This condition is valid as long as the product retains its integrity. To assess the behavior after disintegration or demolition the information obtained in the pH dependence leach test is very relevant, as in this situation the pH is likely to change to more neutral conditions.

Hg Porosimetry

The porosity of the gravel cement, Pb/Zn slag as sand replacement, Pb/Zn slag as coarse aggregate, and mortar with PbO and ZnO has been analyzed by mercury porosimetry using 400 bar and 4000 bar pressure. The equipment used was Micromeritics, Autopore II 9220.

66

Scanning Electron Microscopy

The cubes were subjected to SEM analysis to identify the morphological properties of the cubes prepared with alternative materials. The equipment used was a JEOL JSM-6330 field emission scanning electron microscope.

Geochemical Modeling

The geochemical code MINTEQA2 (Felmy et al., 1984) has been applied for the modeling of the chemical speciation in eluates from crushed cement mortars using data from the pH-dependence experiments. The Davies equation is applied to correct for ionic strength effects. For most pH values at the L/S values used (L/S=10) this correction is usually adequate. The saturation indices for the different chemical phases were calculated under the conditions measured in the eluate. The possible leachability controlling phases for the respective elements, as defined by those phases showing saturation indices close to 0, are discussed.

Results

Physical Characteristics

Hg Porosimetry

The Hg porosimetry data are given in figure H-1. The pore stucture of the Pb/Zn slag used as a true sand replacement (particle size < 2mm) has a significantly different porosity structure than the other cases, including the partial sand replacement with fine ground slag (< 0.125 mm). It has a greater porosity in the 0.1- to 1-µm pore diameter range. The pore structure of the cube with Pb/Zn oxide addition to cement shows just a slight shift in porosity, although this is confirmed through leaching test results (see below).

Scanning Electon Microscopy

In figure H-2, the cross section of the Pb/Zn slag aggregate cube is given. The SEM images provided in figures H-3 through H-5 indicate that use of the Pb/Zn-slag as the sand like aggregate results in a structure with more cracks than regular gravel concrete, the Pb/Zn-slag as coarse aggregate or even the Pb/Zn slag as a fine-ground aggregate. The irregular shape and surface properties of the particles tend to result in cracks along the cement-paste slag boundaries. The relatively large number of particles per unit volume results in an increase in the number of cracks in this specimen. This is consistent with the observations by Hg porosimetry.

Composition and Availability of Constituents in Cement-Based Products

To control the environmental quality of cement-products judgments have been made based on either total concentration of the cement or on leachability of the actual construction product. In the Dutch Building Materials Decree (Building Materials Decree, 1995), the release of constituents from the actual construction product to the soil in a period of 100 years is taken as the basis of reference.
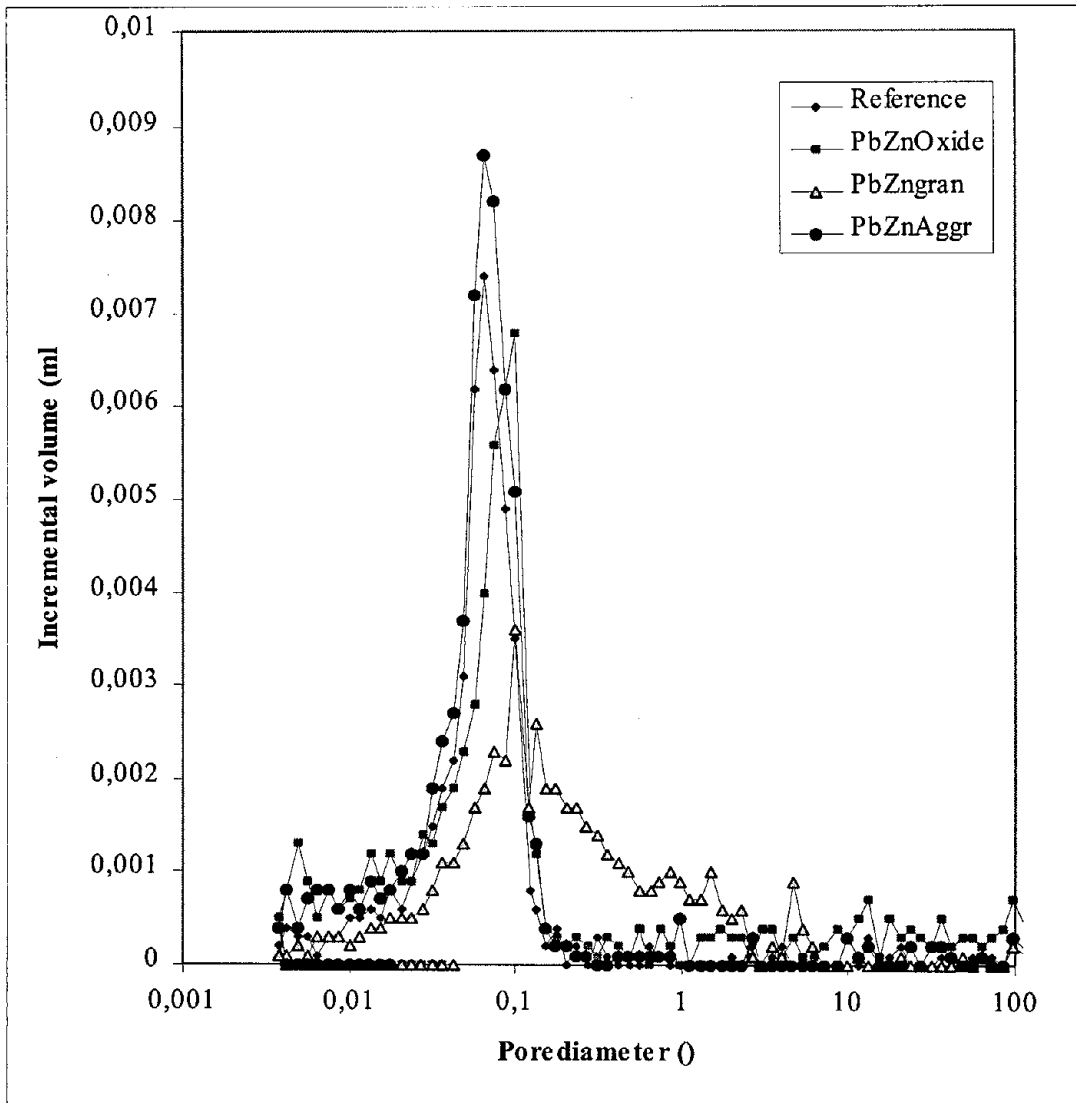
Figure H-1: Mercury porosimetry data for test specimens: incremental volume (ml/g) vs. pore diameter (μm).
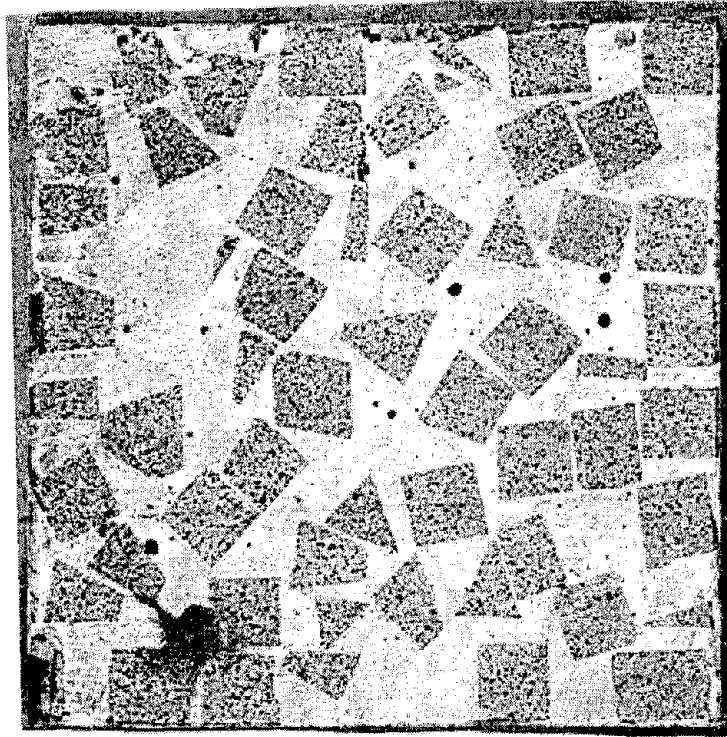
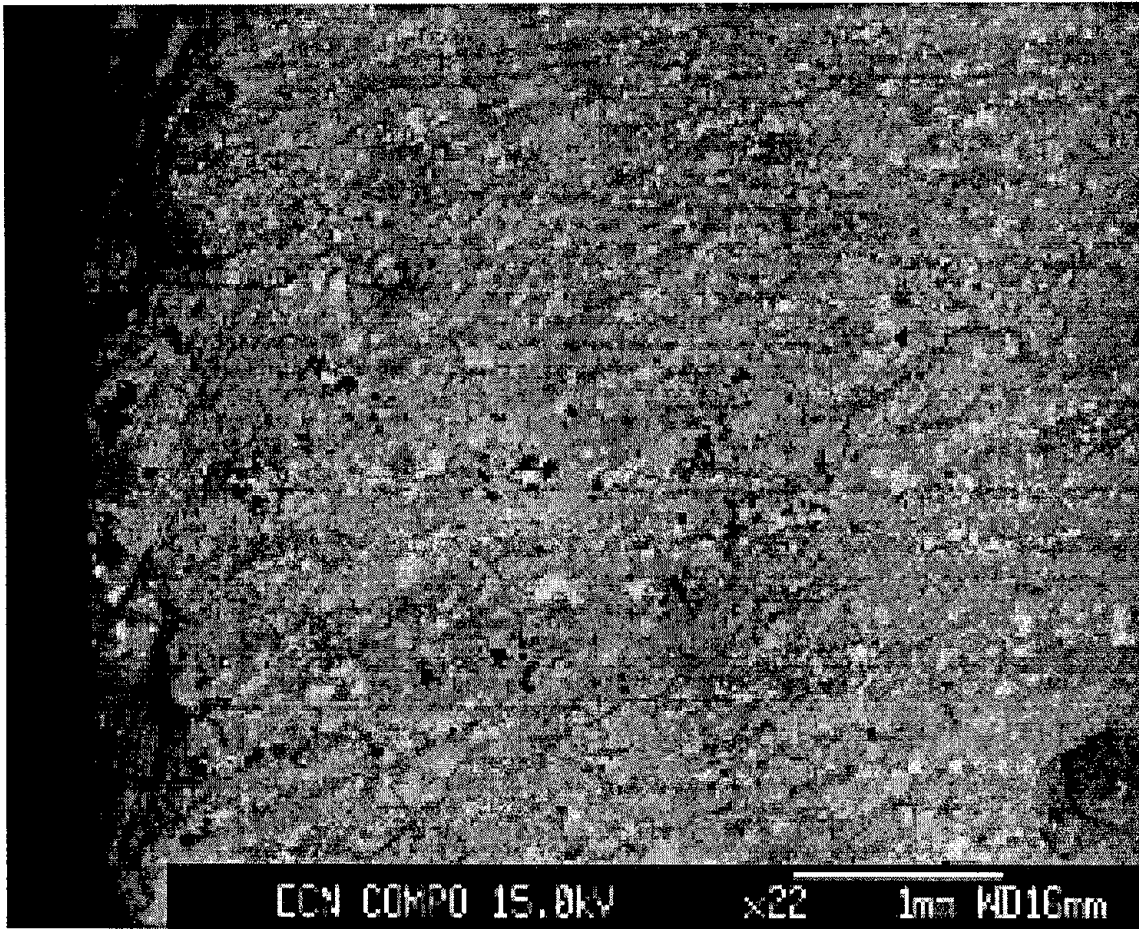Figure H-2: Cross section of Pb/Zn slag aggregate cube.

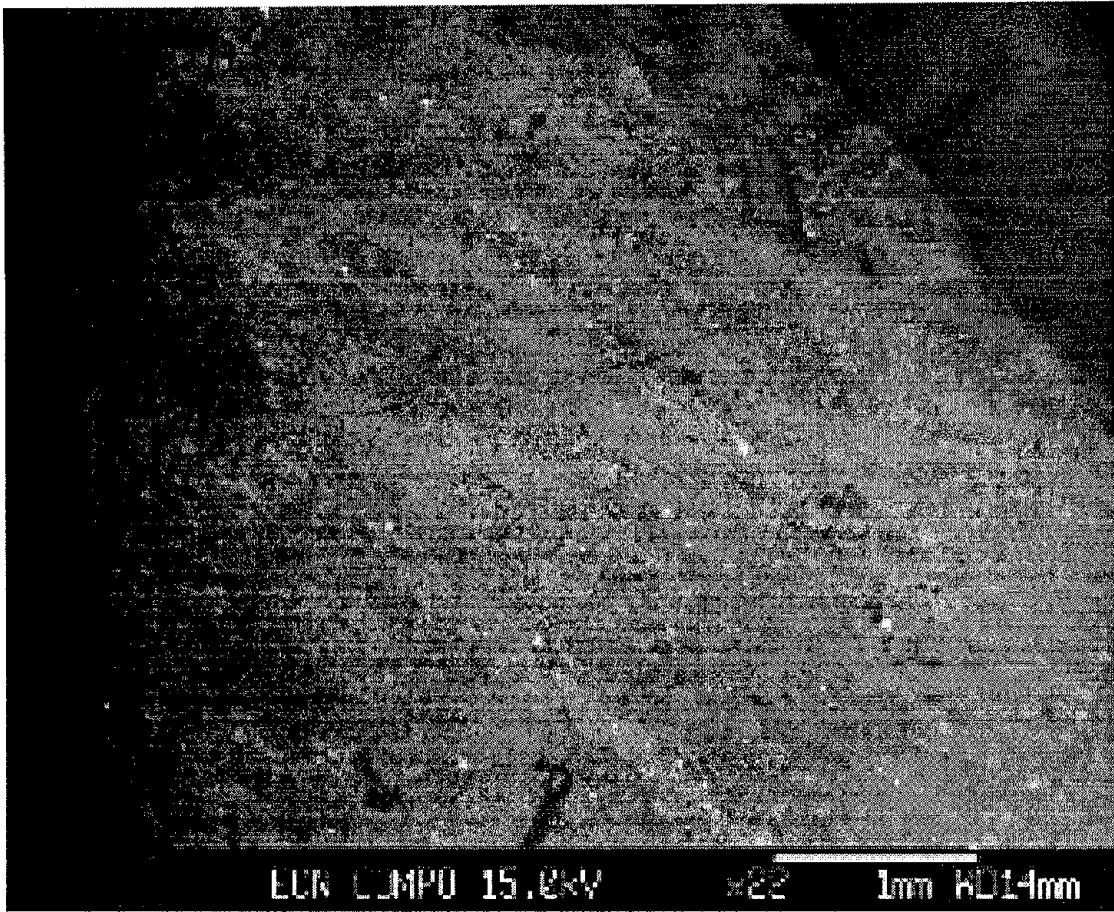Figure H-3: SEM image for gravel cement reference.

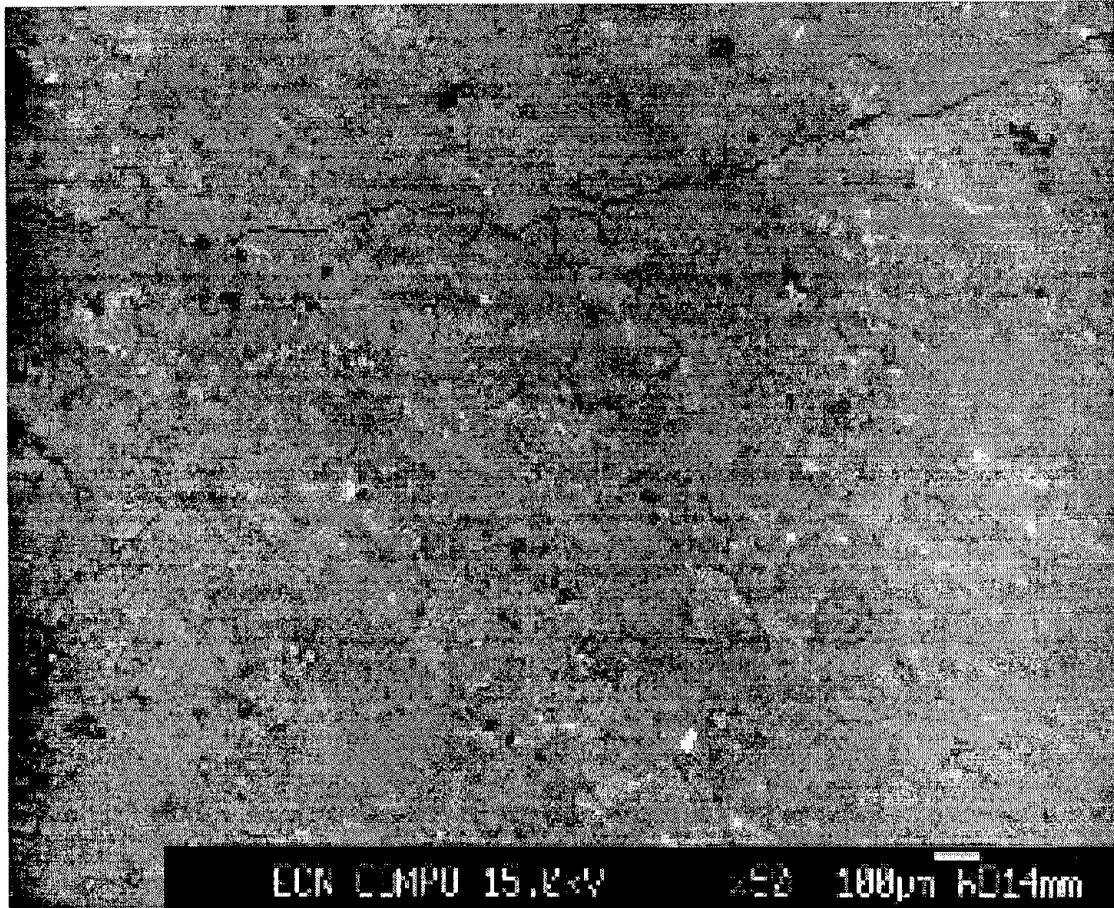Figure H-4: SEM image for Pb/Zn slag as sand replacement (< 0.125 mm).

Figure H-5: SEM image for Pb/Zn slag as sand replacement (<2mm).

A marginal increase in soil burdening has been considered acceptable and has been quantified in relation to leaching tests assessing the release from granular or monolithic materials.

Leaching tests on cured samples provide a basis to focus on the fraction that may be leached under specified circumstances. In this context, the availability test (hydrated product, subsequently crushed) can be considered as a worst case approach. Leaching tests of intact monolithic products and leaching at a controlled pH provide a basis for release under more specific exposure conditions.

In table H-2, a comparison of total concentration (for the prepared case mixture), availability for leaching (after crushing of the complete test cube for each case), and the leaching under specified conditions for a selection of elements is given.

The availability can be a minor fraction of the total composition (e.g. Cr, V). The maximum as observed in the pH static test generally corresponds well with the availability test. In a few cases significant differences are noted (As in Pb/Zn oxide cement; Cr in Pb/Zn slag cement). The Cr leachability as obtained by the availability test may be too high, as the multiplication factor of 100 to correct for the liquid to solid ratio during extraction can exaggerate measurements close to the detection limit. The same may be true for As in Pb/Zn oxide cement. The Cr availability from Pb/Zn slag may be lower due to reducing properties of the slag. The low value may therefore be more realistic than the value around 18 mg/kg.

Time-Dependent Release from Cement-Based Products (Service Life)

During the service life of cement-based products and concrete the material must be judged as a monolith. This implies that release is limited due to transport constraints. Diffusion from the interior of the matrix is slow due to the tortuous path diffusing ions have to follow and chemical interactions with the matrix. The test applied to address this leaching condition is the tank leach test NEN 7345. The release can be modeled as an initial estimation by a one-dimensional diffusion model to assess release over longer time-scales than the duration of the leaching test. Parameters for the extrapolation are derived from the tank leach test. The pH and conductivity data are given in figure H-6 to H-10 together with the release of Na, K, Ca, Pb, Zn, Cr, Cu, Cd, Si, V, As, Mo, Ni, and Al as a function of time.

The initial pH from the Pb/Zn oxide cement (case 4) is slightly greater than the reference case and the Pb/Zn aggregate cube (case 1). This is also true for the conductivity, which is reflected in the higher leachability of K and Na during the tank leach test. In the case of Pb/Zn slag aggregate, the availability for K needs to be corrected for the available K from slag, as it can not contribute in case 1 to the diffusion driving force. The size-reduced Pb/Zn slag used as partial cement replacement (case 3) is more porous judging from the K leaching data. For K, pDe – values of 11.82, 11.86, 11.46, and 11.29 have been calculated for cases 1 – 4, respectively. For Case 3, the fine ground slag only. These results are consistent with the mercury intrusion results; samples with pore size distributions skewed towards larger pores resulted in lower pDe values. This leads to tortuosities of 1670, 1820, 725 and 490, respectively. Unfortunately, data for the true sand replacement (< 2 mm) are lacking.

73

Table H-2: Comparison of total elemental content, availability test results and maximum release during pH stat testing for selected cases and elements.

Element	Pb/Zn slag[1]			Pb/Zn slag cement (case 1)			Pb/Zn Oxide cement (case 4)			Gravel cement[2] (case 2)	
	Total	Avail[3]	pH stat[4]	Total	Avail	pH stat	Total	Avail	pH stat	Total	pH stat
As	1224	< 0.1	0.97	441	10.9	14.16	na[5]	7.46	0.06	11.26	0.36
Cr	895	0.01	0.01	344	18.9	0.37	135	25.6	12.1	82.61	8.71
K	5280	316	209	4261	2363	2181	3999	1785	1642	4589	1920
Mo	125	0.059	0.066	45.6	6.4	4.37	na	1.59	0.27	0.28	0.56
Pb	25100	375	345	8749	416	979	9187	227	822	31	2.58
V	245	0.23	0.12	187.4	12.3	3.58	86	3.39	1.1	178	3.7
Zn	82500	2232	2155	29801	6228	9072	22821	20833	18090	220	70

[1]Results from leaching of Pb/Zn slag alone (previous data)
[2]Availability data is not available for this case
[3]Avail – availability
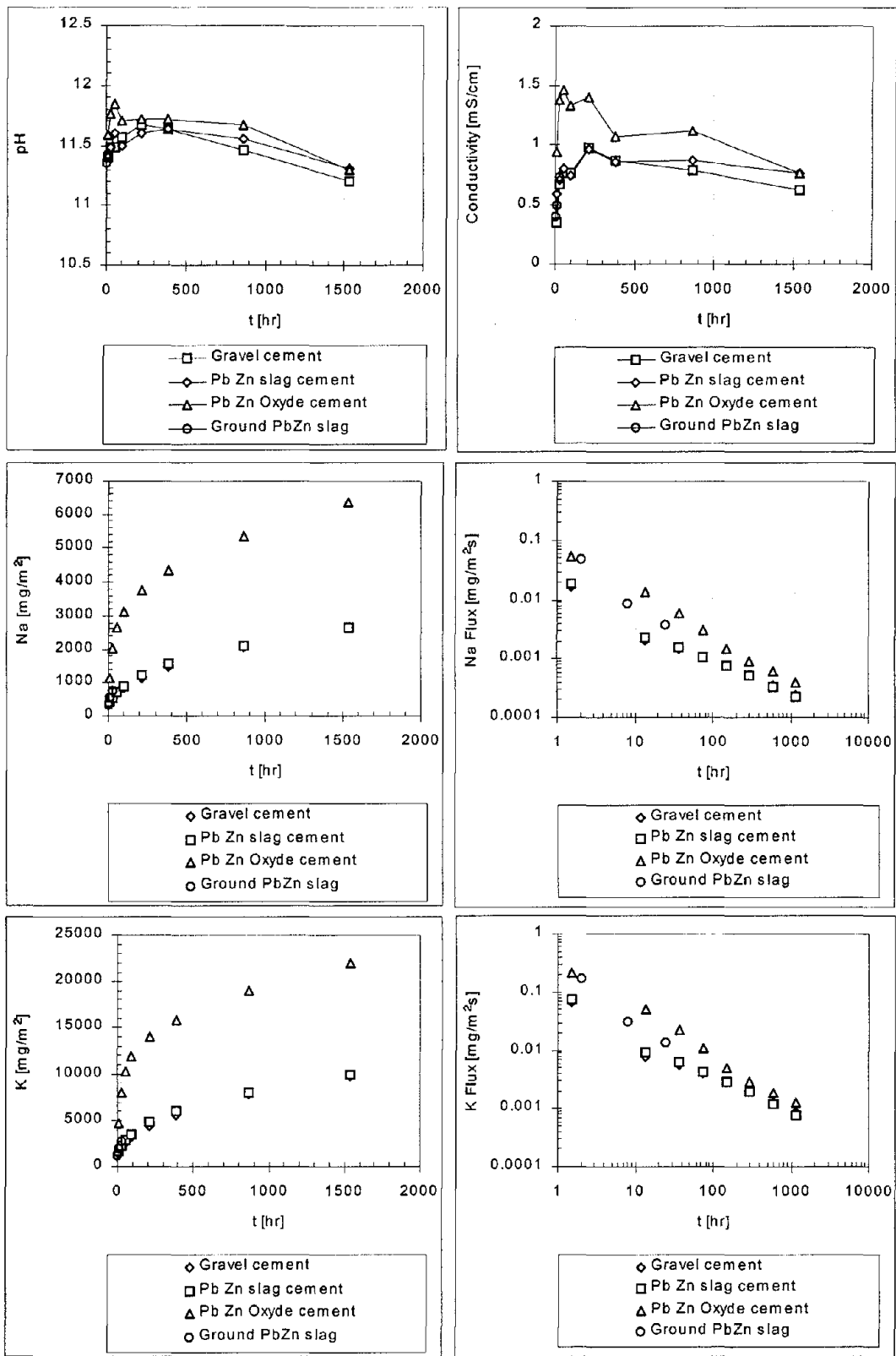[4]Maximum values from pH stat leaching test reported
[5]Not analyzed

Figure H-6: pH and conductivity as a function of time and cumulative release for Na and K.
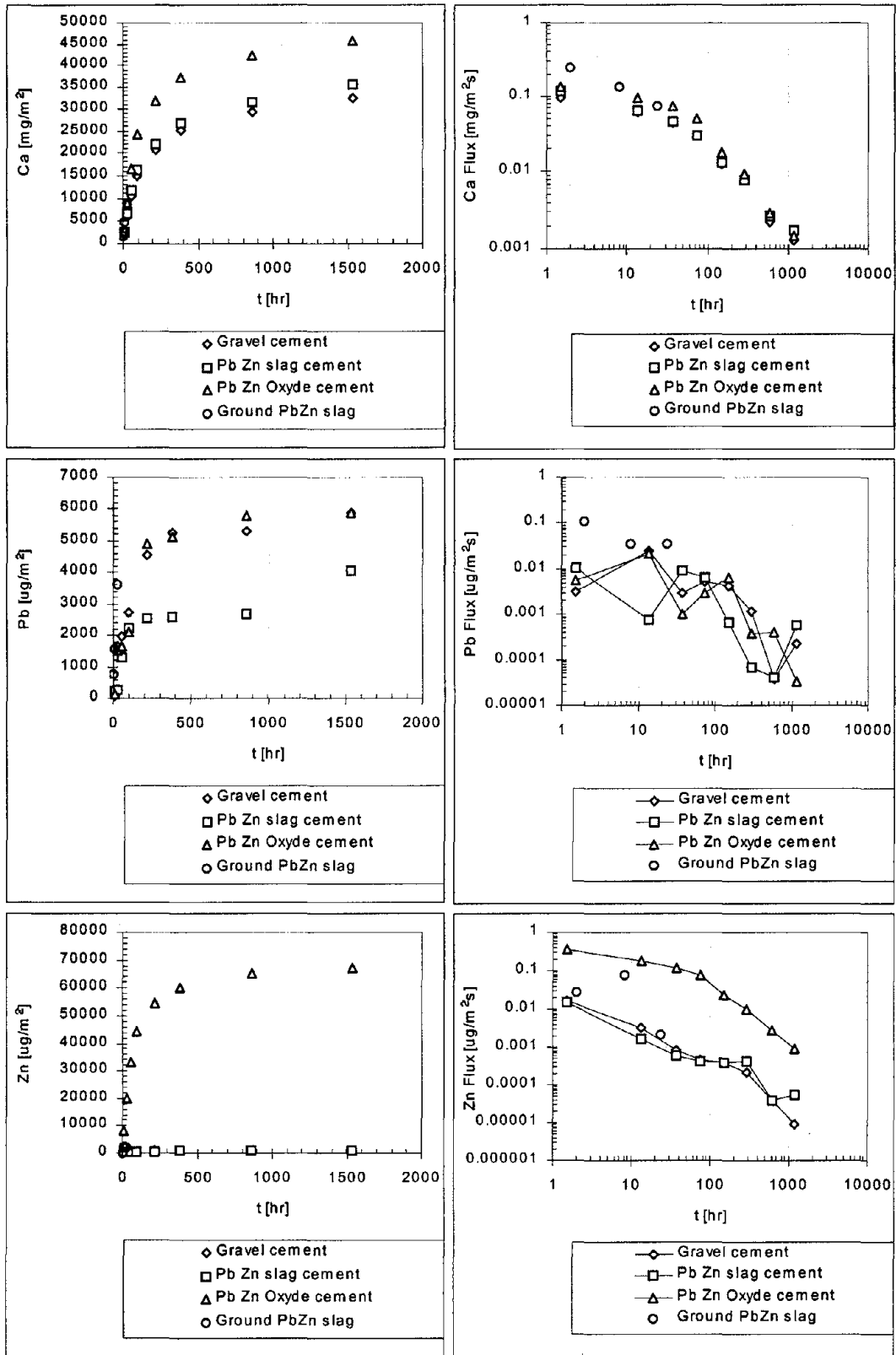
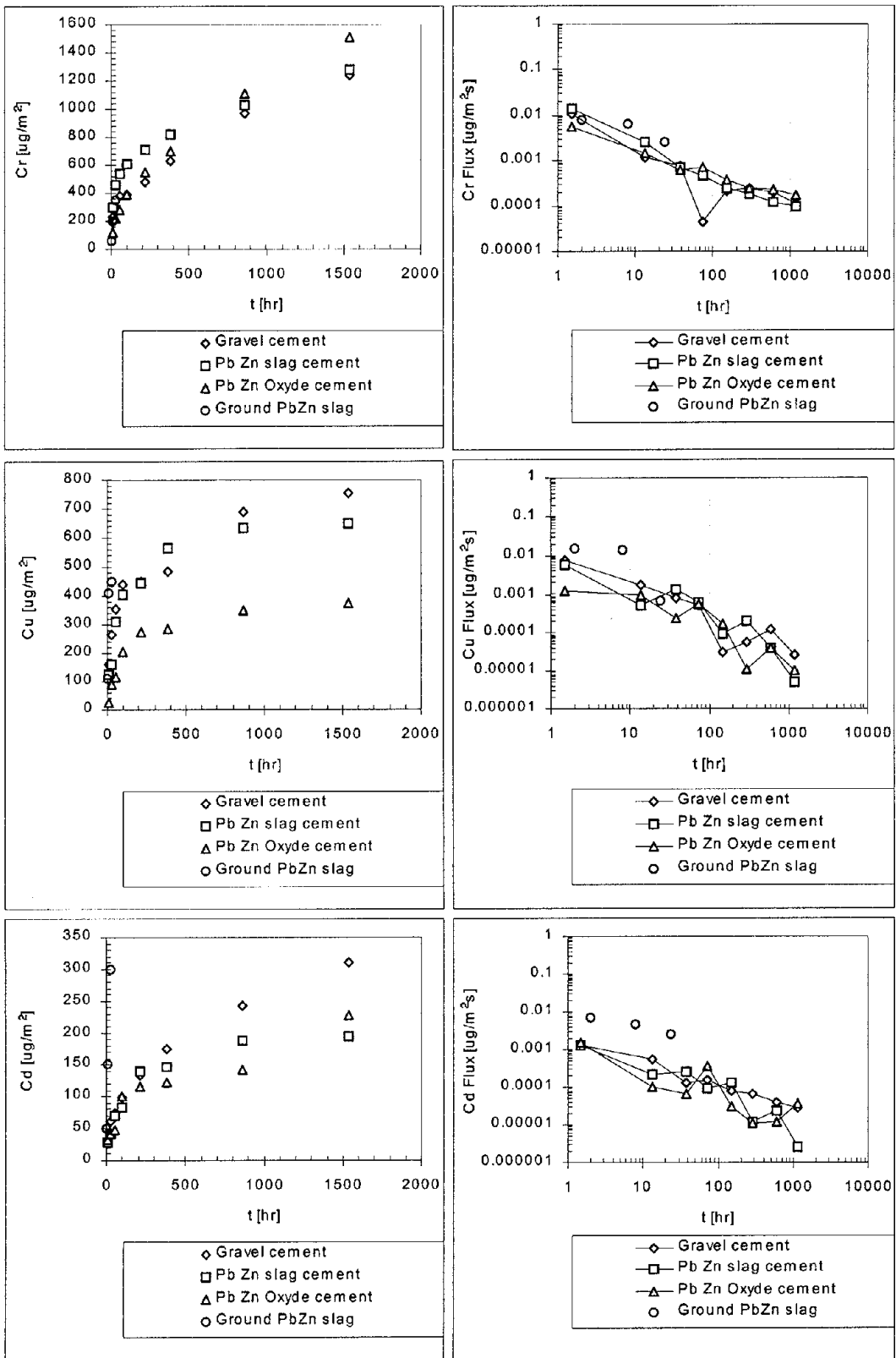Figure H-7: Cumulative release and release flux of Ca, Pb, and Zn.

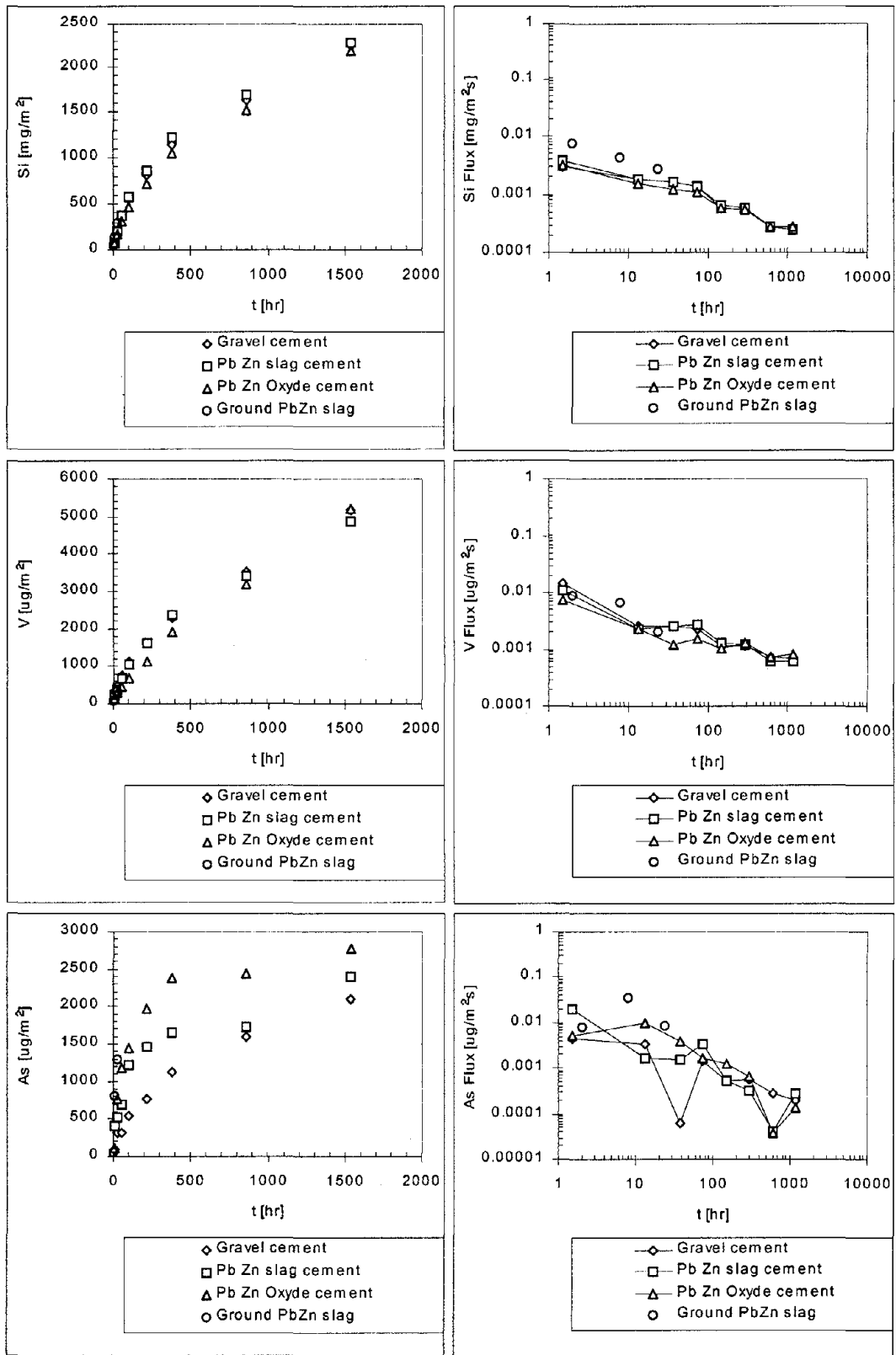Figure H-8: Cumulative release and release flux of Cr, Cu, and Cd.

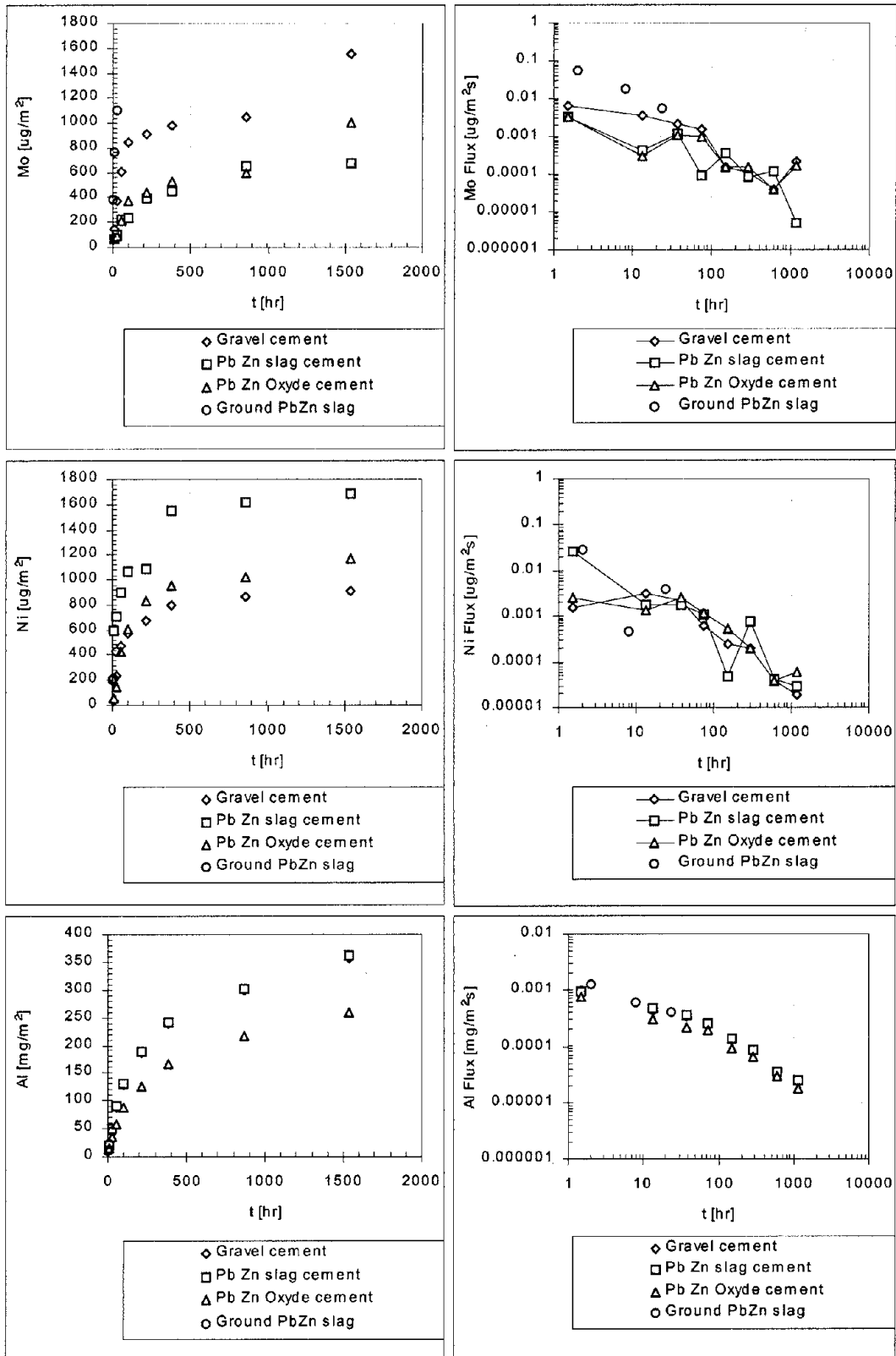Figure H-9: Cumulative release and release flux of Si, V, and As.

Figure H-10: Cumulative release and release flux of Mo, Ni, and Al.

Ca is not diffusion controlled, as the slope in the log flux – log time plot does not approach - 0.5. Ca release most likely is controlled by surface dissolution rates.

For the release of Pb, it is important to note that the release level is only marginally different between the four types of materials. The scatter in the data is such that the cumulative curve indicates a greater difference than may be warranted based on the analytical data. This is very surprising as the Pb availability levels are 980, 2.6, 490 and 822 mg/kg for Pb/Zn slag aggregate, gravel cement, Pb/Zn slag sand replacement and Pb/Zn oxide doped cement cubes, respectively. Solubility control of Pb in the cement matrix (independent of availability) is responsible for this observation.

For Zn, a significant difference is noted for the Pb/Zn oxide doped cement cube. The release as observed is in no way proportional to the availability of Zn in these cubes. The increase of leachability of Zn from the Pb/Zn oxide doped cement is a combination of the lower tortuosity (smallest effect) and the difference in pH during the testing relative to the reference. The slightly higher pH in the PbO and ZnO doped cubes can easily result in a concentration change of an order of magnitude in the pH range concerned (see figure H-11).

The release of Cr was very consistent from all specimens and predominantly diffusion controlled with pDe values of 15.8, 16.38 and 16.11 for gravel reference, Pb/Zn slag aggregate cube and PbO and ZnO doped cubes, respectively. The form of Cr released is largely in the form of chromate, which has been shown to be the predominant species in cement mortars (van der Sloot, 2000).

Copper is rather similar in release between the test specimen and tends to be diffusion controlled. Cd release is quite low and rather similar. The release of Si is not quite diffusion controlled. Surface solubility effects may play a role in the Si release behavior. The V release behaviour indicates control by surface solubility phenomena, as the flux expressed in mg/m^2s tends to become constant.

As, Al and Ni are not very different. In the cumulative release curve, initial wash-off effects (see Ni) may become over-emphasized. Al appears to be diffusion controlled after some initial rapid release effects. The higher release of Mo from gravel cement as compared with the other cements reflects the difference in availability of Mo, which is highest in gravel cement.

The tank leach test according to NEN 7345 (1994) in a closed system does not give the proper information for all situations. In case the material is exposed to a significant level of water refreshment like in flowing water, or in case of exposure to the atmosphere (e.g., drinking water pipes), a tank leach test with externally controlled pH by flushing air through the external solution to reach a constant pH of around 8 provides a better representation of the actual release (SMT-CT96-2066, 2000; van der Sloot, 2000). Under these circumstances other solubility controlling phases may dominate the release from monolithic specimen. For metals, this will generally lead to less release. By applying air, the carbonate level will not be so excessively high as to cause significant bicarbonate levels in solution, which would not be representative of normal exposure conditions. The pH-stat data (to be discussed hereafter) can be used to provide an estimate of the difference in release between the two scenarios and thus allows a decision on the need to carry out such an additional test.
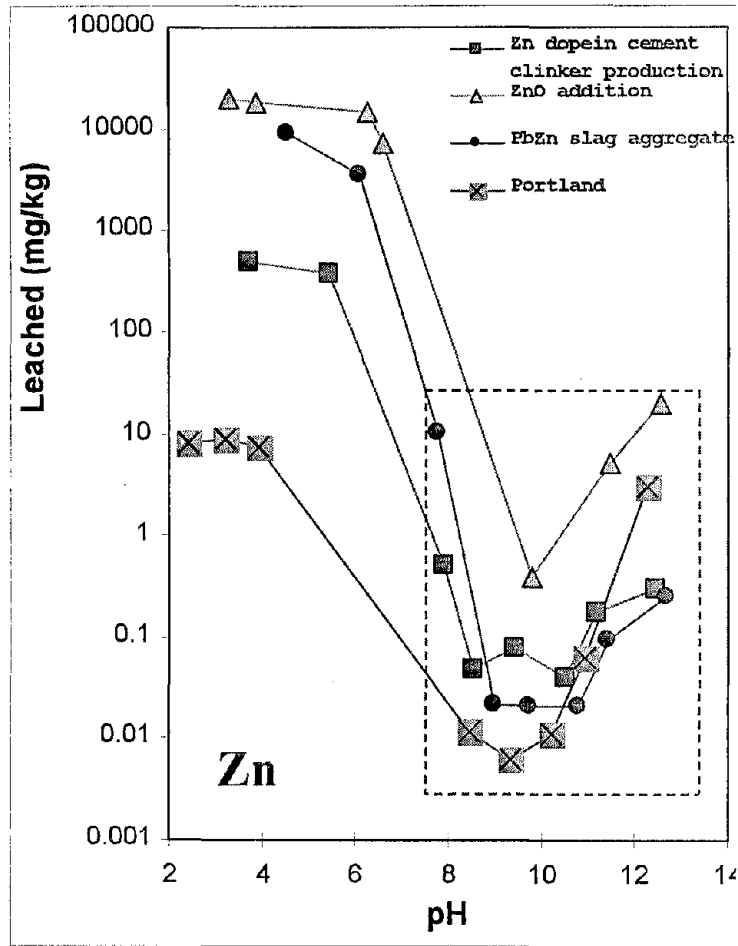
Figure H-11: Zn leaching as a function of pH for cement cubes with different levels
of Zn from slag or doping of cement.

The release data as obtained in the tank leach test are compared with Dutch regulatory criteria for building materials (Building Materials Decree, 1995) in table H-3 to provide a point of reference to assess the magnitude of the releases observed. Only Se exceeds the BMD Cat I limits in two cases. All other elements meet the criteria for service life.

Leachability for Different Manners of Pb and Zn Incorporation into Cement Products

A practical manner to compare the leaching behavior of cement-based products with different modes of Pb and Zn incorporation is by comparing the results from the pH stat test, which reflects the chemical speciation as dictated by the mix. The pH dependence test results have been used for data comparison of cements (van der Sloot et al., 1997). In figures H-12 and H-13, data are given for As, Cr, K, Mo, Pb, V, and Zn.

The acid neutralization capacity data, expressed in mol/kg, are provided in figure H-12. The results for the various concrete cubes are very comparable. Only the case with Pb/Zn oxide addition to the cement shows significantly lower acid neutralization capacity to neutral pH. For K, as expected, there is no influence on leachability as a function of pH nor an influence by the additives or aggregates used. In case of As, an increase in leachability is observed at pH < 6 from when Pb/Zn slag is used as aggregate. Pb leachability is significantly increased at low pH (pH<7) and high pH (pH>11) by the addition of either Pb/Zn slag or Pb/Zn oxide. However, Pb leachabilty remains low for all cases between pH 7 to 11. In the pH domain of the environment, however, there is virtually no distinction between regular and Pb containing cement products.

The leaching behavior of Mo is very consistent between the different cement-based products tested. The leaching of Mo is increased in case of Pb/Zn slag as aggregate. At mildly acidic pH a minimum leachability is observed. From earlier work (van der Sloot et al., 1999) it was indicated that this may be attributed to $CaMoO_4$ or $PbMoO_4$ precipitation.

The Zn leaching behavior is very consistent with a significant difference in leached amounts at pH < 8 and at pH > 10. The Pb/Zn oxide addition shows a more pronounced leachability of Zn at pH >10 than the Pb/Zn slag. This may be due to the speciation of the Pb.

V shows a typical oxyanion behaviour for cement-based products. Low leachability at high pH, maximum leachability at low and mildly alkaline pH, and a minimum leachability at pH = 5. There is no difference between the Pb/Zn containing products (slag or oxide) and regular Portland, indicating that the V originates from the cement rather than from any of the additives.

The Cr leachability in cement-based products is unusual. In portland cement, Cr leachability is rather high over the entire pH range from 3 to11. Only at pH > 11 does the Cr leachability decrease, most likely as a result of substitution in ettringite (Kindness et al., 1994). Upon addition of PbO and ZnO to the cement paste, the Cr leachability is only affected in the pH

Table H-3: Comparison of tank leach test release at 64 d with Dutch regulatory criteria.

Element	BMD Cat1[1]	GravelC[2]	Pb/Zn slag[3]	Pb/Zn oxide in cement[4]
	mg/m^2	mg/m^2	mg/m^2	mg/m^2
As	41	2.11	2.41	2.77
Ba	600	21.7	23.4	73.8
Ca	nas[5]	32640	35915	45966
Cd	1.1	0.31	0.2	0.23
Co	29	1.38	1.03	1.19
Cr	140	1.25	1.29	1.51
Cu	51	0.76	0.65	0.38
Mo	14	1.56	0.67	1
Na		2685	2673	6356
Ni	50	0.91	1.7	1.17
Pb	120	5.92	4.06	5.9
S	9000	282.4	295.2	234.3
Sb	3.7	1.73	1.51	1.44
Se	1.4	1.09	2.1	1.64
Sn	29	1.74	1.12	0.87
V	230	5.19	4.9	5.19
Zn	200	1.13	1.21	67.2

[1]BMD Cat 1 – Building Materials category 1 limit values for free application of materials.
[2]Gravel cement (reference, case 2)
[3]Pb/Zn slag as aggregate in cement (case 1)
[4]Pb/Zn oxide cement (case 4)
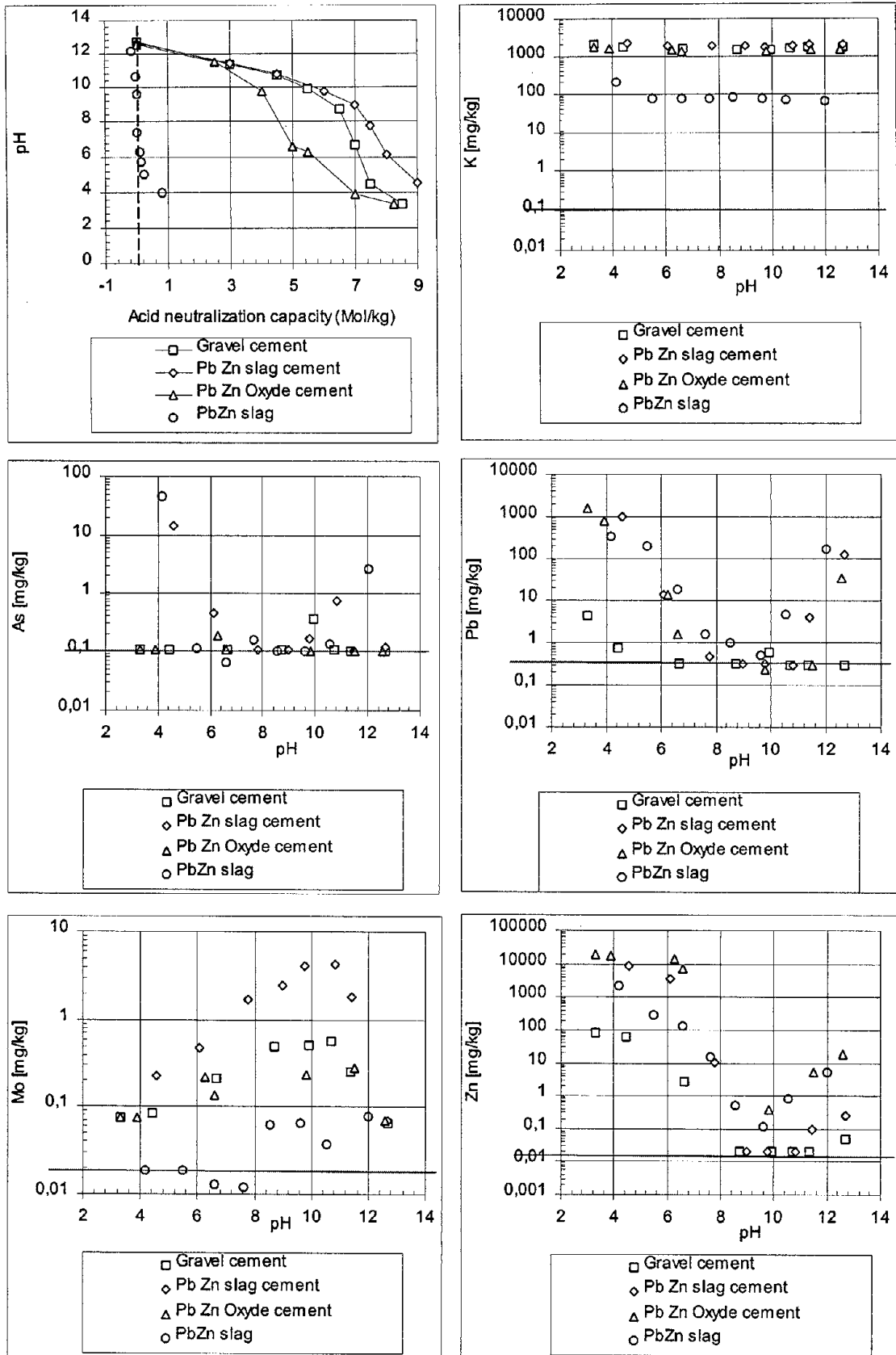
Figure H-12: Acid neutralization capacity data and leaching as a function of pH for K, As, Pb, Mo, and Zn.
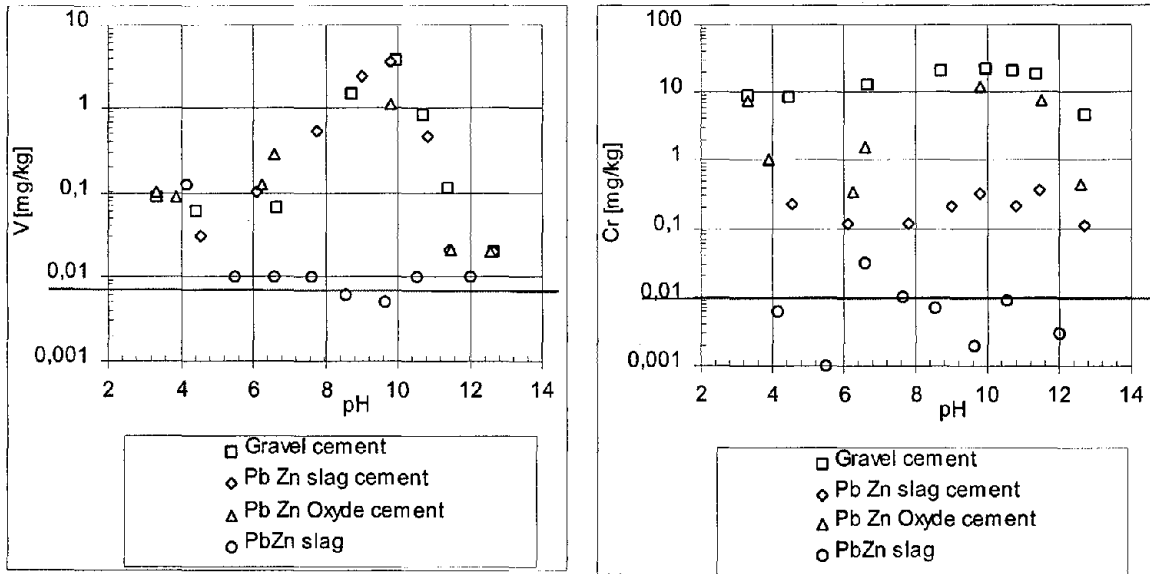
Figure H-13: Leaching as a function of pH for V and Cr.

range of 3 to 6. Based on geochemical modeling (see below), this is attributed to PbCrO4 solubility. When Pb/Zn slag is used as aggregate, the Cr leachability decreases by almost two orders of magnitude. This is a result of the reducing properties of the Pb/Zn slag. As has been shown in previous work (van der Sloot, 2000), any Cr leached above pH 7 is likely to be chromate (Cr VI). In blast furnace slag the reducing conditions cause a low Cr leachability due to reduction of Cr VI to Cr III, which is essentially non-leachable at high pH. The Pb/Zn slag shows a significantly reduced Cr leachability, but not as low as observed for blast furnace slag cement.

The leaching behavior as a function of pH covers a wide range of environmentally relevant conditions, and as such, forms a good basis for evaluation of environmental impact. The relevant pH domain for cement products may range from pH 4 (peat soils) to neutral conditions (most natural soils) extending to alkaline conditions in situations where very limited water transport occurs (e.g. concrete pilings in virtually stagnant ground water). When cement-based products are carbonated they will create their own resistance to pH changes by the formation of calcite.

Geochemical Modeling

The data from pH-dependence leaching tests were used to carry out modeling of the geochemical speciation in eluates obtained from extraction of crushed cement mortars. In figure H-14 results of the modelling are specified for Ba, sulfate, Ni, V, Pb and Zn. The sulphate in ettringite can be partly substituted for oxyanions (e.g. CrO_4^{2-}, MoO_4^-, AsO_4^{3-}, VO_4^{3-}). Metals and alkali earth elements (e.g. Ba, Pb, Cd, Zn, Ni) can partly substitute for Ca, whereas trivalent elements (e.g. Fe, Mn, Co) can substitute for Al (Klemm, 1998; Cougar et al., 1996). Proper information to model incorporation in ettringite phases is still lacking. Recently, some stability data for Cr-ettringite have been published; however, the data do not seem to match very well with our observations.

Based on the modeling the following controlling phases have been identified for regular portland cement mortars:

For Ba, the solid mixed mineral phase $BaCaSO_4$ (50%Ba) reflects the leaching behavior of Ba quite well. $BaCrO_4$ solubility is not a controlling phase, but a solid solution of $Ba(S,Cr)O_4$ (96 percent S and 4 percent Cr) appears to be a good candidate as it matches the leaching behavior quite well.

For SO_4^{2-} - The mortar eluate appears to be controlled by $BaCaSO_4$ (Ba 50 percent) solubility. At high pH ettringite is likely to become a major controlling phase.

Cr is discussed separately in more detail below.

Ni leachability is probably controlled by $Ni(OH)_2$.

For V, in the pH domain of pH 5 to 8 Fe-vanadate appears to be important, while at pH > 9 Pb vanadate may play an important role. The role of ettringite for V in the high pH range (pH > 11) needs to be verified in further work.
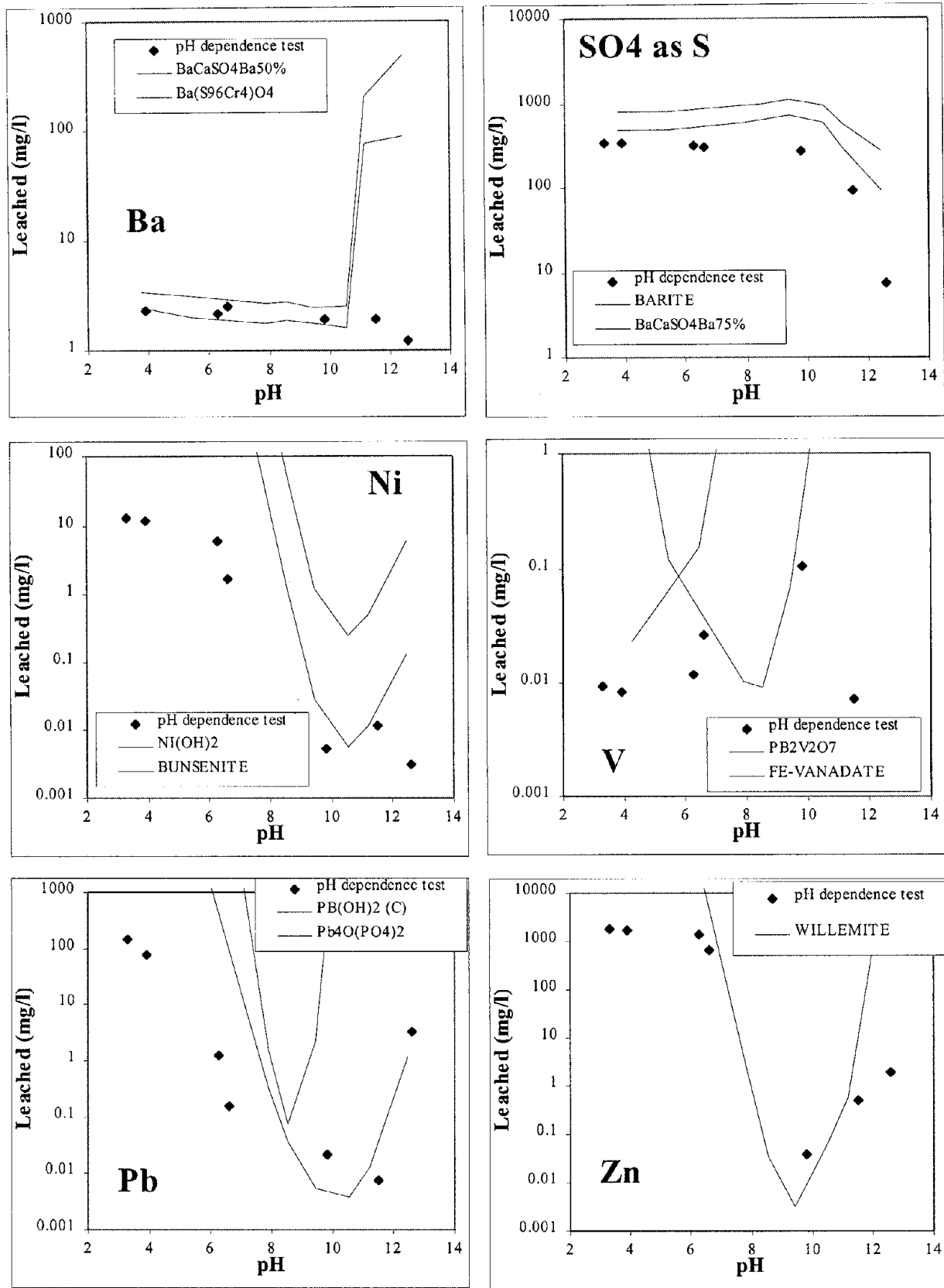
Figure H-14: Geochemical modeling of pH-dependent leaching of size reduced cubes (PbO and ZnO addition to cement).

For Pb, lead hydroxide is a potential solubility controlling phase, which matches the data reasonably well.

For Zn, willemite is a potential solubility controlling phase.

In the cement products with Pb/Zn slag as aggregate and with Pb/ZnO as addition to the cement paste, other solubility controlling phases in addition to the above specified controlling phases become active. Geochemical modeling of Cr in the cubes containing Pb/Zn slag aggregate, the concrete containing PbO and ZnO addition to cement paste and the reference gravel cement has been carried out. Figure H-15 shows that the $BaSO_4CrO_4$ solid solution match the solubility of Cr quite well in all three cases. The shape of the leaching curves is quite nicely matched. $BaCrO_4$ as such does not match the data very well. $PbCrO_4$ matches the data fairly well in the pH domain < 7 in the PbO and ZnO doped cube.

Evaluation of Environmental Aspects of Cement-Based Products

In the environmental evaluation of cement-based products, the initial high ANC (dictated largely by $Ca(OH)_2$) is converted to calcite. During the service life of the products in its intended application, this will first take place at the surface (moving front). During secondary use of construction debris as unbound aggregate, the carbonation may increase rapidly depending on the degree of exposure to atmospheric CO_2 or CO_2 from biological degradation processes (soil atmosphere has about 10 times the CO_2 level of the atmosphere). In surface water with a mainly neutral pH, the change in pH at the surface of cement-based products proceeds fairly rapidly. This implies that in many situations a neutral pH is more likely to occur than a high pH condition as dictated by fresh cement products. The buffer capacity created by calcite formation forms a resistance to pH change below the pH dictated by the calcite system. In the evaluation of cement based products from an environmental point of view, this implies that the relevant pH range ranges from 7.8 to about 12.6. These pH limits are used in the pH-dependence test graphs as vertical boundaries (figure H-16). The lower horizontal boundary is dictated by the analytical detection limit and the upper horizontal boundary is determined by the highest interception point between one of the two vertical lines and the pH dependence leaching curve. The resulting boundaries are indicated for As, Pb, Zn, Mo, V, and Cr. The Building Materials Decree (BMD) criteria for granular materials may be used as a reference point for environmental limits (see G-3).

It can be concluded that Pb will not be a problem from an environmental point of view, when it is assumed that the concrete surface is rapidly neutralized, and provided that the material is not utilized in an acidic environment that would be able to partially overcome the inherent buffer created in cement-based materials. Given the high concentration of Pb in the matrix, this is a remarkable observation. The difference in Pb leachability between the Pb/Zn slag aggregate and the Pb/Zn oxide addition to the cement paste is small. For Zn the release at high pH is well below the criteria from the BMD category I. At pH < 8 the Zn level may increase over the limit value. The Pb/Zn oxide addition to cement exceeds the limit for Zn at pH values > 11. Since this is an extreme case, which certainly cannot be seen as a potential product, exceeding the limit is not an issue. V mildly exceeds the criteria in the pH range 9 to 10.5. All cement-based products show the same leaching behavior for V, which implies that portland cement is responsible for the V leachability. The Pb/Zn slag and the As is below the limit under all circumstances. Mo
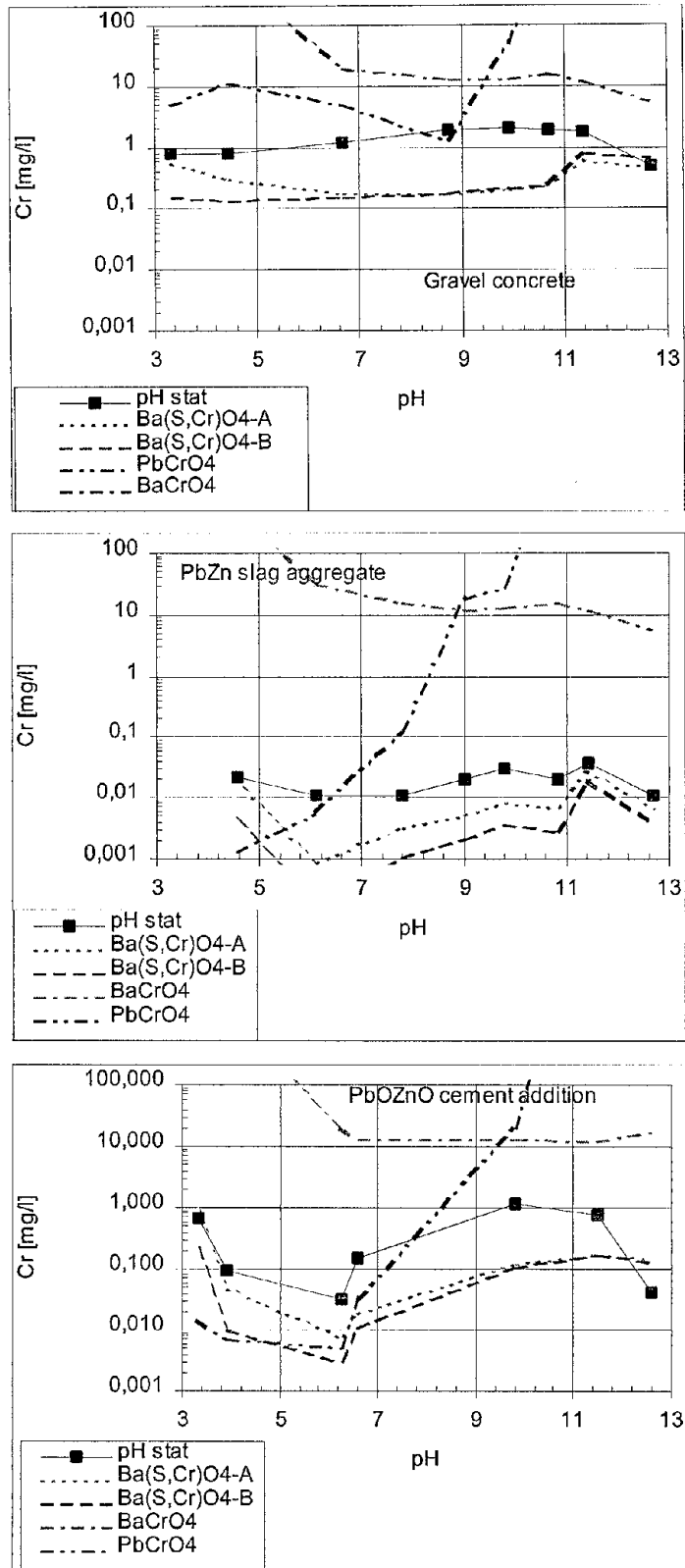
Figure H-15: Geochemical modeling of Cr phases in the different cubes after size reduction.
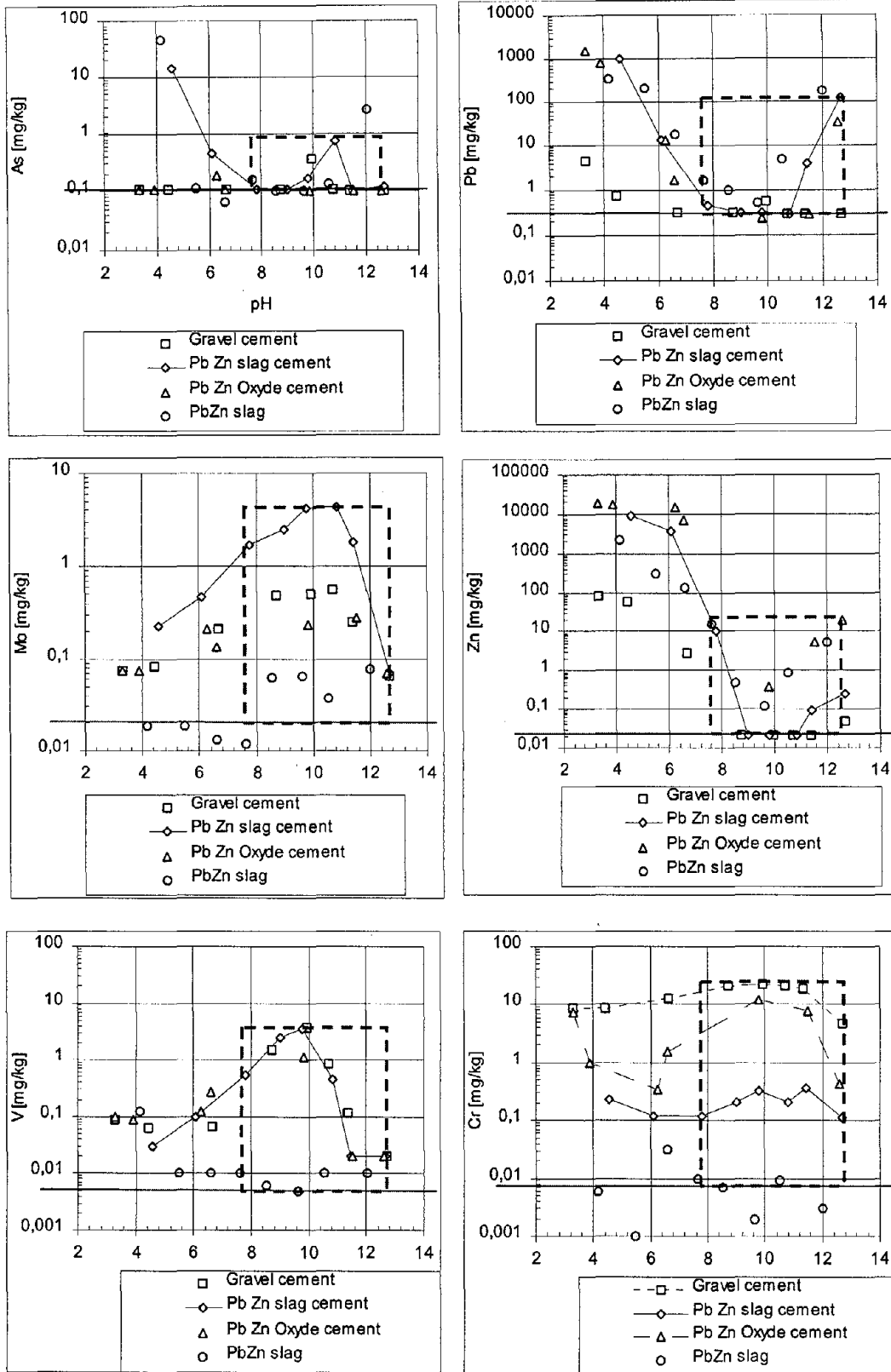
Figure H-16: Comparison of leaching data on size-reduced cubes with regulatory limit
values according the Dutch Building Materials Decree to simulate long-term
behavior of construction debris.

exceeds the limit at all pH values below 12, but Mo in portland cement also exceeds the limit, although by a smaller factor than the Pb/Zn slag. Mo leachability seems to be enhanced in the Pb/Zn slag. Cr in Portland cement reference exceeds the criteria over the entire pH range. Cr leachability from cement with Pb/Zn slag aggregate is lower than that from portland cement. This is attributed to the reducing properties of Pb/Zn slag, which causes reduction of Cr VI to Cr III. These observations indicate that oxyanions are more critical from a leaching point of view than the metals.

Conclusions

The leachability from the concrete containing Pb/Zn slag as aggregate based on tank leaching was not significantly different from regular portland cement over the period of testing. The only element that is significantly increased relative to portland cement is Mo.

Based on the experimental and modeling results, significantly longer periods of tank leaching than 64 days will be required to observe differences in constituent release, when present, that are a consequence of the heterogeneity of the matrix in comparison with a homogeneous matrix.

The pH at the interface between the leaching solution and the external boundary of the concrete matrix is the most important factor controlling short-term release of constituents of interest, when the solubility of the constituent is strongly dependent on pH.

Geochemical speciation modeling has revealed that for Cr, the Ba sulphate chromate solid solution is determining the solubility of Cr. In concrete containing Pb/Zn slag as aggregate, the Cr leachability is much lower than in ordinary portland cement due to reduction of Cr VI to Cr III by the reducing properties of the slag.

Mercury porosimetry on the concrete cubes is consistent with SEM observations, both of which indicate that the concrete was more porous when Pb/Zn slag (<125 mm) was used as a partial sand replacement.

The release of Pb and Zn from concrete under normal exposure conditions during service life is very low in spite of a much increased availability for leaching in case of Pb/Zn oxide addition or ground Pb/Zn slag as aggregate relative to the reference. This is even true for construction debris in its recycling or ultimate disposal stage.

References

Building Materials Decree. Staatsblad van het Koninkrijk der Nederlanden, 1995.

CEN TC 51. *Test methods for cement.* CEN TC 51 Working Group, EN196-1, 1996.

CEN TC 292. *Methodology Document.* CEN TC 292 Working Group 6: ENV 12920, 1996.

CEN/TC 292. *Characterisation leaching test: Influence of pH under steady state conditions.* CEN TC 292 Working Group 6: Work item 292015, 2000.

Cougar, M.L.D., Scheetz, B. E., and Roy, D.M. . Ettringite and C-S-H Portland cement phases for waste ion immobilization : a review. *Waste Manage.* 16(4), 295-303, 1996.

Felmy, A.R , Girvin, D.C., and Jenne, E.A. *MINTEQA2 computer program for calculating aqueous geochemical equilibria,* EPA-600/3-84-032, U.S. Environmental Protection Agency, Athens, Georgia, 1984.

Kindness, A. , Macias, A., and Glasser, F.P. Immobilization of Cr in cement matrices. *Waste Manage.,* 14 (1), 3-11, 1994.

Klemm, W.A. *Ettringite and oxyanion substituted ettringites – their characterization and applications in the fixation of heavy metals: A synthesis of the literature.* Portland Cement Association Report, Washington, D.C., 1998.

Kosson, D.S., and van der Sloot, H.A. Integration of testing protocols for evaluation of contaminant release from monolithic and granular wastes, pp. 201-216. In: (Goumans, J.J.J.M, Senden, G.J., van der Sloot, H.A., eds.) *Waste Materials In Construction - Putting Theory into Practice,* Elsevier Science Publishers, Amsterdam, 1997.

Mandin, D., van der Sloot, H.A., Cervais, C., Barna, R., and Mehu, J. Valorization of lead-zinc primary smelter slags, pp.122-128. In: (Goumans, J.J.J.M, Senden, G.J., van der Sloot, H.A., eds.) *Waste Materials In Construction - Putting Theory into Practice,* Elsevier Science Publishers, Amsterdam, 1997.

NEN 7341. *Determination of the availability for leaching from granular and monolithic construction materials and waste materials.* NNI, Amsterdam, 1994.

NEN 7345. *Determination of leaching from monolithic construction materials and waste materials by means of a diffusion test.* NNI, Amsterdam, 1994.

SMT4-CT96-2066. *Technical work in support of the Network Harmonization of Leaching Extraction Test.* Leaching Harmonization Network, Petten, the Netherlands, 2000.

van der Sloot, H.A. Environmental efficiency of immobilization techniques for wastes in relation to utilization and disposal, pp 327-337. In: *Waste Solidification-Stabilization Processes,* Universite de Nancy, Nancy, France, 1995.

van der Sloot, H.A. *Leaching characteristics of lead-zinc primary smelters slags*, ECN-97-C0098, Petten, the Netherlands, 1997.

van der Sloot, H.A. Characterization of the leaching behaviour of concrete mortars and of cement - stabilized wastes with different waste loading for long term environmental assessmen, pp. 167 - 172. In: *Proceedings: Waste Stabilization & Environment*, INSA Lyon, Lyon, France, 1999.

van der Sloot, H.A. Comparison of the characteristic leaching behaviour of cements using standard (en 196-1) cement-mortar and an assessment of their long-term environmental behaviour in construction products during service life and recycling. *Cement & Concrete Res.* 30, 1 – 18, 2000.

van der Sloot, H.A., Kosson, D.S., Eighmy, T.T., Comans, R.N.J., and Hjelmar, O. An approach towards international standardization: a concise scheme for testing of granular waste leachability, 453- 466. In: (Goumans, J.J.J.M. , van der Sloot, H.A., Aalbers, Th.G. , eds.) *Environmental Aspects of Construction with Waste Materials*, Elsevier Science Publishers, Amsterdam, 1994.

van der Sloot, H.A., Heasman, L., and Quevauviller, Ph. *Harmonization of leaching/extraction tests*. Elsevier Science, Amsterdam, 1997.

APPENDIX I. MIX COMPONENT CHARACTERIZATION

Table I-1: Total elemental composition (+/- standard deviation) of major elements in CFA-C (>10,000 ppm).

Element	CFA-C (ppm)	EPRI sub-bituminous/ lignite CFA (ppm)
Al	120600 +/- 2200	45,700 - 128,800
Ca	185,000 +/- 15,400	31,700 - 223,000
Fe	40300 +/- 1,200	25,200 - 102,700
Na	20010 +/- 340	1,300 - 47,500
S	22,500 +/- 2,100	1,300 - 47,600
Si	173,000 +/- 12,000	138,300 - 275,000
Ti	10,300 +/- 900	4,230 - 10,420

Table I-2: Total elemental composition (+/- standard deviation) of minor elements in CFA-C (1,000 - 10,000 ppm).

Element	CFA-C (ppm)	EPRI sub-bituminous/ lignite CFA (ppm)
Ba	5,249 +/- 309	673 - 7,180
K	4,074 +/- 636	5,330 - 142,700
Mg	7,530 +/- 650	7,800 - 41,800
P	6,600 +/- 500	950 - 6,270
Sr	3,334 +/- 140	925 - 4,720

Table I-3: Total element composition (+/- standard deviation) of trace elements in CFA-C (<1,000 ppm).

Element	CFA-C (ppm)			EPRI sub-bituminous/ lignite CFA (ppm)
Ag	<[1]	3		BDL[2] - 7.9
As		15.88	+/- 0.58	7.7 - 55
Au	<	1		
Br	<	2.00		BDL - 4.88
Cd	<	2		BDL
Ce		145.76	+/- 7.42	49 - 118
Cl	<	50		BDL - 1,190
Co		27.25	+/- 1.40	
Cr		95.05	+/- 3.19	BDL - 651
Cs		3.61	+/- 0.38	BDL
Cu		246.40	+/- 2.20	48.1 - 223
Dy		8.69	+/- 0.79	
Eu		2.76	+/- 0.16	
Hf		7.85	+/- 0.51	
Hg	<	1		
I	<	2		BDL
In	<	1		BDL
La		57.74	+/- 0.49	40.1 - 90
Lu		0.80	+/- 0.06	
Mn		115.58	+/- 1.61	148 - 1,332
Mo	<	1		3.7 - 55.2
Nd		68.14	+/- 5.34	
Ni		59.70	+/- 1.86	22.8 - 309
Pb		44.30	+/- 2.13	21.1 - 92
Rb		30.56	+/- 4.67	13.4 - 81.5
Sb		2.11	+/- 0.16	BDL
Sc		27.22	+/- 1.33	
Se		8.68	+/- 1.47	
Sm		7.89	+/- 0.05	
Ta		2.19	+/- 0.21	
Tb		1.20	+/- 0.17	
Th		27.68	+/- 1.43	
U		11.80	+/- 0.64	BDL - 15.4
V		301.29	+/- 10.30	BDL - 292
W	<	2		
Yb		4.69	+/- 0.45	
Zn		160.60	+/- 1.70	24.8 - 658
Zr	<	100		207 - 344

1   < denotes detection limit
2   BDL = below detection limit

Table I-4: Total elemental composition (+/- standard deviation)
of major elements in CFA-F (>10,000 ppm).

Element	CFA-F (ppm)	EPRI bituminous CFA (ppm)
Al	168500 +/- 3100	51,400 - 152,400
Fe	22,000 +/- 700	34,600 - 177,100
K	22050 +/- 880	8,000 - 26,600
Si	319,000 +/- 20,000	93,600 - 258,000
Ti	10800 +/- 900	3,000 - 8,520

Table I-5: Total elemental composition (+/- standard deviation)
of minor elements in CFA-F (1,000 - 10,000 ppm).

Element	CFA-F (ppm)	EPRI bituminous CFA (ppm)
Ca	5100 +/- 900	7,700 - 22,4000
Mg	4240 +/- 438	3,900 - 23,900
Na	2768 +/- 51	2,000 - 15,000
S	2000 +/- 200	2,100 - 64,800

Table I-6: Total element composition (+/- standard deviation)
of trace elements in CFA-F (<1,000 ppm).

Element		CFA-F (ppm)	EPRI bituminous CFA (ppm)
Ag	<	3	BDL - 6.7
As		28.25 +/- 0.64	11 - 391
Au	<	1	
Ba		853 +/- 55	239 - 2110
Br	<	1.00	BDL - 13.9
Cd	<	2	BDL - 8
Ce		186.62 +/- 9.47	34 - 233
Cl	<	30	BDL - 940
Co		73.28 +/- 3.72	
Cr		169.33 +/- 5.1	37 - 507
Cs		10.84 +/- 0.81	
Cu		166.30 +/- 1.98	44.6 - 214
Dy		17.57 +/- 1.57	
Eu		3.40 +/- 0.19	
Hf		7.51 +/- 0.49	
Hg	<	1	
I	<	2	BDL
In	<	1	BDL - 19.5
La		87.92 +/- 0.48	BDL - 120
Lu		1.26 +/- 0.08	
Mn		127.41 +/- 1.75	44 - 651
Mo	<	2	7.1 - 138.9
Nd		78.98 +/- 5.58	
Ni		159.2 +/- 1.95	50 - 300
P		500 +/- 50	800 - 4000
Pb		85.20 +/- 2.32	32.6 - 273
Rb		122.96 +/- 10.13	47.8 - 173
Sb		4.93 +/- 0.17	
Sc		36.86 +/- 1.8	
Se		7.68 +/- 1.33	BDL - 36.52
Sm		17.31 +/- 0.06	
Sr		677 +/- 46	199 - 1131
Ta		2.30 +/- 0.22	
Tb		2.42 +/- 0.26	
Th		30.39 +/- 1.57	
U		12.49 +/- 0.69	BDL - 30.4
V		338.43 +/- 11.88	99 - 459
W		4.80 +/- 0.60	
Yb		6.97 +/- 0.57	
Zn		137.20 +/- 1.81	64.9 - 2050
Zr	<	80	108 - 459

1   < denotes detection limit

2   BDL = below detection limit

Table I-7: Total elemental composition (+/- standard deviation)
of the major elements in unhydrated portland cement (>10,000 ppm).

Element	Portland cement (ppm)
Al	33,700 +/- 600
Ca	506,500 +/- 41,600
Fe	16,200 +/- 500
S	35,900 +/- 2,500
Si	99,000 +/- 7000

Table I-8: Total elemental composition (+/- standard deviation)
of the minor elements in unhydrated portland cement (1,000 – 10,000 ppm).

Element	Portland cement (ppm)
K	5,726 +/- 598
Mg	3,320 +/- 294
Ti	1,100 +/- 300

Table I-9: Total elemental composition (+/- standard deviation) of the trace elements in unhydrated portland cement (<1,000 ppm).

Element		Portland cement (ppm)	Element		Portland cement (ppm)
Ag	<[1]	1	Mo	<	1
As		4.8 +/- 0.2	Na		469.12 +/- 15.03
Au	<	1	Nd		16.49 +/- 1.64
Ba	<	42.57	Ni		13.6 +/- 0.62
Br	<	3	P	<	40
Cd	<	2	Pb		8.8 +/- 1.89
Ce		44.3 +/- 2.3	Rb		16.83 +/- 2.62
Cl	<	50	Sb		0.35 +/- 0.04
Co		10.08 +/- 0.5	Sc		4.13 +/- 0.2
Cr		40.48 +/- 1.4	Se	<	0.78
Cs		0.57 +/- 0.1	Sm		3.65 +/- 0.02
Cu		7.6 +/- 0.9	Sr		253.05 +/- 35.28
Dy		1.82 +/- 0.2	Ta		0.39 +/- 0.05
Eu		0.51 +/- 0	Tb		0.26 +/- 0.06
Hf		2.05 +/- 0.2	Th		9.8 +/- 0.51
Hg	<	1	U		3.21 +/- 0.23
I	<	2	V		32.21 +/- 2.86
In	<	1	W	<	1
La		26.44 +/- 0.2	Yb		1.03 +/- 0.18
Lu		0.15 +/- 0	Zn		31.50 +/- 1.01
Mn		356.3 +/- 4.8	Zr	<	100

1   < denotes detection limit

Table I-10: Total elemental composition (+/- standard deviation)
of the major elements in mixed aggregate sample (>10,000 ppm).

Element	Mixed aggregate (ppm)
Al	21,700 +/- 400
Ca	266,400 +/- 22,000
Si	162,000 +/- 10000

Table I-11: Total elemental composition (+/- standard deviation)
of the minor elements in mixed aggregate sample (1,000 – 10,000 ppm).

Element	Mixed aggregate (ppm)
Fe	6,700 +/- 200
K	6,346 +/- 655
Na	6,702 +/- 115
S	1,400 +/- 100

Table I-12: Total elemental composition (+/- standard deviation) of the trace elements in mixed aggregate sample (<1,000 ppm).

Element	Mixed aggregate (ppm)		Element	Mixed aggregate (ppm)	
Ag	<[1]	1	Mo	<	1
As		2.25 +/- 0.25	Nd		4.31 +/- 0.82
Au	<	1	Ni		35.8 +/- 1.25
Ba		285.23 +/- 28.36	P	<	10
Br	<	2.00	Pb		12.2 +/- 1.56
Cd	<	2	Rb		19.15 +/- 2.32
Ce		10.17 +/- 0.6	Sb		0.79 +/- 0.09
Cl	<	50	Sc		1.34 +/- 0.07
Co		6.45 +/- 0.35	Se	<	0.52
Cr		129.04 +/- 3.67	Sm		0.9 +/- 0.02
Cs	<	0.15	Sr		205.65 +/- 31.73
Cu		5.1 +/- 1.27	Ta	<	0.05
Dy		0.87 +/- 0.11	Tb	<	0.06
Eu		0.25 +/- 0.02	Th		1.19 +/- 0.08
Hf		0.95 +/- 0.08	Ti	<	300
Hg	<	1	U		0.29 +/- 0.09
I	<	1	V		14.06 +/- 1.7
In	<	1	W	<	1
La		5.41 +/- 0.17	Yb		0.35 +/- 0.08
Lu		0.08 +/- 0.01	Zn		30.4 +/- 0.67
Mg		994 +/- 198	Zr	<	70
Mn		157.53 +/- 2.16			

1 < denotes detection limit

Table I-13: Crystalline phases identified by XRPD in CFA-C.

PDF #	Name	Chemical formula	Replicate FOM			Weighted average FOM
			1	2	3	
02-0077	Calcium Aluminum Oxide Hydrate	$Ca_4Al_2O_7 \cdot xH_2O$	1.7		3.3	2.5
09-0472	Cordierite, ferroan	$(Mg,Fe)_2Al_4Si_5O_{18}$		4.7		9.4
11-0188	Potassium Aluminum Silicate Hydrate	$2(KAlSiO_4) \cdot 3H_2O$			3.1	6.2
12-0530	Norsethite	$BaMg(CO_3)_2$	4.1			8.2
12-0725	Barium Aluminum Silicate	$BaAl_2Si_2O_8$	2.9			5.8
18-1166	Silicon Hydrogen Phosphate	$Si(HPO_4)_2$			3.1	6.2
23-1042	Calcium Silicate	Ca_2SiO_4	3.6	2.6	3.3	2.1
26-0153	Barium Hydrogen Phosphite	$Ba(H_2PO_2)_2$	1.3		9.6	5.5
26-0909	Annite-1M, aluminian	$K_2(Fe_5Al)Si_5Al_3O_{20}(OH)_4$	2.9			5.8
26-1057	Mitridatite	$Ca_3Fe_4(PO_4)_4(OH)_6 \cdot 3H_2O$	3.3			6.6
26-1372	Ferropargasite, syn	$NaCa_2Fe_4AlSi_6Al_2O_{22}(OH)_2$	2.1			4.2
27-0020	Brammallite-2M#1 [NR]	$NaAl_2(Si,Al)_4O10(OH)_2$			2.5	5
27-0731	Sodium Magnesium Aluminum Silicate Hydroxide	$NaMg_3AlSi_3O_{10}(OH)_2$	3.8			7.6
29-1489	Halloysite-10A	$Al_2Si_2O_5(OH)_4 \cdot 2H_2O$		1.9	1.4	1.7
31-0804	Magnesium Oxide Carbonate	$Mg_3O(CO3)_2$			1.3	2.6
31-1262	Sodium Aluminum Oxide	$NaAl_2O_8$	1.1			2.2
32-0069	Barium Hydrogen Phosphate	$Ba(H_2PO_4)_2$	3.3			6.6
32-0861	Potassium Titanium Oxide	$K_2Ti_4O_9$	4.1			8.2
32-0993	Silicon Oxide	SiO_2	2.5			5
35-0591	Merwinite, syn	$Ca_3Mg(SiO_4)_2$	6	9.1	5.7	4.6
35-0734	Tausonite, syn	$SrTiO_3$			3.4	6.8
35-0964	Magnesium Aluminum Hydroxide Hydrate	$Mg_4Al_2(OH)_{14} \cdot 3H_2O$			2.2	4.4
37-0545	Sodium Magnesium Titanium Oxide	$Na_{0.7}(Ti_{1.75}Mg_{0.35})O_4$			1.9	3.8
37-1496	Anhydrite, syn	$CaSO_4$	11	9.1	5.6	5.6

Table I-13: Crystalline phases identified by XRPD in CFA-C (Con't).

PDF #	Name	Chemical formula	Replicate FOM			Weighted average FOM
			1	2	3	
38-0032	Iron Hydroxide	$Fe(OH)_3$		3.5		7
39-0341	Sarcopside, syn	$Fe_3(PO_4)_2$	10	16	8.7	7.7
41-0753	Calcium Iron Oxide	$CaFeO_3$	6.3	9.6		8
42-1368	Loveringite	$CaTi_{21}O_{38}$		3.9		7.8
43-0662	Clinochrysotile	$Mg_3Si_2O_5(OH)_4$	2			4
45-0946	Periclase, syn	MgO	4.2	3.8	3.3	2.5
46-1045	Quartz, syn	SiO_2	5.8	8	7.8	4.8
46-1312	Wustite	FeO		3.1		6.2
47-0226	Strontium Titanium Oxide	$SrTiO_{2.72}$			3	6
48-1467	Calcium Oxide	CaO	3.5			7
48-1471	Calcium Strontium Oxide	$Ca_{0.6}Sr_{0.4}O$	3.7	2		2.9

Table I-14: Crystalline phases identified by XRPD in CFA-F.

PDF #	Name	Chemical formula	Replicate FOM 1	Replicate FOM 2	Replicate FOM 3	Weighted average FOM
06-0494	Geikielite, syn	$MgTiO_3$		4.4		8.8
09-0472	Cordierite, ferroan	$(Mg,Fe)_2Al_4Si_5O_{18}$	21	26	23	15.5
10-0063	Titanium Oxide	Ti_2O_3	3.8			7.6
15-0776	Mullite, syn	$Al_6Si_2O_{13}$	2.7	1.8	1.6	1.4
19-0629	Magnetite, syn	$FeFe_2O_4$	4.4			8.8
20-0452	Gismondine	$CaAl_2Si_2O_8 \cdot 4H_2O$	24	27	25	16.9
26-0031	Aluminum Oxide	Al_2O_3	6.5	7.9	6.2	4.6
26-1076	Carbon	C	16	28	16	13.2
26-1077	Carbon	C	9.4		13	11.0
33-0664	Hematite, syn	Fe_2O_3	22	6.1		13.9
34-0192	Hercynite, syn	$FeAl_2O_4$		19	5.8	12.3
35-1393	Magnesium Iron Oxide	Mg_1-xFe_xO	4.2		4.5	4.4
38-0360	Moganite	SiO_2	12	13	12	8.1
38-0449	Allophane	$Al_2O_3(SiO_2)_2 \cdot 3H_2O$			6.2	12.4
38-0471	Sillimanite	Al_2SiO_5	7.6	7.4	10	5.6
40-0170	Calcium Magnesium Silicate	$CaMgSi_2O_6$	4.5			9
46-1045	Quartz, syn	SiO_2	1.9	3.2	2.2	1.6
47-0320	Sodium Aluminum Oxide	$NaAl_6O_{9.5}$	3.6			7.2
47-0321	Potassium Aluminum Oxide	$KAl_6O_{9.5}$		3.5		7

Table I-15: XRPD identification of typical hydration products
in portland cement paste.

PDF #	Name	Chemical formula	Replicate FOM			Weighted average FOM	Reference
			1	2	3		
02-0077	Calcium Aluminum Oxide Hydrate	$Ca_4Al_2O_7 \cdot xH_2O$	4.5	4.3	5.9	3.3	2
02-0083	Calcium Aluminum Oxide Hydrate	$Ca_3Al_2O_6 \cdot xH_2O$		4.9	6.1	5.5	1
03-0548	Calcium Silicate Hydrate	$2Ca_3Si_2O_7 \cdot 3H_2O$	5.7			11.4	1
04-0733	Portlandite, syn	$Ca(OH)_2$	1.1	3.1	1.2	1.2	1, 2
29-0285	Stratlingite, syn	$Ca_2Al_2SiO_7 \cdot 8H_2O$	7.5			15	2
33-0018	Gibbsite, syn	$Al(OH)_3$	5.1	5.3	5.4	3.5	1
41-1451	Ettringite, syn	$Ca_6Al_2(SO_4)_3(OH)_{12} \cdot 26H_2O$	3.4	3.2	3.6	2.3	1, 2
42-0062	Calcium Aluminum Sulfate Hydrate	$Ca_4Al_2O_6(SO_4) \cdot 14H_2O$	5.9	6.1	4.2	3.6	1
44-0601	Calcium Iron Sulfate Hydrate	$Ca_4Fe_2S_2O_9 \cdot 12H_2O$	5.8	5.1		5.5	1, 2

1   (Cook, 1992)
2   (Glasser, 1993)

Table I-16: Crystalline phases identified by XRPD in combined aggregate.

PDF #	Name	Chemical formula	Replicate FOM 1	Replicate FOM 2	Replicate FOM 3	Weighted average FOM
05-0586	Calcite, syn	$CaCO_3$	5.5	1.8		3.7
05-0613	Arcanite, syn	K_2SO_4	18	9.2	24	11.2
06-0711	Iron Oxide	FeO			5.2	10.4
07-0025	Muscovite	$KAl_2Si_3AlO_{10}(OH)_2$			8.6	17.2
09-0466	Albite, ordered	$NaAlSi_3O_8$		7.8	28	17.7
09-0472	Cordierite, ferroan	$(Mg,Fe)_2Al_4Si_5O_{18}$	19		15	17
18-1202	Anorthite, sodian, intermediate	$(Ca,Na)(Si,Al)_4O_8$	6.9			13.8
25-1402	Maghemite-Q, syn	Fe_2O_3	16		24	19.9
26-1076	Carbon	C		14	17	15.5
26-1077	Carbon	C	17		19	17.9
27-0714	Ferroglaucophane	$Na_2(Fe,Al,Mg)_5Si_8O_{22}(OH)_2$			8.7	17.4
29-1489	Halloysite	$Al_2Si_2O_5(OH)_4 \cdot 2H_2O$			3.6	7.2
31-0616	Sekaninaite	$Fe_2Al_4Si_5O_{18}$			4.2	8.4
35-1393	Magnesium Iron Oxide	$Mg_1\text{-}xFe_xO$	5.4	9		7.2
36-0426	Dolomite	$CaMg(CO_3)_2$	16	11		13.8
41-0586	Ankerite	$Ca(Fe,Mg)(CO_3)_2$	24		13	18.5
41-1480	Albite, calcian, ordered	$(Na,Ca)Al(Si,Al)_3O_8$	14		9.6	11.9
42-0217	Sodium Aluminum Silicate	$Na_6[AlSiO_4]_6$			8.8	17.6
43-0596	Silicon Oxide	SiO_2	8.7			17.4
46-1045	Quartz, syn	SiO_2	5.6	5.3	3	3.1
46-1312	Wustite	FeO	6.4			12.8
47-1743	Calcite	$CaCO_3$	0.9	1.7	0.6	0.7

APPENDIX J. SLAB CHARACTERIZATION DATA

Table J-1: Average total elemental composition (+/- standard deviation) of major elements in the U.S. 20 slab   (>10,000 ppm).

Element	Concentration (ppm)
Al	19985 +/- 375
Ca	372200 +/- 46900
Si	65500 +/- 3800

Table J-2: Average total elemental composition (+/- standard deviation) of minor elements in the U.S. 20 slab   (1,000 - 10,000 ppm).

Element	Concentration (ppm)
Fe	7137 +/- 219
K	3469 +/- 88
Na	3573 +/- 54
S	5993 +/- 23

Table J-3: Average total element composition (+/- standard deviation) of trace elements in the U.S. 20 slab (<1,000 ppm).

Element		Concentration (ppm)	Element		Concentration (ppm)
Ag	<[1]	1	Mo	<	1.5
As		1.21 +/- 0.107	Nd		8.9 +/- 1.11
Au	<	1.5	Ni		81.6 +/- 1.3
Ba		148.73 +/- 11.607	P	<	100
Br	<	0.41	Pb		11.7 +/- 2.15
Cd	<	3.04	Rb		15.71 +/- 1.74
Ce		16.01 +/- 0.85	Sb		0.37 +/- 0.05
Cl		109.61 +/- 13.14	Sc		2.33 +/- 0.11
Co		2.98 +/- 0.16	Se	<	0.41
Cr		20.6 +/- 0.75	Sm		0.87 +/- 0.02
Cs		0.37 +/- 0.05	Sr		90.37 +/- 11.98
Cu		8.75 +/- 1.3	Ta		0.07 +/- 0.01
Dy		0.67 +/- 0.08	Tb		0.09 +/- 0.02
Eu		0.25 +/- 0.02	Th		2.31 +/- 0.13
Hf		1.48 +/- 0.09	Ti	<	214.95
Hg	<	1	U		0.50 +/- 0.16
I		3.66 +/- 1.59	V		21.16 +/- 2.3
In	<	0.06	W	<	2
La		6.40 +/- 0.13	Yb	<	1.1
Lu		0.1 +/- 0.01	Zn		13.80 +/- 1.3
Mg	<	333	Zr		30.6 +/- 8.05
Mn		211.79 +/- 2.78			

1 < denotes detection limit

Table J-4: ANOVA of albite concentration in the
three regions of the U.S. 20 slab.

Source	SS	df	MS	Computed F	Significant at
Effect	7.047	2	3.524	0.93	none
Error	45.309	14	3.776		
Total	52.356	12			

Table J-5: ANOVA of calcite concentration in the
three regions of the U.S. 20 slab.

Source	SS	df	MS	Computed F	Significant at
Effect	61.915	2	30.958	1.30	none
Error	285.562	14	23.797		
Total	347.477	12			

Table J-6: ANOVA of portlandite concentration in the
three regions of the U.S. 20 slab.

Source	SS	df	MS	Computed F	Significant at
Effect	0.075	2	0.038	0.10	none
Error	4.322	14	0.360		
Total	4.397	12			

Table J-7: ANOVA of quartz concentration in the
three regions of the U.S. 20 slab.

Source	SS	df	MS	Computed F	Significant at
Effect	6.711	2	3.356	0.87	none
Error	46.469	14	3.872		
Total	53.180	12			

Table J-8: ANOVA of changing albite concentration with
changing depth in the U.S. 20 slab.

Source	SS	df	MS	Computed F	Significant at
Effect	42.827	2	21.413	1.29	none
Error	149.833	9	16.648		
Total	192.660	11			

Table J-9: ANOVA of changing calcite concentration
with changing depth in the U.S. 20 slab.

Source	SS	df	MS	Computed F	Significant at
Effect	70.048	2	35.024	0.90	none
Error	348.575	9	38.731		
Total	418.623	11			

Table J-10: ANOVA of changing portlandite concentration
with changing depth in the U.S. 20 slab.

Source	SS	df	MS	Computed F	Significant at
Effect	0.303	2	0.151	0.35	none
Error	3.907	9	0.434		
Total	4.209	11			

Table J-11: ANOVA of changing quartz concentration
with changing depth in the U.S. 20 slab.

Source	SS	df	MS	Computed F	Significant at
Effect	163.648	2	81.824	3.93	>90%
Error	187.362	9	20.818		
Total	351.009	11			

Table J-12: Tukey-Kramer comparison of means of changing quartz
concentration with changing depth in the U.S. 20 slab.

Mix type	top	mid	bottom
top	8.735	7.250	9.933
mid	-7.250	8.735	2.683
bottom	-9.933	-2.683	8.735
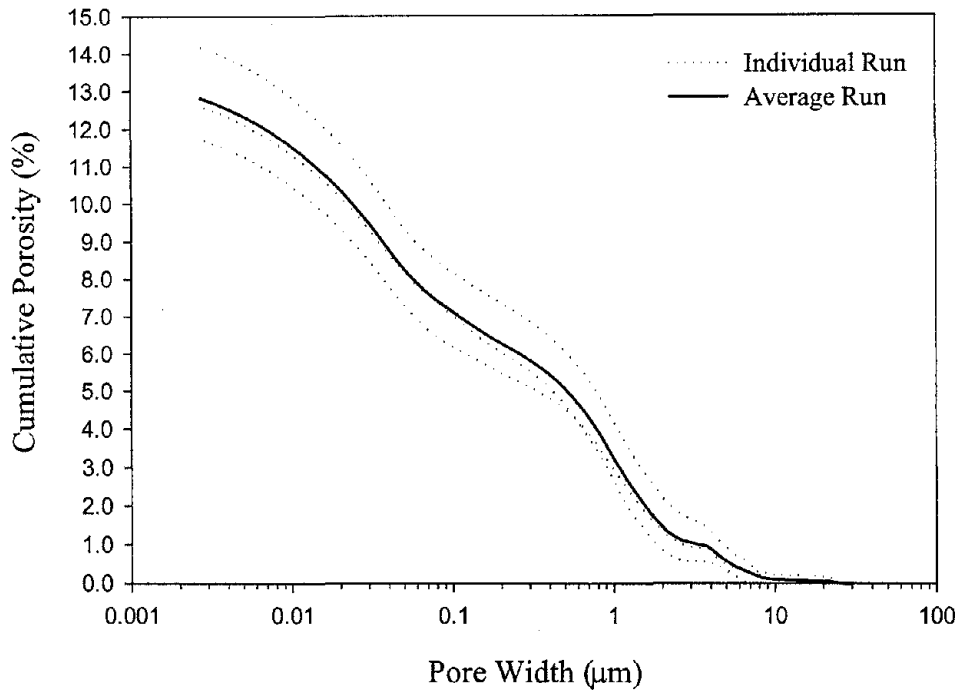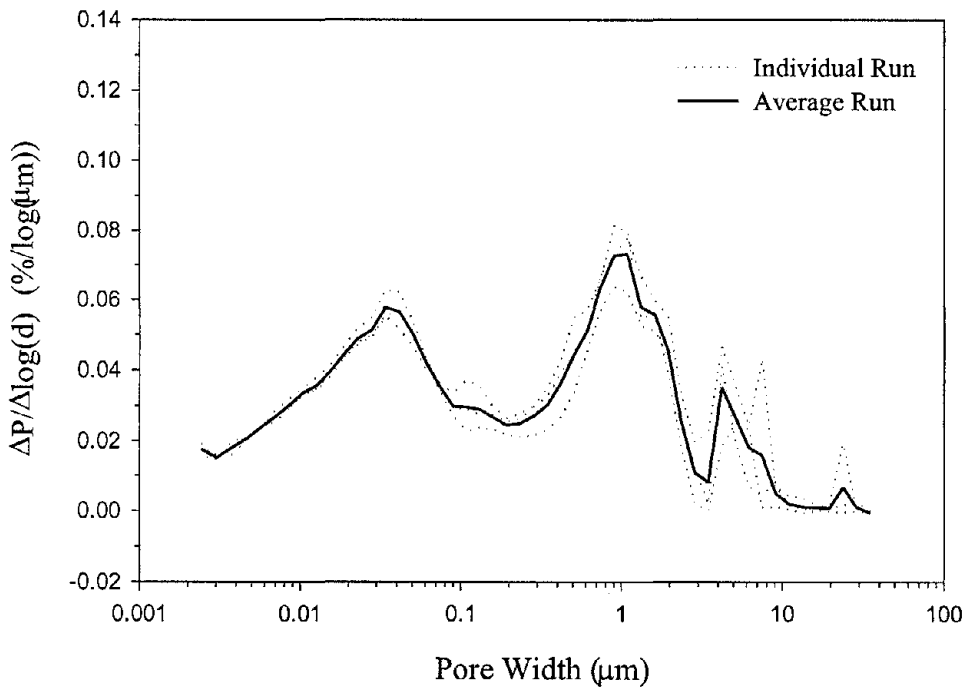
Figure J-1: MIP results for 5-C(1): (a) cumulative porosity vs. pore width;
(b) average differential pore size distribution vs. pore width.
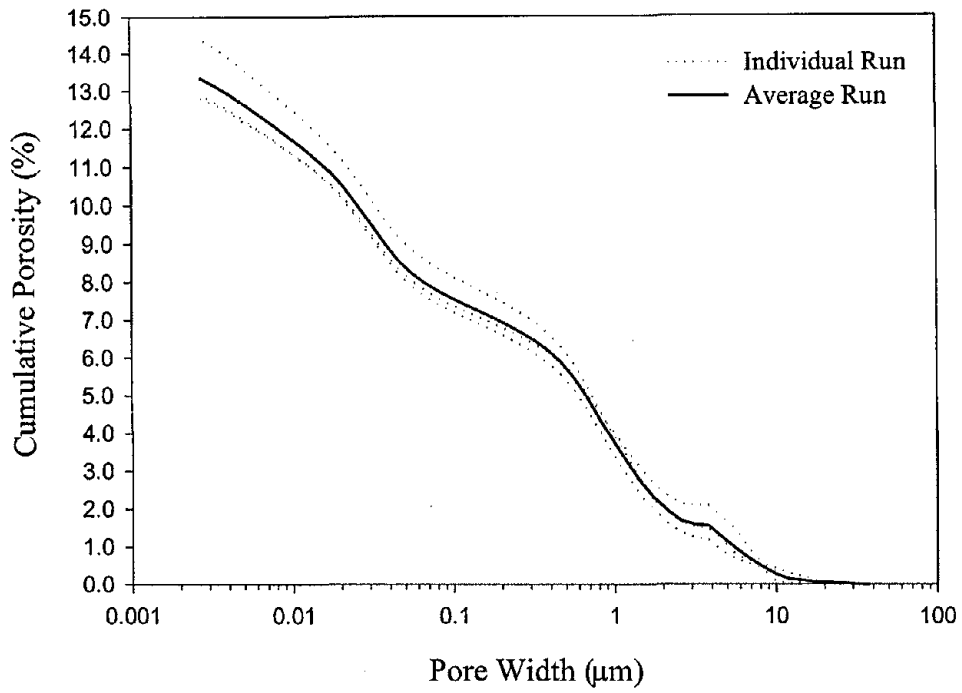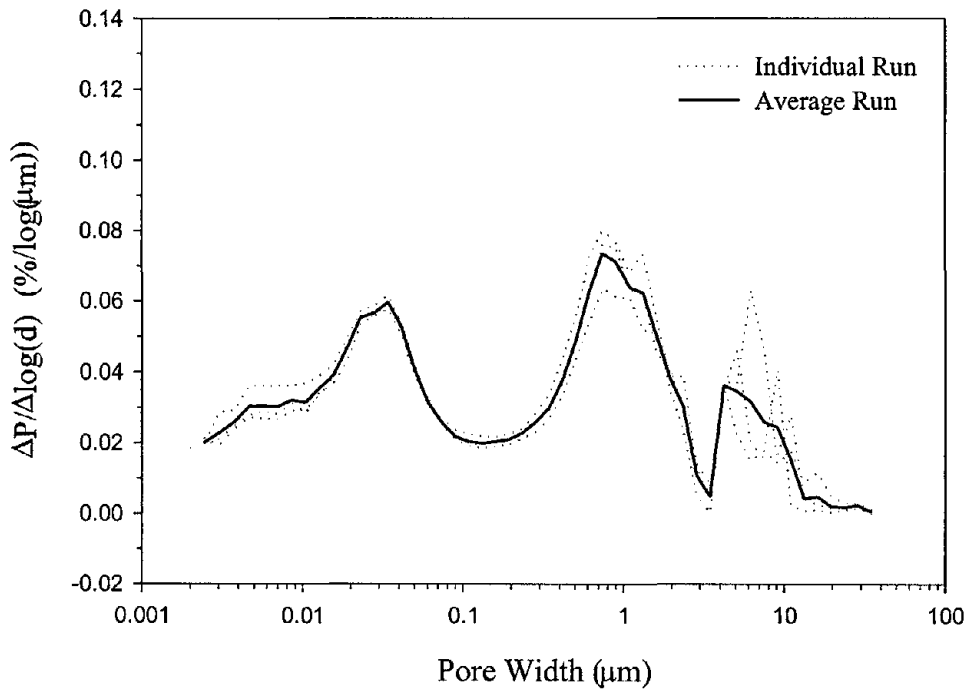
Figure J-2: MIP results for 5-C(4): (a) cumulative porosity vs. pore width;
(b) average differential pore size distribution vs. pore width.
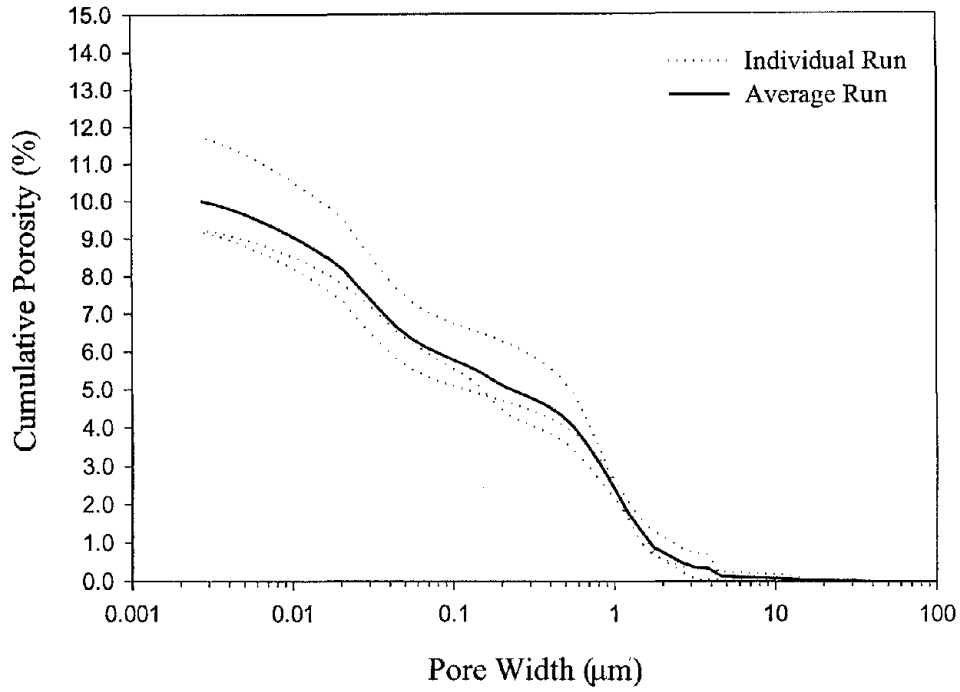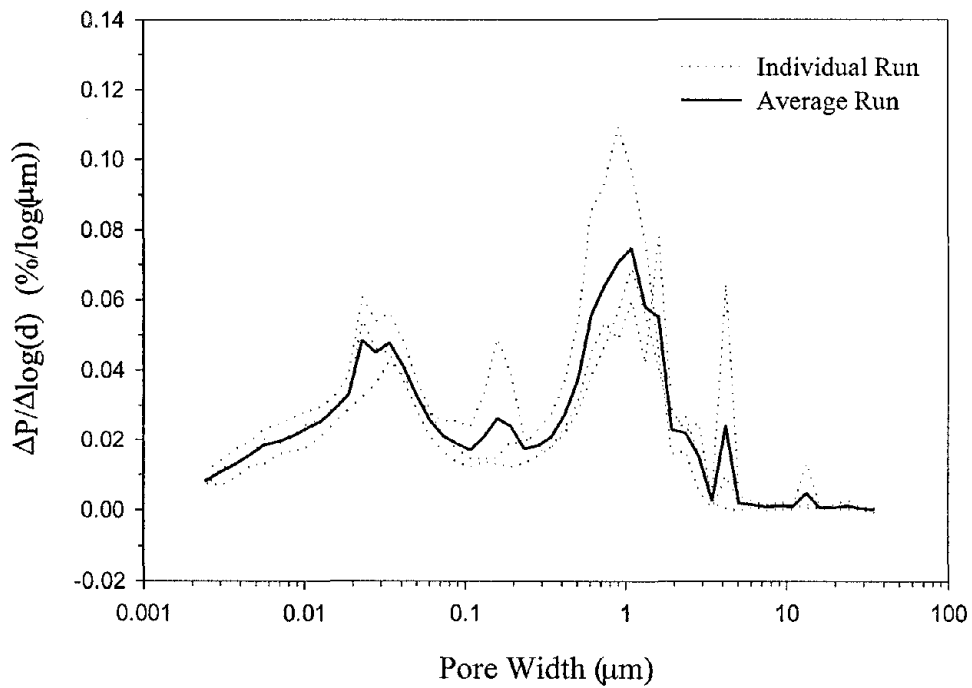
Figure J-3: MIP results for 5-C(8): (a) cumulative porosity vs. pore width; (b) average differential pore size distribution vs. pore width.
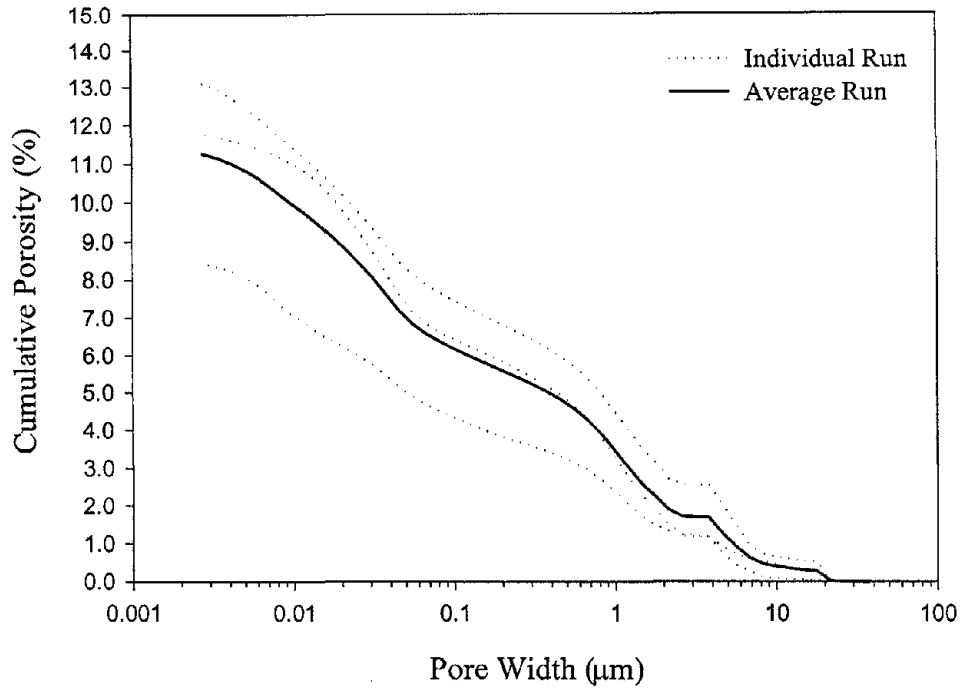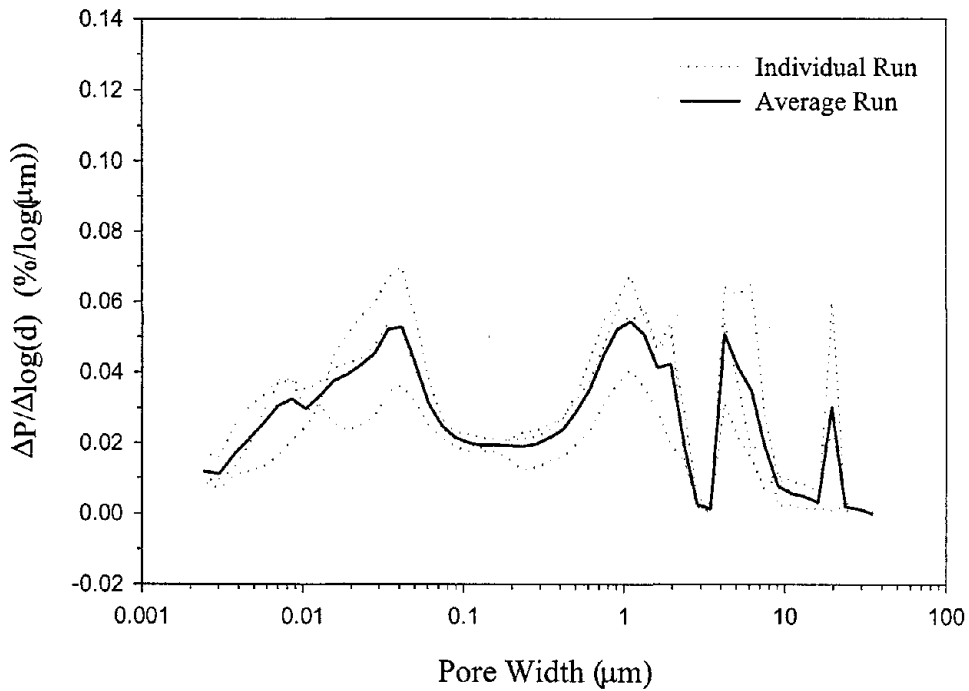
Figure J-4: MIP results for 15-C(4): (a) cumulative porosity vs. pore width; (b) average differential pore size distribution vs. pore width.
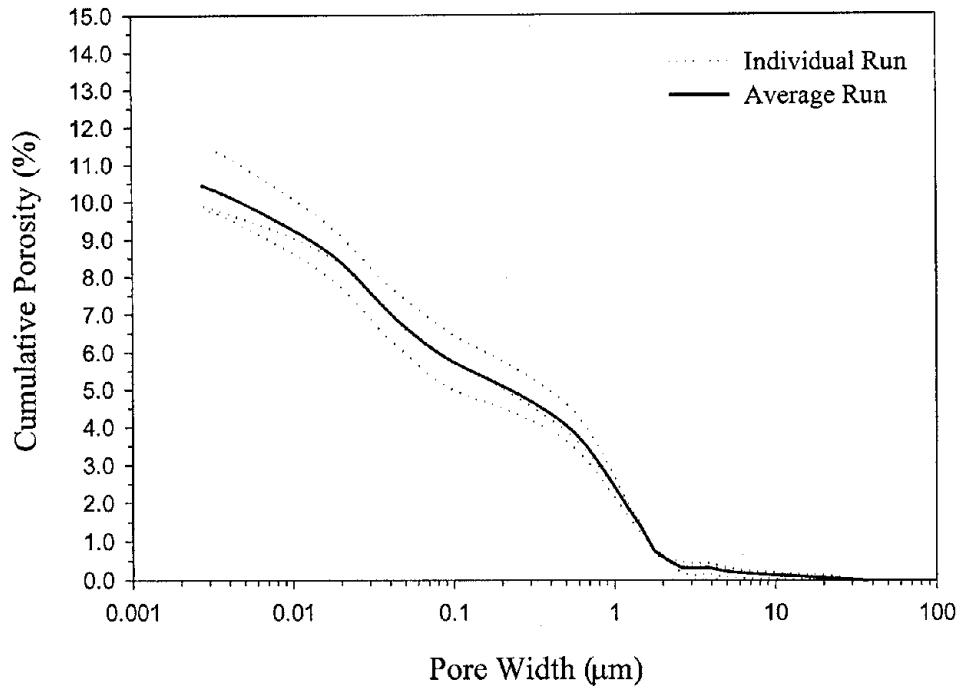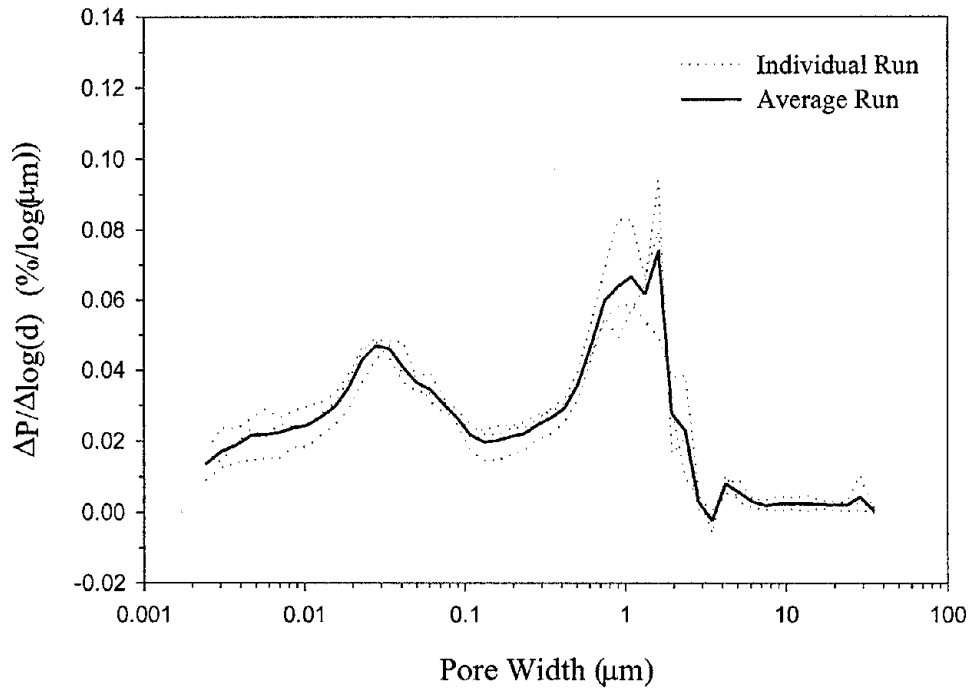
Figure J-5: MIP results for 17-S(4): (a) cumulative porosity vs. pore width; (b) average differential pore size distribution vs. pore width.
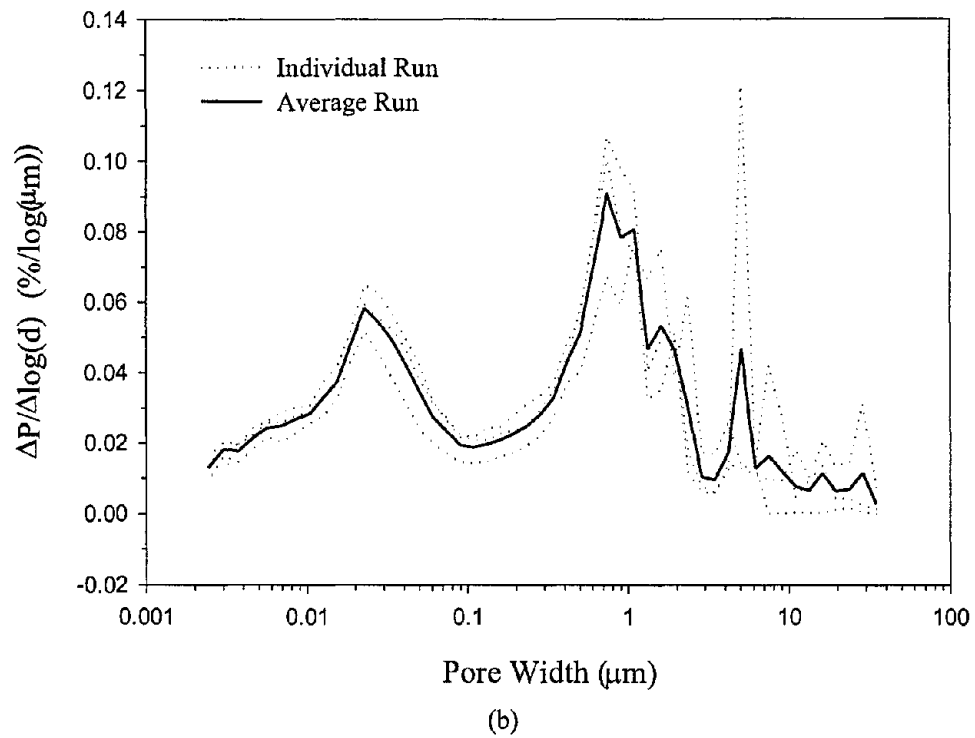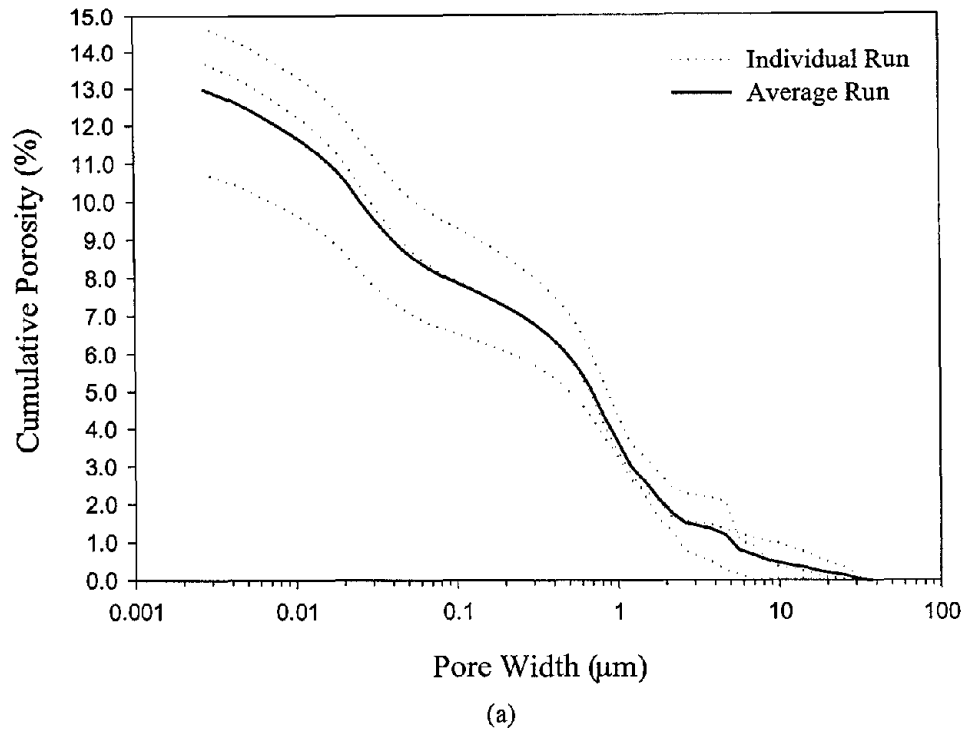
Figure J-6: MIP results for 26-J(4): (a) cumulative porosity vs. pore width; (b) average differential pore size distribution vs. pore width.
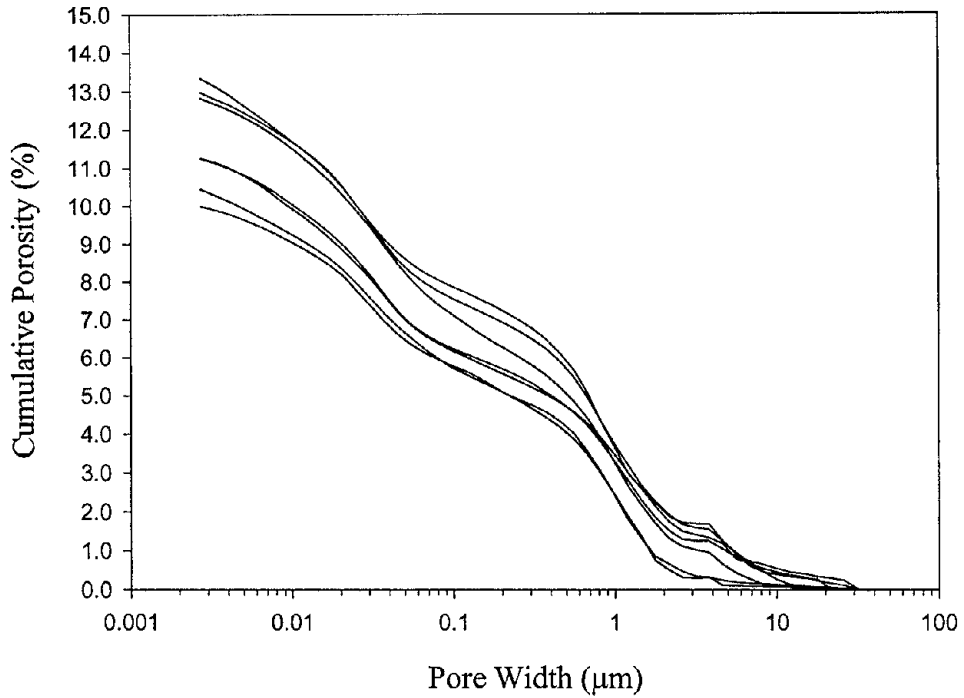
Figure J-7: Summary of MIP results for slab samples.
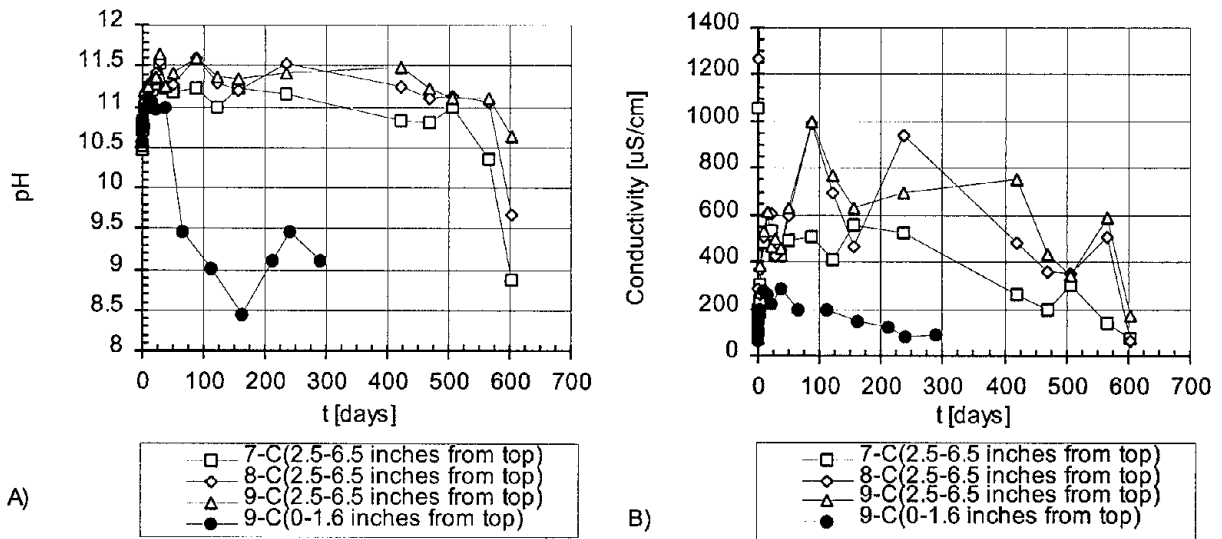
Figure J-8: K release for three samples representing the
bulk of the U.S. 20 slab and a sample representing the surface:
A) cumulative mass released in mg/m^2; B) flux released in mg/m^{2}s.
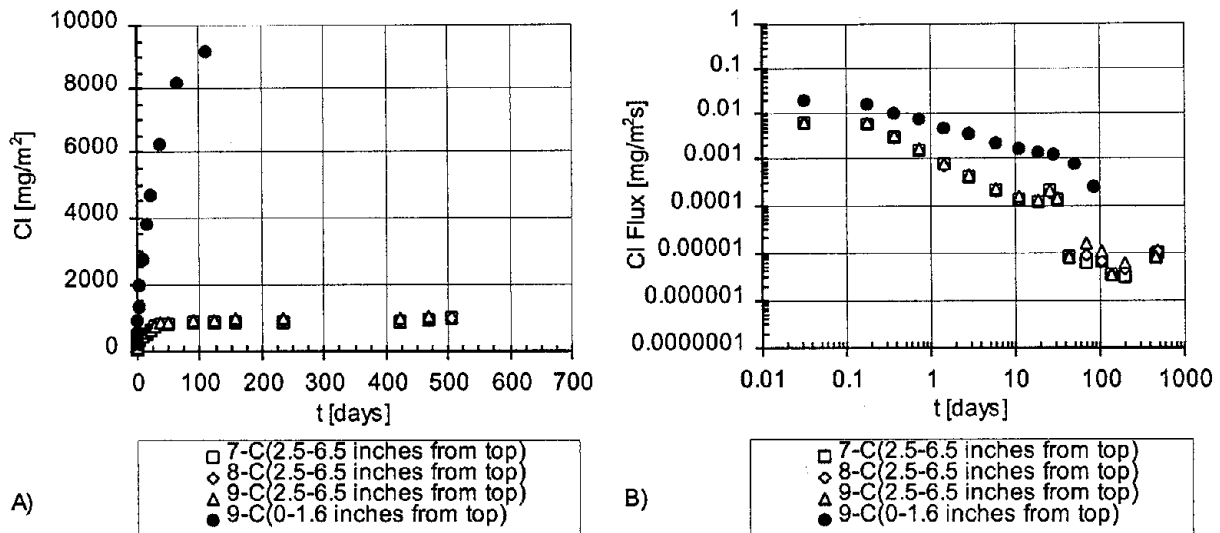
Figure J-9: Cl release for three samples representing the bulk
of the U.S. 20 slab and a sample representing the surface:
A) cumulative mass released in mg/m²; B) flux released in mg/m²s.
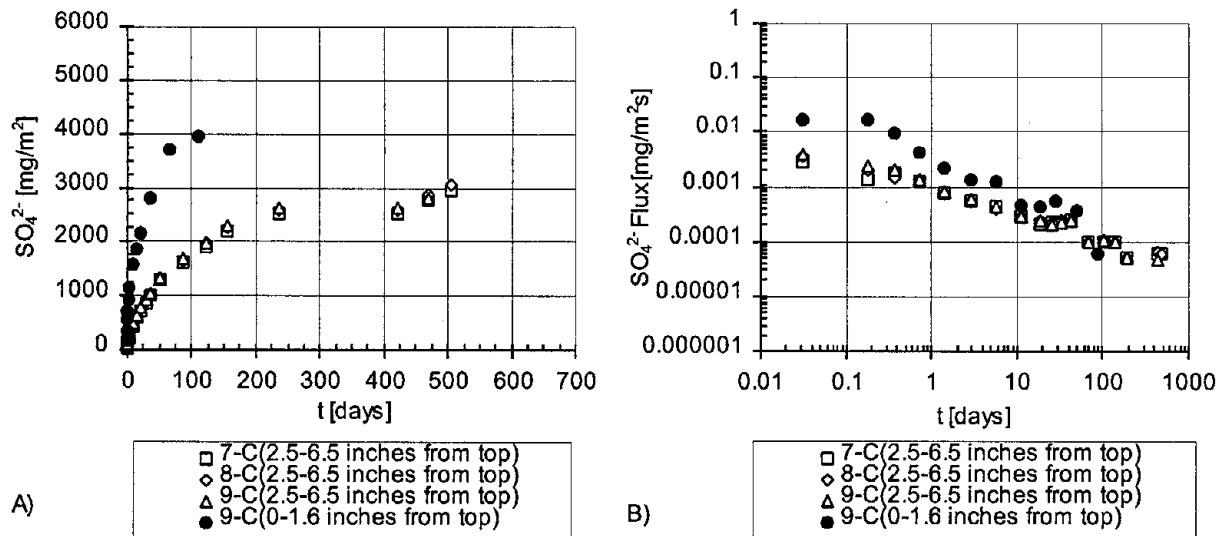
Figure J-10: SO_4^{2-} release for three samples representing the bulk of
the 20 slab and a sample representing the surface:
A) cumulative mass released in mg/m²; B) flux released in mg/m²s.

118
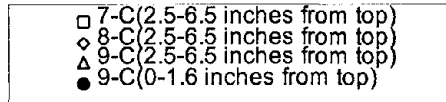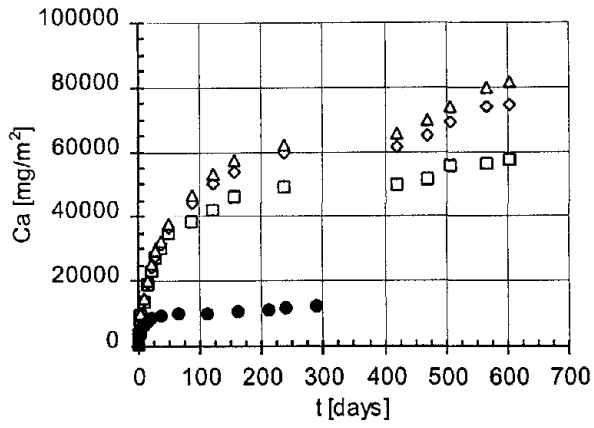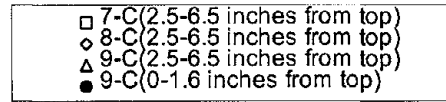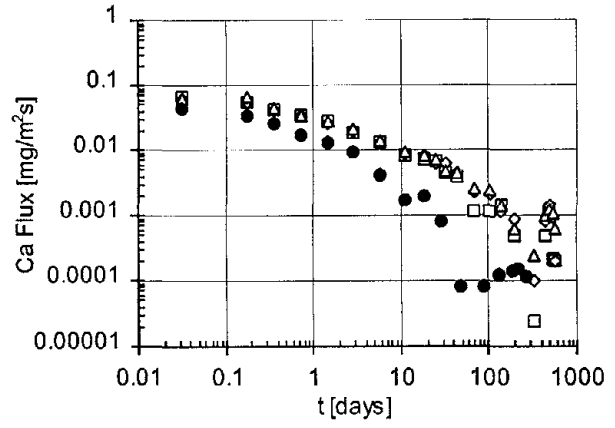
Figure J-11: Ca release for three samples representing the bulk
of the U.S. 20 slab and a sample representing the surface:
A) cumulative mass released in mg/m²; B) flux released in mg/m²s.

APPENDIX K. CFA-C FACTORIAL EXPERIMENT DATA

Table K-1: Type-C ANOVA of the effects of aging
treatments on compressive strength.

Source	Effect	Sum of squares	DF	Mean square	F ratio	Significant at
AA	-2024	24590252	1	24590252	144	99%
CL	-125	94028	1	94028	0.6	–
FT	-1094	7184420	1	7184420	42.1	99%
AAxCL	-127	96830	1	96830	0.6	–
AAxFT	-247	365615	1	365615	2.1	–
CLxFT	-285	486084	1	486084	2.8	–
AAxCLxFT	9	455	1	455	0.0	–
Curvature		25633607	1	25633607	150.1	99%
Pure error		4097917	24	170747		
Total		62549208	32			

Table K-2: ANOVA for crack density results for CFA-C prism specimens.

Source	Effect	SS	df	MS	Computed F
AA	0.352	0.248	1	0.248	4.312
CL	0.512	0.525	1	0.525	9.115
FT	0.167	0.056	1	0.056	0.974
AAxCL	0.352	0.248	1	0.248	4.312
AAxFT	-0.002	0.000	1	0.000	0
CLxFL	0.097	0.019	1	0.019	0.33
AAxCLxFT	-0.032	0.002	1	0.002	0.037
Curvature		0.349	1	0.349	6.07
Pure error		0.115	2	0.057	
Total		1.564	10		

Table K-3: Type-C ANOVA of the effects of aging treatments on RDM.

Source	Effect	Sum of Squares	DF	Mean Square	F Ratio	Significant at
AA	-8.12	1060	1	1060	15.8	99%
CL	-1.29	34.2	1	34.2	0.5	–
AAxCL	-3.01	158.3	1	158.3	2.4	–
Curvature		20840	1	20840	311	99%
Pure error		6895	103	67		
Total			10			

Table K-4: CFA-C prism porosity ANOVA.

Source	Effect	Sum of squares	DF	Mean square	F ratio	Significant at
AA	-0.025	0.001	1	0.001	0	–
CL	-0.285	0.162	1	0.162	0.203	–
FT	-0.66	0.871	1	0.871	1.09	–
AAxCL	0.965	1.862	1	1.862	2.33	–
AAxFT	0.15	0.045	1	0.045	0.06	–
CLxFT	-0.32	0.205	1	0.205	0.256	–
AAxCLxFT	-0.25	0.125	1	0.125	0.156	–
Curvature		0.236	1	0.236	0.296	–
Pure error		1.598	2	0.799		
Total		5.107	10			

Table K-5: CFA-C prism first peak uniformity indicator ANOVA.

Source	Effect	Sum of squares	DF	Mean square	F ratio	Significant at
AA	-0.003	0.0000163	1	0	1.161	–
CL	0.0014	0.000004	1	0	0.277	–
FT	0.0024	0.0000111	1	0	0.794	–
AAxCL	0.0045	0.0000399	1	0	2.841	–
AAxFT	0	0	1	0	0.061	–
CLxFT	0.0022	0.00001	1	0	0.688	–
AAxCLxFT	0.0017	0.000005	1	0	0.391	–
Curvature		0.0000163	1	0	1.16	–
Pure error		0.0000281	2	0		
Total		0.00013162	10			

Table K-6: CFA-C prism first peak weighted average threshold pore width ANOVA.

Source	Effect	Sum of squares (SS)	DF	Mean square	F ratio	Significant at
AA	-0.132	0.03484	1	0.0348	1.445	–
CL	0.0773	0.01195	1	0.012	0.496	–
FT	0.1039	0.02161	1	0.0216	0.896	–
AAxCL	-0.0705	0.00995	1	0.01	0.413	–
AAxFT	0.0652	0.00851	1	0.009	0.353	–
CLxFT	0.0225	0.00101	1	0.001	0.042	–
AAxCLxFT	-0.0344	0.00237	1	0.002	0.098	–
Curvature		0.00277	1	0.003	0.115	–
Pure error		0.04821	2	0.0241		
Total		0.14122	10			

Table K-7: CFA-C prism second peak uniformity indicator ANOVA.

Source	Effect	Sum of squares	DF	Mean square	F ratio	Significant at
AA	-0.006	0.0000653	1	0	74.2	95%
CL	-0.003	0.0000131	1	0	14.9	–
FT	-0.003	0.0000213	1	0	24.2	95%
AAxCL	0.001	0.000001	1	0	1.5	–
AAxFT	0	0	1	0	0.55	–
CLxFT	0.001	0.000002	1	0	2.2	–
AAxCLxFT	0	0	1	0	0.14	–
Curvature		0.0000274	1	0	31.1	95%
Pure error		0.000002	2	0		
Total		0.0001327	10			

Table K-8: CFA-C prism second peak weighted average
threshold pore width ANOVA.

Source	Effect	Sum of squares	DF	Mean square	F ratio	Significant at
AA	0.0054	0.00006	1	0.000057	4180	99%
CL	0	0	1	0	16.77	–
FT	-0.002	0	1	0.00001	381	99%
AAxCL	-0.001	0	1	0	285	99%
AAxFT	0	0	1	0	6.88	–
CLxFT	0.001	0	1	0	45.4	95%
AAxCLxFT	0.0014	0	1	0	300	99%
Curvature		0.00004	1	0.000036	2590	99%
Pure error		0	2	0		
Total		0.000107	10			

Table K-9: CFA-C prism first peak threshold pore width ANOVA.

Source	Effect	Sum of squares	DF	Mean square	F ratio	Significant at
AA	-0.037	0.0027	1	0.00274	0.066	–
CL	0.044	0.0039	1	0.00387	0.093	–
FT	0.2	0.08	1	0.08	1.922	–
AAxCL	-0.163	0.0531	1	0.05314	1.276	–
AAxFT	0.081	0.0131	1	0.01312	0.315	–
CLxFT	0	0	1	0	0	–
AAxCLxFT	-0.119	0.0283	1	0.02832	0.68	–
Curvature		0.009	1	0.00903	0.217	–
Pure error		0.0833	2	0.04163		
Total		0.2735	10			

Table K-10: CFA-C prism second peak threshold pore
width ANOVA.

Source	Effect	Sum of squares	DF	Mean square	F ratio	Significant at
AA	0.0031	0.0000192	1	0	4.99	–
CL	-0.001	0.000004	1	0	1.02	–
FT	-0.003	0.0000192	1	0	4.99	–
AAxCL	-0.003	0.0000192	1	0	4.99	–
AAxFT	-0.001	0.00000392	1	0.00000392	1.02	–
CLxFT	0.0031	0.00001922	1	0.00001922	4.99	–
AAxCLxFT	0.0014	0.00000392	1	0.00000392	1.02	–
Curvature		0.00001920	1	0.00001920	4.98	–
Pure error		0.00000771	2	0.00000385		
Total		0.00011555	10			

Table K-11: CFA-C BET-N_2 surface area ANOVA.

Source	Effect	Sum of squares	DF	Mean square	F ratio	Significant at
AA	0.648	0.8	1	0.839	0.063	–
CL	-1	2	1	2.01	0.152	–
FT	1.048	2.2	1	2.195	0.166	–
AAxCL	3.603	26	1	25.956	1.958	–
AAxFT	1.403	3.9	1	3.934	0.297	–
CLxFT	3.453	23.8	1	23.84	1.798	–
AAxCLxFT	3.178	20.2	1	20.193	1.523	–
Curvature		1.4	1	1.409	0.106	–
Pure error		26.5	2	13.257		
Total		106.9	10			

Table K-12: ANOVA of the effects of accelerated aging on
albite concentration in the CFA-C prisms.

Source	Effect	Sum of squares	DF	Mean square	F ratio	Significant at
AA	1.308	10.270	1	10.270	0.5577	none
CL	-2.475	36.754	1	36.754	1.9956	none
FT	-1.975	23.404	1	23.404	1.2708	none
AAxCL	-1.858	20.72	1	20.72	1.1251	none
AAxFT	-1.492	13.350	1	13.350	0.7249	none
CLxFT	2.425	35.284	1	35.284	1.9158	none
AAxCLxFT	0.542	1.760	1	1.760	0.0956	none
Curvature		4.146	1	4.146	0.2251	none
Pure error		442.007	24	18.417		
Total		587.695	32			

Table K-13: ANOVA of the effects of accelerated aging on calcite
concentration in the CFA-C prisms.

Source	Effect	Sum of squares	DF	Mean square	F ratio	Significant at
AA	-2.117	26.882	1	26.882	1.1493	none
CL	-0.650	2.535	1	2.535	0.1084	none
FT	-1.800	19.440	1	19.440	0.8311	none
AAxCL	-0.700	2.940	1	2.940	0.1257	none
AAxFT	0.150	0.135	1	0.135	0.0058	none
CLxFT	-2.417	35.042	1	35.042	1.4981	none
AAxCLxFT	-2.000	24.000	1	24.000	1.0261	none
Curvature		37.702	1	37.702	1.6119	none
Pure error		561.360	24	23.390		
Total		710.035	32			

Table K-14: ANOVA of the effects of accelerated aging on
ettringite concentration in the CFA-C prisms.

Source	Effect	Sum of squares	DF	Mean square	F ratio	Significant at
AA	0.025	0.004	1	0.004	0.0154	none
CL	-0.058	0.020	1	0.020	0.0836	none
FT	-0.325	0.634	1	0.634	2.5946	none
AAxCL	0.192	0.220	1	0.220	0.9024	none
AAxFT	-0.108	0.070	1	0.070	0.2883	none
CLxFT	0.075	0.034	1	0.034	0.1382	none
AAxCLxFT	-0.275	0.454	1	0.454	1.8577	none
Curvature		0.223	1	0.223	0.9144	none
Pure error		5.862	24	0.244		
Total		7.522	32			

Table K-15: ANOVA of the effects of accelerated aging on
gypsum concentration in the CFA-C prisms.

Source	Effect	Sum of squares	DF	Mean square	F ratio	Significant at
AA	-0.275	0.454	1	0.454	7.3803	>95%
CL	0.025	0.004	1	0.004	0.0610	none
FT	-0.242	0.350	1	0.350	5.6995	>95%
AAxCL	0.008	0.000	1	0.000	0.0068	none
AAxFT	0.008	0.000	1	0.000	0.0068	none
CLxFT	-0.092	0.050	1	0.050	0.8200	none
AAxCLxFT	0.025	0.004	1	0.004	0.0610	none
Curvature		0.002	1	0.002	0.0347	none
Pure error		1.476	24	0.061		
Total		2.341	32			

Table K-16: ANOVA of the effects of accelerated aging on
portlandite concentration in the CFA-C prisms.

Source	Effect	Sum of squares	DF	Mean square	F ratio	Significant at
AA	-0.183	0.202	1	0.202	0.4730	none
FT	-0.200	0.240	1	0.240	0.5629	none
CL	-0.417	1.042	1	1.042	2.4430	none
AAxCL	0.033	0.0067	1	0.0067	0.0156	none
AAxFT	-0.150	0.1350	1	0.1350	0.3166	none
CLxFT	0.200	0.240	1	0.240	0.5629	none
AAxCLxFT	-0.067	0.027	1	0.027	0.0625	none
Curvature		0.055	1	0.055	0.1290	none
Pure error		10.233	24	0.426		
Total		12.180	32			

Table K-17: ANOVA of the effects of accelerated aging on
quartz concentration in the CFA-C prisms.

Source	Effect	Sum of squares	DF	Mean square	F ratio	Significant at
AA	0.300	0.540	1	0.540	0.1210	none
CL	-0.733	3.227	1	3.227	0.7232	none
FT	-1.733	18.027	1	18.027	4.0406	> 90%
AAxCL	-1.067	6.8267	1	6.8267	1.5302	none
AAxFT	1.067	6.8267	1	6.8267	1.5302	none
CLxFT	0.033	0.007	1	0.007	0.0015	none
AAxCLxFT	-0.433	1.127	1	1.127	0.2525	none
Curvature		2.227	1	2.227	0.4992	none
Pure error		107.073	24	4.461		
Total		145.881	32			

Table K-18: Summary of significant differences in phase concentration
in CFA-C prisms due to main effects.

	Mineral phase					
Source	Albite	Calcite	Ettringite	Gypsum	Portlandite	Quartz
AA	none	none	none	> 95%	none	none
CL	none	none	none	none	none	none
FT	none	none	none	> 95%	none	> 90%

Table K-19: Summary of significant differences in phase concentration in CFA-C prisms due to treatment interactions.

Interaction Effect	Mineral phase					
	Albite	Calcite	Ettringite	Gypsum	Portlandite	Quartz
AAxCL	none	none	none	none	none	none
AAxFT	none	none	none	none	none	none
CLxFT	none	none	none	none	none	none
AAxCLxFT	none	none	none	none	none	none

Table K-20: pH-Dependent leaching ANOVA: Ca at pH = 12.0.

Source	Effect	Sum of squares	DF	Mean square	F ratio	Significant at
AA	-368	2.701E+05	1	2.701E+05	13.996	> 90%
CL	-458	4.186E+05	1	4.186E+05	21.690	> 95%
FT	68	9.113E+03	1	9.113E+03	0.472	none
AAxCL	123	3.001E+04	1	3.001E+04	1.555	none
AAxFT	98	1.901E+04	1	1.901E+04	0.985	none
CLxFT	-123	3.001E+04	1	3.001E+04	1.555	none
AAxCLxFT	-93	1.711E+04	1	1.711E+04	0.887	none
Curvature		1.665E+05	1	1.665E+05	8.627	> 90%
Pure error		3.860E+04	2	1.930E+04		
Total		9.991E+05	10			

Table K-21: pH-Dependent leaching ANOVA: Al at pH = 5.0.

Source	Effect	Sum of squares	DF	Mean square	F ratio	Significant at
AA	-0.450	0.405	1	0.405	9.346	> 90%
CL	-0.650	0.845	1	0.845	19.500	> 95%
FT	-0.750	1.125	1	1.125	25.962	>95%
AAxCL	-0.350	0.245	1	0.245	5.654	none
AAxFT	0.450	0.405	1	0.405	9.346	>90%
CLxFT	-0.050	0.005	1	0.005	0.115	none
AAxCLxFT	0.050	0.005	1	0.005	0.115	none
Curvature		1.044	1	1.044	24.087	> 95%
Pure error		0.087	2	0.043		
Total		4.165	10			

Table K-22: pH-Dependent leaching ANOVA: Cr at pH = 9.7.

Source	Effect	Sum of squares	DF	Mean square	F ratio	Significant at
AA	-0.004	3.613E-05	1	3.613E-05	36.125	> 95%
CL	0.003	2.113E-05	1	2.113E-05	21.125	> 95%
FT	0.001	3.130E-06	1	3.130E-06	3.125	none
AAxCL	0.003	2.113E-05	1	2.113E-05	21.125	> 95%
AAxFT	0.002	1.013E-05	1	1.013E-05	10.125	> 90%
CLxFT	-0.003	2.113E-05	1	2.113E-05	21.125	> 95%
AAxCLxFT	-0.001	3.120E-06	1	3.120E-06	3.125	none
Curvature		8.500E-07	1	8.500E-07	0.852	none
Pure error		2.000E-06	2	1.000E-06		
Total		1.187E-04	10			

Table K-23: pH-Dependent leaching ANOVA: K at pH = 12.0.

Source	Effect	Sum of squares	DF	Mean square	F ratio	Significant at
AA	-14.750	435.125	1	435.125	15.540	> 90%
CL	4.750	45.125	1	45.125	1.612	none
FT	-2.750	15.125	1	15.125	0.540	none
AAxCL	-9.250	171.125	1	171.125	6.112	none
AAxFT	0.250	0.125	1	0.125	0.005	none
CLxFT	2.750	15.125	1	15.125	0.540	none
AAxCLxFT	5.750	66.125	1	66.125	2.362	none
Curvature		405.034	1	405.034	14.466	> 90%
Pure error		56.000	2	28.000		
Total		1208.909	10			

Table K-24: ANOVA on the effects of accelerated aging on Na observed diffusivities - CFA-C prisms.

Source	Effect	Sum of squares	DF	Mean square	F ratio	Significant at
AA	1.75e-13	6.125000e-26	1	6.12500e-26	0.024	none
CL	7.50e-14	1.125000e-26	1	1.12500e-26	0	none
FT	3.25e-13	2.113000e-25	1	2.11300e-25	0.082	none
AAxCL	-7.5e-14	1.125000e-26	1	1.12500e-26	0	none
AAxFT	-1.3e-13	3.125000e-26	1	3.12500e-26	0.012	none
CLxFT	7.50e-14	1.125000e-26	1	1.12500e-26	0	none
AAxCLxFT	-7.5e-14	1.125000e-26	1	1.12500e-26	0	none
Curvature		1.819000e-23	1	1.81900e-23	7.024	none
Pure error		5.180000e-24	2	2.59000e-24		
Total		2.372000e-23	10			

128

Table K-25: ANOVA on the effects of accelerated aging on K observed diffusivities - CFA-C prisms.

Source	Effect	Sum of squares	DF	Mean square	F ratio	Significant at
AA	-3.08e-13	1.891000e-25	1	1.89100e-25	0.623	none
CL	7.750e-14	1.201000e-26	1	1.20100e-26	0.04	none
FT	1.925e-13	7.411000e-26	1	7.41100e-26	0.244	none
AAxCL	-1.83e-13	6.661000e-26	1	6.66100e-26	0.22	none
AAxFT	-5.75e-14	6.612000e-27	1	6.61200e-27	0.022	none
CLxFT	-2.25e-14	1.013000e-27	1	1.01300e-27	0.003	none
AAxCLxFT	-2.03e-13	8.201000e-26	1	8.20100e-26	0.27	none
Curvature		2.963000e-24	1	2.96300e-24	9.769	>90%
Pure error		6.067000e-25	2	3.03300e-25		
Total		4.001000e-24	10			

Table K-26: ANOVA on the effects of accelerated aging on Ca observed diffusivities - CFA-C prisms.

Source	Effect	Sum of squares	DF	Mean square	F ratio	Significant at
AA	1.50e-15	4.500000e-30	1	4.50000e-30	1.929	none
CL	-4.0e-15	3.200000e-29	1	3.20000e-29	13.714	>90%
FT	2.00e-15	8.000000e-30	1	8.00000e-30	3.429	none
AAxCL	-3.0e-15	1.800000e-29	1	1.80000e-29	7.714	none
AAxFT	-2.0e-15	8.000000e-30	1	8.00000e-30	3.429	none
CLxFT	-5.0e-16	5.000000e-31	1	5.00000e-31	0.214	none
AAxCLxFT	-5.0e-16	5.000000e-31	1	5.00000e-31	0.214	none
Curvature		2.100000e-29	1	2.10000e-29	8.89	>90%
Pure error		4.700000e-30	2	2.30000e-30		
Total		9.700000e-29	10			
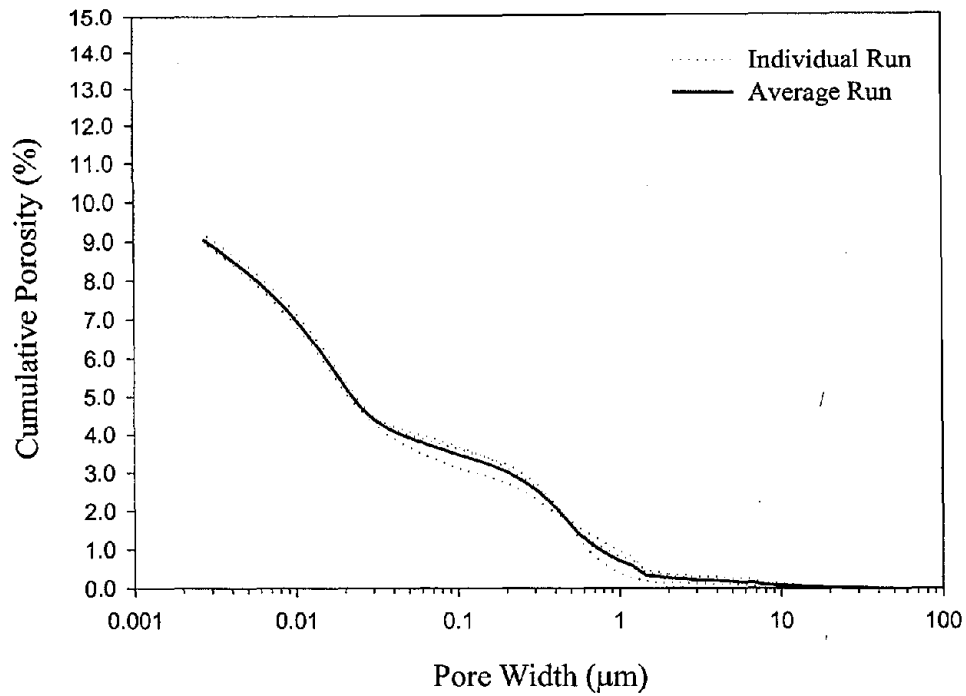
(a)
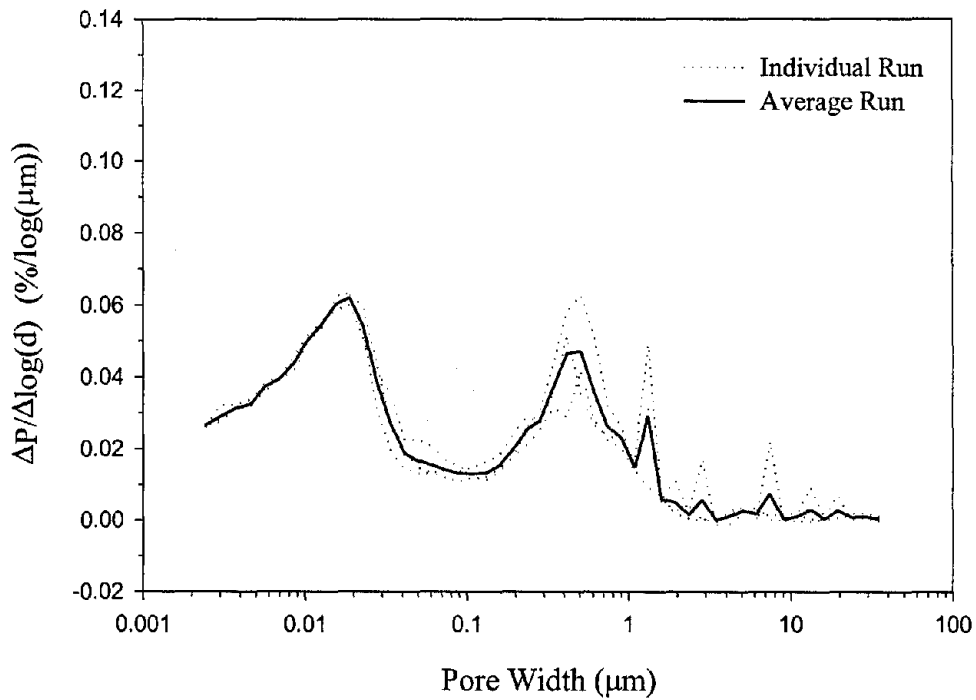
(b)

Figure K-1: MIP results for C(NHN)09: (a) cumulative porosity
vs. pore width; (b) average differential pore size distribution vs. pore width.
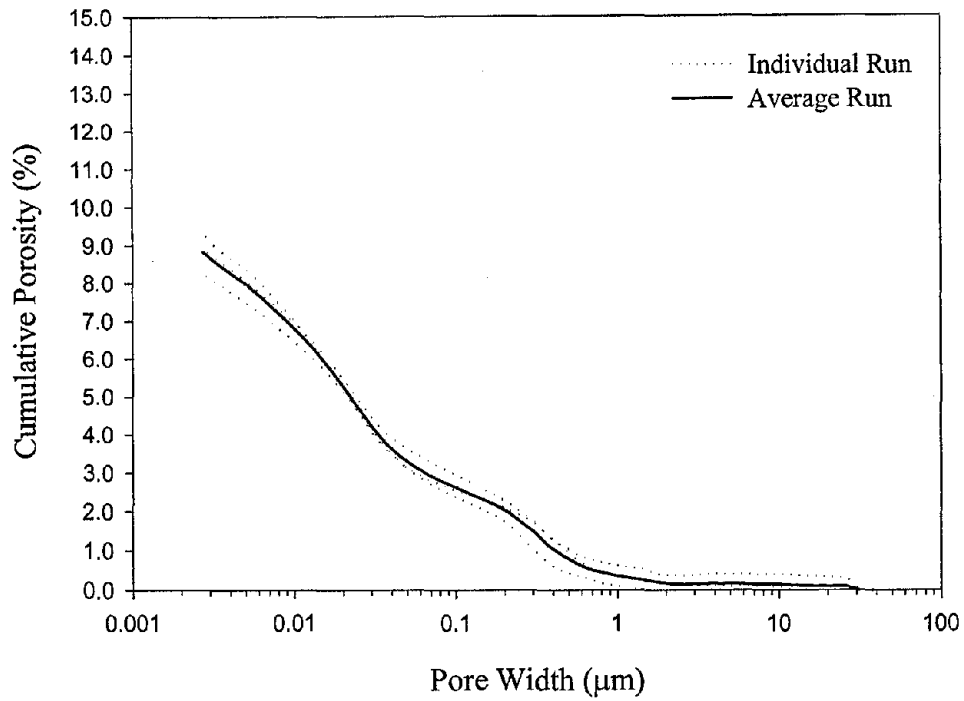
(a)
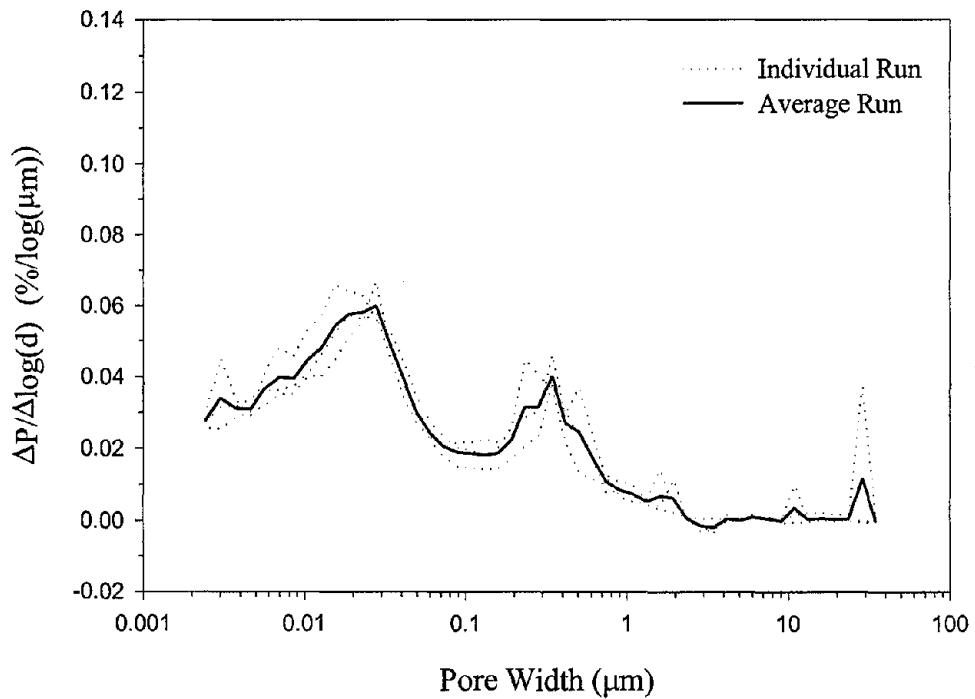
(b)

Figure K-2: MIP results for C(HNN)09: (a) cumulative porosity
vs. pore width; (b) average differential pore size distribution vs. pore width.

131
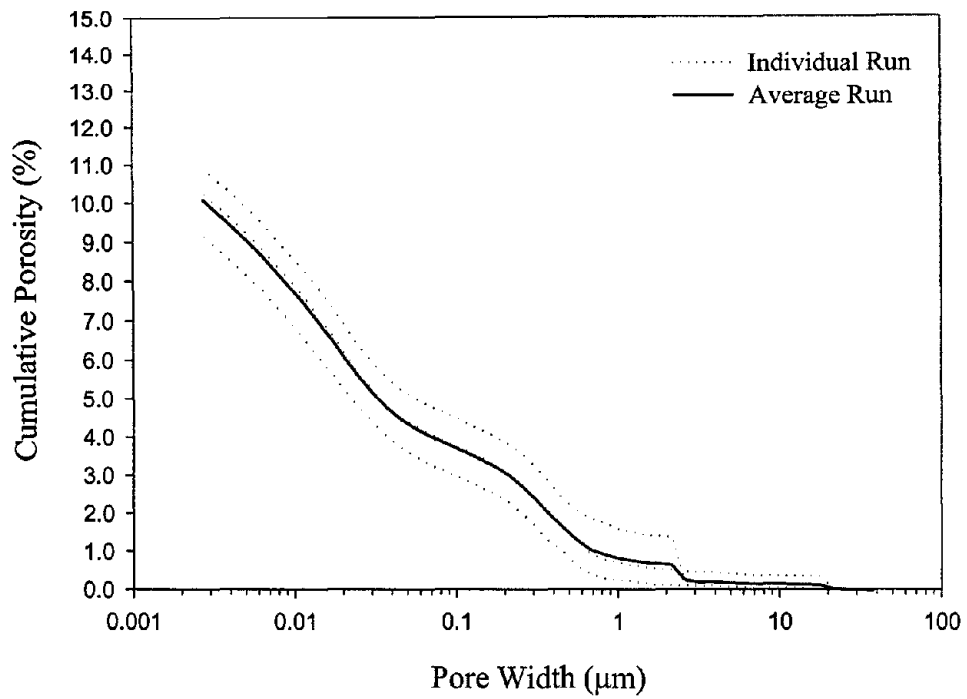
(a)
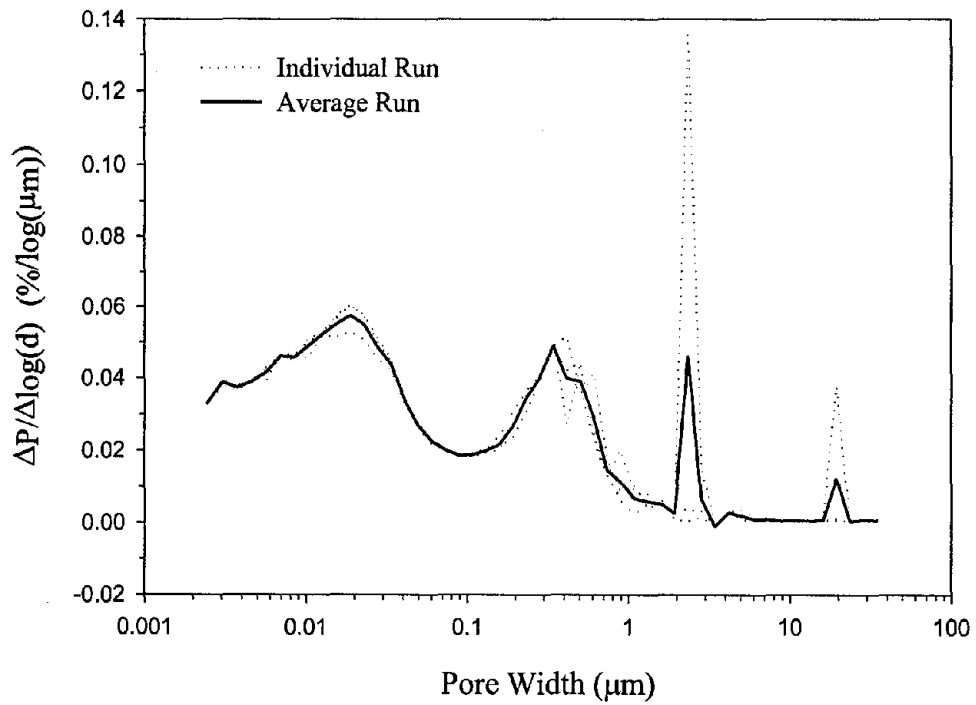
(b)

Figure K-3: MIP results for C(HHN)09: (a) cumulative porosity
vs. pore width; (b) average differential pore size distribution vs. pore width.

132
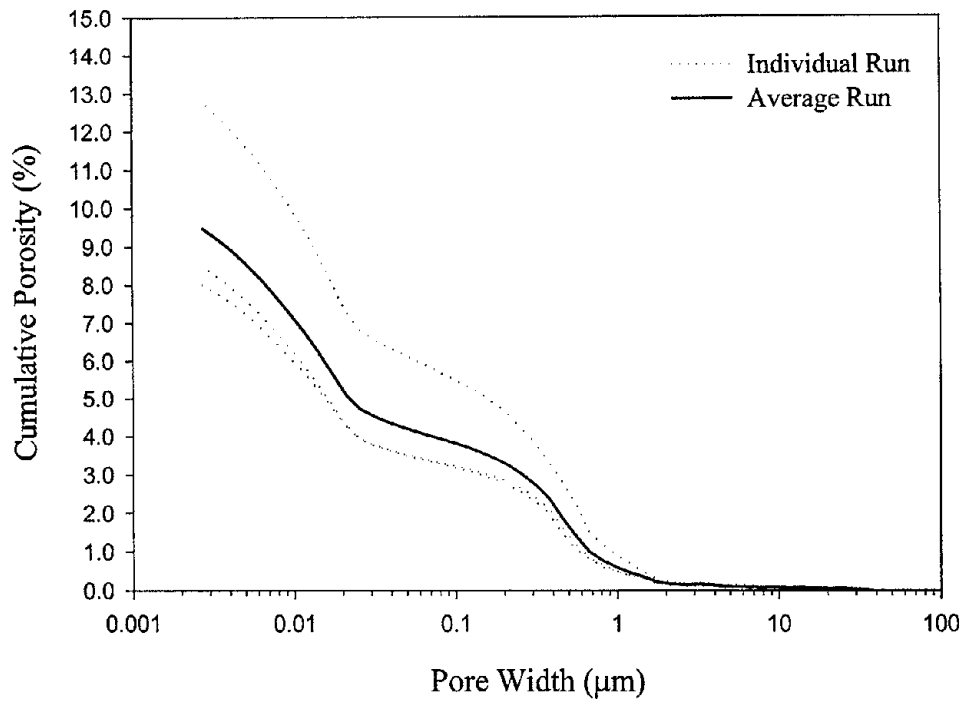
(a)
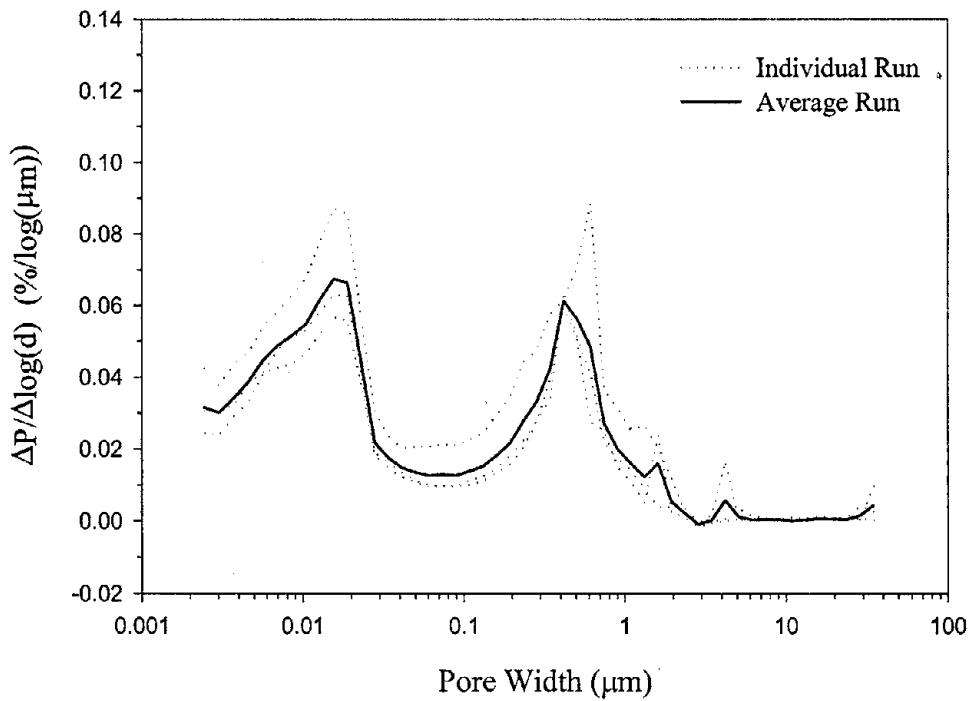
(b)

Figure K-4: MIP results for C(NNH)09: (a) cumulative porosity
vs. pore width; (b) average differential pore size distribution vs. pore width.

133
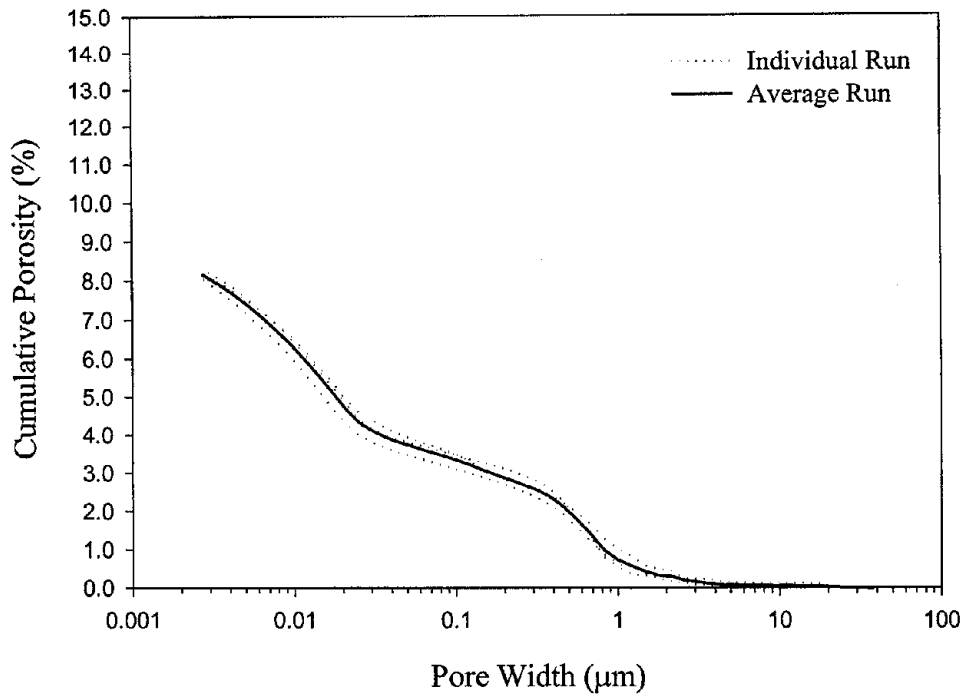
(a)
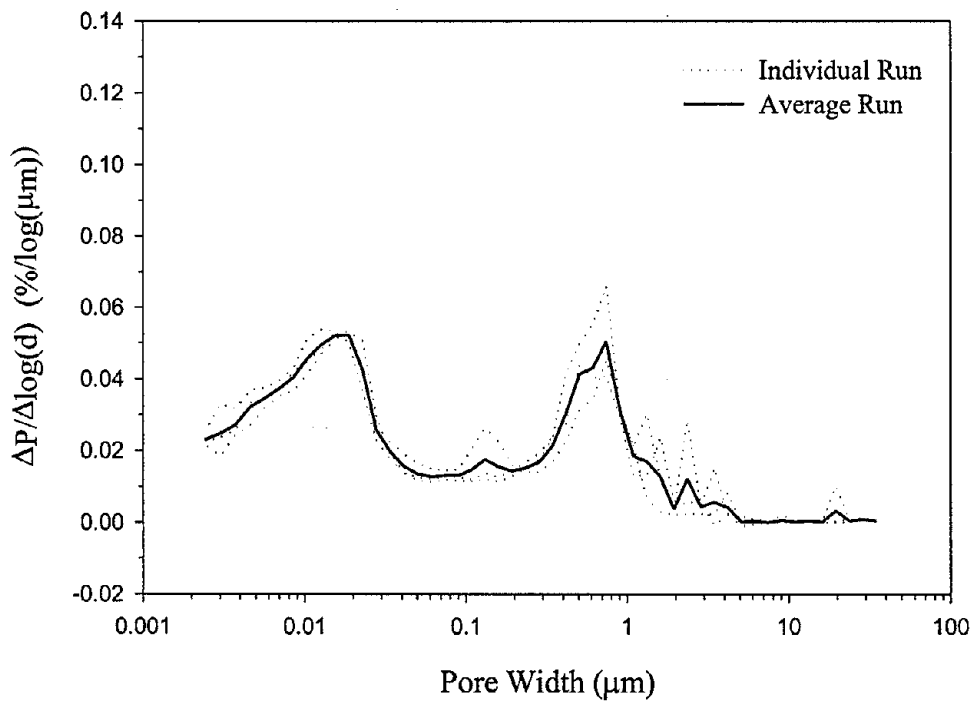
(b)

Figure K-5: MIP results for C(NHH)09: (a) cumulative porosity
vs. pore width; (b) average differential pore size distribution vs. pore width.
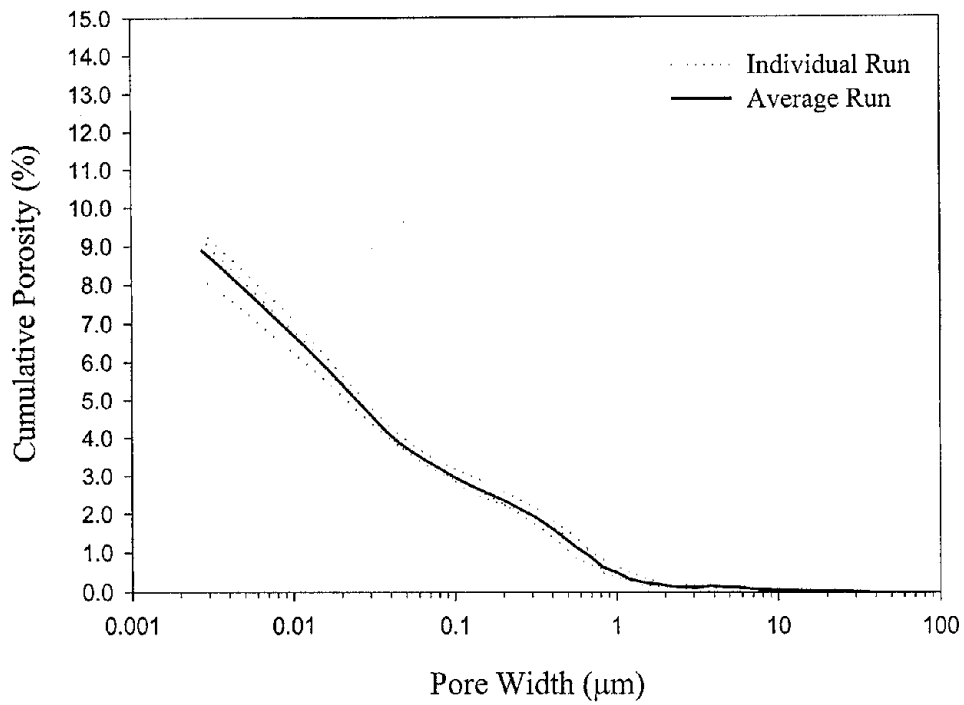
(a)
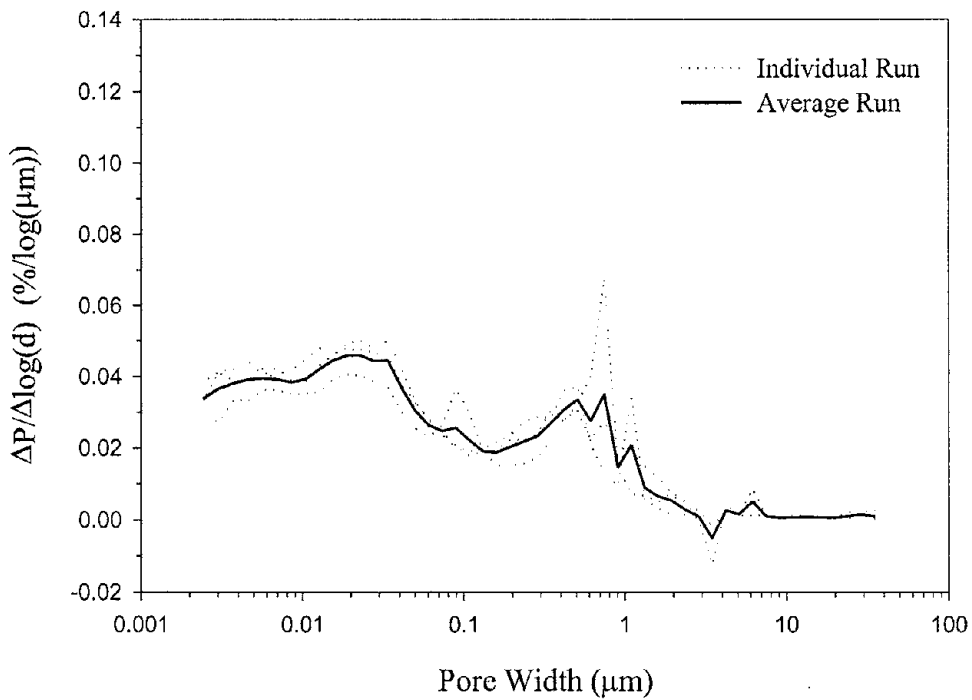
(b)

Figure K-6: MIP results for C(HNH)09: (a) cumulative porosity
vs. pore width; (b) average differential pore size distribution vs. pore width.

135
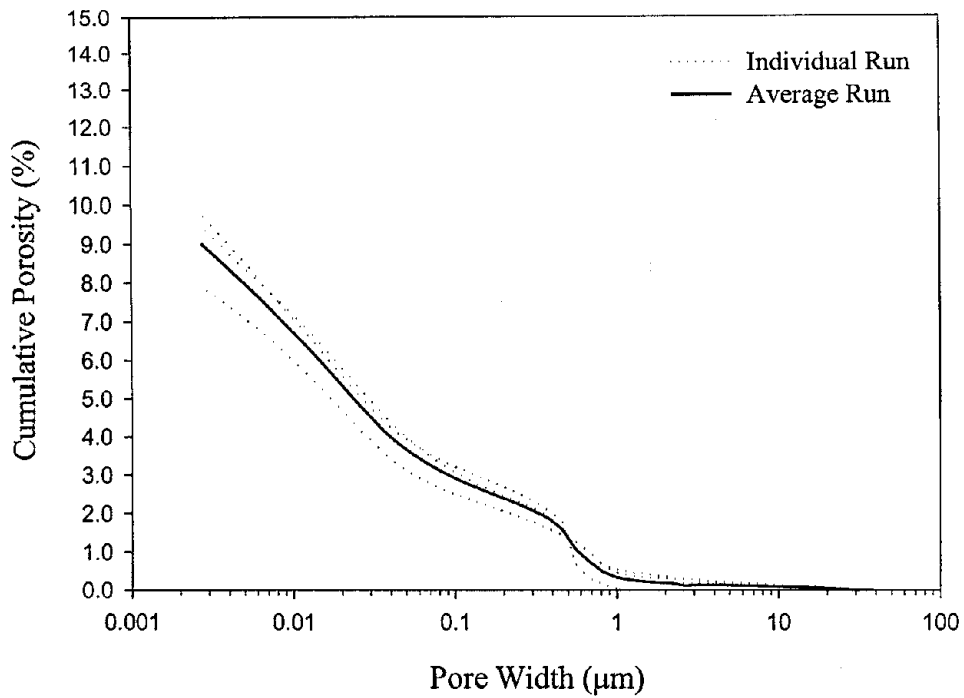
(a)
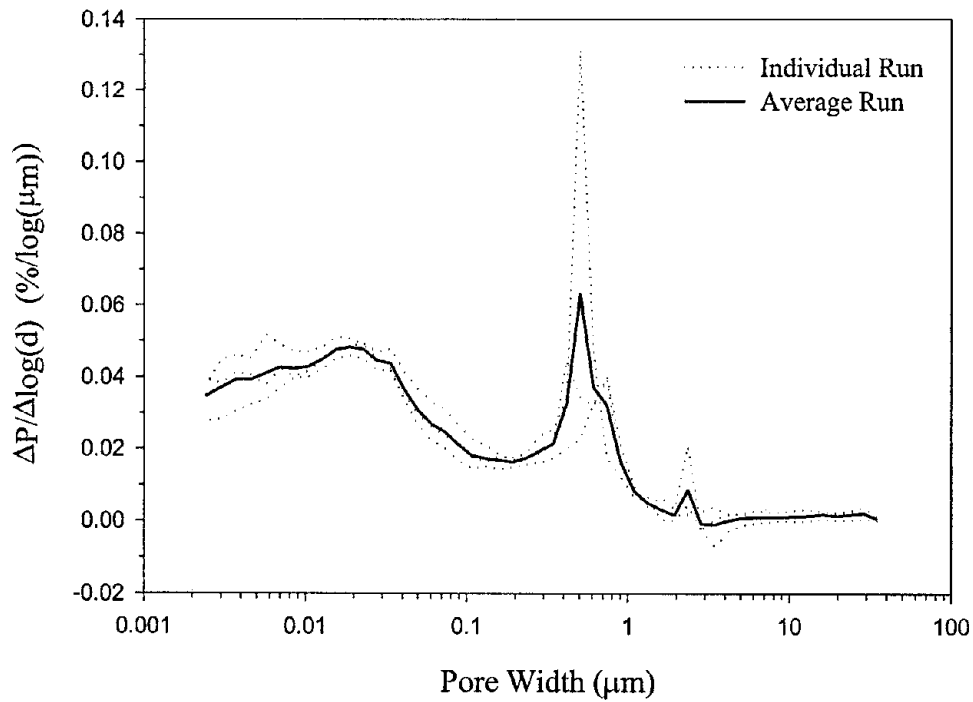
(b)

Figure K-7: MIP results for C(HHH)09: (a) cumulative porosity
vs. pore width; (b) average differential pore size distribution vs. pore width.

136
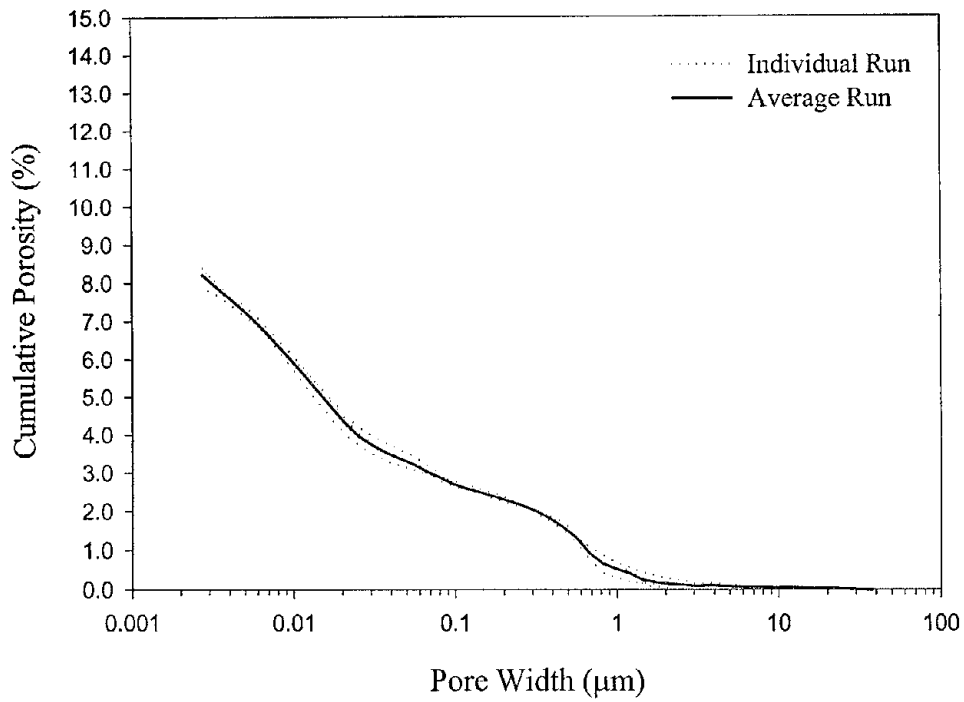
(a)
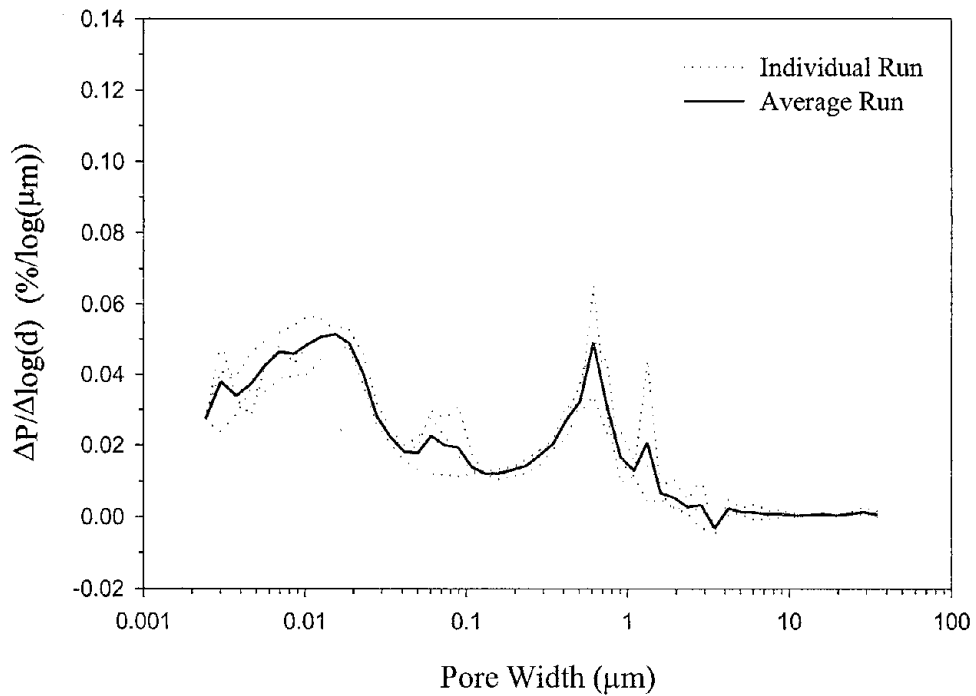
(b)

Figure K-8: MIP results for C(LLL)09: (a) cumulative porosity
vs. pore width; (b) average differential pore size distribution vs. pore width.
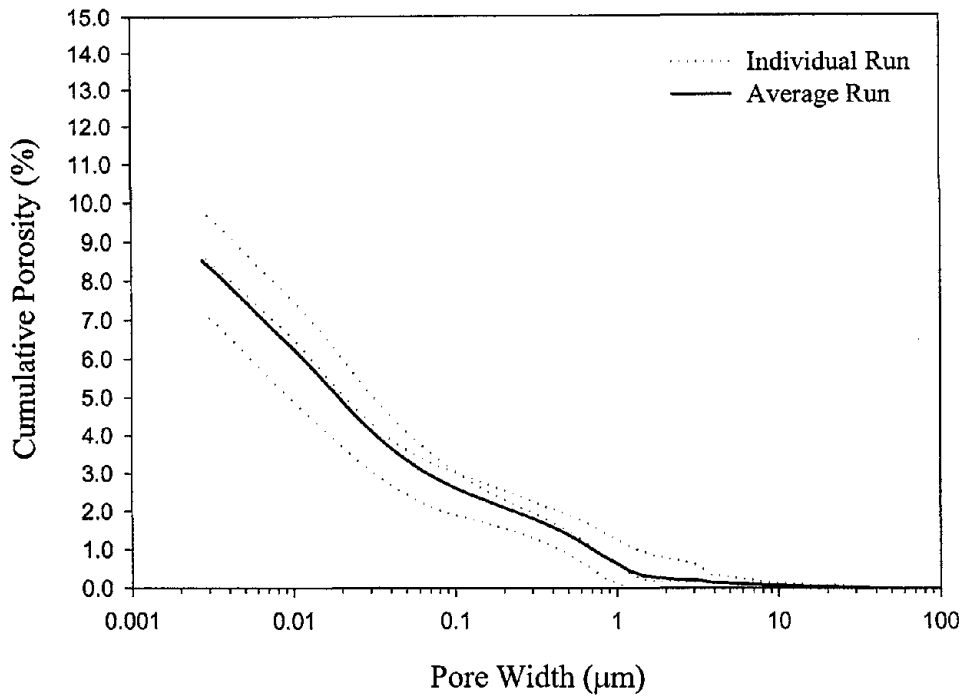
(a)
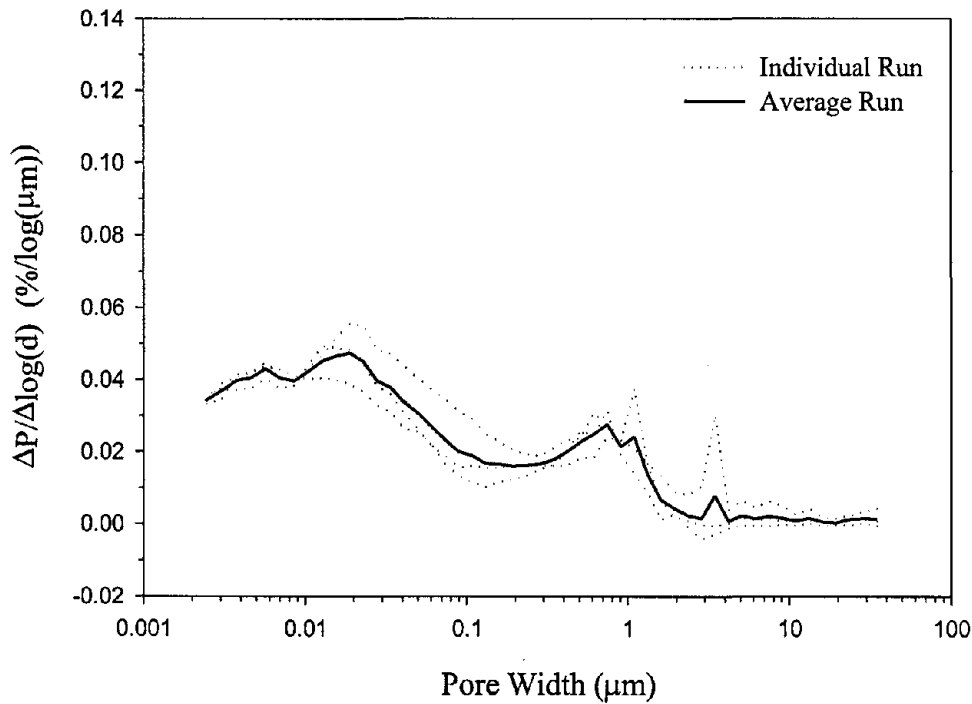
(b)

Figure K-9: MIP results for C(LLL)25: (a) cumulative porosity
vs. pore width; (b) average differential pore size distribution vs. pore width.
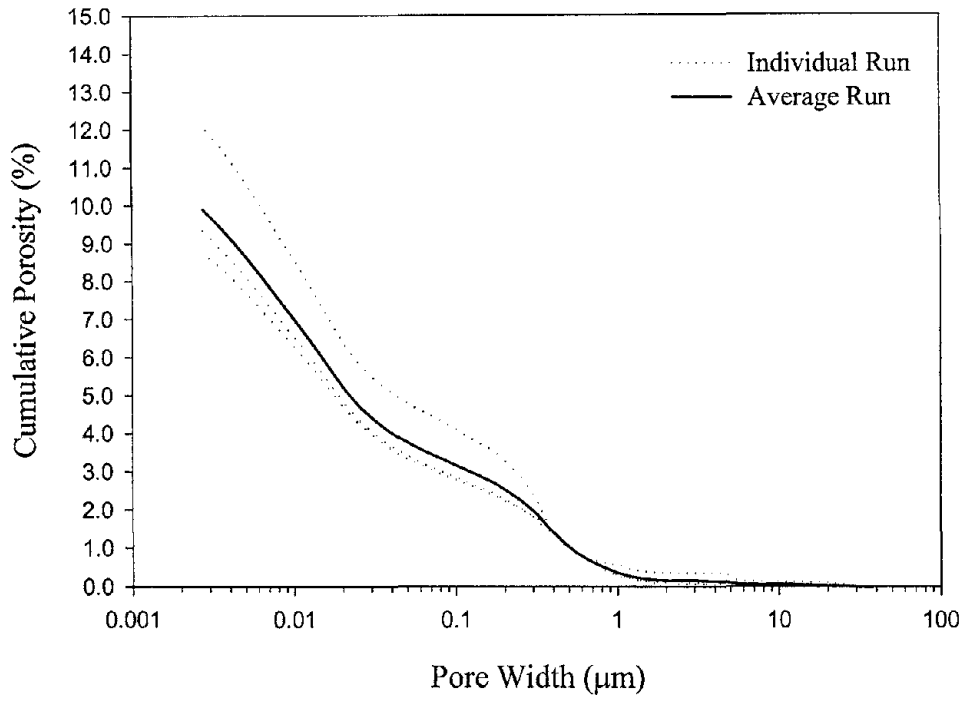
(a)
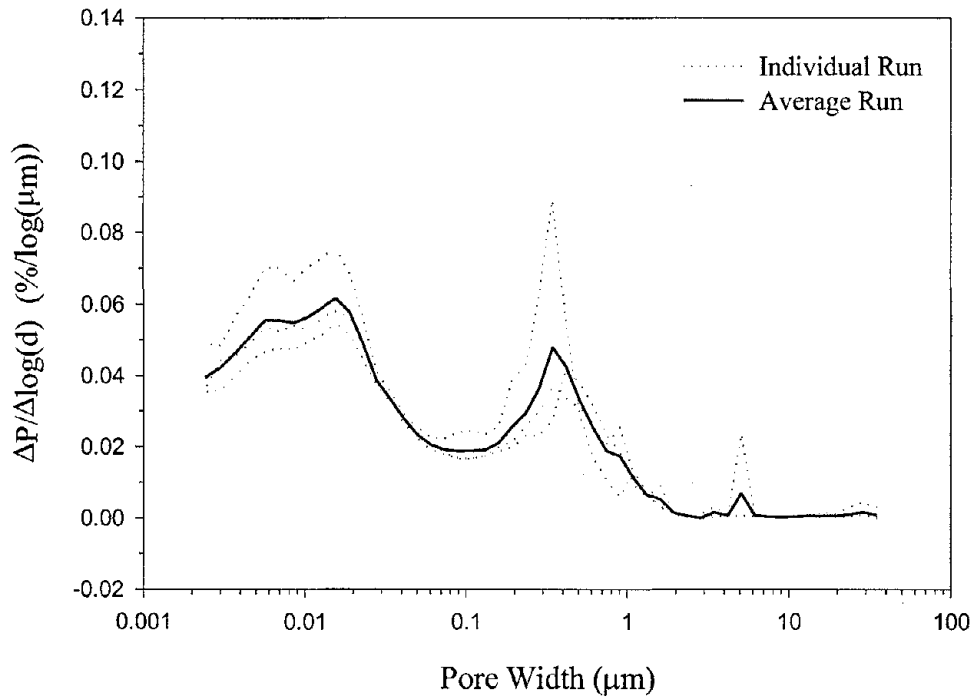
(b)

Figure K-10: MIP results for C(LLL)41: (a) cumulative porosity
vs. pore width; (b) average differential pore size distribution vs. pore width.

Figure K-12: Mg modeling of
the CFA-C prisms.

● Highest Leaching Value ■ Lowest Leaching Value
■ Lowest Leaching Value BDL
[F] – Dolomite   [JJ] – Brucite
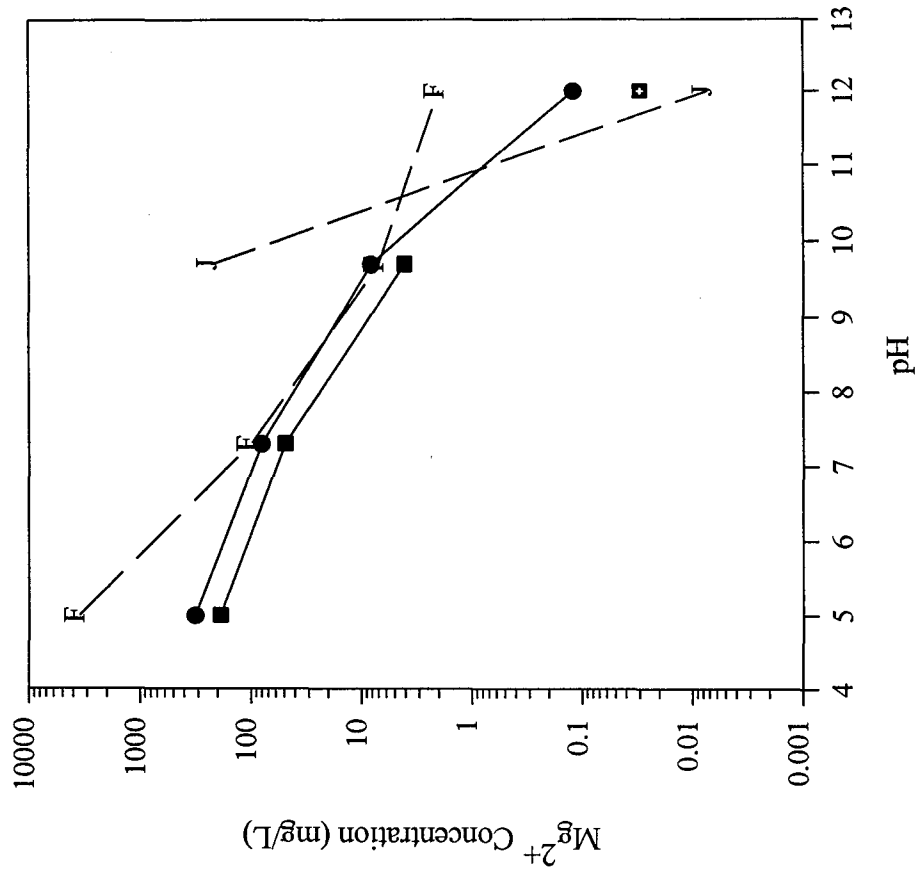
Figure K-11: Ca modeling of
the CFA-C prisms.

● Highest Leaching Value ■ Lowest Leaching Value
[B] – Gypsum [D] – Portlandite [E] – Calcite
[F] – Dolomite [P] – Ettringite [E] and [F] are completely overlapped

140

Figure K-14: Si modeling of
the CFA-C prisms.

● Highest Leaching Value   ■ Lowest Leaching Value
[C] – Quartz   [K] – SiO₂*amorphous
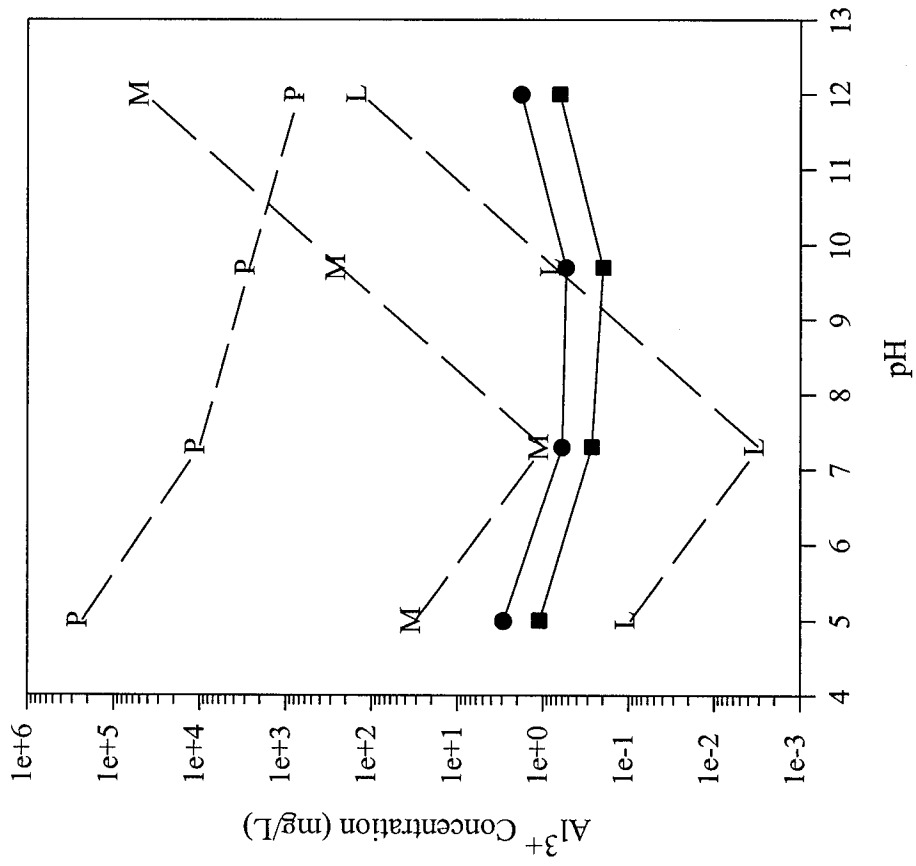
Figure K-13: Al modeling of
the CFA-C prisms.

● Highest Leaching Value   ■ Lowest Leaching Value
[L] – Gibbsite   [M] – Al(OH)₃*amorphous
[P] – Ettringite

141

Figure K-16: Zn modeling of the
CFA-C prisms

● Highest Leaching Value ■ Lowest Leaching Value
[A] – Zincite
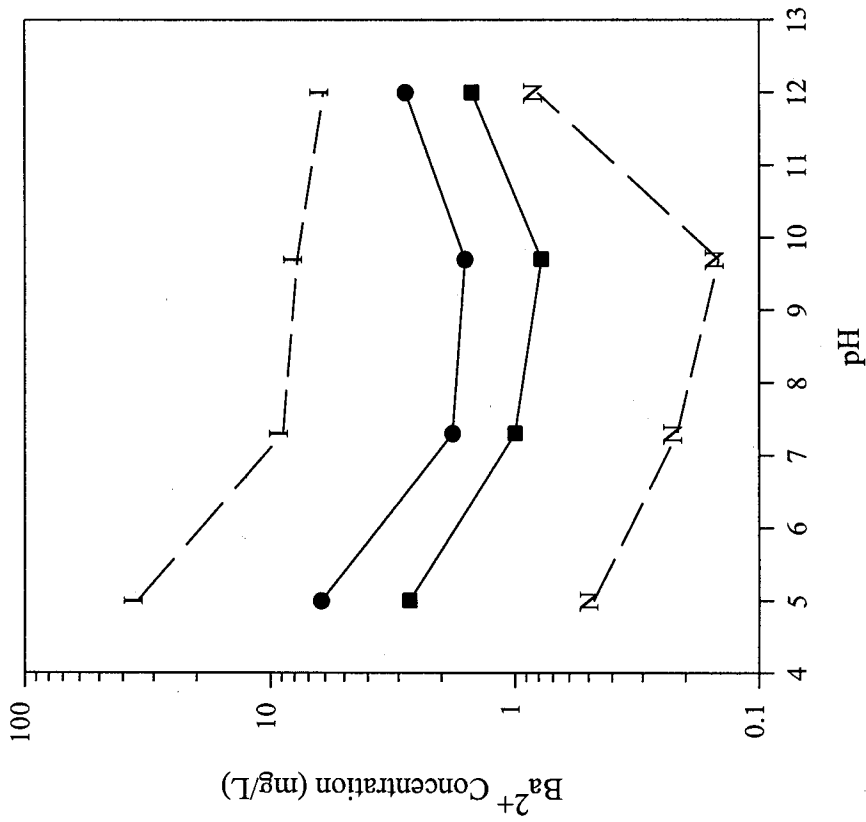
Figure K-15: Ba modeling of the
CFA-C prisms

● Highest Leaching Value ■ Lowest Leaching Value
[I] – BaCrO₄   [N] – Barite

142

Figure K-18: Cr modeling of
the CFA-C prisms.

• Highest Leaching Value ■ Lowest Leaching Value
■ Lowest Leaching Value BDL
[I] – BaCrO$_4$
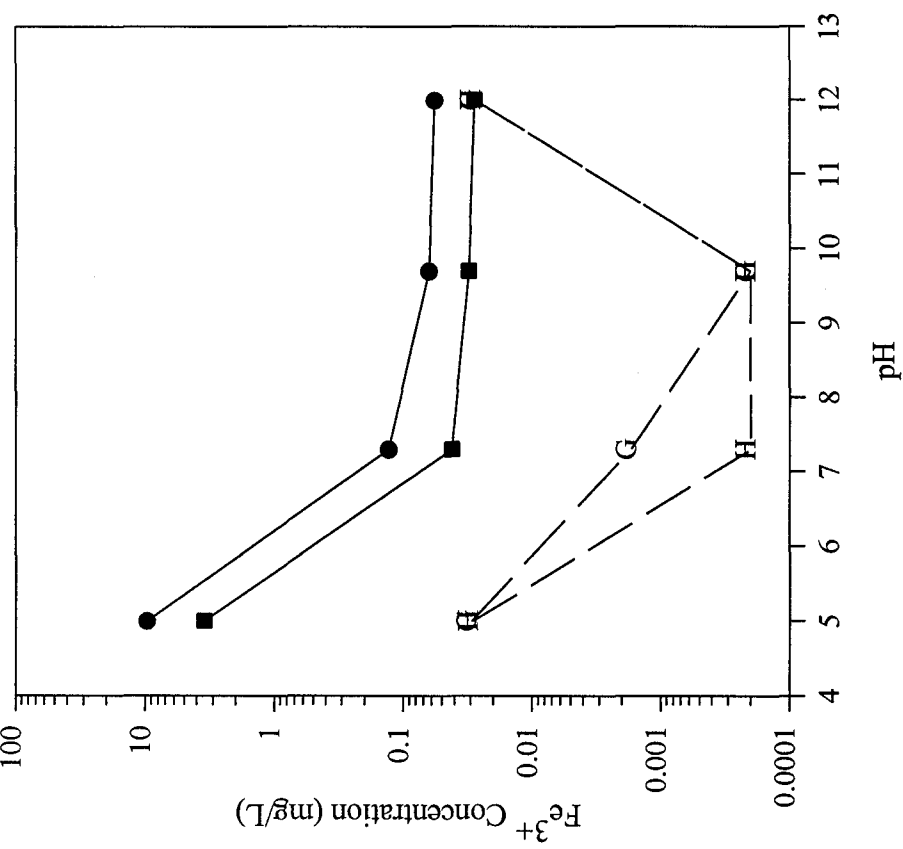
Figure K-17: Fe modeling of
the CFA-C prisms.

• Highest Leaching Value ■ Lowest Leaching Value
[G] – Ferrihydrite [H] – Maghemite

143

Figure K-20: SO_4^{2-} modeling of the CFA-C prisms.

● Highest Leaching Value ■ Lowest Leaching Value
■ Lowest Leaching Value BDL
[N] – Barite [P] – Ettringite
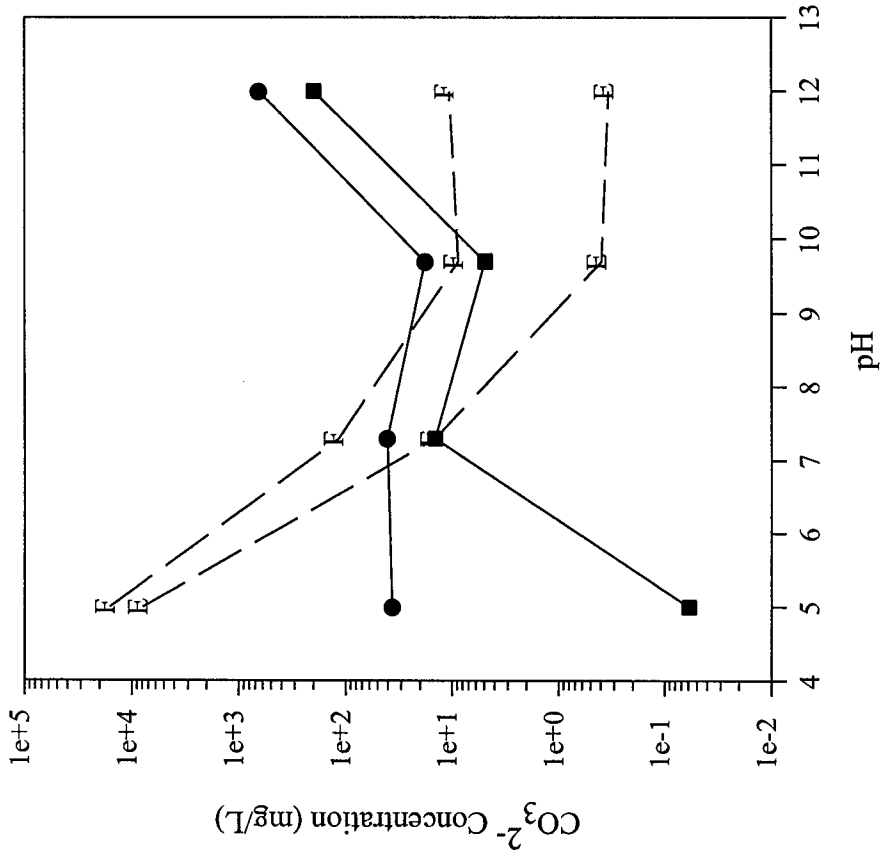
Figure K-19: CO_3^{2-} modeling of the CFA-C prisms.

● Highest Leaching Value ■ Lowest Leaching Value
[E] – Calcite [F] – Dolomite

144
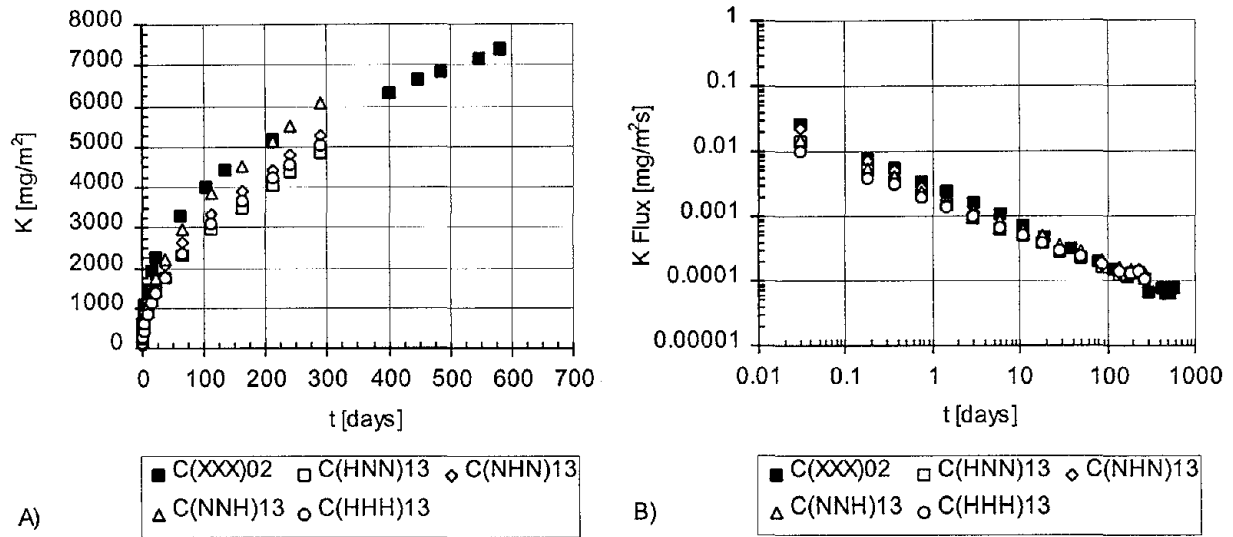
Figure K-21: K release for 28-day cured and high level aged samples.
A) cumulative mass released in mg/m^2; B) flux released in mg/m^{2}s.
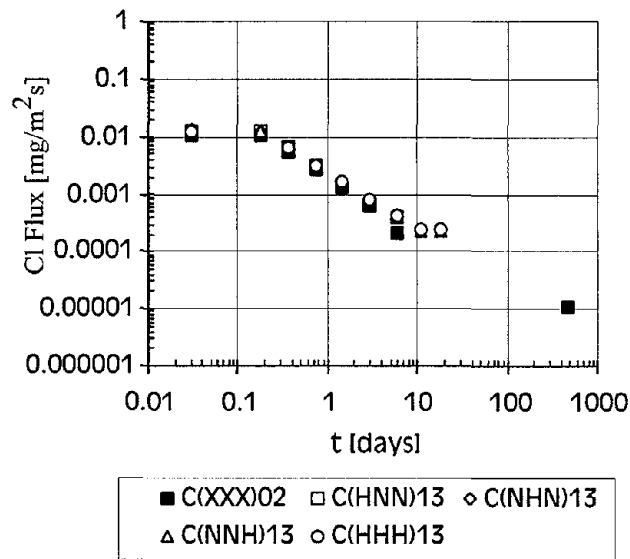
Figure K-22: Cl release for 28-day cured and high level aged samples:
flux released in mg/m^{2}s.
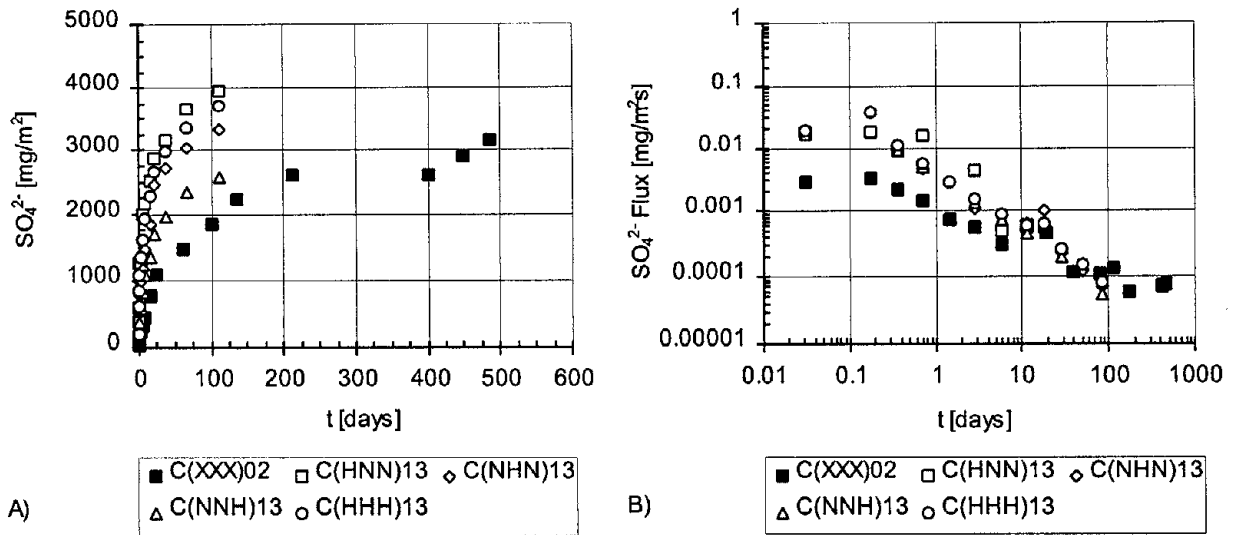
Figure K-23: SO_4^{2-} release for 28-day cured and high level aged samples:
A) cumulative mass released in mg/m^2; B) flux released in mg/m^{2}s.
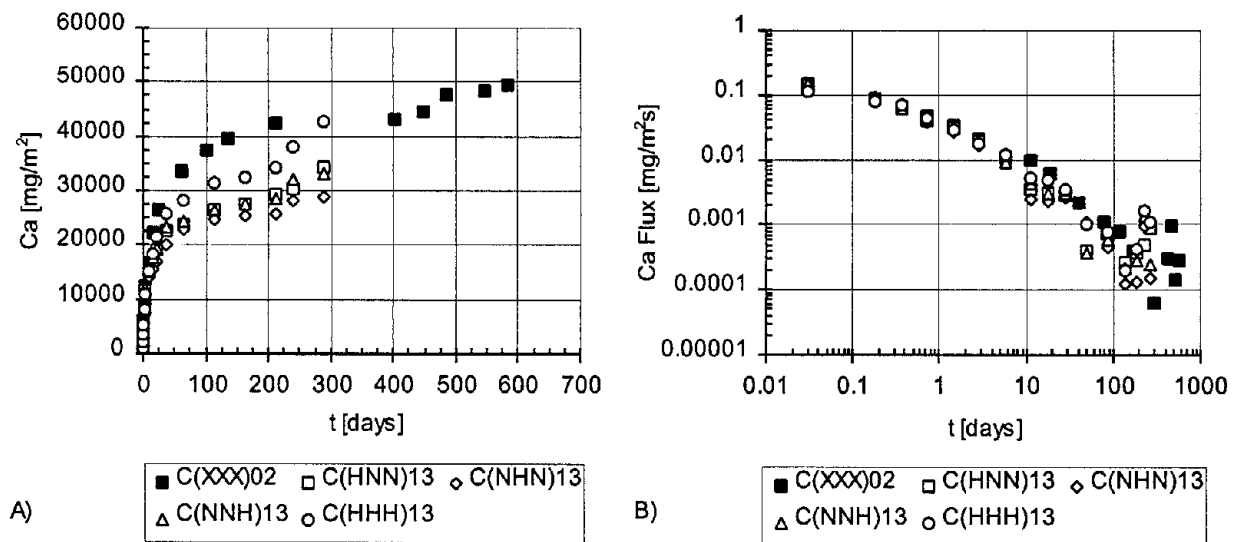
Figure K-24: Ca release for 28-day cured and high level aged samples:
A) cumulative mass released in mg/m^2; B) flux released in mg/m^{2}s.
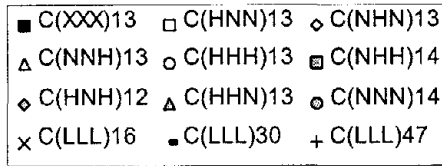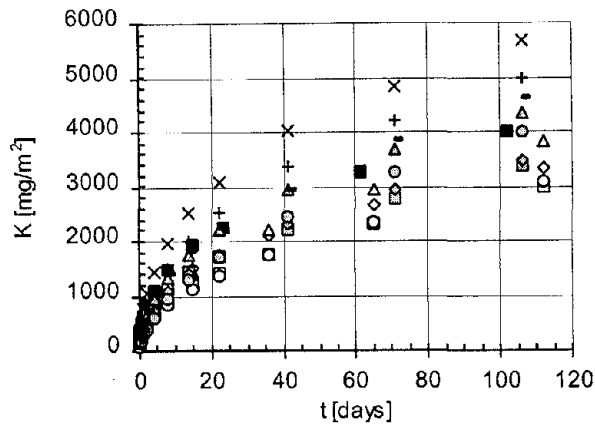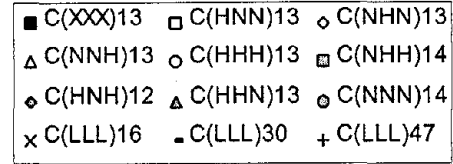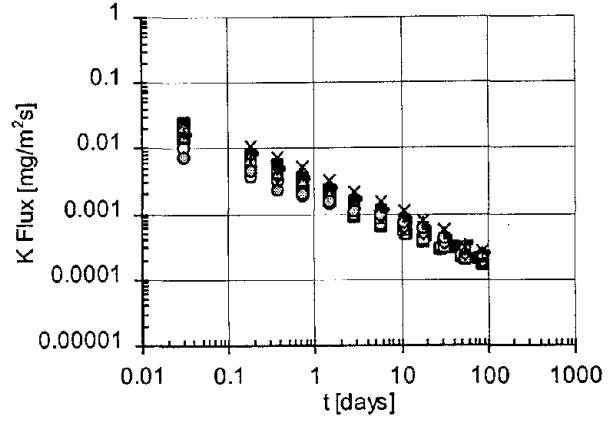
Figure K-25: K release for 28-day cured and aged samples:
A) cumulative mass released in mg/m²; B) flux released in mg/m²s.
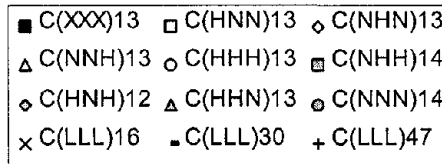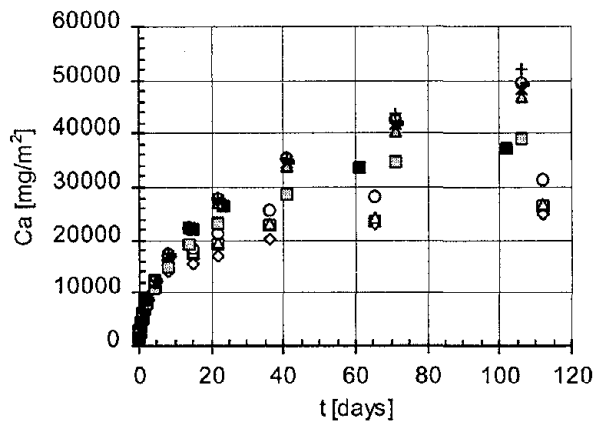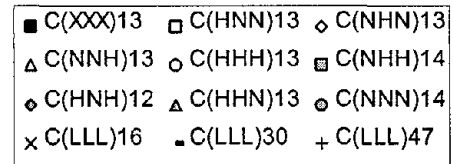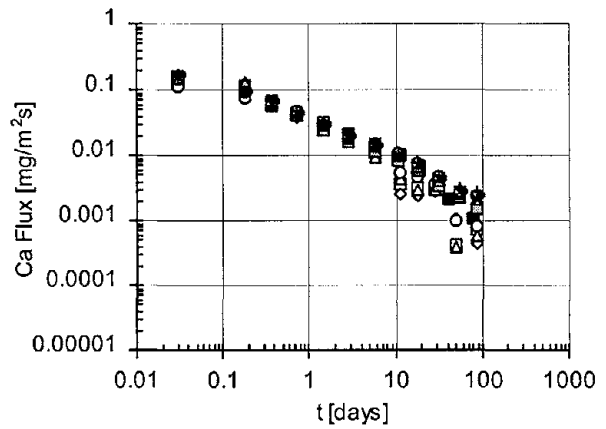
Figure K-26: Ca release for 28-day cured and aged samples:
A) cumulative mass released in mg/m²; B) flux released in mg/m²s.

147

APPENDIX L. CFA-C, CFA-F and PCC CENTER POINT EXPERIMENT DATA

Table L-1: ANOVA for the effects of mixture
on compressive strengths.

Source of variation	Sum of squares	DF	Mean square	F ratio	Significant at
Mix type	9923605	2	4961803	17.7	99%
Error	6715246	24	279802		
Total	16639254	26			

Table L-2: Tukey-Kramer analysis of the compressive
strengths of the three mix types.

Treatment	CFA-C	CFA-F	PCC
Average	4399	3803	2923
CFA-C	± 1325*	596	1476
CFA-F	-596	± 1325*	880
PCC	-1476	-880	± 1325*

*Tukey range at 95.5 percent confidence interval.

Table L-3: ANOVA for crack density results for prism specimens.

Source	SS	df	MS	Computed F
Effect	3.139	2	1.570	9.659
Error	0.975	6	0.163	
Total	4.114	8		

Table L-4: Tukey-Kramer comparison for crack density
center point data.

Mix Type	CFA-C	CFA-F	PCC
CFA-C	1.010	-0.713	-1.447
CFA-F	-0.713	1.010	-0.733
PCC	-1.447	-0.733	1.01

Table L-5: ANOVA for the effect of mixture on RDM.

Source of variation	Sum of squares	DF	Mean square	F ratio	Significant at
Mixture	5083	2	2541.4	15.83	99%
Error	21836	136	160.6		
Total	26919	138	195.1		

Table L-6: Tukey-Kramer analysis of RDM values for the three mixtures.

Treatment	CFA-C	CFA-F	PCC
Average	59.8	64	49.7
CFA-C	-6.33	-4.15	10.16
CFA-F	4.15	-6.19	14.3
PCC	-10.16	-14.3	-6.19

Table L-7: CFA-C, CFA-F, and PCC low treated concrete porosity ANOVA.

Source of variation	Sum of squares	DF	Mean square	F ratio	Significant at
Mixture	0.4	2	0.198	0.347	–
Error	3.42	6	0.57		
Total	3.81	8			

Table L-8: CFA-C, CFA-F, and PCC low treated concrete first peak uniformity indicator ANOVA.

Source of variation	Sum of squares	DF	Mean square	F ratio	Significant at
Mixture	0	2	0	0.944	–
Error	0.0001	6	0		
Total	0.0002	8			

Table L-9: CFA-C, CFA-F, and PCC low treated concrete
first peak average weighted threshold pore width ANOVA.

Source of variation	Sum of squares	DF	Mean square	F ratio	Significant at
Mixture	0.0961	2	0.048	2.29	–
Error	0.1261	6	0.021		
Total	0.222	8			

Table L-10: CFA-C, CFA-F, and PCC low treated concrete
second peak uniformity indicator ANOVA.

Source of variation	Sum of squares	DF	Mean square	F ratio	Significant at
Mixture	0	2	0	11.48	99%
Error	0	6	0		
Total	0	8			

Table L-11: CFA-C, CFA-F, and PCC low treated concrete
second peak average weighted threshold pore width ANOVA.

Source of variation	Sum of squares	DF	Mean square	F ratio	Significant at
Mixture	0.0001957	2	0.0001	4612	99%
Error	0	6	0		
Total	0.0001958	8			

Table L-12: CFA-C, CFA-F, and PCC low treated concrete
first peak threshold pore width ANOVA.

Source of variation	Sum of squares	DF	Mean square	F ratio	Signficant at
Mixture	0.1986	2	0.0993	1.359	–
Error	0.438	6	0.073		
Total	0.637	8			

Table L-13: CFA-C, CFA-F, and PCC low treated concrete
second peak threshold pore width ANOVA.

Source of variation	Sum of squares	DF	Mean square	F ratio	Signficant at
Effect	0	2	0.00017	2.97	–
Error	0	6	0.0001		
Total	0.001	8			

Table L-14: Tukey-Kramer analysis of CFA-C,
CFA-F, and PCC low treated concrete second peak uniformity indicator.

Treatment	CFA-C	CFA-F	PCC
Average	0.00377	0.00912	0.00279
CFA-C	± 0.00436*	-0.0054	0.001
CFA-F	0.00535	± 0.00436*	0.00633
PCC	-0.001	-0.0063	± 0.00436*

* Tukey range at 95.5 percent confidence interval

Table L-15: Tukey-Kramer analysis of CFA-C,
CFA-F, and PCC low treated concrete weighted average threshold pore width.

Treatment	CFA-C	CFA-F	PCC
Average	0.01174	0.00614	0.01756
CFA-C	± 0.000365*	0.0056	-0.00582
CFA-F	0.0056	± 0.000365*	-0.01142
PCC	-0.00582	-0.01142	± 0.000365*

* Tukey range at 95.5 percent confidence interval

Table L-16: Qualitative comparison between the second peaks of intrusion for the low treatment
samples*.

Mix	Uniformity indicator	Weighted average threshold pore width
CFA-C	Low	Medium
CFA-F	High	Low
PCC	Low	High

*Differences are significant at the 95 percent confidence level

Table L-17: Summary of the effects on the second peak of
intrusion for the CFA-C concrete.

Source	Uniformity indicator	Confidence level	Weighted average threshold pore width	Confidence level
AA	Decrease	95%	Increase	98.5%
CL	None		None	
FT	Decrease	95%	Decrease	98.5%
AAxCL	None		Decrease	98.5%
AAxFT	None		None	
CLxFT	None		Increase	95%
AAxCLxFT	None		Increase	98.5%

Table L-18: CFA-C concrete BET-N_2 surface area ANOVA.

Source	Effect	Sum of squares (SS)	Degrees of freedom (v)	Mean square	F-statistic	Tabular F-values 99%	95%
AA	0.648	0.8	1	0.839	0.063	98.5	18.51
CL	-1.003	2.0	1	2.010	0.152	98.5	18.51
FT	1.048	2.2	1	2.195	0.166	98.5	18.51
AAxCL	3.603	26.0	1	25.956	1.958	98.5	18.51
AAxFT	1.403	3.9	1	3.934	0.297	98.5	18.51
CLxFT	3.453	23.8	1	23.840	1.798	98.5	18.51
AAxCLxFT	3.178	20.2	1	20.193	1.523	98.5	18.51
Curvature		1.4	1	1.409	0.106	98.5	18.51
Pure error		26.5	2	13.257			
Total		106.9	10				

153

Table L-19: CFA-C, CFA-F and PCC low treated concrete BET-N_2
surface area ANOVA.

Source of variation	Sum of squares	Degrees of freedom	Mean square	F-statistic	Tabular F-values 99%	95%
Effect	30.9	2	15.47	2.81	10.92	5.14
Error	33.0	6	5.50			
Total	63.9	8				

Table L-20: Total elemental composition (+/- standard deviation)
of major elements of three types of experimental prisms (>10,000 ppm).

Element	PCC	CFA-C	CFA-F
Al	17,260 +/- 320	18,200 +/- 340	20,090 +/- 380
Ca	379,800 +/- 47,800	363,900 +/- 45,800	374,200 +/- 47,200
Si	139,400 +/- 7,400	140,500 +/- 7,500	99,300 +/- 6100

Table L-21: Total elemental composition (+/- standard deviation) of
minor elements of three types of experimental prisms   (1,000 - 10,000 ppm).

Element	PCC	CFA-C	CFA-F
Fe	6,572 +/- 203	9,075 +/- 275	5,908 +/- 181
K	4,114 +/- 106	3,144 +/- 83	3,339 +/- 84
Na	3,892 +/- 58	3,771 +/- 57	3,242 +/- 49
S	4,940 +/- 20	3,801 +/- 18	4,415 +/- 21

Table L-22: Total element composition (+/- standard deviation) of trace elements of three types of experimental prisms (<1,000 ppm).

Element		PCC		CFA-C		CFA-F
Ag	<[1]	0.9	<	1	<	1
As		1.76 +/- 0.13		0.87 +/- 0.1		1.2 +/- 0.13
Au	<	2	<	2	<	2
Ba		240.49 +/- 15.82		138.38 +/- 9.28		175.79 +/- 13.45
Br	<	0.34	<	0.34		0.52 +/- 0.19
Cd	<	3.11	<	2.85	<	2.63
Ce		14.58 +/- 0.78		17.46 +/- 0.92		17.01 +/- 0.89
Cl		110.38 +/- 15.59		119.58 +/- 10.8		102.14 +/- 16.66
Co		2.24 +/- 0.12		4.65 +/- 0.24		3.81 +/- 0.2
Cr		15.94 +/- 0.61		278.71 +/- 7.2		15.52 +/- 0.58
Cs		0.32 +/- 0.05		0.4 +/- 0.1		0.46 +/- 0.05
Cu		18.5 +/- 1.5		14 +/- 1.4		8.3 +/- 1.3
Dy		0.98 +/- 0.1		0.67 +/- 0.1		0.84 +/- 0.09
Eu		0.28 +/- 0.02		0.32 +/- 0		0.35 +/- 0.02
Hf		2.62 +/- 0.15		0.97 +/- 0.1		3 +/- 0.17
Hg	<	1	<	1	<	1
I		4.15 +/- 1.67		3.99 +/- 1.66		5.06 +/- 1.98
In		0.05 +/- 0.02	<	0.06	<	0.06
La		6.74 +/- 0.12		6.16 +/- 0.11		7.15 +/- 0.11
Lu		0.1 +/- 0.01		0.08 +/- 0		0.1 +/- 0.01
Mg		858 +/- 326	<	230		684 +/- 84
Mn		161.83 +/- 2.13		37.77 +/- 0.51		172.15 +/- 2.26
Mo	<	2	<	1	<	3
Nd		8.52 +/- 1.11		8.59 +/- 1.02		8.33 +/- 0.83
Ni	<	1		0.8 +/- 0.1		64.1 +/- 1.5
P	<	100	<	100	<	100
Pb		8.5 +/- 2.1		13.3 +/- 2.2		6.7 +/- 2
Rb		14.4 +/- 1.8		18.67 +/- 2.03		17.74 +/- 1.97
Sb	<	0.05		0.45 +/- 0.1		0.28 +/- 0.05
Sc		1.77 +/- 0.09		2.18 +/- 0.11		2.31 +/- 0.11
Se	<	0.38	<	0.31		0.51 +/- 0.14
Sm		0.99 +/- 0.02		0.89 +/- 0.01		1.00 +/- 0.01
Sr		229.91 +/- 17.91		221.18 +/- 11.1		123.18 +/- 10.05
Ta		0.08 +/- 0.02		0.08 +/- 0		0.08 +/- 0.02
Tb		0.12 +/- 0.02		0.09 +/- 0		0.15 +/- 0.02
Th		2.29 +/- 0.12		2.57 +/- 0.14		2.45 +/- 0.13
Ti	<	609.12	<	544.08	<	548.93
U		0.72 +/- 0.20		0.37 +/- 0.13		0.39 +/- 0.12
V		8.42 +/- 1.71	<	4.14		15.64 +/- 1.82
W	<	2	<	1	<	2
Yb	<	0.69	<	0.6		1.52 +/- 0.32
Zn		15.2 +/- 1.3		18 +/- 1.3		17.3 +/- 1.3
Zr		45.2 +/- 9.2		20.9 +/- 7.2		41.5 +/- 8.4

1 < denotes detection limit

155

Table L-23: ANOVA of albite concentration in the three
types of concrete mixes.

Source	SS	df	MS	Computed F	Significant at
Effect	1.372	2	0.686	0.18	none
Error	91.716	24	3.821		
Total	93.087	26			

Table L-24: ANOVA of calcite concentration in the three
types of concrete mixes.

Source	SS	df	MS	Computed F	Significant at
Effect	25.992	2	12.996	0.68	none
Error	458.249	24	19.094		
Total	484.241	26			

Table L-25: ANOVA of ettringite concentration in the
three types of concrete mixes.

Source	SS	df	MS	Computed F	Significant at
Effect	0.909	2	0.454	0.98	none
Error	11.178	24	0.466		
Total	12.087	26			

Table L-26: ANOVA of gypsum concentration in the three
types of concrete mixes.

Source	SS	df	MS	Computed F	Significant at
Effect	0.349	2	0.174	4.77	>95%
Error	0.878	24	0.037		
Total	1.227	26			

Table L-27: ANOVA of portlandite concentration in the three
types of concrete mixes.

Source	SS	df	MS	Computed F	Significant at
Effect	3.681	2	1.840	4.41	>95%
Error	10.016	24	0.417		
Total	13.696	26			

Table L-28: ANOVA of quartz concentration in the three
types of concrete mixes.

Source	SS	df	MS	Computed F	Significant at
Effect	18.299	2	9.149	1.36	none
Error	161.684	24	6.737		
Total	179.983	26			

Table L-29: Tukey-Kramer analysis of gypsum concentration in the
three types of concrete mixes.

Mix type	CFA-C	CFA-F	PCC
CFA-C	-0.225	0.122	0.278
CFA-F	-0.122	-0.225	0.156
PCC	-0.278	-0.156	-0.225

Table L-30: Tukey-Kramer analysis of portlandite concentration in the
three types of concrete mixes.

Mix type	CFA-C	CFA-F	PCC
CFA-C	-0.760	0.300	-0.589
CFA-F	-0.300	-0.760	-0.889
PCC	0.589	0.889	-0.76

Table L-31: ANOVA for the leaching of Ca in
three types of concrete at pH = 12.0.

Source	SS	df	MS	Computed F	Significant at
Effect	4.933E+05	2	2.466E+05	16.10	>99%
Error	9.193E+04	6	1.532E+04		
Total	5.852E+05	8			

Table L-32: ANOVA for the leaching of Al in
three types of concrete at pH = 12.0.

Source	SS	df	MS	Computed F	Significant at
Effect	2.468	2	1.234	19.06	>99%
Error	0.389	6	0.065		
Total	2.857	8			

Table L-33: ANOVA for the leaching of Si in
three types of concrete at pH = 12.0.

Source	SS	df	MS	Computed F	Significant at
Effect	3.469	2	1.734	8.48	>95%
Error	1.227	6	0.204		
Total	4.696	8			

Table L-34: ANOVA for the leaching of SO_4^{2-} in
three types of concrete at pH = 12.0.

Source	SS	df	MS	Computed F	Significant at
Effect	58.296	2	29.148	0.82	none
Error	214.367	6	35.728		
Total	272.662	8			

Table L-35: ANOVA of Na cumulative release at 22 days of
leaching for the three types of concrete.

Source	SS	df	MS	Computed F	Significant at
Effect	7000000	2	3470000	33.4	>99.9%
Error	600000	6	104000		
Total	8000000	8			

Table L-36: ANOVA of K cumulative release at 22 days of
leaching for the three types of concrete.

Source	SS	df	MS	Computed F	Significant at
Effect	400000	2	213000	0.5	none
Error	2000000	6	391000		
Total	3000000	8			

Table L-37: ANOVA of Ca cumulative release at 22 days of
leaching for the three types of concrete.

Source	SS	df	MS	Computed F	Significant at
Effect	900000000	2	430000000	15.5	>99%
Error	200000000	6	27800000		
Total	1000000000	8			

Table L-38: ANOVA of Na observed diffusivities for the
three types of concrete.

Source	SS	df	MS	Computed F	Significant at
Effect	3.00000e-22	2	1.450000e-22	2.2	75%
Error	4.00000e-22	6	6.680000e-23		
Total	7.00000e-22	8			

Table L-39: ANOVA of K observed diffusivities for
the three types of concrete.

Source	SS	df	MS	Computed F	Significant at
Effect	2.00000e-24	2	9.220000e-25	1.4	none
Error	4.00000e-24	6	6.780000e-25		
Total	6.00000e-24	8			

Table L-40: ANOVA of Ca observed diffusivities for
the three types of concrete.

Source	SS	df	MS	Computed F	Significant at
Effect	8.00000e-27	2	3.890000e-27	13.6	>99%
Error	2.00000e-27	6	2.850000e-28		
Total	9.00000e-27	8			

Table L-41: Turkey-Kramer analysis of Na cumulative release at
22 days of leaching for the three types of concrete.

Mix Type	CFA-C	CFA-F	PCC
CFA-C	807	1910	1810
CFA-F	1910	807	-90.4
PCC	1810	-90.4	807

Table L-42: Turkey-Kramer analysis of K cumulative release at
22 days of leaching for the three types of concrete.

Mix Type	CFA-C	CFA-F	PCC
CFA-C	1570	-24.2	449
CFA-F	-24.2	1570	474
PCC	449	474	1570

Table L-43: Turkey-Kramer analysis of Ca cumulative release at
22 days of leaching for the three types of concrete mixes.

Mix Type	CFA-C	CFA-F	PCC
CFA-C	13200	4550	-18100
CFA-F	4550	13200	-22600
PCC	-18100	-22600	13200

Table L-44: Turkey-Kramer analysis of Na observed diffusivities
for the three types of concrete.

Mix Type	CFA-C	CFA-F	PCC
CFA-C	0	0	0
CFA-F	0	0	0
PCC	0	0	0

Table L-45: Turkey-Kramer analysis of K observed diffusivities
for the three types of concrete.

Mix Type	CFA-C	CFA-F	PCC
CFA-C	0	0	0
CFA-F	0	0	0
PCC	0	0	0

Table L-46: Turkey-Kramer analysis of Ca observed diffusivities
for the three types of concrete mixes.

Mix Type	CFA-C	CFA-F	PCC
CFA-C	0	0	0
CFA-F	0	0	0
PCC	0	0	0
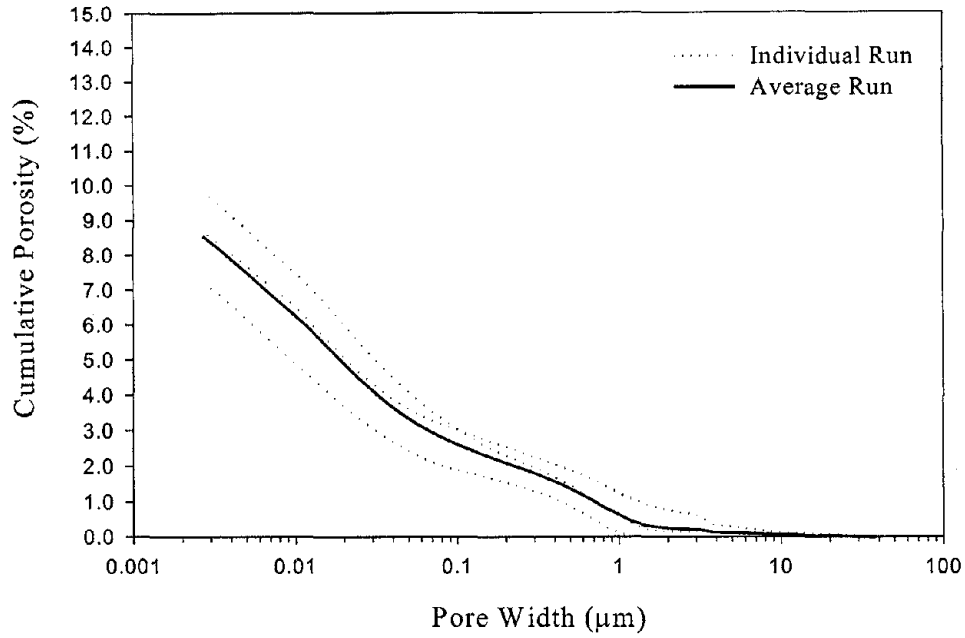
(a)
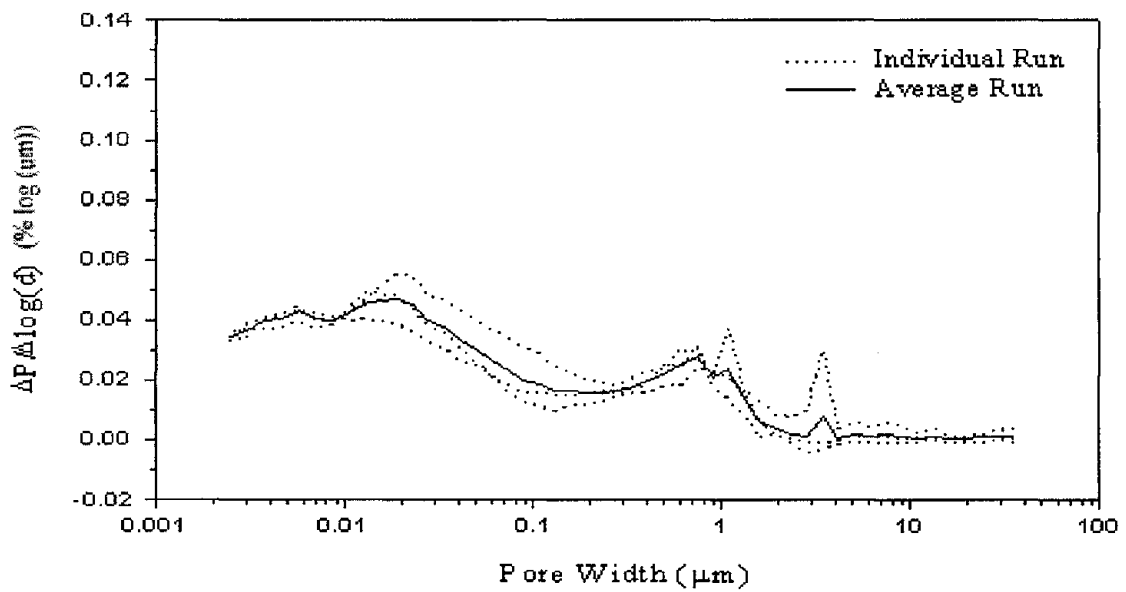
(b)

Figure L-1: MIP results for C(LLL)25: (a) cumulative porosity
vs. pore width; (b) average differential pore size distribution vs. pore width.

(a)

(b)
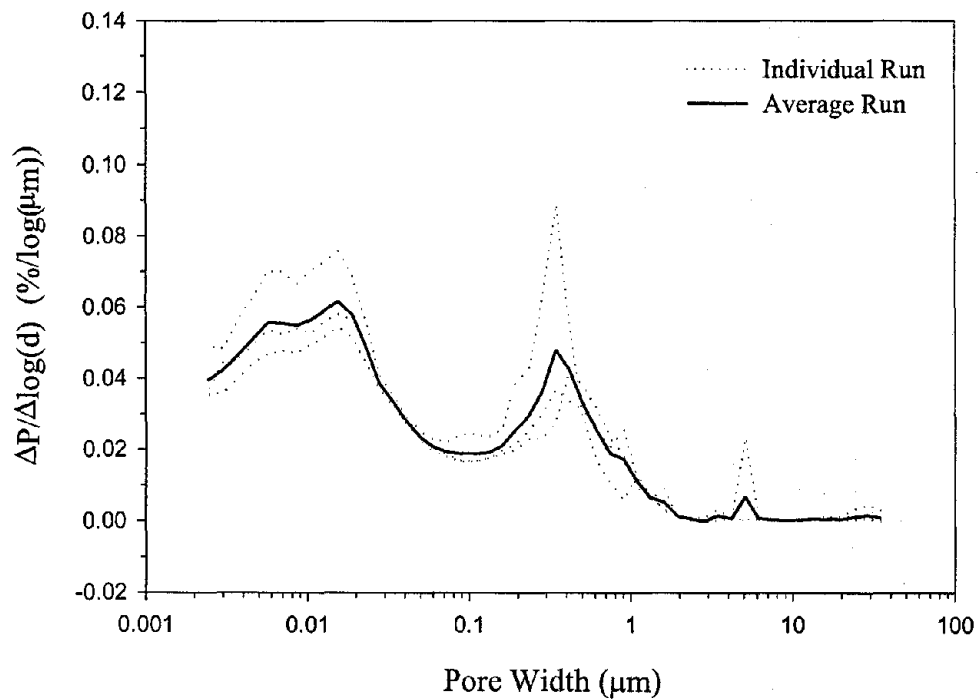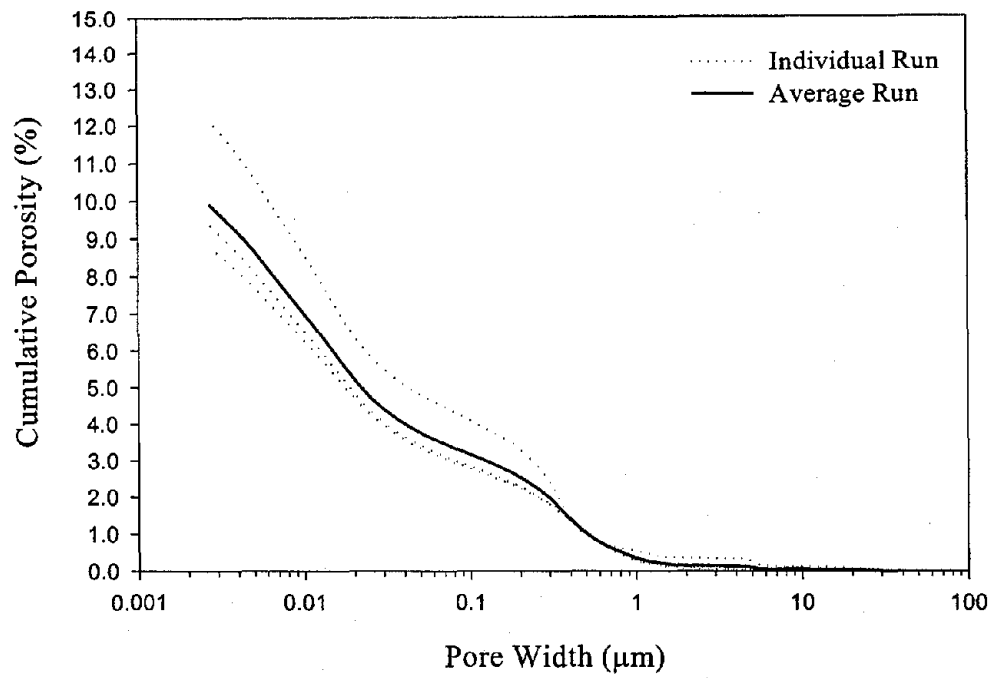
Figure L-2: MIP results for C(LLL)41: (a) cumulative porosity vs.
pore width; (b) average differential pore size distribution vs. pore width.
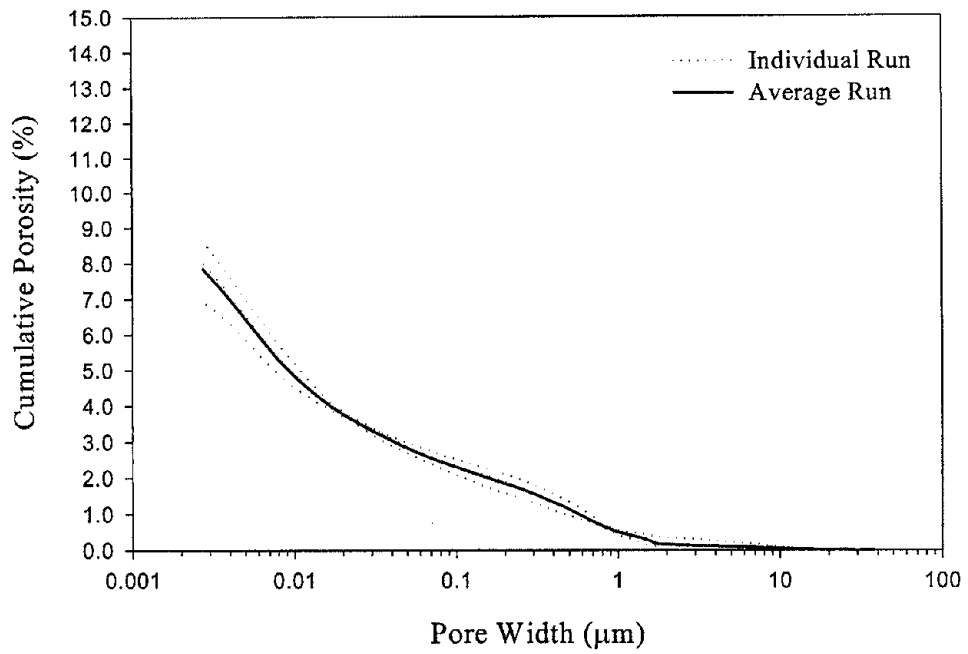
(a)
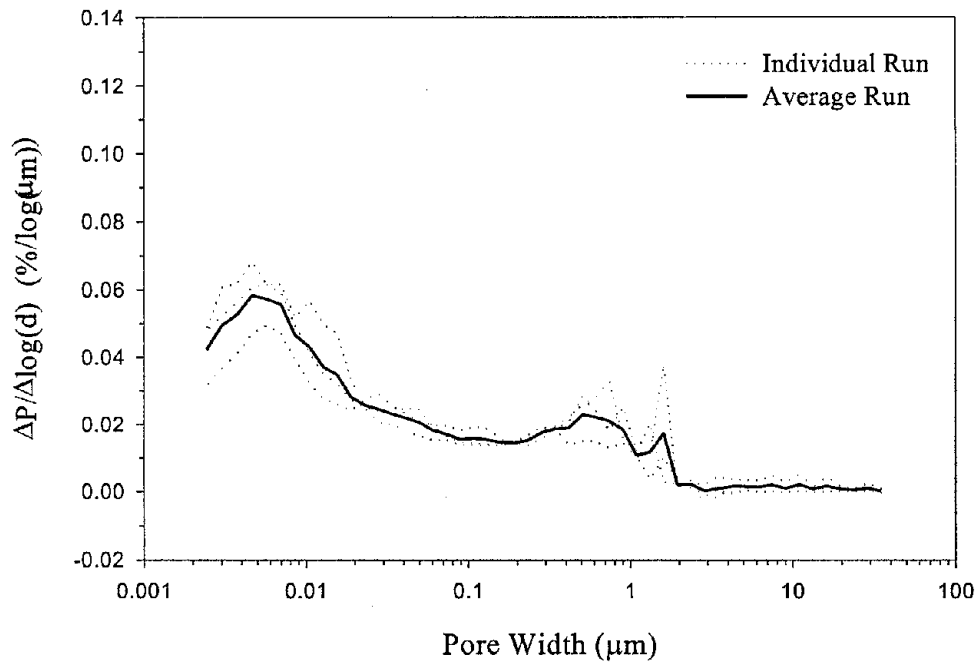
(b)

Figure L-3: MIP results for F(LLL)09: (a) cumulative porosity
vs. pore width; (b) average differential pore size distribution vs. pore width.
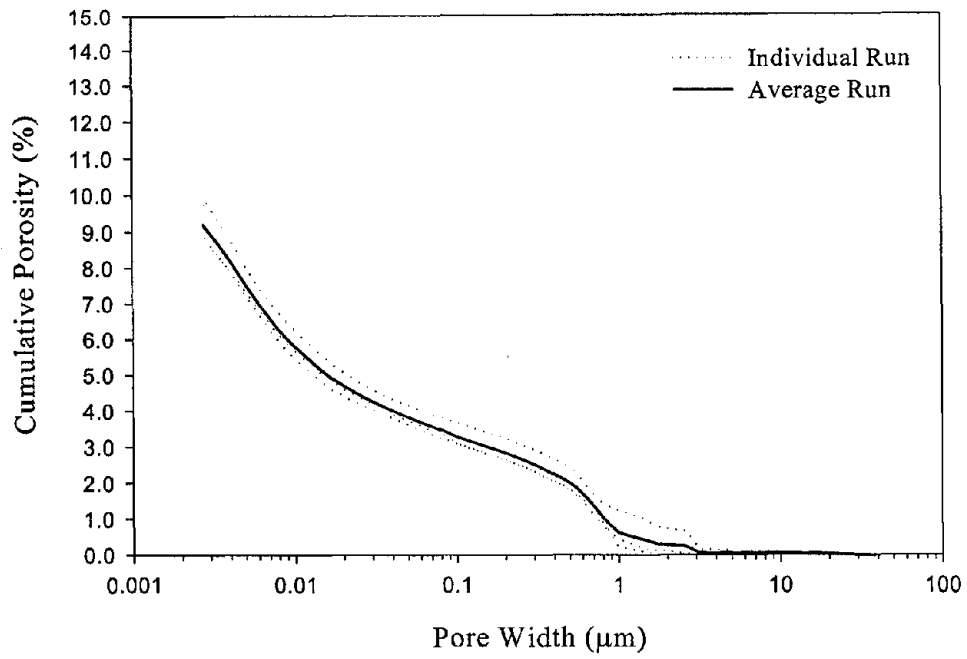
(a)
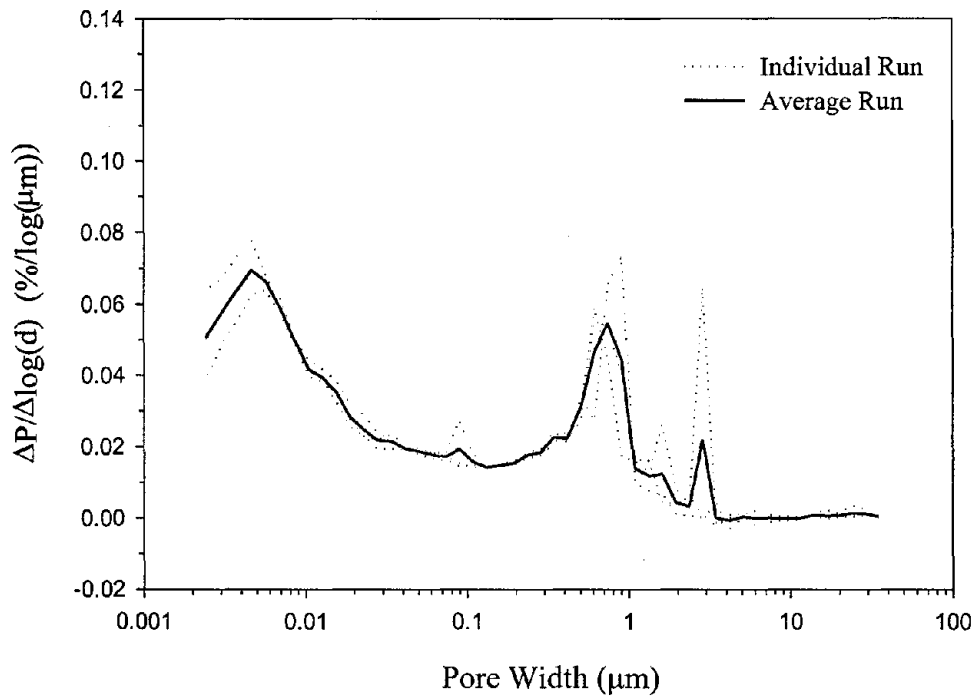
(b)

Figure L-4: MIP results for F(LLL)25: (a) cumulative porosity
vs. pore width; (b) average differential pore size distribution vs. pore width.
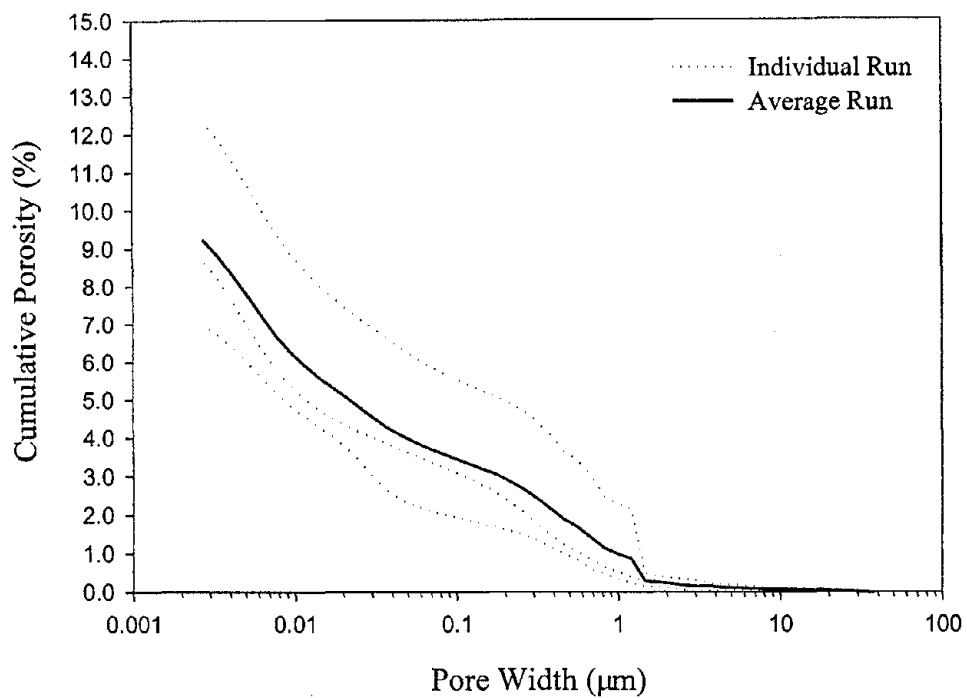
(a)
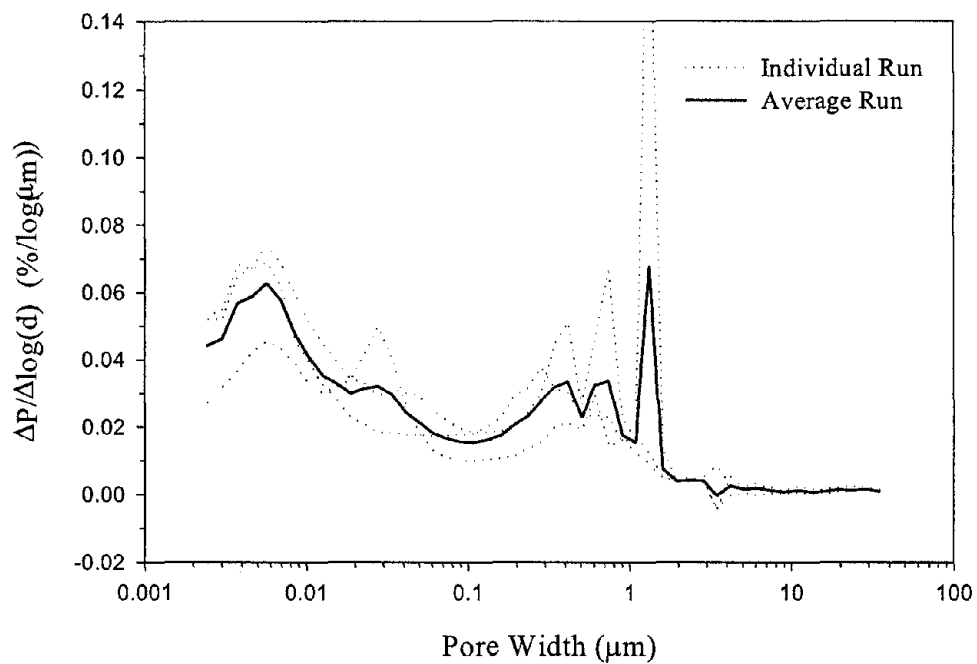
(b)

Figure L-5: MIP results for F(LLL)41:(a) cumulative porosity
vs. pore width; (b) average differential pore size distribution vs. pore width.
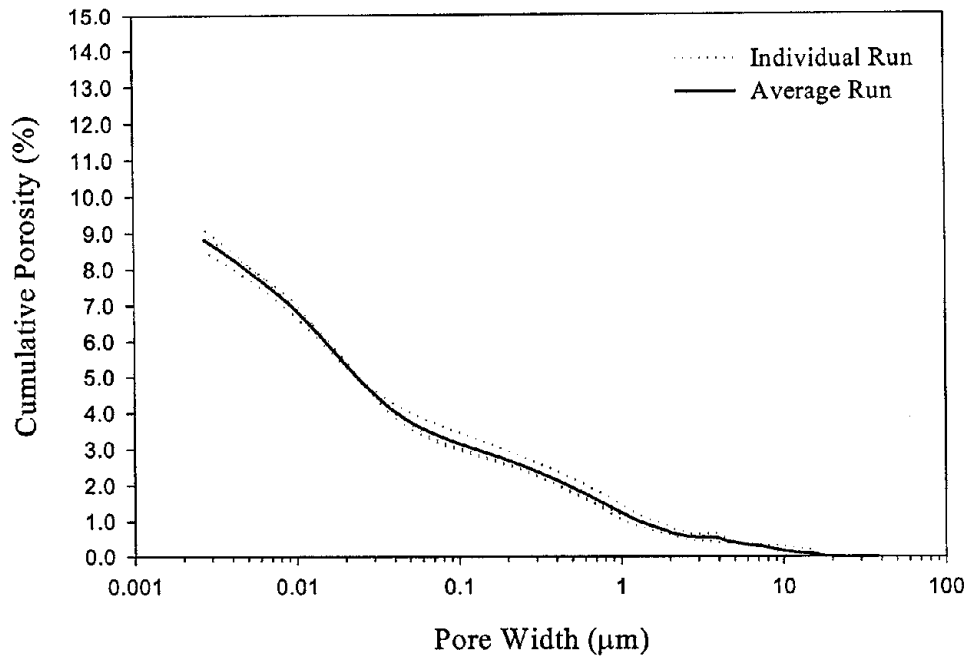
(a)
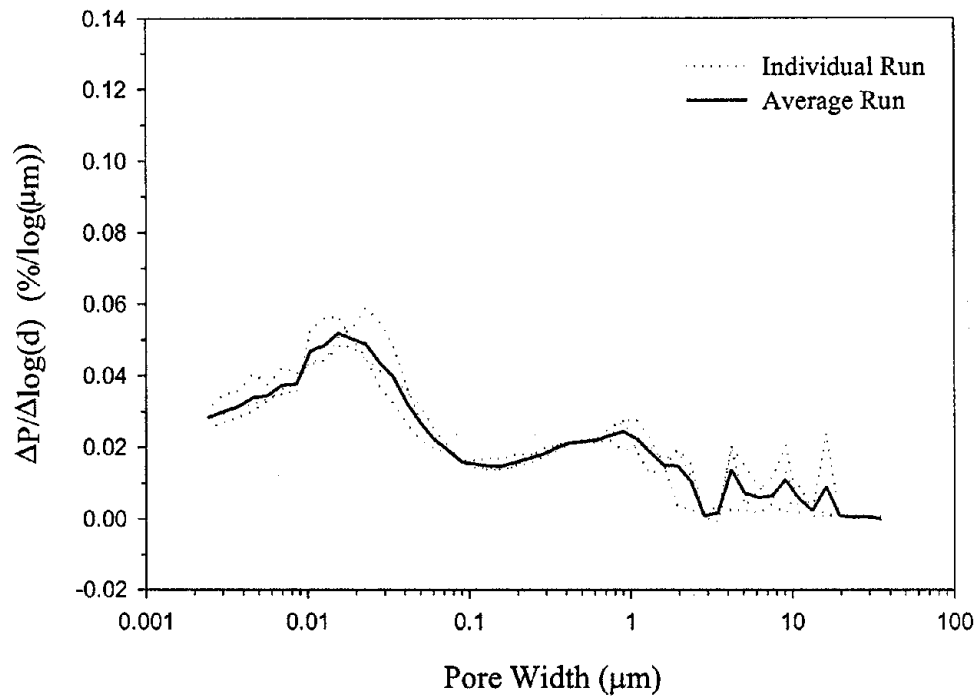
(b)

Figure L-6: MIP results for P(LLL)09: (a) cumulative porosity
vs. pore width; (b) average differential pore size distribution vs. pore width.
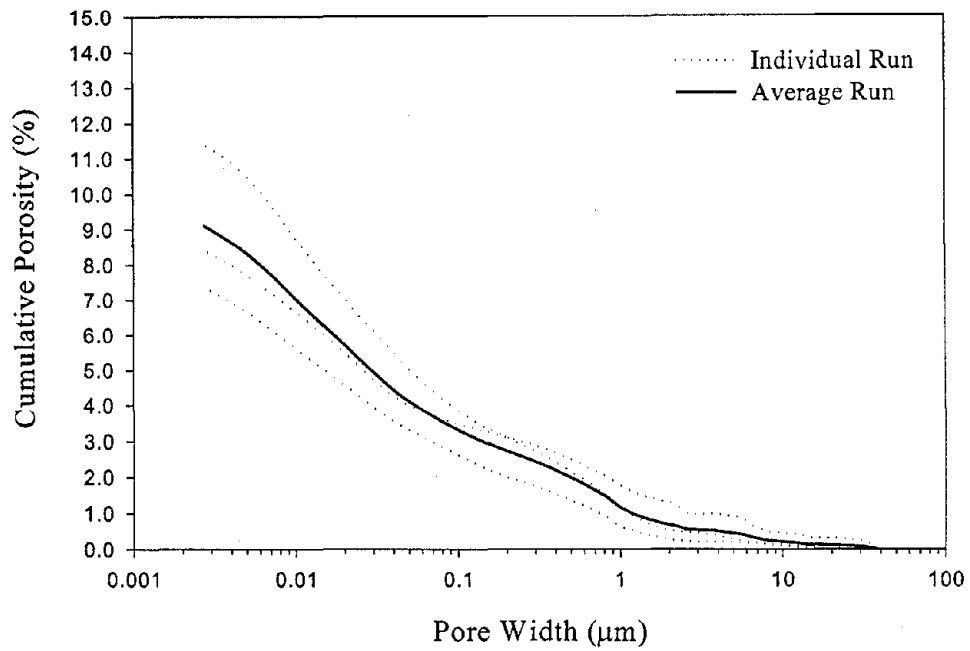
(a)
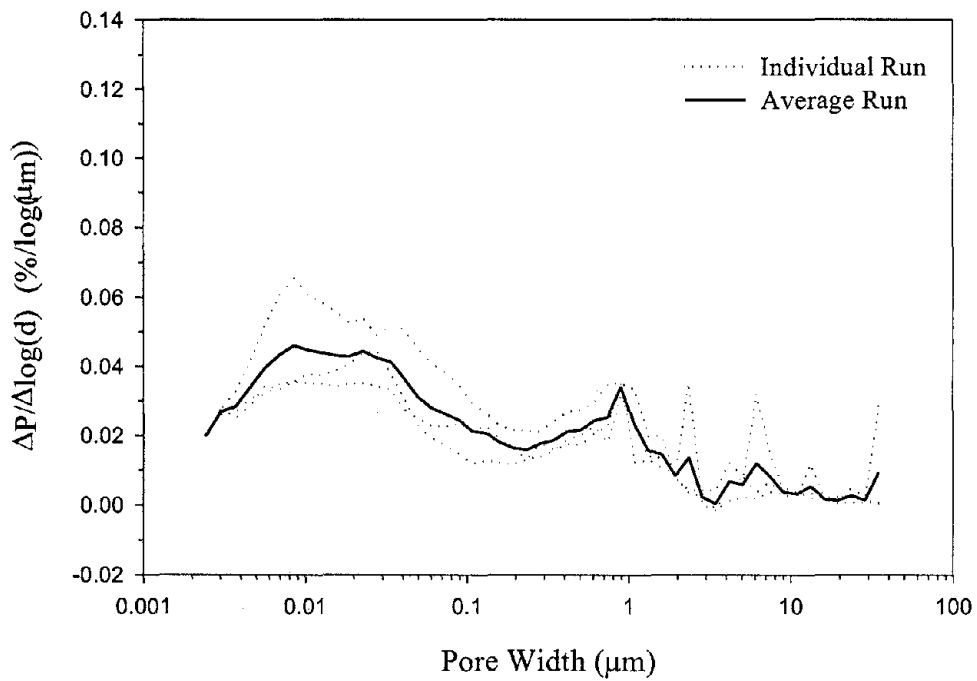
(b)

Figure L-7: MIP results for P(LLL)25: (a) cumulative porosity
vs. pore width; (b) average differential pore size distribution vs. pore width.
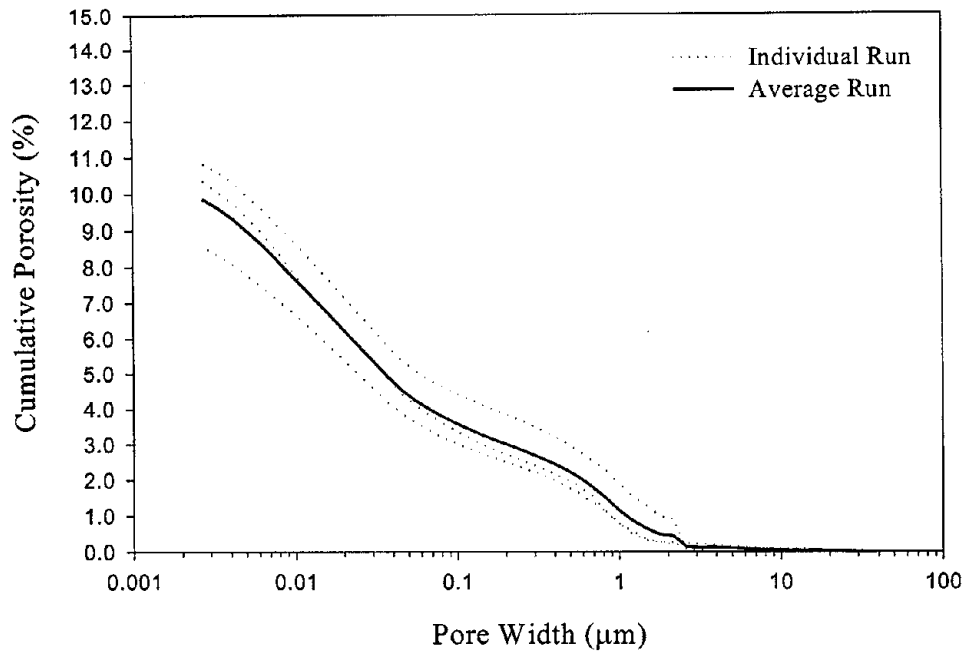
(a)
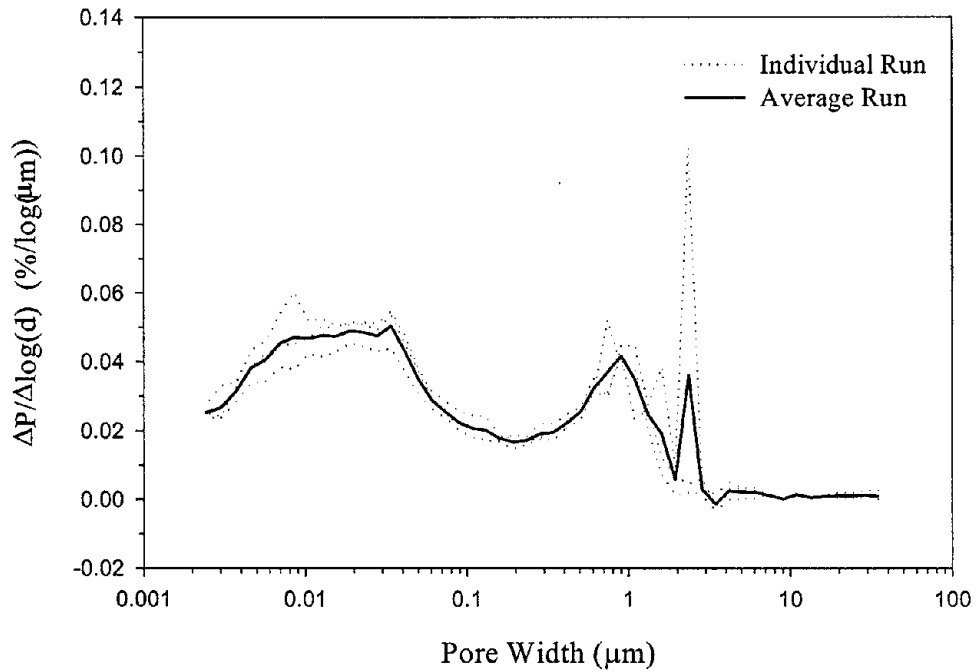
(b)

Figure L-8: MIP results for P(LLL)41: (a) cumulative porosity
vs. pore width; (b) average differential pore size distribution vs. pore width.
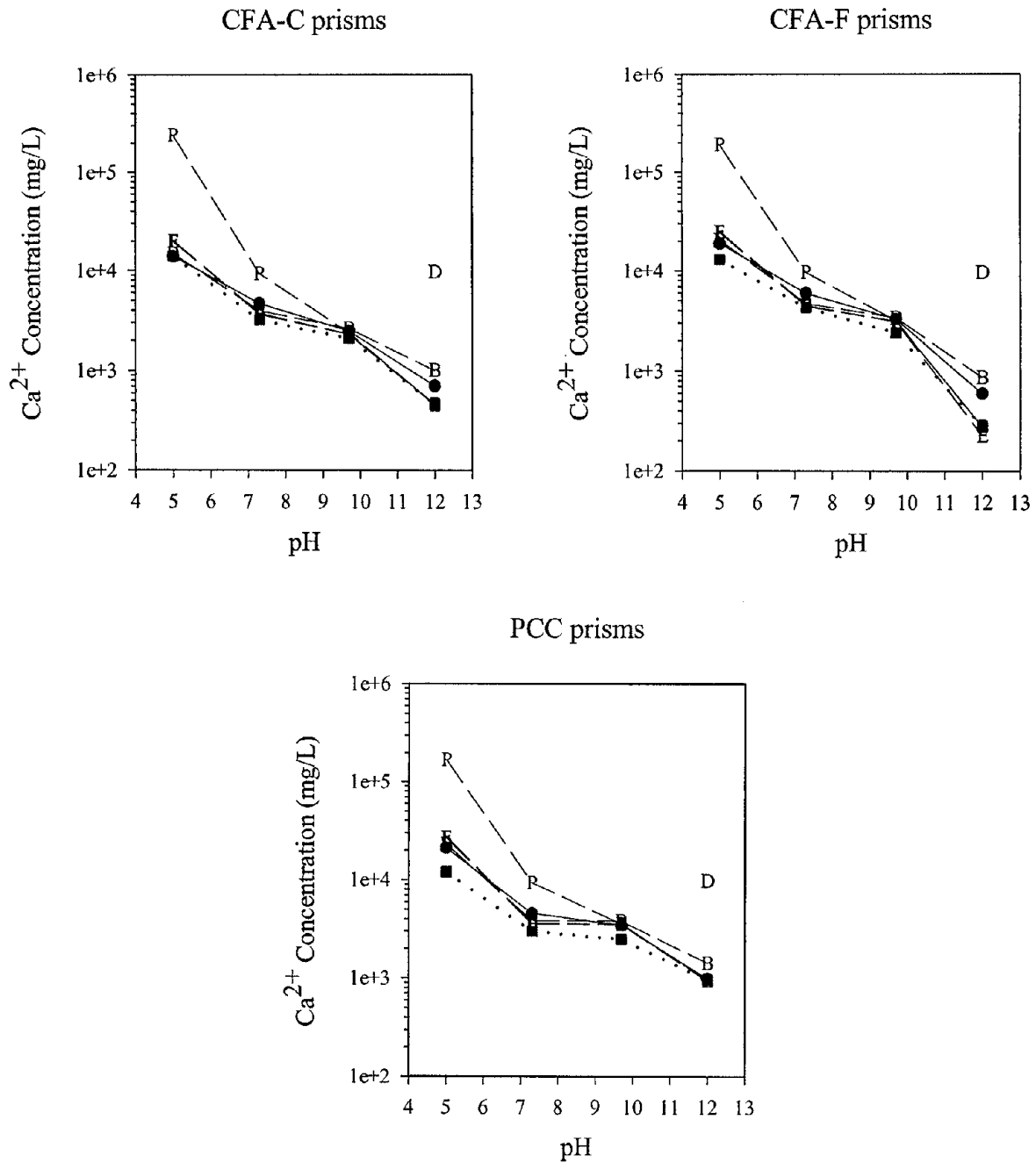
Figure L-9: Geochemical modeling of Ca in
three types of concrete.

● Highest Leaching Value ■ Lowest Leaching Value [B] – Gypsum
[D] – Portlandite [E] – Calcite [F] – Dolomite [P] – Ettringite
[B], [E] and [F] are completely overlapped

CFA-C prisms

CFA-F prisms

PCC prisms
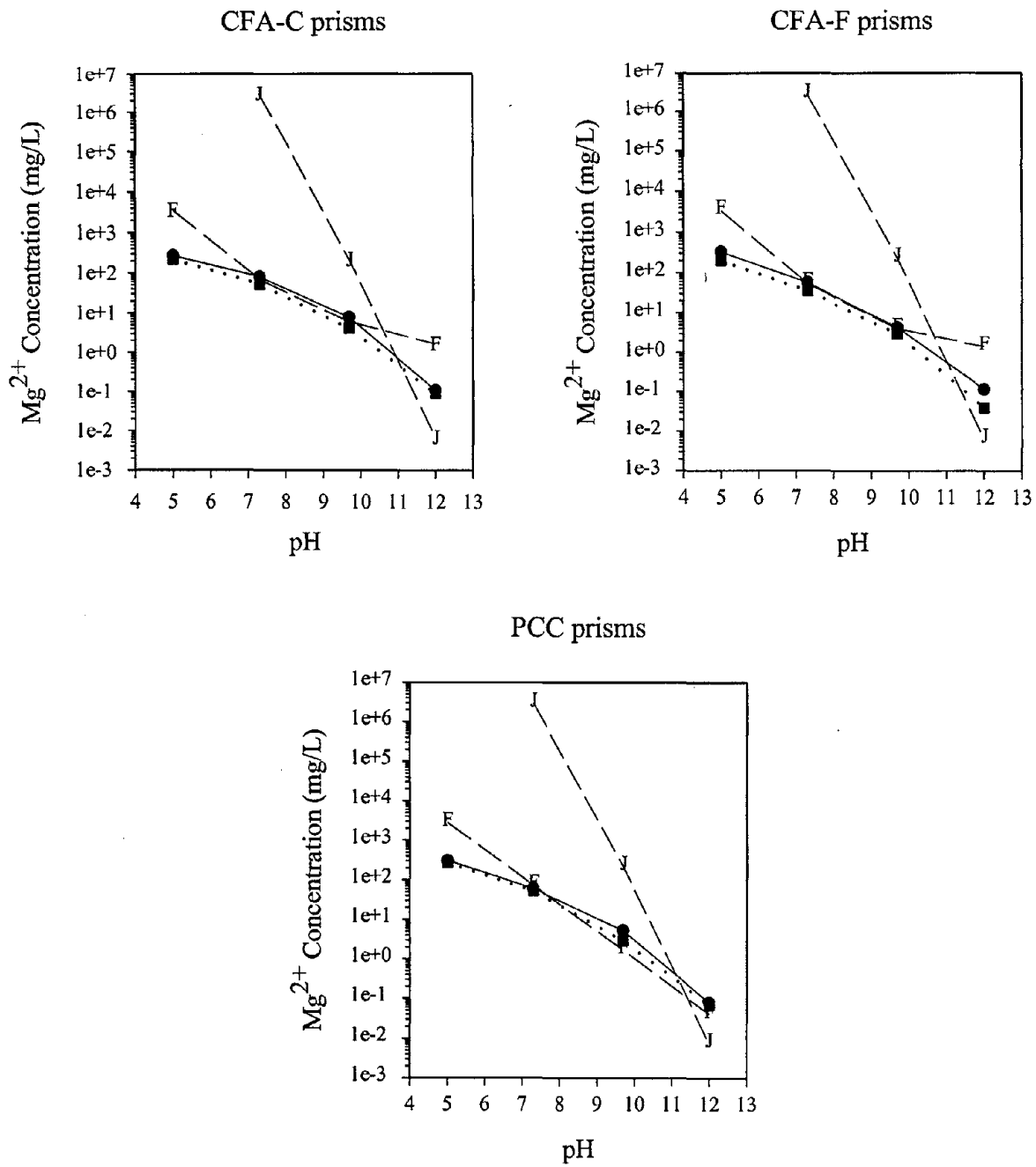
Figure L-10: Geochemical modeling of Mg in
three types of concrete.
● Highest Leaching Value   ■ Lowest Leaching Value
[F] – Dolomite   [J] – Brucite

CFA-C prisms

CFA-F prisms

PCC prisms
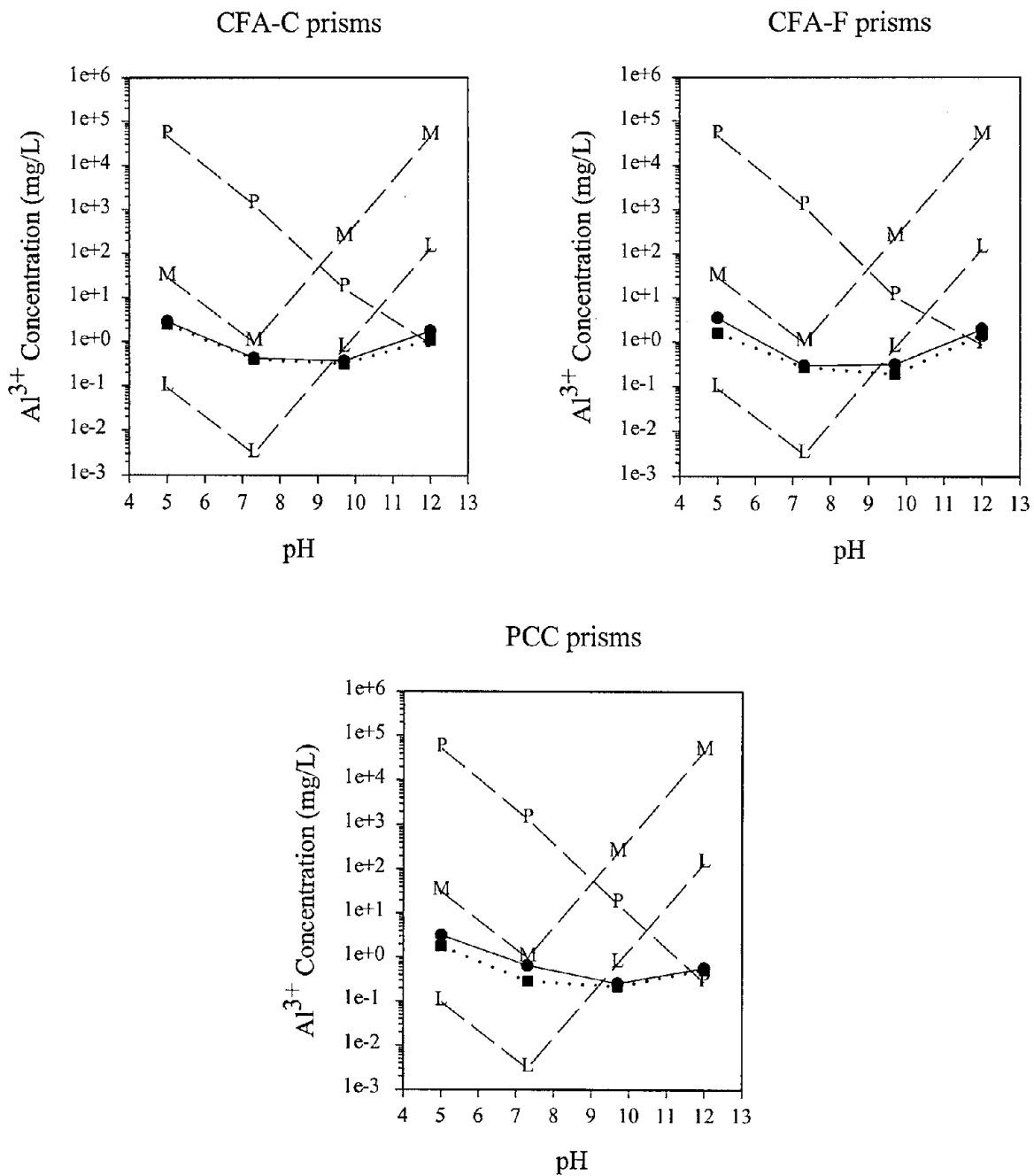
Figure L-11: Geochemical modeling of Al in
three types of concrete.
● Highest Leaching Value   ■ Lowest Leaching Value
[L] – Gibbsite   [M] – Al(OH)$_3$*amorphous   [P] – Ettringite

CFA-C prisms

CFA-F prisms

PCC prisms
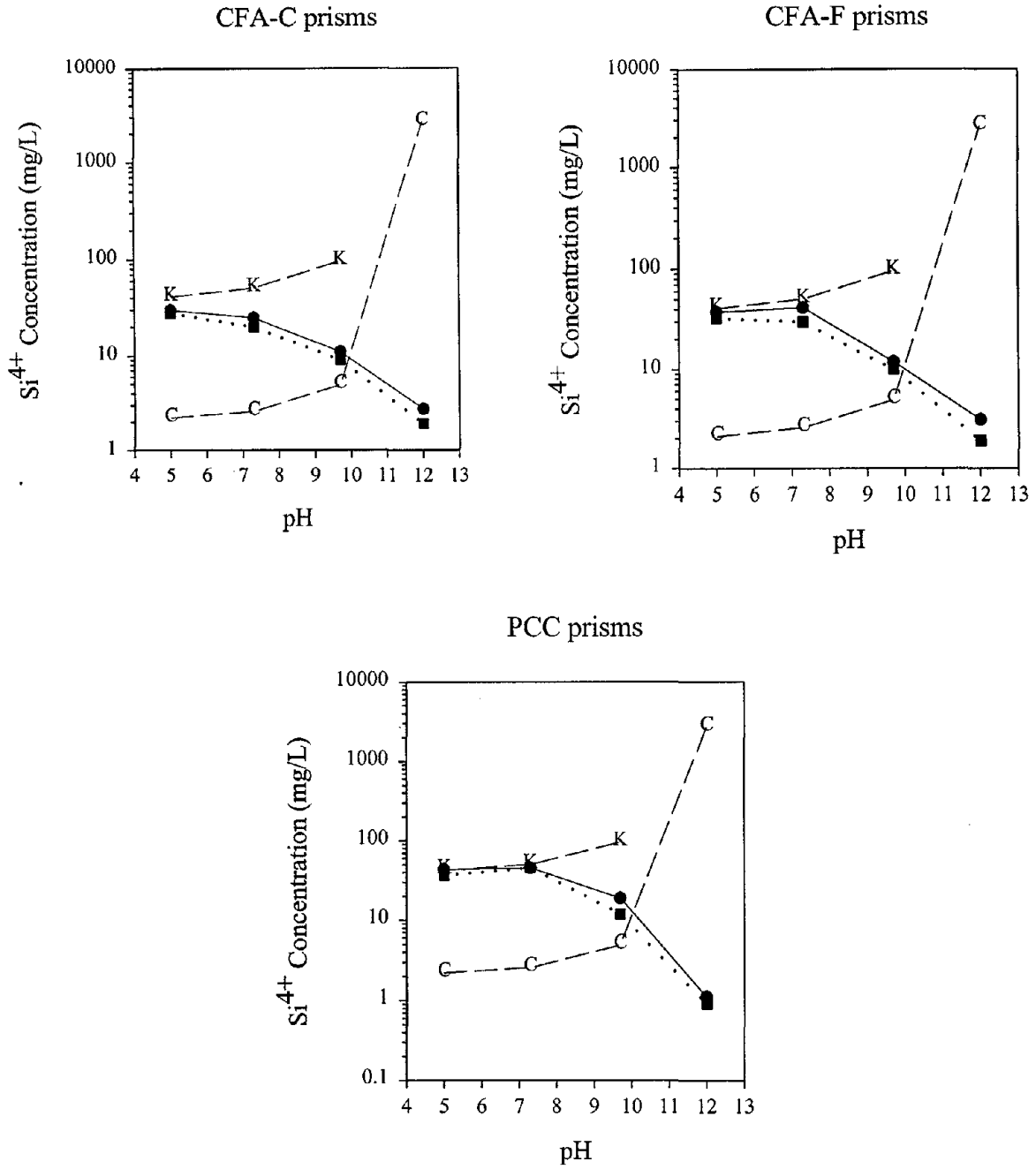
Figure L-12: Geochemical modeling of Si in
three types of concrete.

● Highest Leaching Value   ■ Lowest Leaching Value
[C] – Quartz   [K] – SiO_2*amorphous

172

CFA-C prisms

CFA-F prisms

PCC prisms
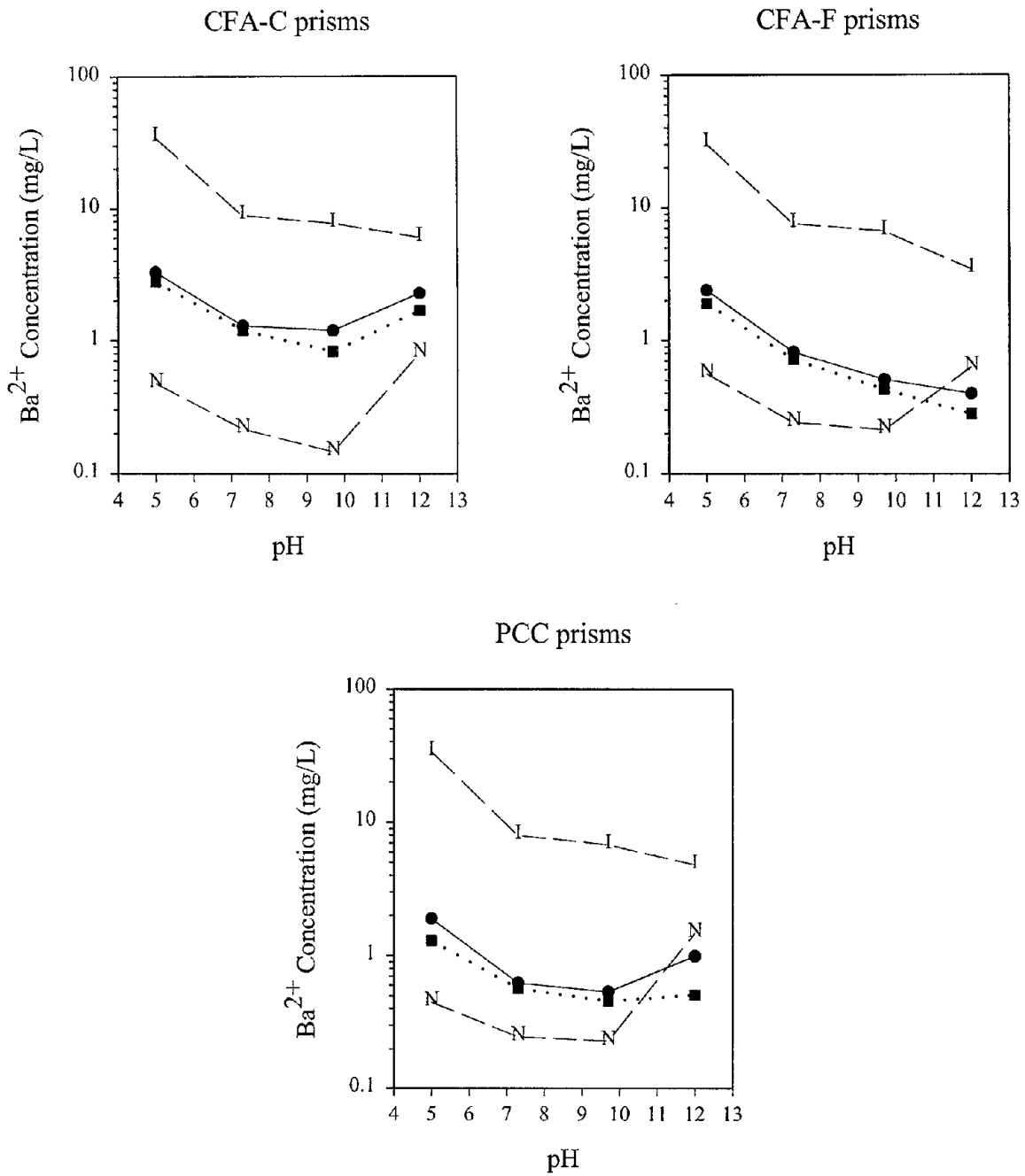
Figure L-13: Geochemical modeling of Ba in
three types of concrete.

● Highest Leaching Value   ■ Lowest Leaching Value
[I] – BaCrO$_4$ [N] – Barite

173

CFA-C prisms

CFA-F prisms

PCC prisms
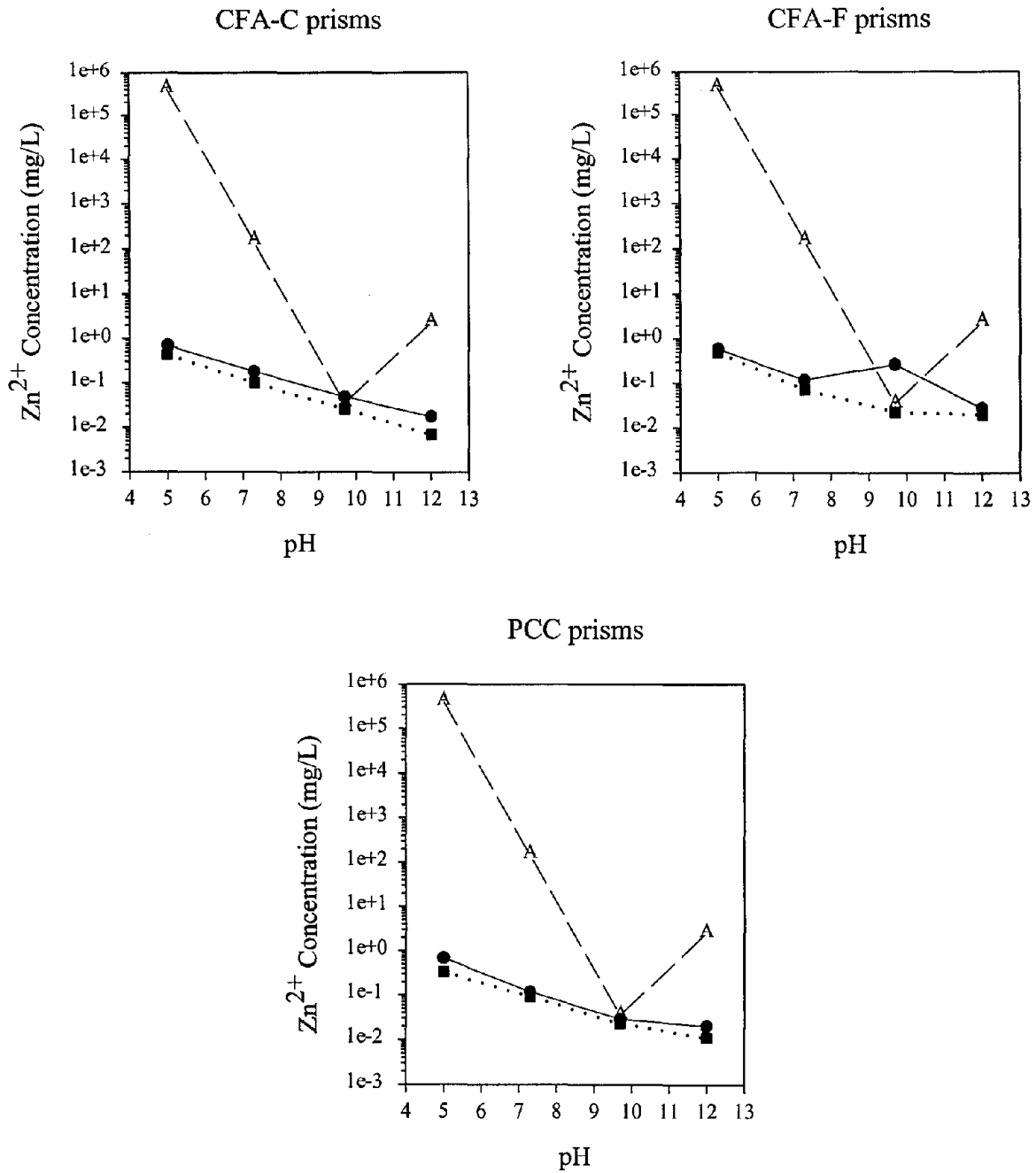
Figure L-14: Geochemical modeling of Zn in
three types of concrete.

● Highest Leaching Value ■ Lowest Leaching Value
[A] – Zincite

174
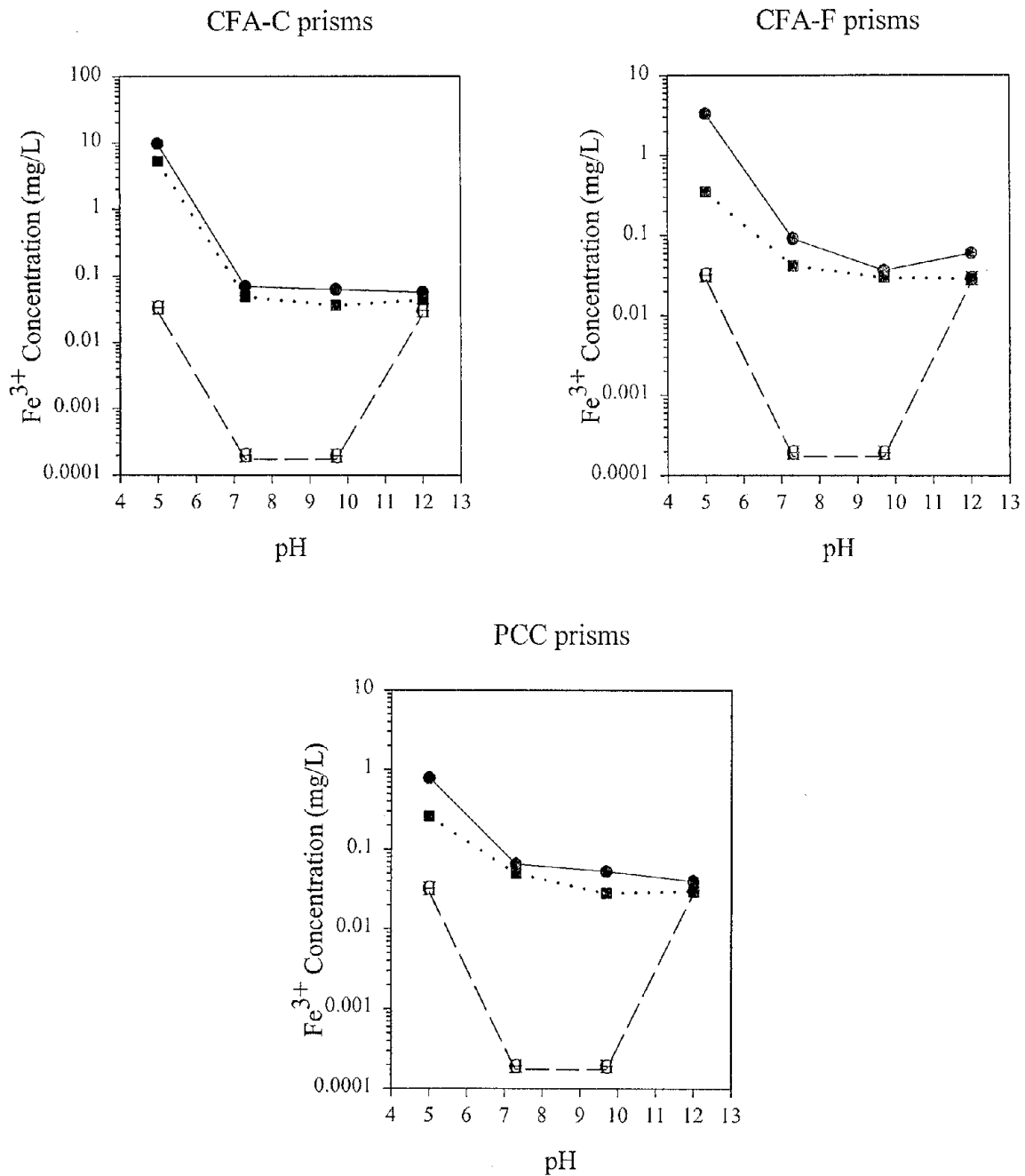
Figure L-15: Geochemical modeling of Fe in
three types of concrete.

● Highest Leaching Value   ■ Lowest Leaching Value
[G] – Ferrihydrite   [H] – Maghemite

CFA-C prisms

CFA-F prisms

PCC prisms
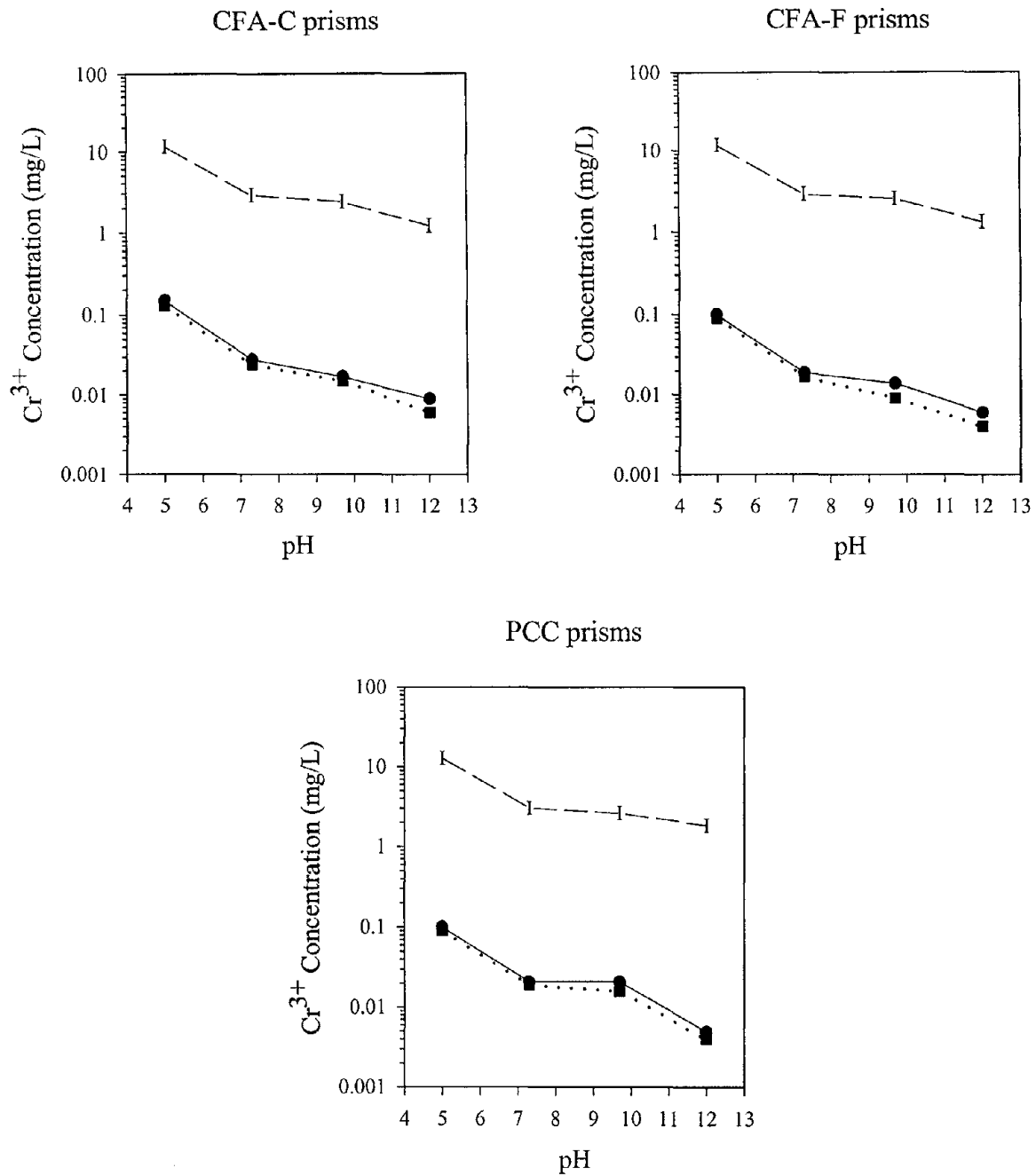
Figure L-16: Geochemical modeling of Cr in
three types of concrete.

● Highest Leaching Value ■ Lowest Leaching Value
[I] – $BaCrO_4$

176

CFA-C prisms

CFA-F prisms

PCC prisms
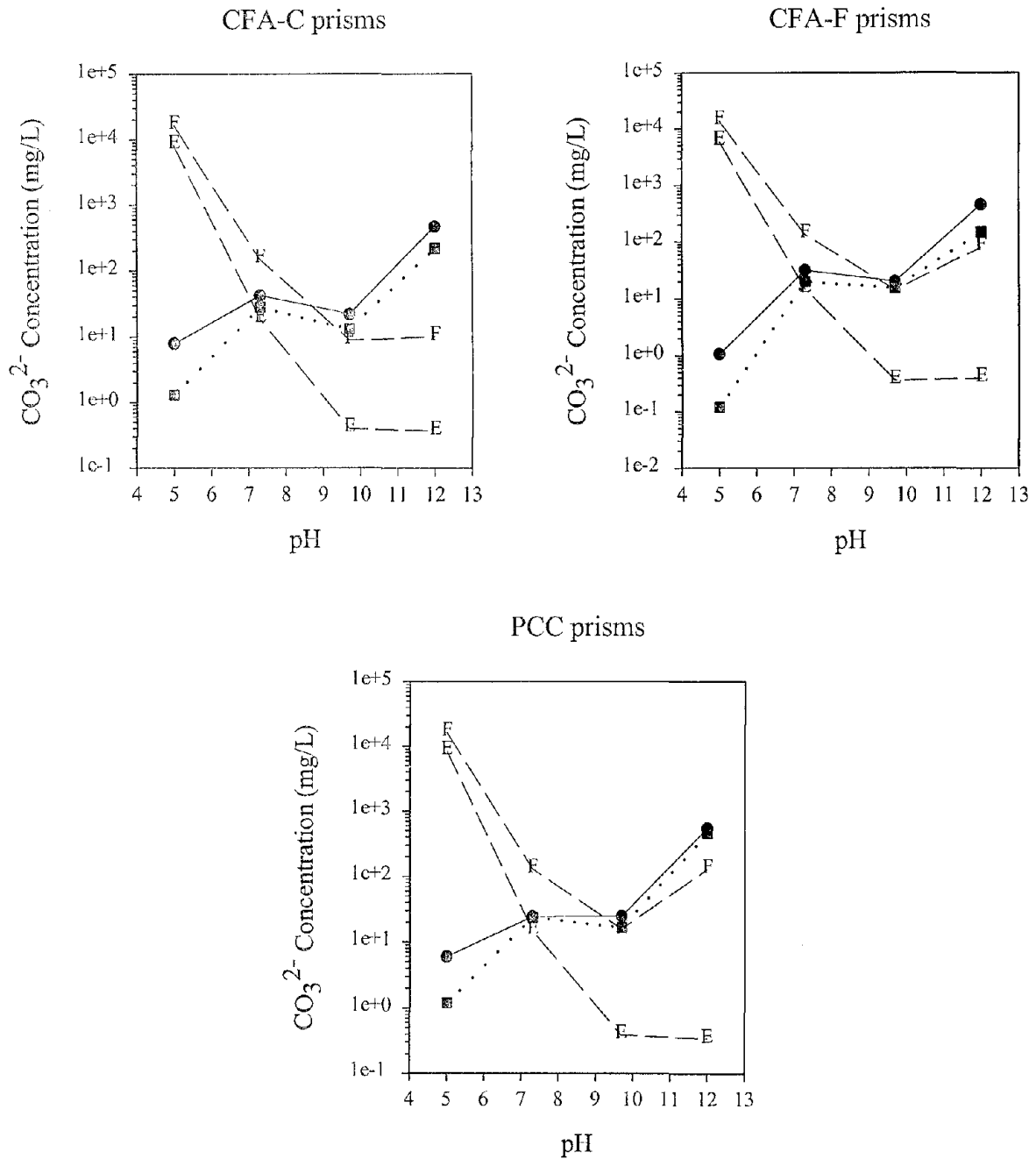
Figure L-17: Geochemical modeling of CO_3^{2-} in three types of concrete.

⊕ Highest Leaching Value ▨ Lowest Leaching Value

[E] – Calcite   [F] – Dolomite

177

CFA-C prisms

CFA-F prisms

PCC prisms
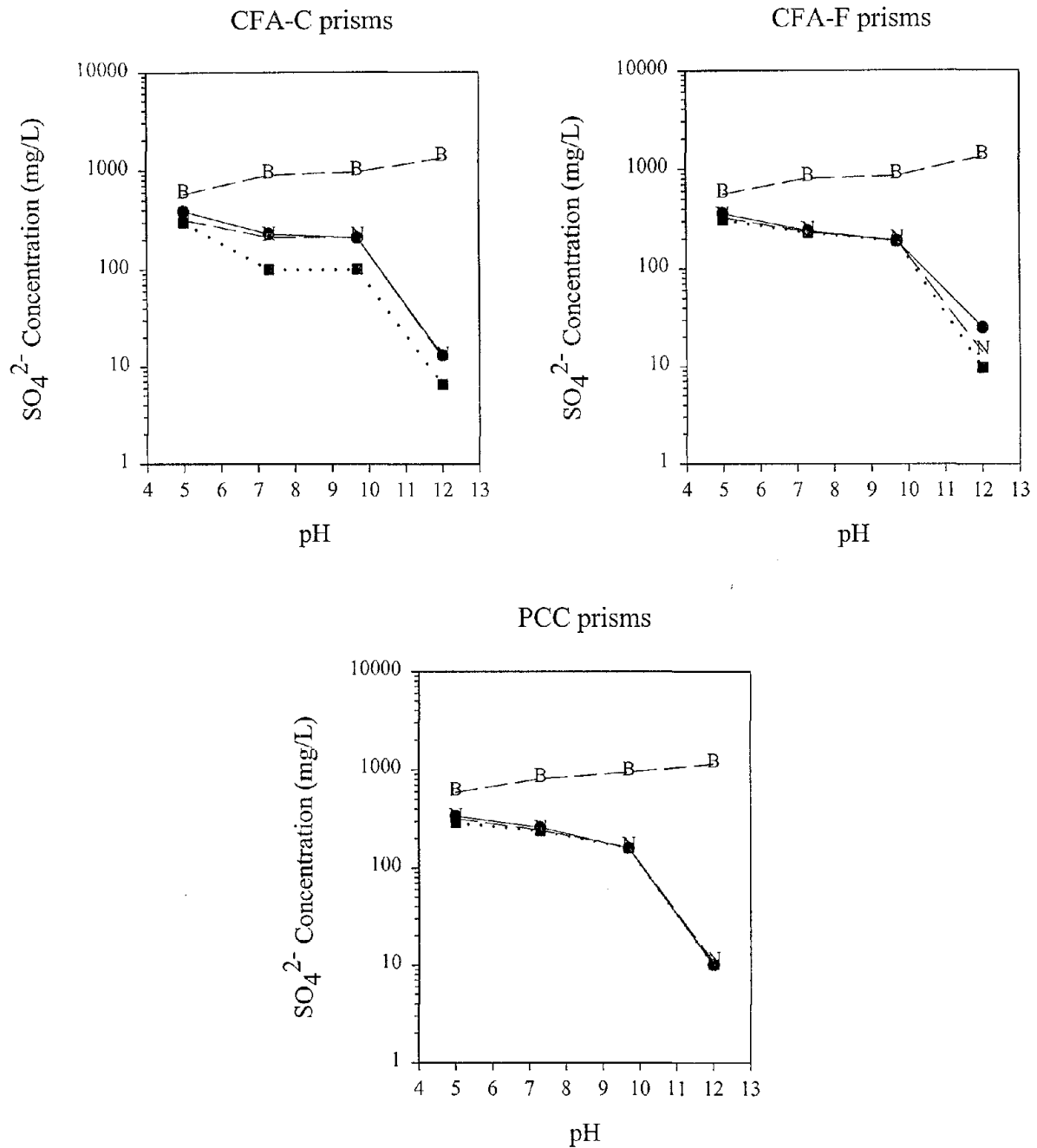
Figure L-18: Geochemical modeling of SO_4^{2-} in
three types of concrete.
● Highest Leaching Value   ■ Lowest Leaching Value
[N] – Barite   [P] – Ettringite

178
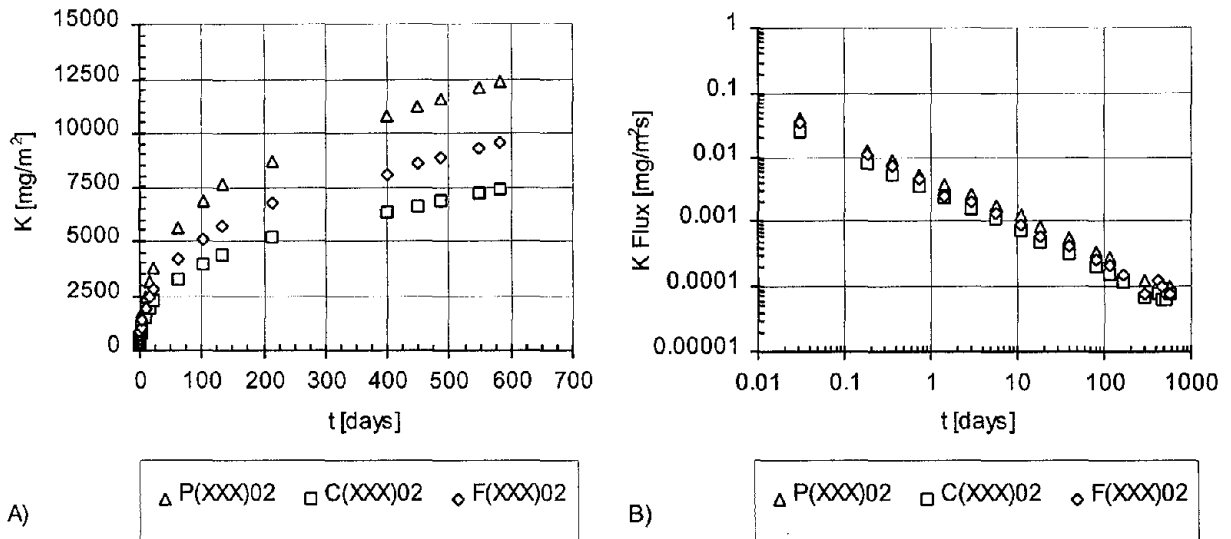
Figure L-19: K release from the three 28-day cured material types:
A) cumulative mass released in mg/m^2; B) flux released in mg/m^{2}s.
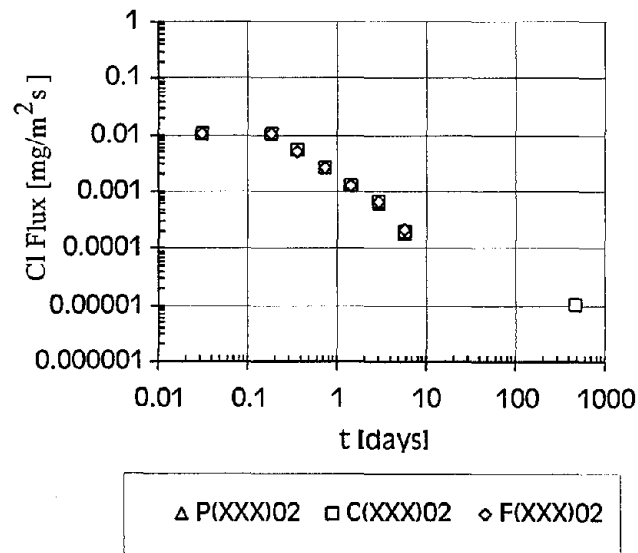
Figure L-20: Cl release from the three 28-day cured material types:
flux released in mg/m^{2}s.
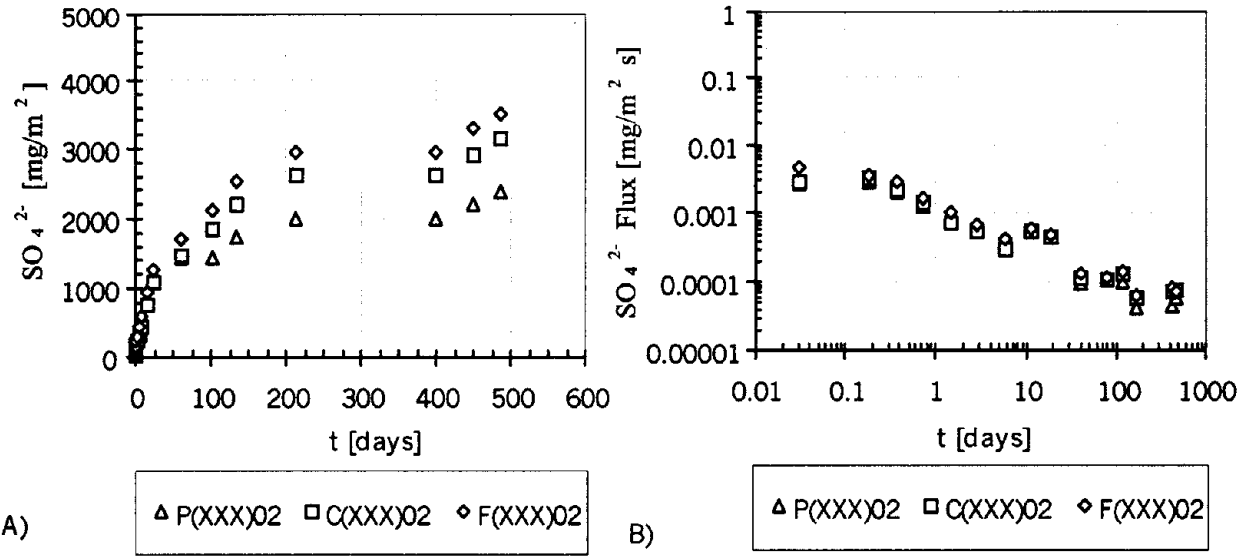
Figure L-21: SO_4^{2-} release from the three 28-day cured material types:
A) cumulative mass released in mg/m^2; B) flux released in mg/m^{2}s.
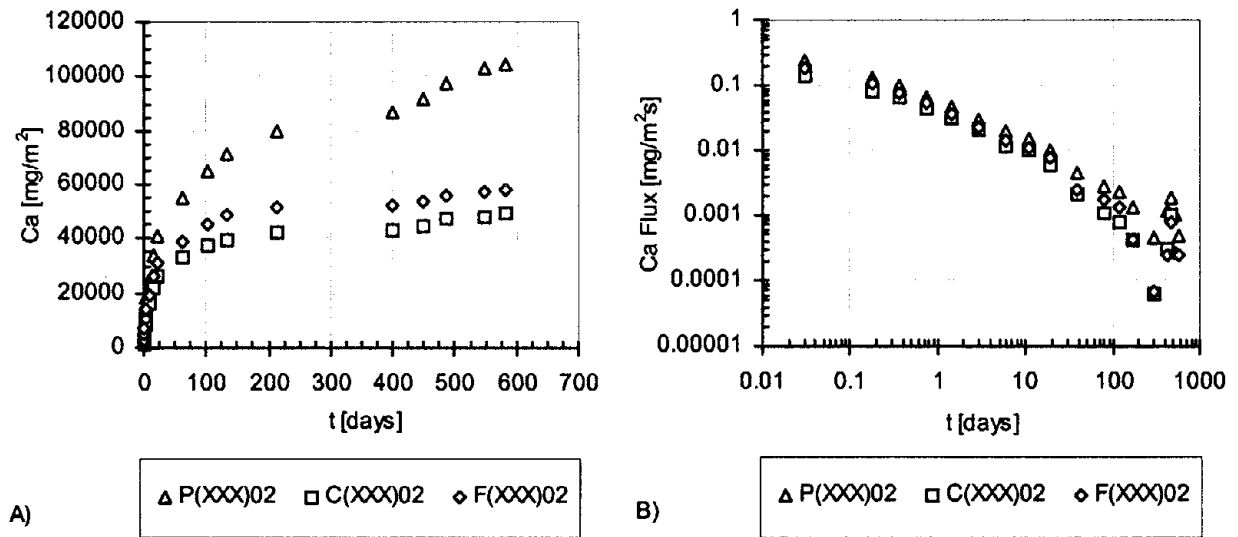
Figure L-22: Ca release from the three 28-day cured material types:
A) cumulative mass released in mg/m^2; B) flux released in mg/m^{2}s.
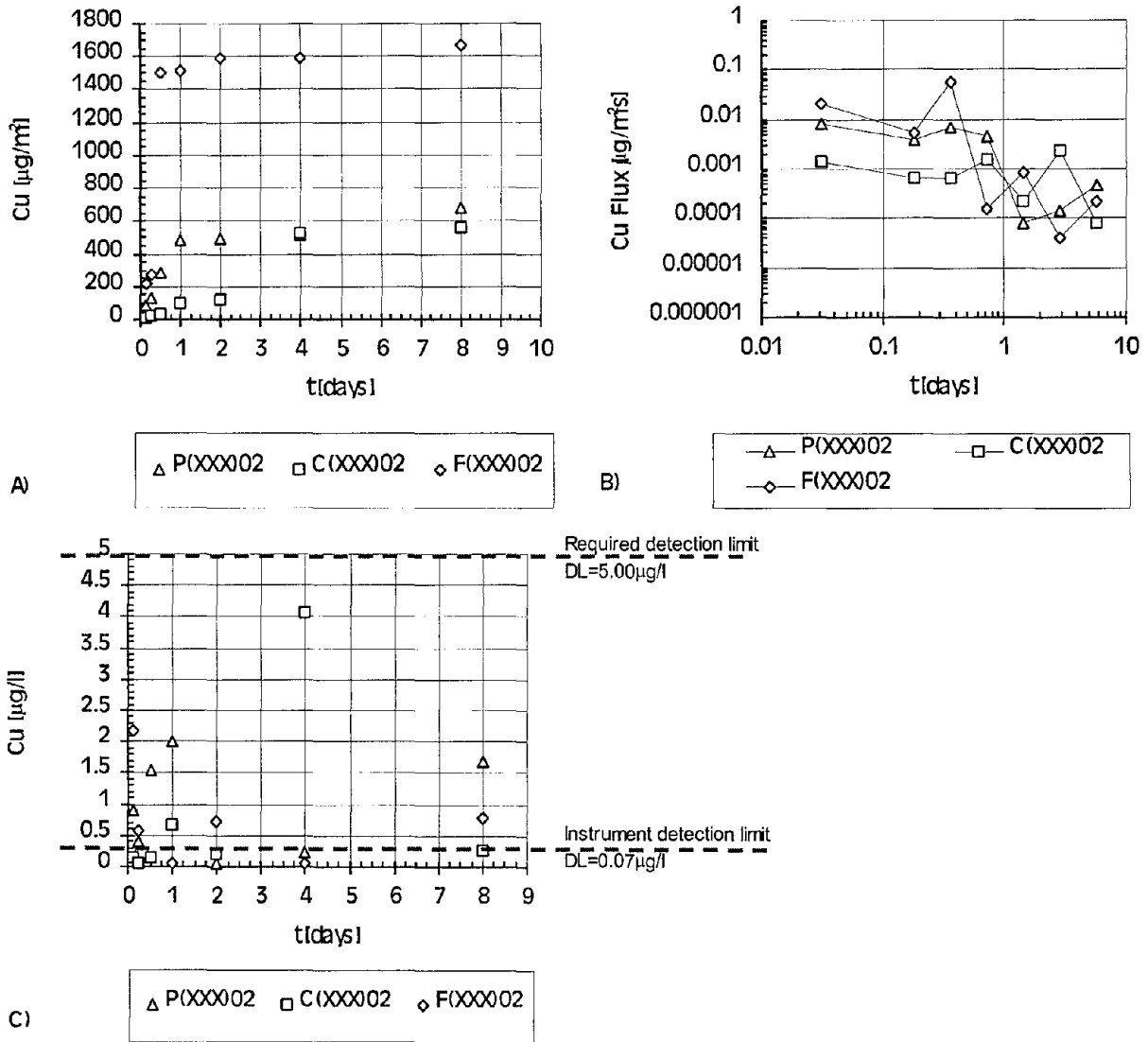
Figure L-23: Cu release from the three 28-day cured material types:
A) cumulative mass released in μ/m^2; B) flux released in μ/m^2s; and
C) leachate concentrations in $\mu g/l$.
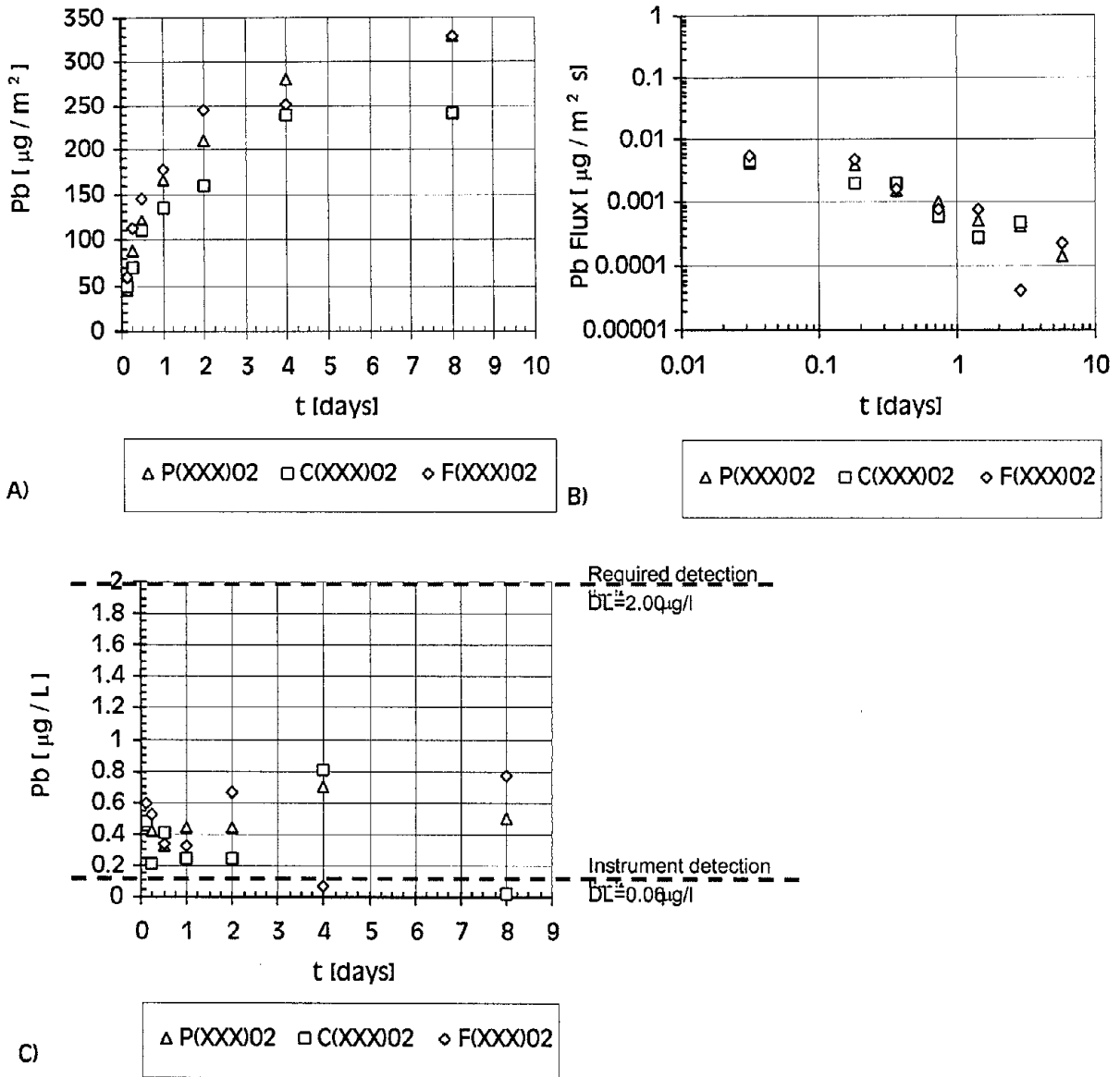
Figure L-24: Pb release from the three 28-day cured material types:
A) cumulative mass released in μg/m²; B) flux released in μg/m²s; and
C) leachate concentrations in μg/l.
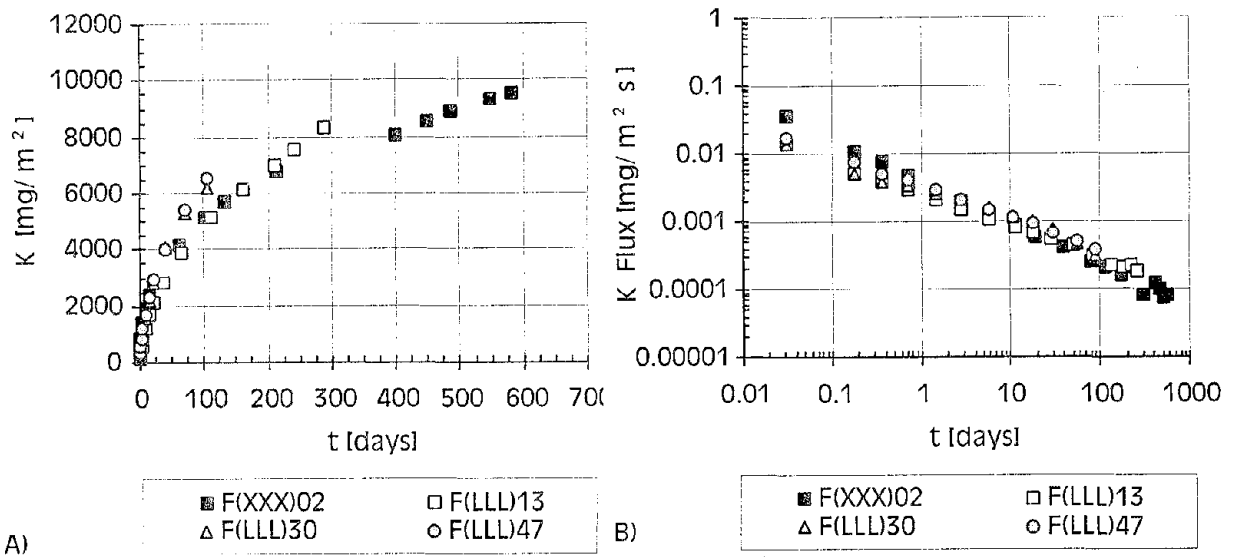
Figure L-25: K release for CFA-F mix:
A) cumulative mass released in mg/m²; B) flux released in mg/m²s.
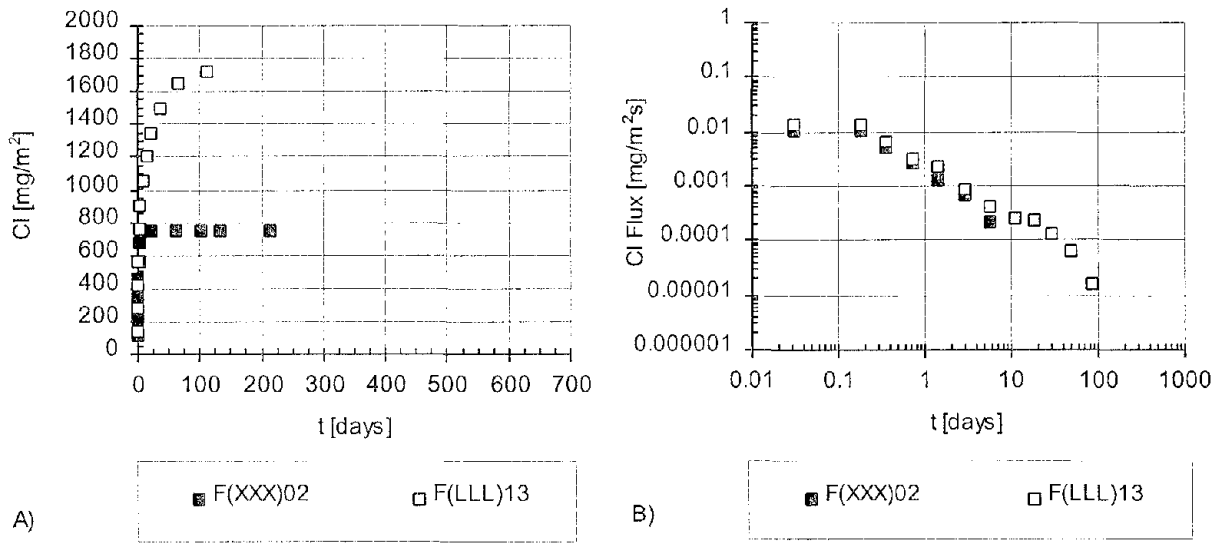
Figure L-26: Cl release for CFA-F mix:
A) cumulative mass released in mg/m²; B) flux released in mg/m²s.
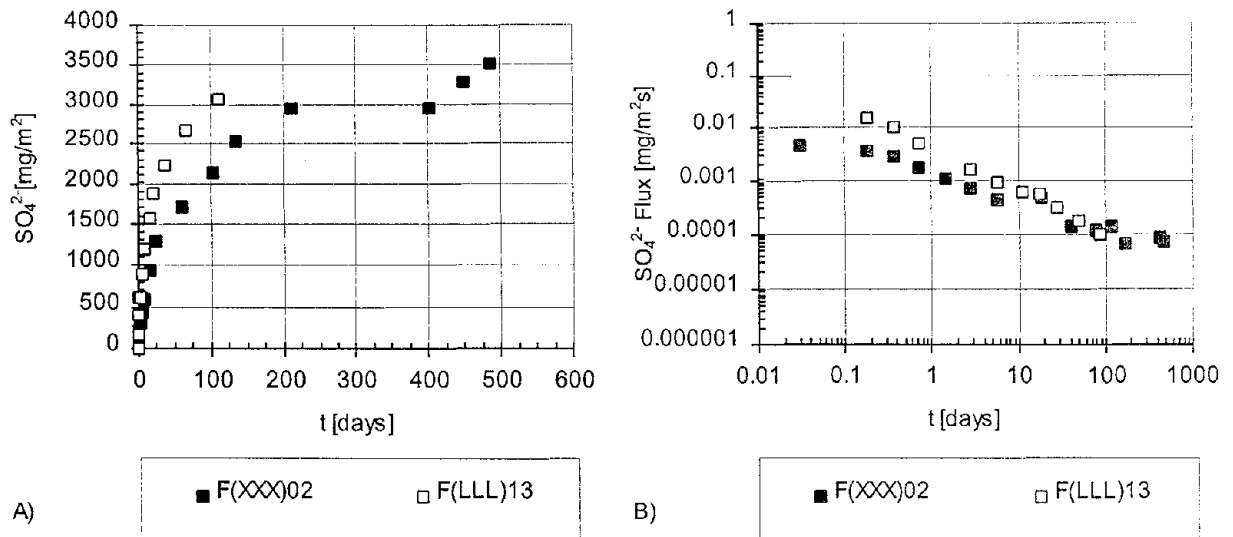
Figure L-27: SO_4^{2-} release for CFA-F mix:
A) cumulative mass released in mg/m^2; B) flux released in mg/m^2s.
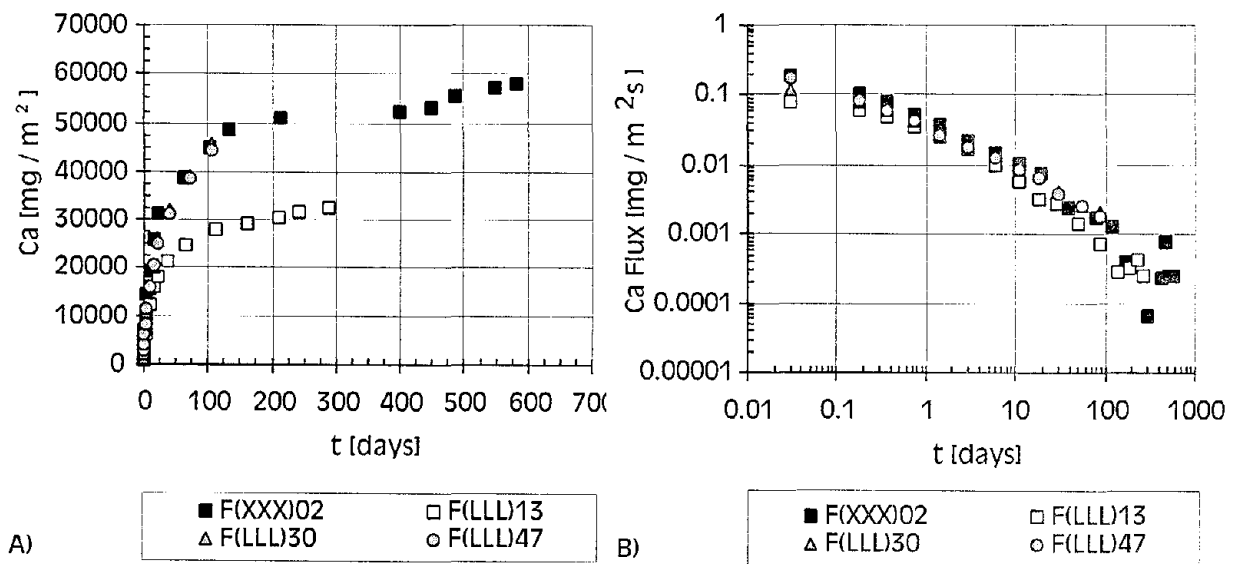
Figure L-28: Ca release for CFA-F mix:
A) cumulative mass released in mg/m^2; B) flux released in mg/m^2s.
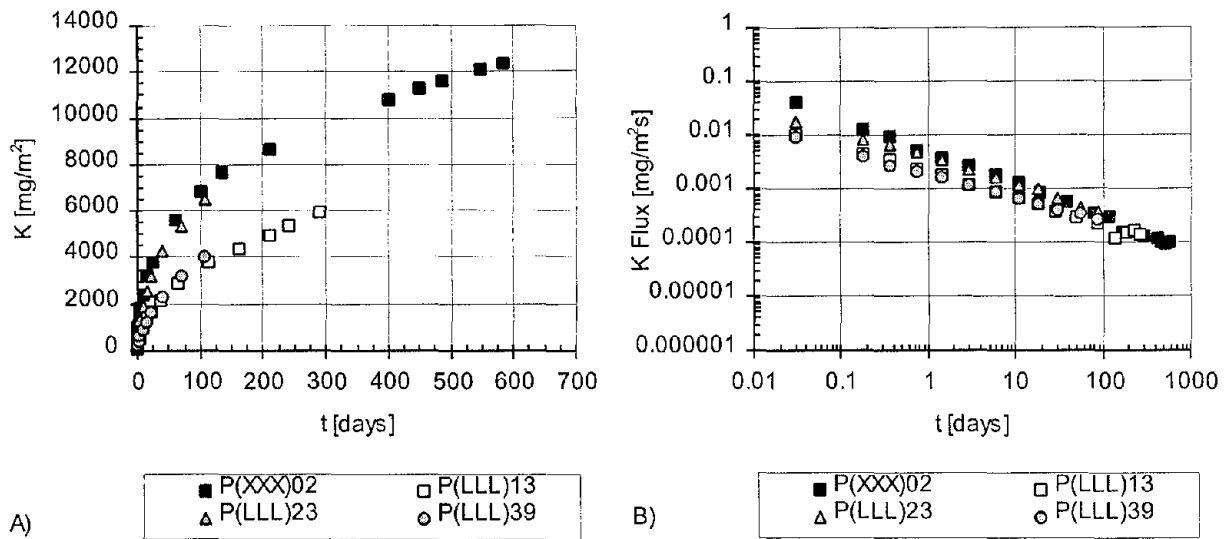
Figure L-29: K release for PCC control.
A) cumulative mass released in mg/m^2; B) flux released in mg/m^{2}s.
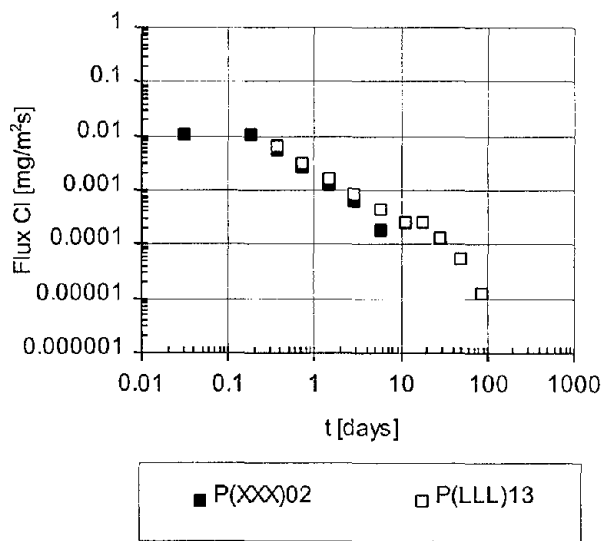
Figure L-30: Cl release for PCC control: flux released in mg/m^{2}s.
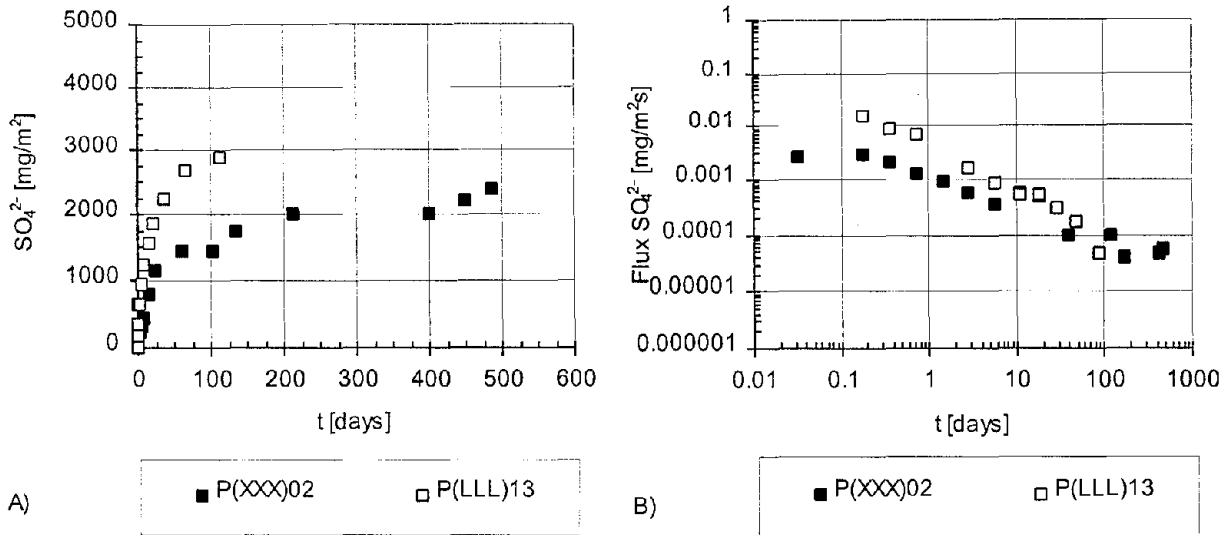
Figure L-31: SO_4^{2-} release for PCC control:
A) cumulative mass released in mg/m²; B) flux released in mg/m²s.
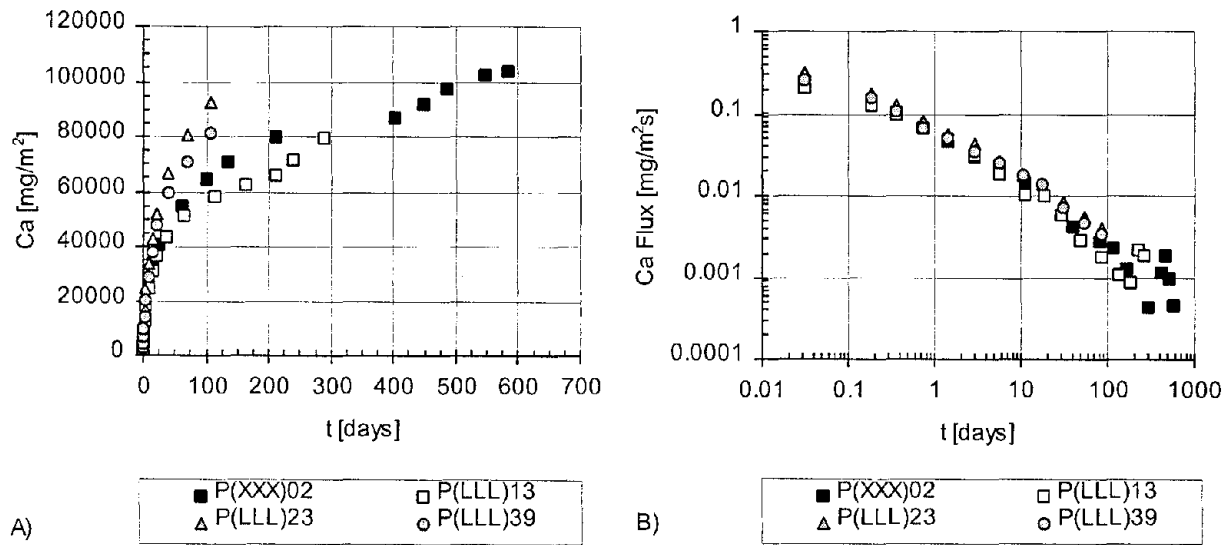
Figure L-32: Ca release for PCC control:
A) cumulative mass released in mg/m²; B) flux released in mg/m²s.
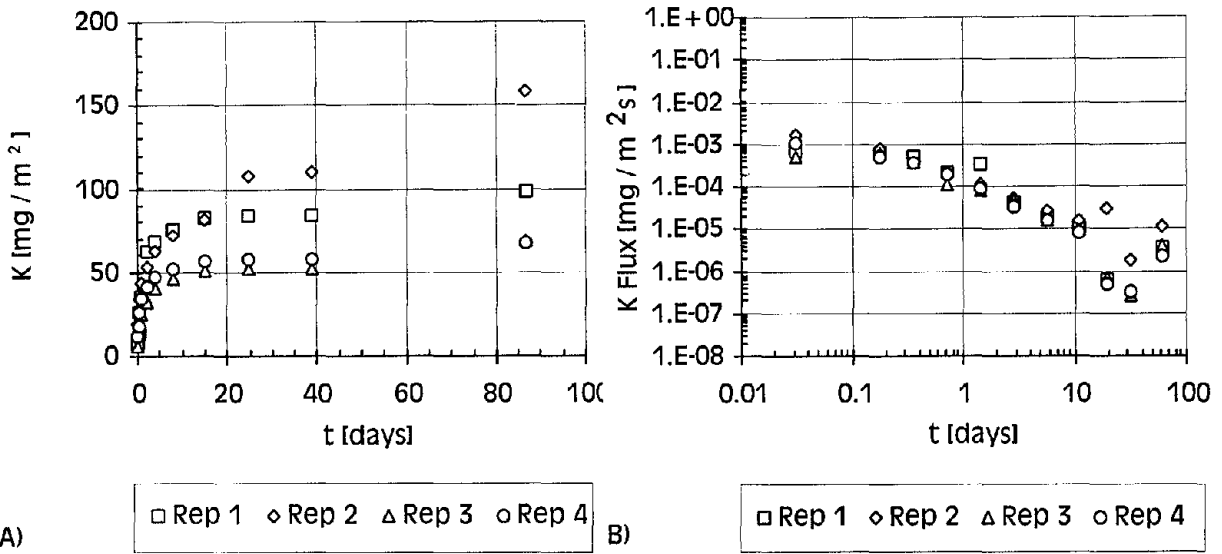
Figure L-33: K release from the coarse aggregates:
A) cumulative mass released in mg/m²; B) flux released in mg/m²s.
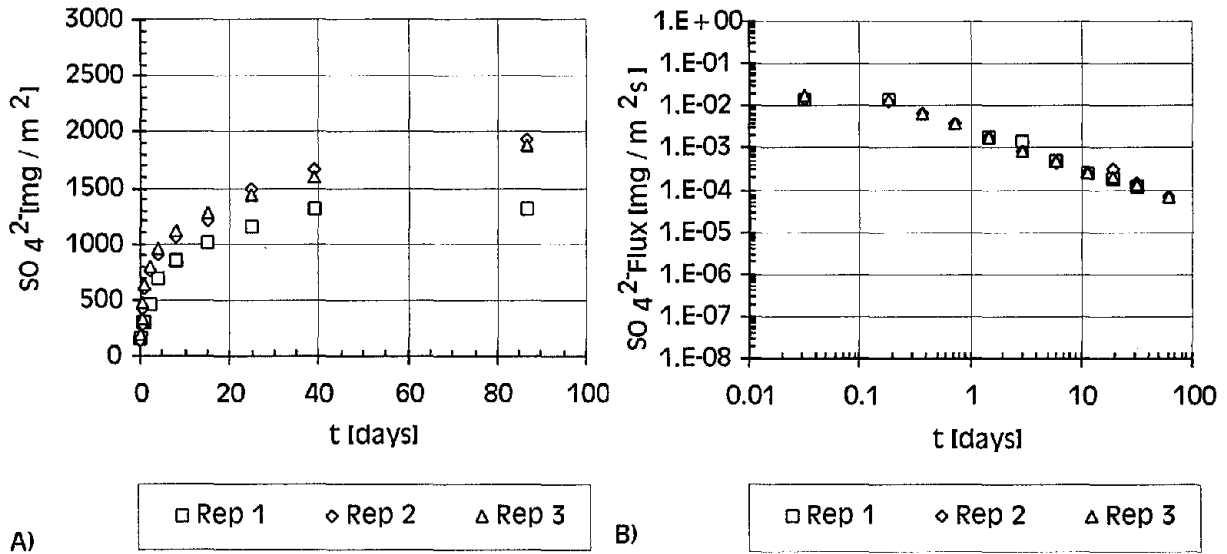
Figure L-34: SO_4^{2-} release from the coarse aggregates:
A) cumulative mass released in mg/m²; B) flux released in mg/m²s.
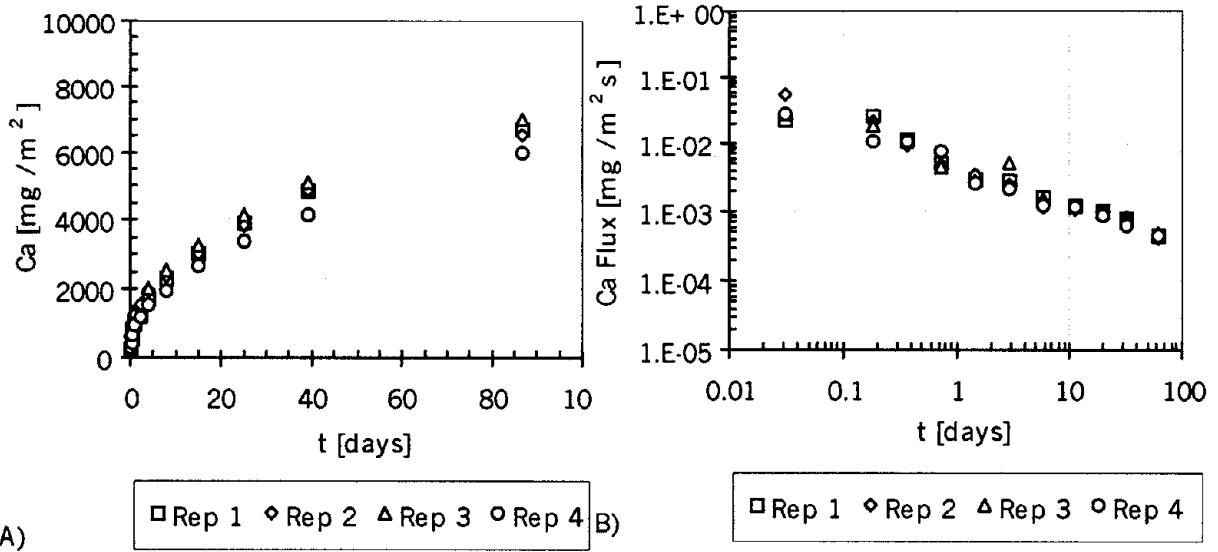
Figure L-35: Ca release from the coarse aggregates:
A) cumulative mass released in mg/m²; B) flux released in mg/m²s.
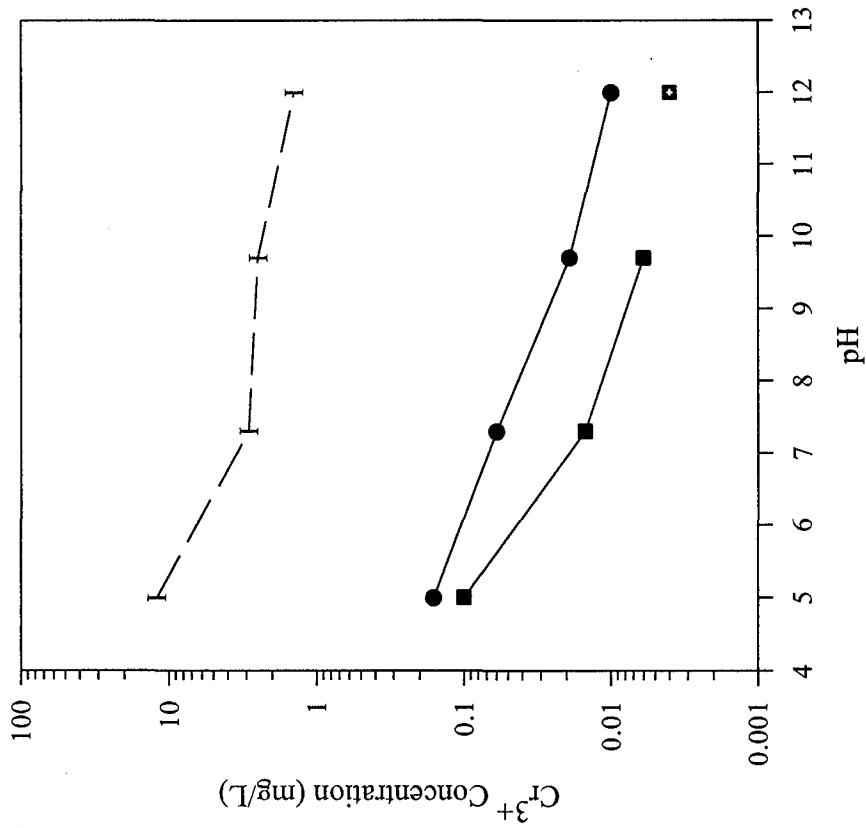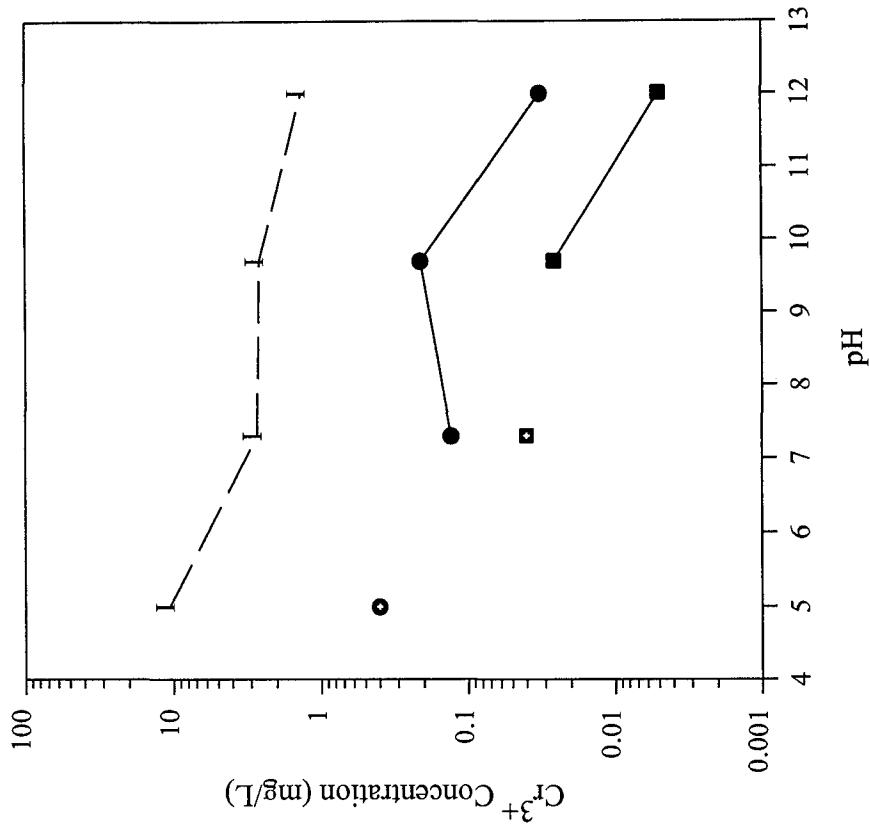
APPENDIX M. SLAB AND CFA-C PRISM COMPARATIVE DATA
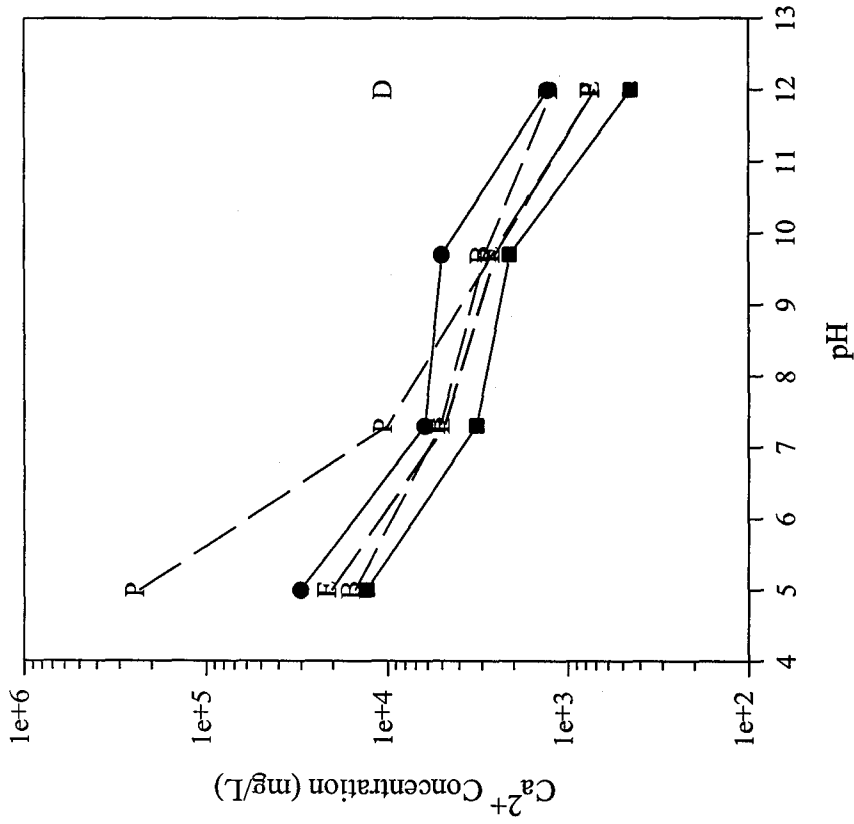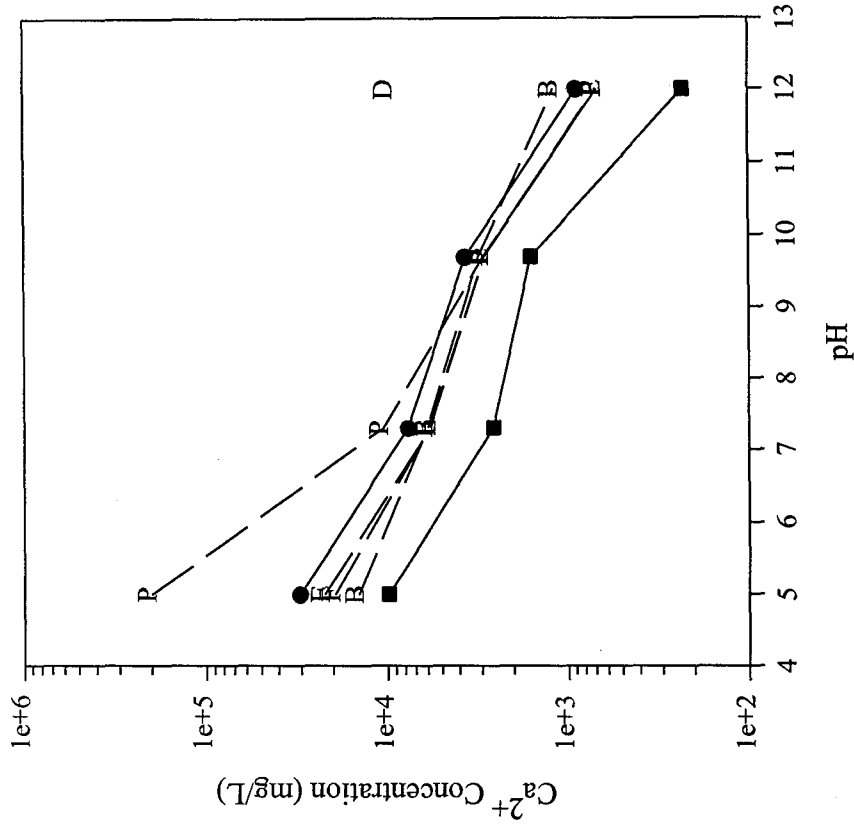
Figure M-1: Comparison Ca modeling in CFA-C prism and U.S. 20 slab concrete.

● Highest Leaching Value   ■ Lowest Leaching Value   [B] – Gypsum   [D] – Portlandite
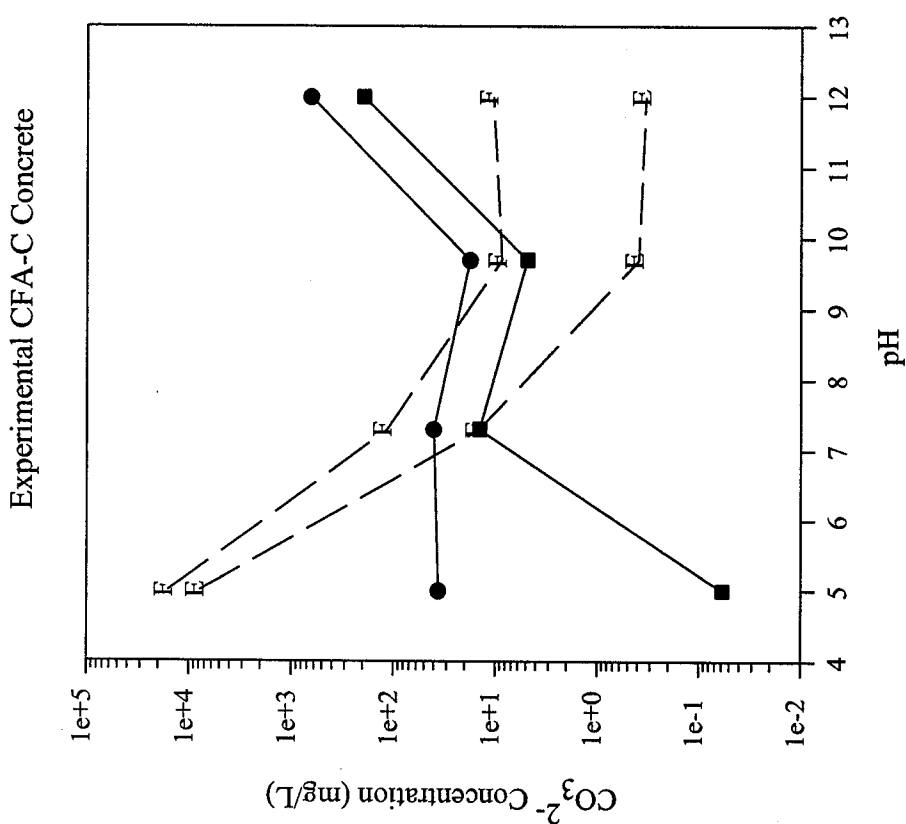[E] – Calcite   [F] – Dolomite   [P] – Ettringite   [E] and [F] are overlapped

190
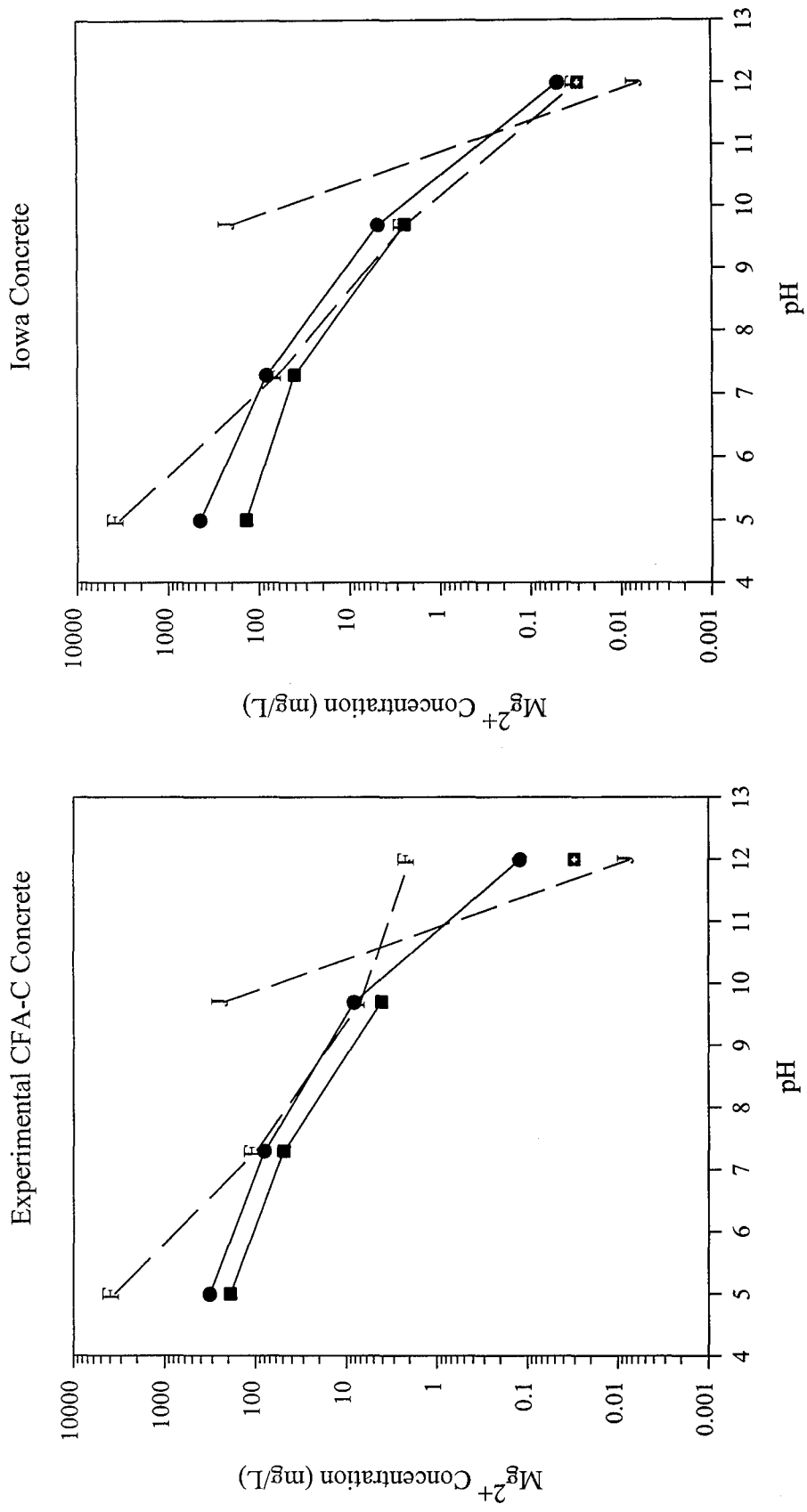
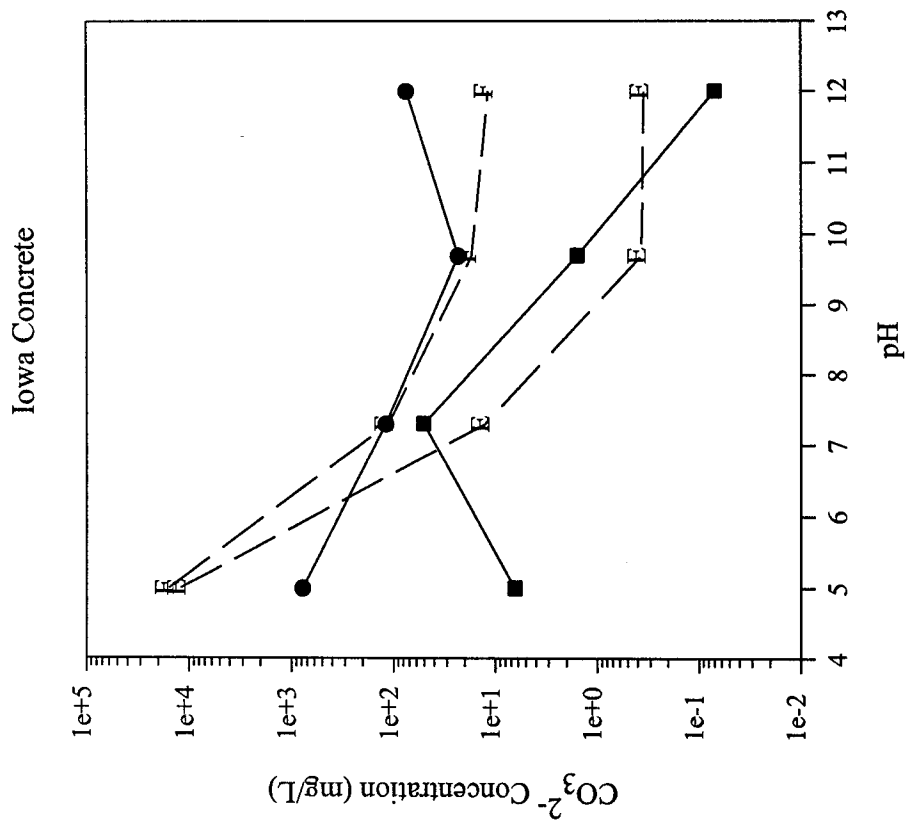Figure M-2: Comparison Mg modeling in CFA-C prism and U.S. 20 slab concrete.

● Highest Leaching Value ■ Lowest Leaching Value ◫ Lowest Leaching Value BDL

[F] – Dolomite [J] – Brucite

Iowa Concrete

Experimental CFA-C Concrete
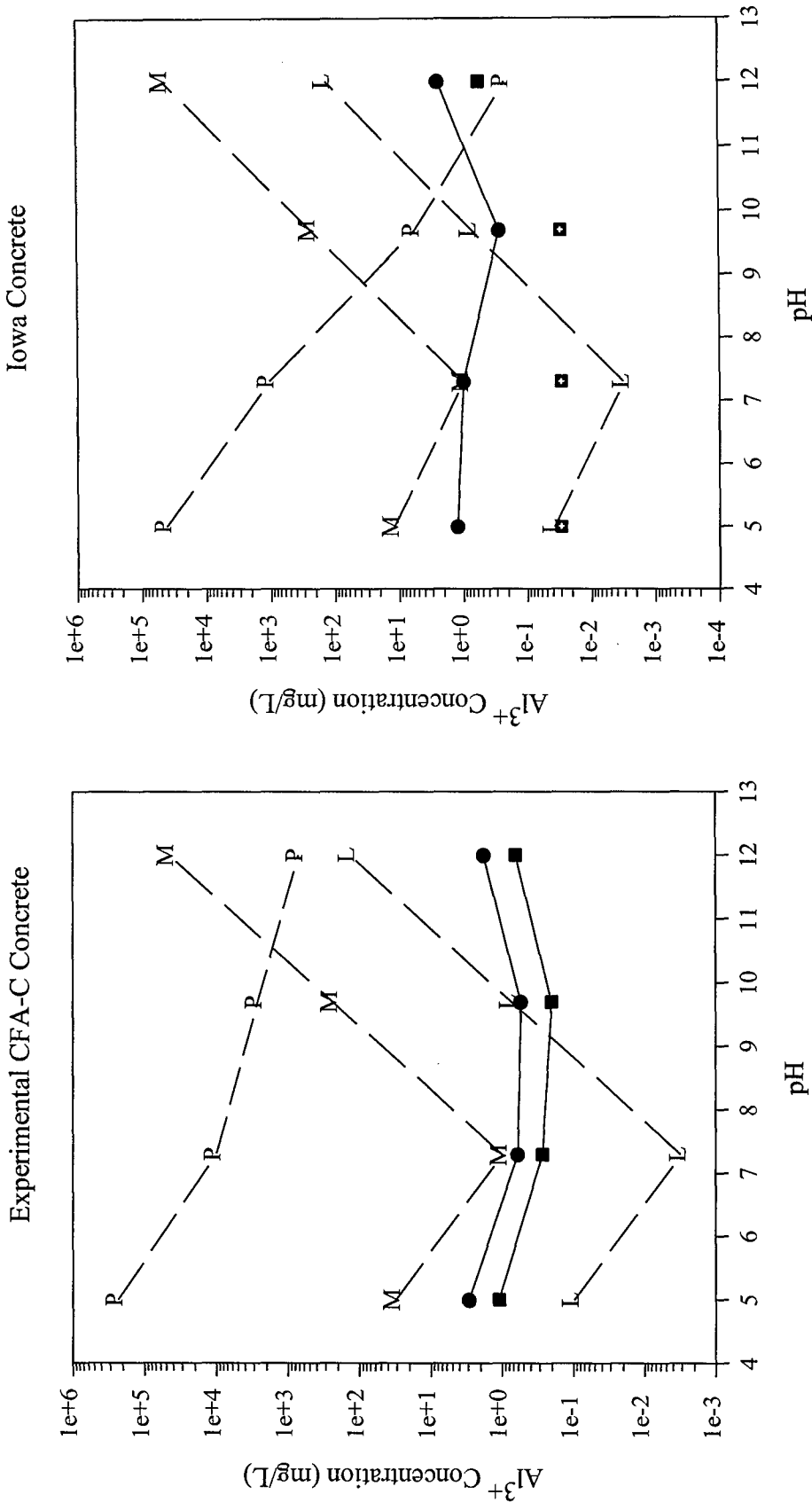
Figure M-3: Comparison Al modeling in CFA-C prism and U.S. 20 slab concrete.

• Highest Leaching Value ■ Lowest Leaching Value ⊞ Lowest Leaching Value BDL [L] – Gibbsite
[M] – Al(OH)$_3$*amorphous [P] – Ettringite

192
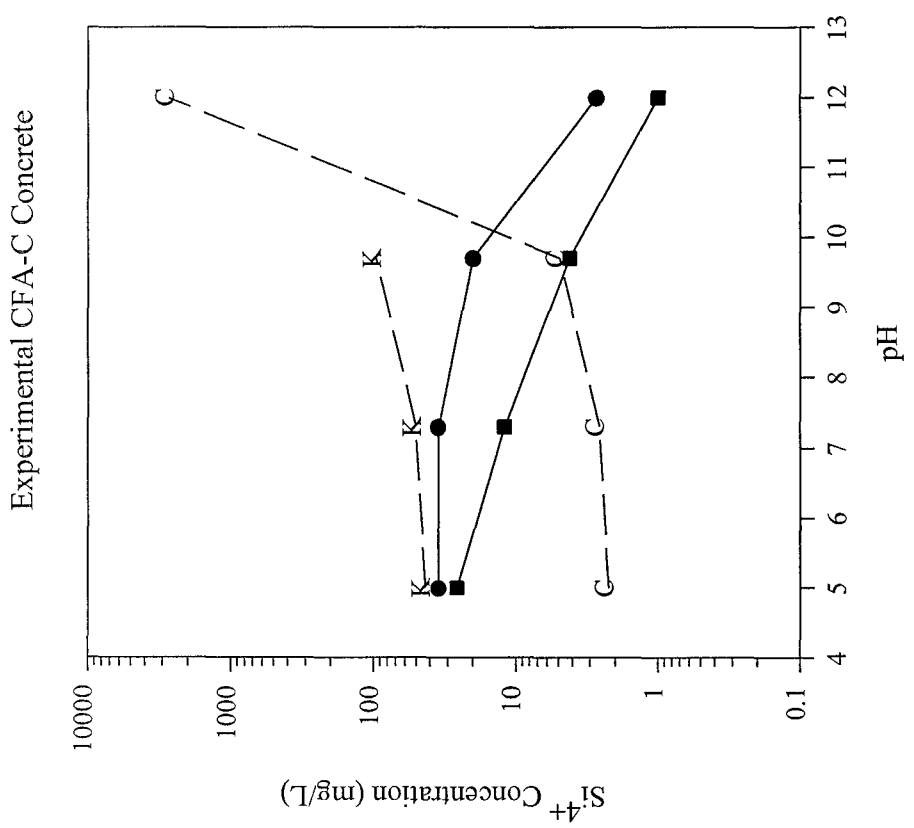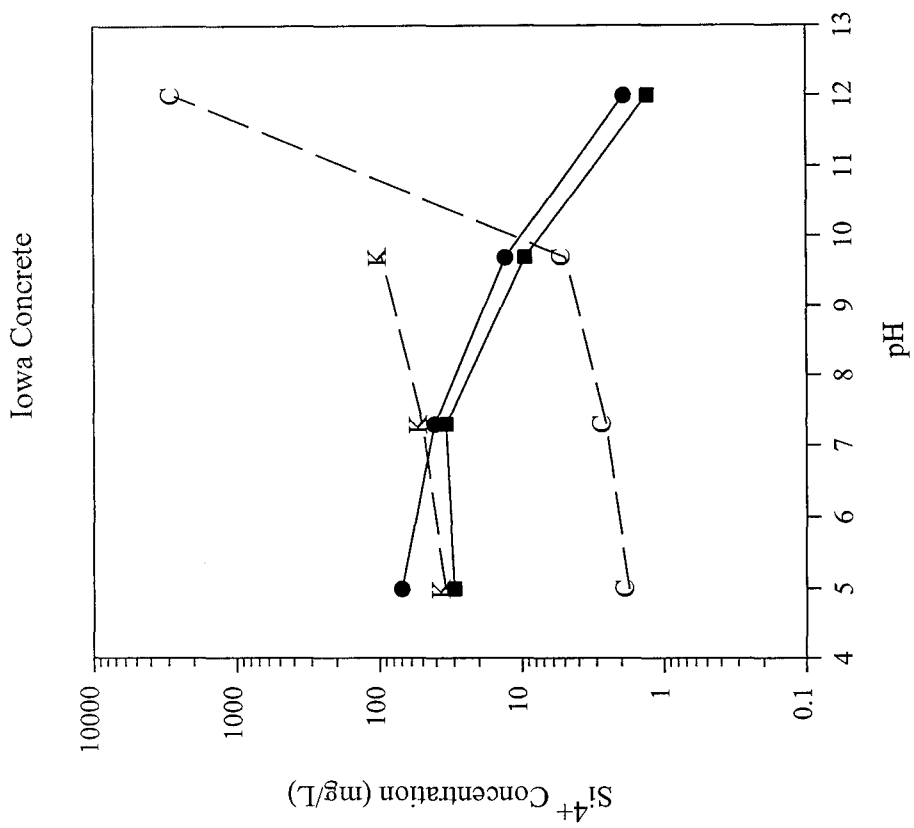
Figure M-4: Comparison Si modeling in CFA-C prism and U.S. 20 slab concrete.

● Highest Leaching Value   ■ Lowest Leaching Value   [C] – Quartz   [K] – SiO$_2$*amorphous
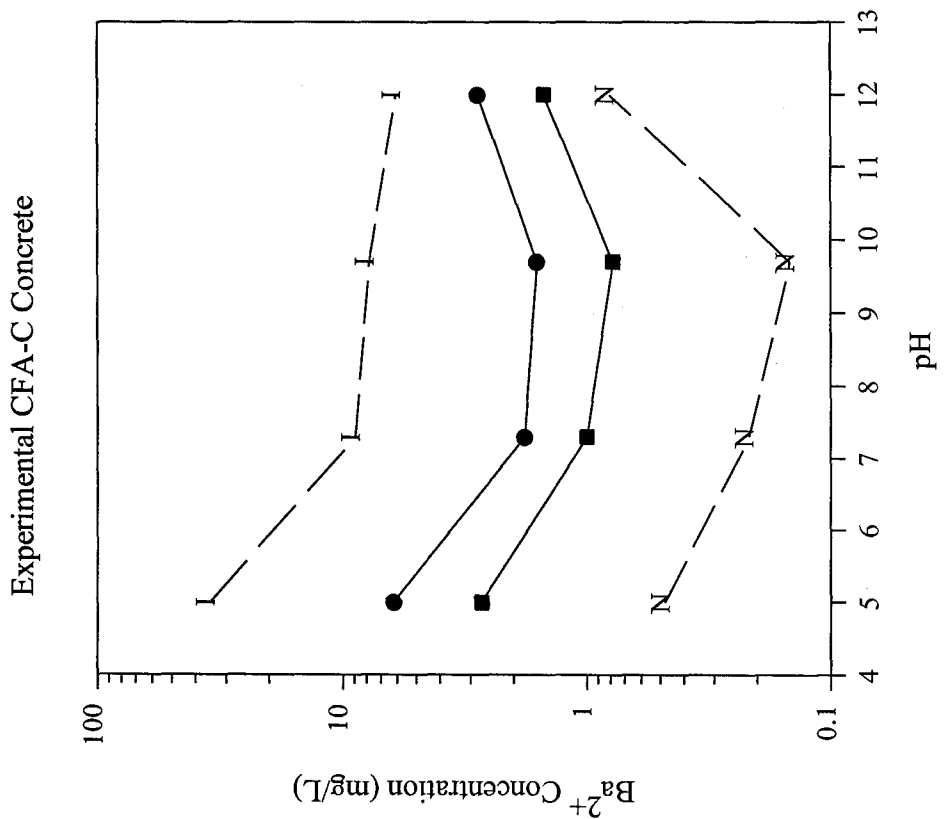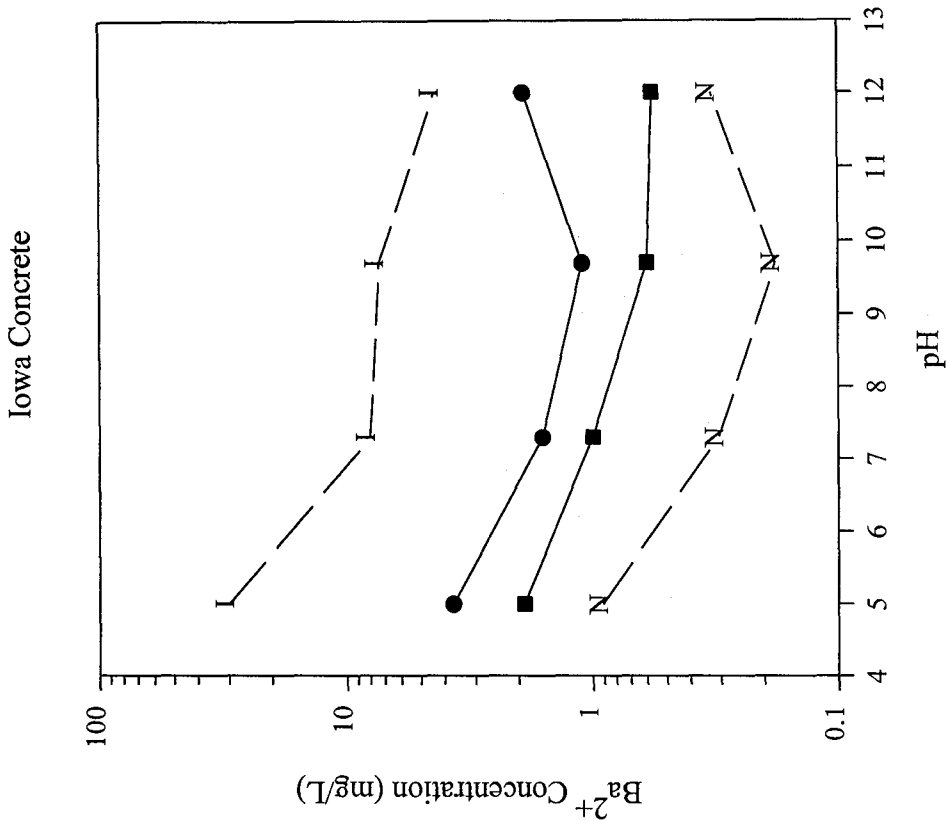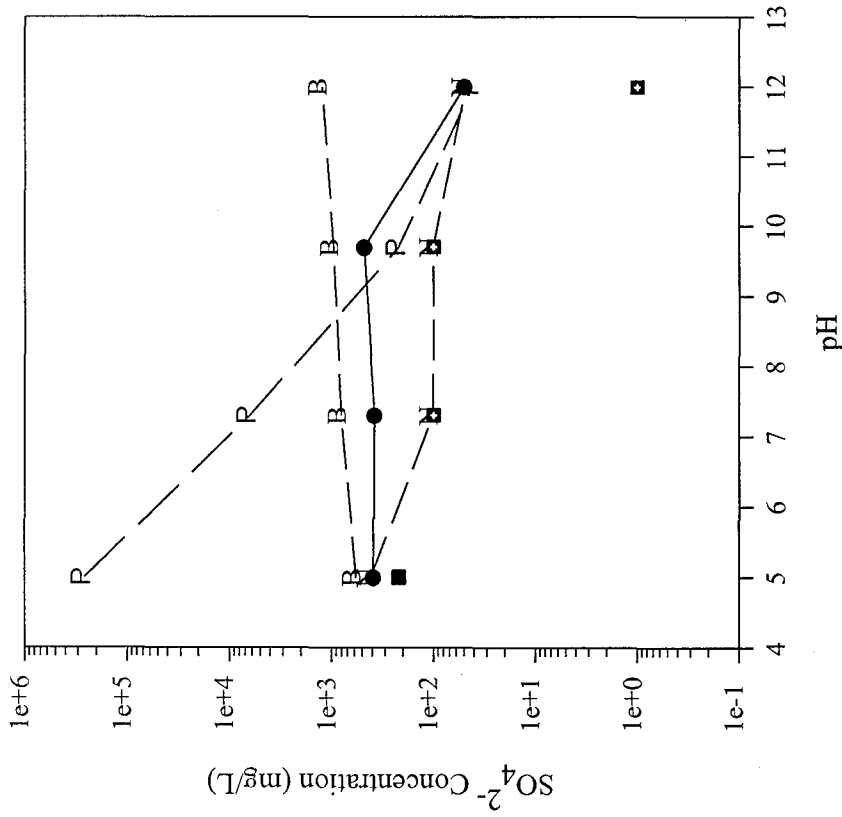
Figure M-5: Comparison Ba modeling in CFA-C prism and U.S. 20 slab concrete.

● Highest Leaching Value   ■ Lowest Leaching Value   [I] – BaCrO₄   [N] – Barite

194
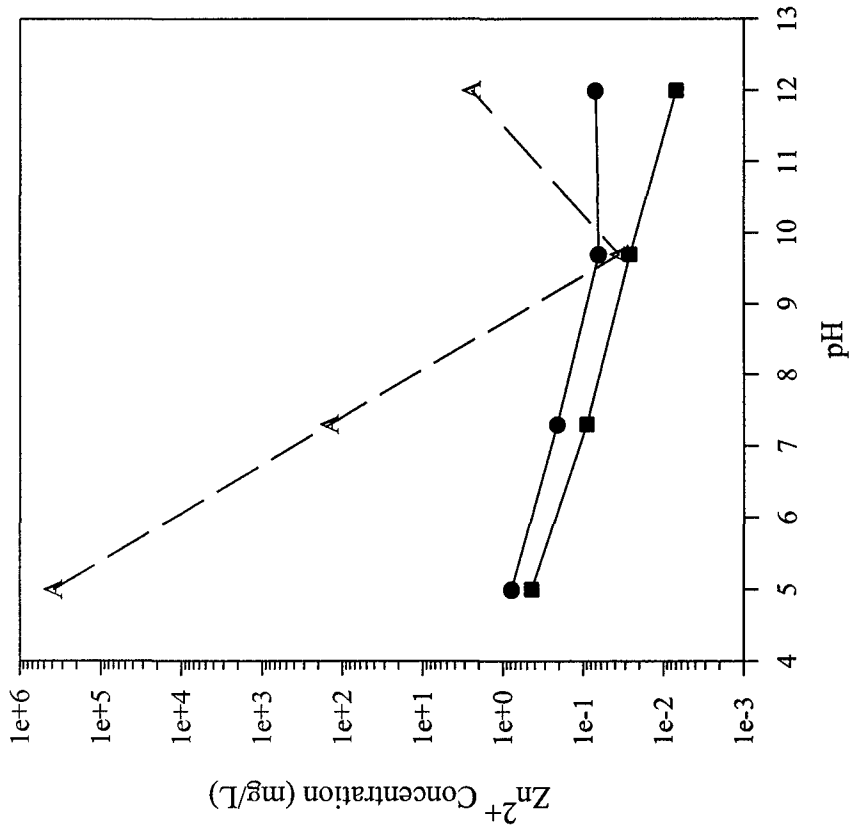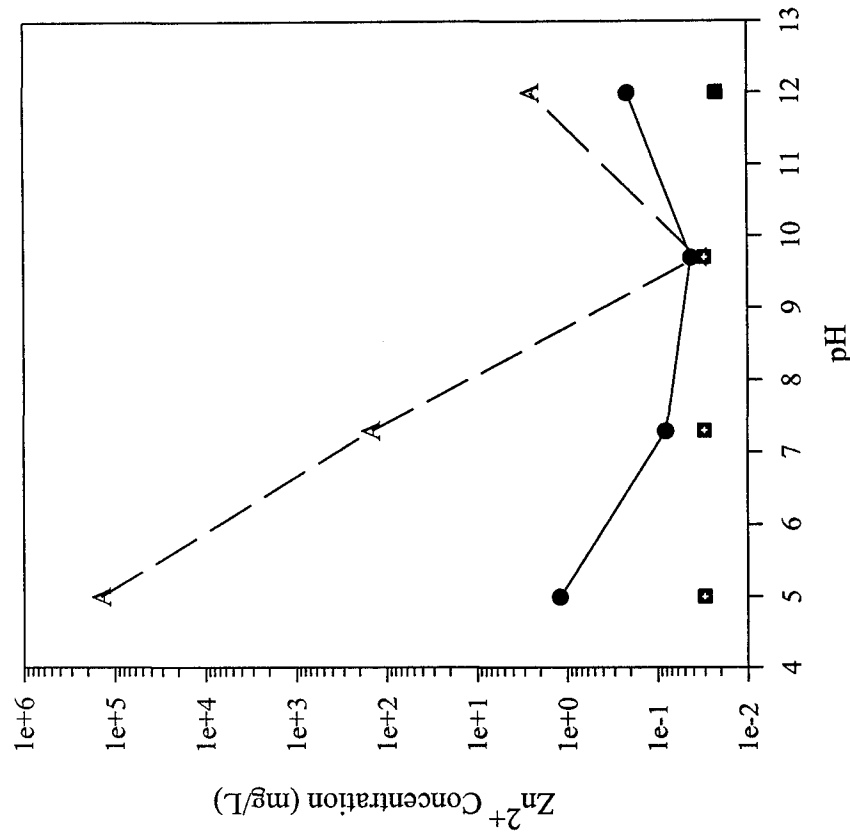
Figure M-6: Comparison Zn modeling in CFA-C prism and U.S. 20 slab concrete. [A] – Zincite

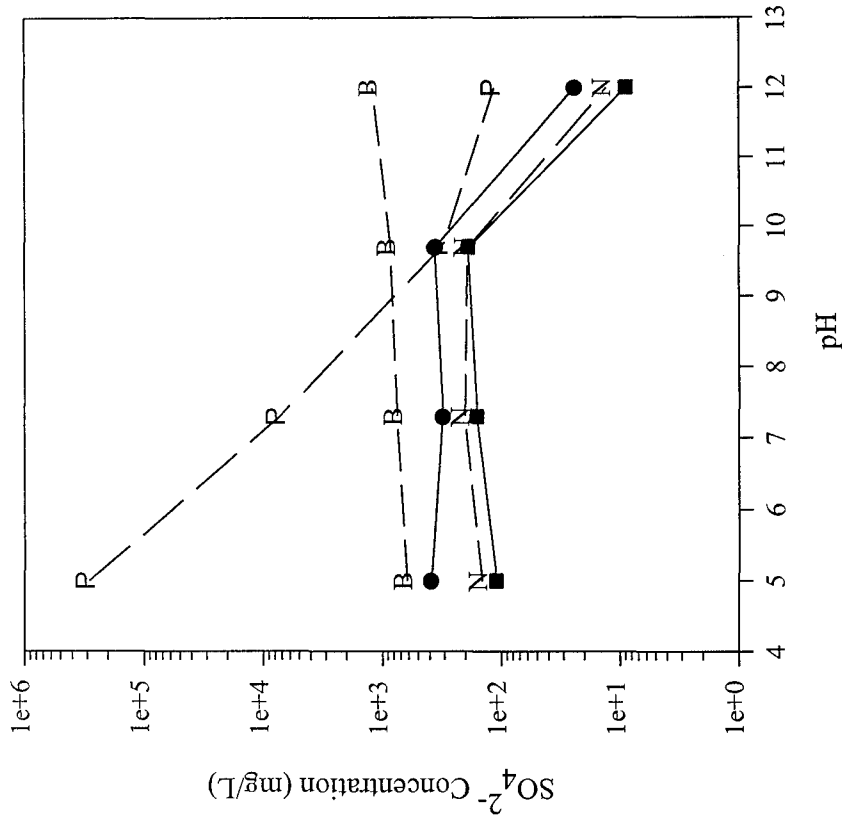• Highest Leaching Value   ■ Lowest Leaching Value   ⊞ Lowest Leaching Value BDL
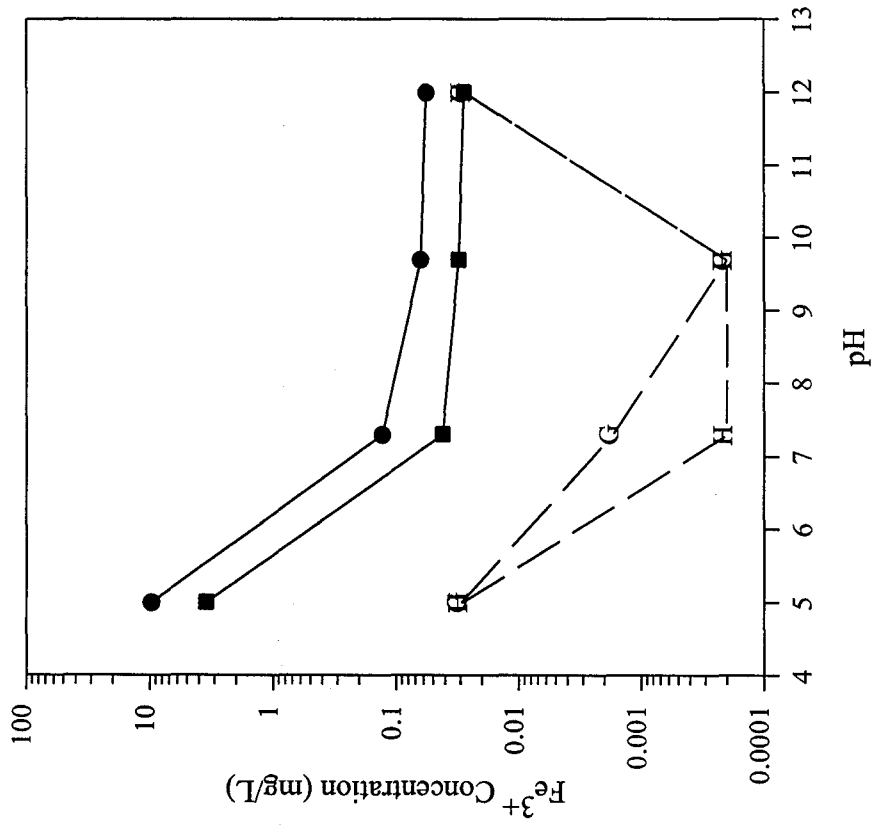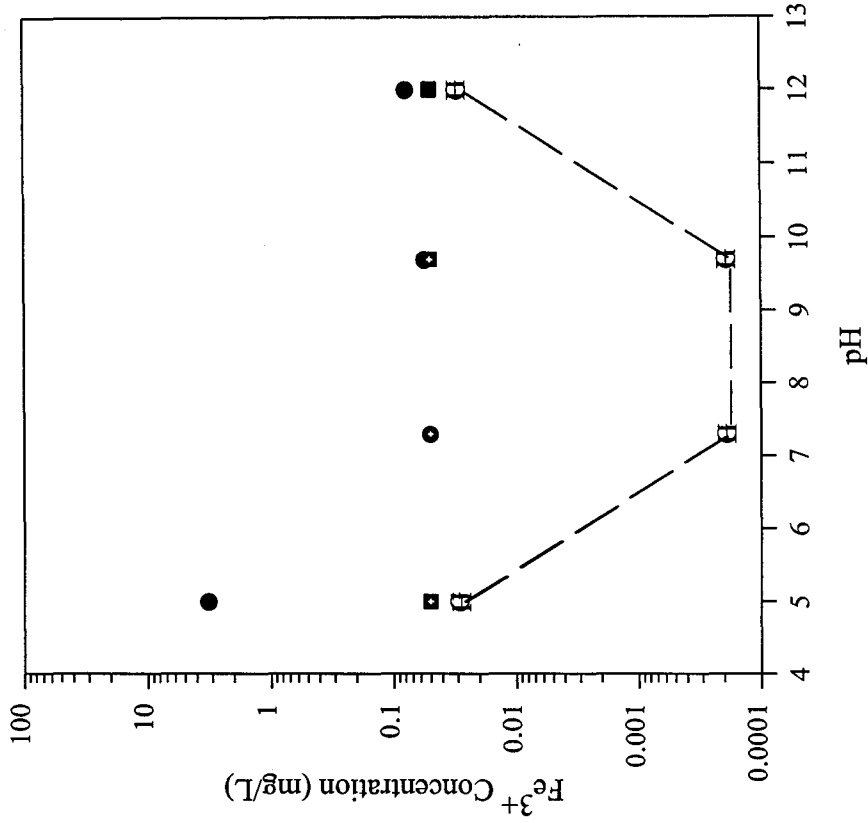
Figure M-7: Comparison Fe modeling in CFA-C prism and U.S. 20 slab concrete.

● Highest Leaching Value ◐ Highest Leaching Value BDL ■ Lowest Leaching Value ▣ Lowest Leaching Value BDL

[G] – Ferrihydrite [H] – Maghemite

Figure M-8: Comparison Cr modeling in CFA-C prism and U.S. 20 slab concrete.

● Highest Leaching Value ◉ Highest Leaching Value BDL ■ Lowest Leaching Value ⊞ Lowest Leaching Value BDL

[I] – BaCrO₄

197

Figure M-9: Comparison CO_3^{2-} modeling in CFA-C prism and U.S. 20 slab concrete.

● Highest Leaching Value ■ Lowest Leaching Value   [E] – Calcite   [F] – Dolomite

Iowa Concrete

Experimental CFA-C Concrete

Figure M-10: Comparison SO_4^{2-} modeling in CFA-C prism and U.S. 20 slab concrete.

● Highest Leaching Value   ■ Lowest Leaching Value   ⊞ Lowest Leaching Value BDL

[N] – Barite   [P] – Ettringite
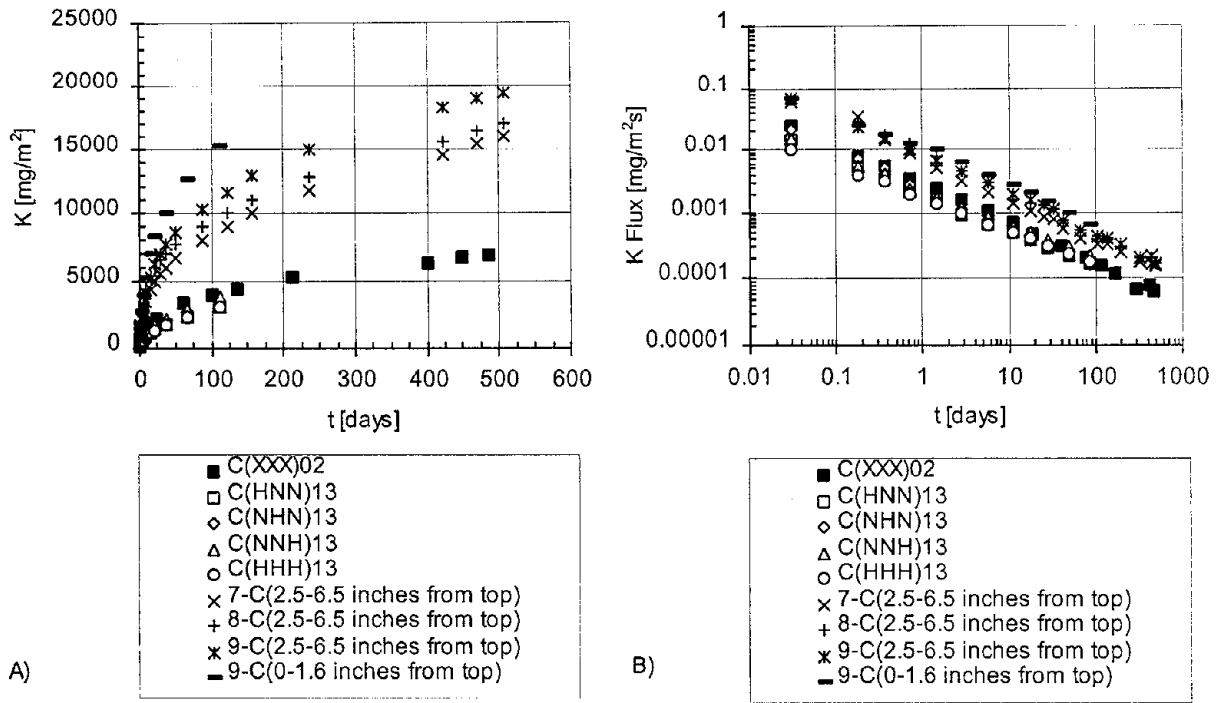
Figure M-11: K release:
A) cumulative mass released in mg/m^2; B) flux released in mg/m^2s.
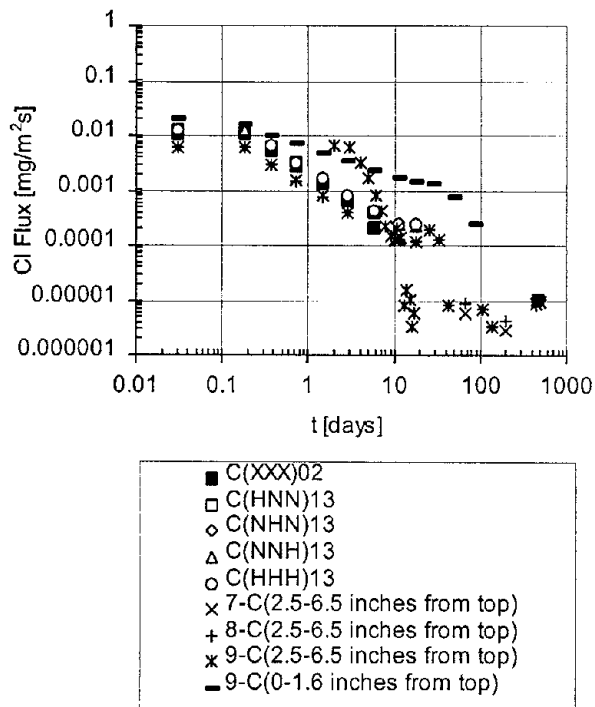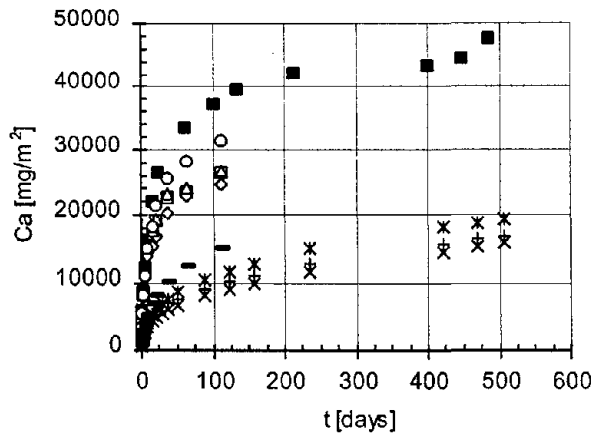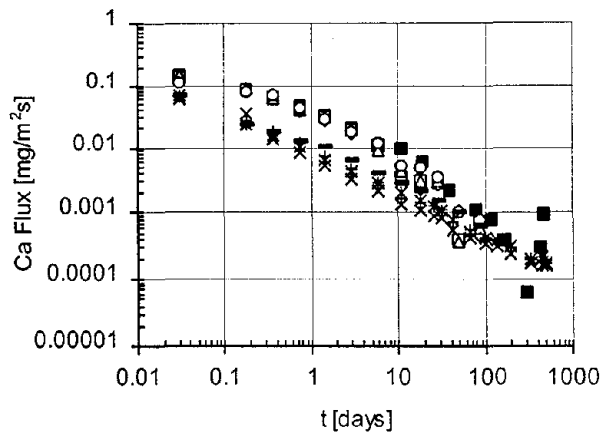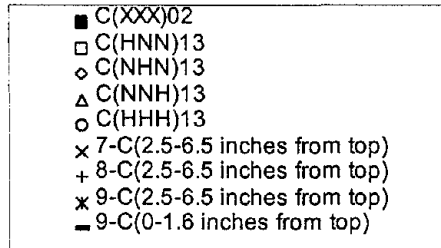

Figure M-12: Cl release: flux released in mg/m^2s.
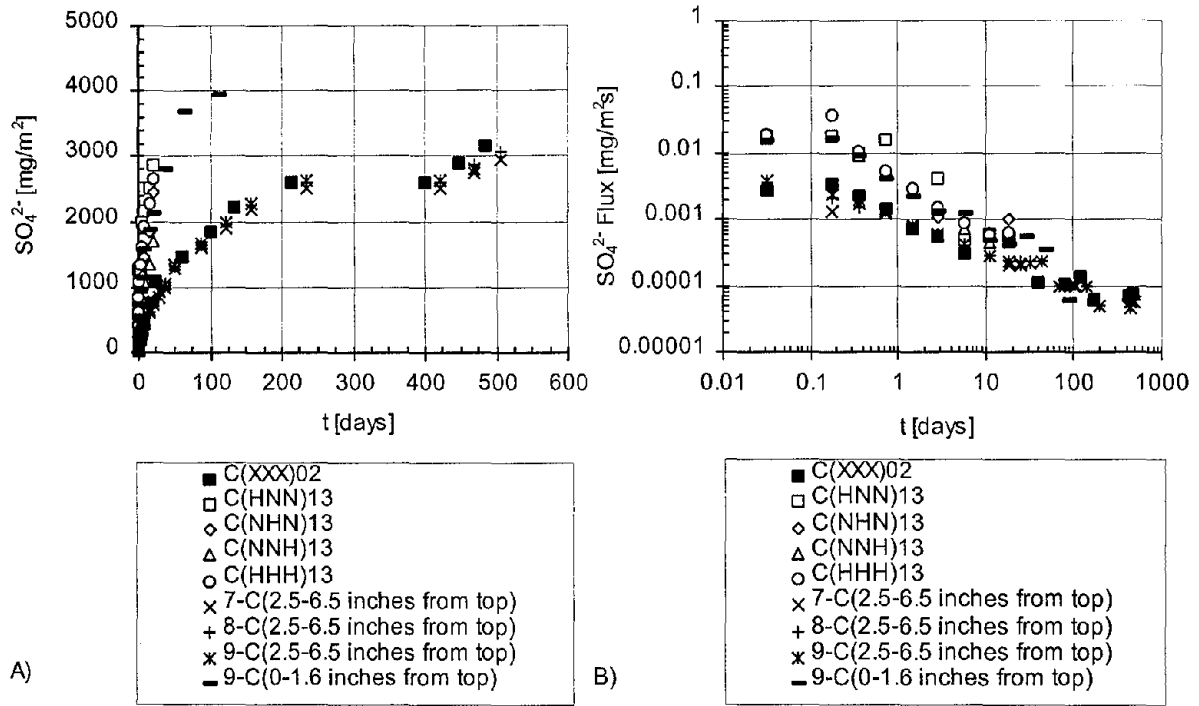
Figure M-13: SO_4^{2-} release:
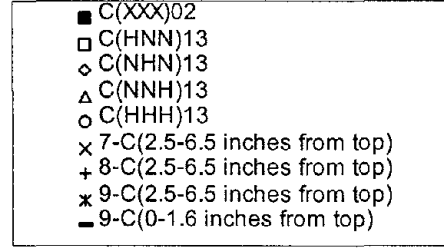A) cumulative mass released in mg/m^2; B) flux released in mg/m^2s.

Figure M-14: Ca release:
A) cumulative mass released in mg/m²; B) flux released in mg/m²s.